

FUNCTION AND DESIGN OF CONFINEMENT REINFORCEMENT IN
PRETENSIONED CONCRETE I-GIRDERS

By

BRANDON E. ROSS

A DISSERTATION PRESENTED TO THE GRADUATE SCHOOL
OF THE UNIVERSITY OF FLORIDA IN PARTIAL FULFILLMENT
OF THE REQUIREMENTS FOR THE DEGREE OF
DOCTOR OF PHILOSOPHY

UNIVERSITY OF FLORIDA

2012

© 2012 Brandon E. Ross

To my wife, Michelle and to my children, Zane, Annie, and Soren

ACKNOWLEDGMENTS

I express gratitude to the many individuals and organizations that have assisted me through the research and writing phases of my dissertation. Foremost I thank my wife, Michelle and my children, Zane, Annie, and Soren. Their sacrifices and support were and are essential fuel to the pursuit of my personal and professional goals.

I also thank my advisor Dr. Trey Hamilton. Dr. Hamilton's superior technical expertise is only surpassed by his exceptional humanity –the perfect combination of attributes for a graduate advisor. Dr. Gary Consolazio served as my co-advisor. Through his encouragement and teaching I was able to lose my fear of finite elements (at least the linear-elastic ones). I am appreciative of the comments and support from my other committee members: Dr. Ronald Cook, Dr. Mang Tia, and Dr. Bhavani Sankar.

Technical and financial assistance for my research was provided by the Florida Department of Transportation. The late Marc Ansley served as the FDOT project manager until his sudden passing in June 2010. I will remember Mr. Ansley for this pearl of wisdom: "You can't tell me how a concrete beam fails unless you can tell me how a concrete cylinder fails."

In summer of 2010 Sam Fallaha took over the role as project manager for the FDOT. I appreciate Mr. Fallaha's technical guidance, which has improved both the quality and the breadth of my research. Mr. Fallaha was also instrumental in seeing that the research schedule did not conflict with the birth of my son, Soren. My wife, son, and I are grateful for this act of kindness.

I thank the other FDOT structures research center personnel who assisted in my project: David Allen, Steve Eudy, Tony Hobbs, Will Potter, Paul Tighe, David Wagner,

and Chris Weigly. Assistance was also given by personnel at the FDOT state materials office: Mark Conley, Alfred Camps, Richard DeLorenzo, and Jordan Nelson.

Many fellow graduate students and other colleagues at the University of Florida worked on aspects of my research. I thank Abraham Alende, Rafael Asencio, Natassia Brenkus, Kunal Malpani, Scott Maul, Kinsman Pearson, Abhay Singh, and Michael Willis. Dr. Chris Ferraro of the University of Florida provided technical assistance to my project, as well as a good laugh when needed.

Test specimens were built by Dura-Stress, Inc. of Leesburg, FL and Standard Concrete Products of Tampa, FL. Material for test samples was donated by Erico, Inteel, and CEMEX.

My research was funded in-part by a University of Florida Alumni Fellowship. I thank the University of Florida for providing me with these funds.

Finally, I wish to thank my parents Ann Marie and Dale Ross, and my late grandmother Martha (Tilly) Goodrich Johnson. Each has provided me with a love of learning that inspires my work past, present, and future.

Go Gators.

TABLE OF CONTENTS

	<u>page</u>
ACKNOWLEDGMENTS.....	4
LIST OF TABLES.....	10
LIST OF FIGURES.....	12
LIST OF ABBREVIATIONS	21
ABSTRACT.....	22
CHAPTER	
1 INTRODUCTION	24
Motivation.....	24
Document Organization.....	25
Original Contribution.....	26
Background.....	26
2 REVIEW OF LITERATURE.....	34
End Region Failure Modes.....	34
Bond-Shear Failure.....	34
Lateral-Splitting Failure.....	35
Code Requirements.....	35
Confinement Reinforcement during Prestress Transfer.....	36
Confinement Reinforcement during Loading.....	37
Shear Capacity.....	38
Transverse Reinforcement	38
Vertical Reinforcement	39
Ductility	40
Development Length.....	40
Shear Friction.....	41
Hoyer Effect	41
Summary of Literature	42
3 TEST GIRDER DESIGN AND CONSTRUCTION.....	50
Test Girder Classification	50
Test Girder Design.....	51
Girder Construction.....	54
Material Properties.....	58
4 SETUP AND TEST PROCEDURES.....	83

	Data Collection during Fabrication	83
	Load Test Setup and Procedures	84
	Coordinate System	86
5	INSTRUMENTATION	90
	Types and Descriptions	90
	Strain Gage Coordinates	92
6	RESULTS AND DISCUSSION: FABRICATION	108
	Strain Data	108
	Concrete Strain	108
	Confinement Reinforcement and Bearing Plate Strain	111
	Transfer Length	117
	Crack Data	120
	Girders H and V	122
	Girders W, F, and D	124
	Variable Comparison and Discussion	126
	Summary and Conclusions	130
7	RESULTS AND DISCUSSION: LOAD TESTS	157
	Failure Modes	157
	Load Test Results	159
	HC	159
	HU	160
	VC	161
	VU	162
	WN	163
	WB	164
	FN	166
	FB	168
	DC	168
	DM	169
	Confinement Reinforcement and Bearing Plates	171
	Girders W and F	171
	Girders H and V	174
	Bearing Plates	175
	Variable Comparisons	176
	Horizontal Reinforcement	177
	Embedded Steel Bearing Plate	177
	Confinement Reinforcement	178
	Strand Quantity	179
	Strand Placement	180
	Code Comparisons	181
	Summary and Conclusions	184

8	ANALYTICAL EVALUATION OF GIRDERS UNDER APPLIED LOADS	211
	Model Configuration	211
	Small Beam Model.....	213
	Model Validation and Verification.....	213
	Parametric Studies	216
	Bearing Pad Stiffness	216
	Bearing Pad Geometry	216
	Effect of Steel Bearing Plate.....	220
	Bearing Pad Width Effect on Transverse Force	221
	Parametric Study Conclusions	223
9	ANALYTICAL EVALUATION OF GIRDERS DURING PRESTRESS TRANSFER.....	247
	Model Configuration	247
	Model Validation and Verification.....	250
	Transverse Force Quantification	253
	Parametric Studies	254
	Strand Release Parametric Study	254
	Bearing Plate Contribution.....	256
	Transfer Length Parametric Study	257
	End Stresses due to Prestress Forces.....	258
	Transverse Action due to Self-Weight.....	261
	Parametric Study Summary and Conclusions	263
10	ULTIMATE STRENGTH DESIGN MODEL	285
	Model Derivation.....	287
	Transverse Tie Force.....	287
	Strand Anchorage Force.....	289
	Quantity and Placement	292
	Model Comparison with Experimental Results.....	294
	Summary and Conclusions	296
11	SERVICABILITY MODEL.....	302
	Causes of Bottom Flange Splitting at Prestress Transfer	303
	Hoyer Effect.....	303
	Eccentric Prestress Forces.....	304
	Self-Weight Reaction	304
	Transverse Splitting Stress Model Derivation.....	305
	Hoyer Stress.....	306
	Peeling Stress	310
	Self-Weight Reaction Stress.....	312
	Superposition of Stresses.....	312
	Stress Calculations for Experimental Girders.....	313

Model Comparison with Experimental Crack Data.....	316
Summary and Conclusions	317
12 CONCLUDING REMARKS	330
Experimental Program Summary	330
Analytical Program Summary.....	331
Conclusions	332
Function of Confinement Reinforcement	332
Interaction of Variables with Confinement Reinforcement	333
Bottom Flange Serviceability Design Model	333
Confinement Reinforcement Ultimate Strength Design Model.....	334
Recommendations.....	334
Final Comments.....	336
LIST OF REFERENCES	337
BIOGRAPHICAL SKETCH	340

LIST OF TABLES

<u>Table</u>	<u>page</u>
3-1 Test girder and specimen variables.....	78
3-2 Specified material properties	78
3-3 Fabrication important dates	79
3-4 Tested concrete compressive strengths.....	80
3-5 Prestressing steel properties	81
3-6 Grout strength for NASP Tests	81
3-7 NASP Test Results	81
3-8 Steel reinforcement properties.....	82
4-1 Load test dates	89
5-1 Instrumentation types and labels.....	100
5-2 Specimen HC strain gage coordinates.....	101
5-3 Specimen HU strain gage coordinates.....	102
5-4 Specimen VC strain gage coordinates	103
5-5 Specimen VU strain gage coordinates	104
5-6 Specimen WN strain gage coordinates	104
5-7 Specimen WB strain gage coordinates	105
5-8 Specimen FN strain gage coordinates	105
5-9 Specimen FB strain gage coordinates	106
5-10 Specimen DC strain gage coordinates.....	106
5-11 Specimen DM strain gage coordinates	107
6-1 Girders H and V fabrication events and stages	153
6-2 Tensile strain girders H and V	153
6-3 Girders W and F fabrication stages.....	153

6-4	Confinement reinforcement strain after prestress transfer	154
6-5	Confinement and plate forces	154
6-6	Recommended action for web splitting cracks (Tadros et al. 2010)	154
6-7	Girders H and V construction events and inspection dates	155
6-8	Girders W, F, & D construction events and inspection dates	156
7-1	Transverse forces in W and F specimens	208
7-2	Maximum superimposed shear	208
7-3	Variable comparisons	209
7-4	Material properties for capacity calculations	209
7-5	Experimental moments and nominal moment capacities	210
7-6	Experimental shear and nominal shear capacities	210
8-1	Small beam FE model geometry	245
8-2	Bearing stiffness sensitivity study details	245
8-3	Model details: parametric study of bearing pad width	245
8-4	Bearing pad properties	246
9-1	Bearing plate study summary of transverse (x-x) stresses and forces	284
9-2	Summary of transverse (x-x) stress at girder end due to strand cutting	284
9-3	Summary of transverse (x-x) stress at girder end due to strand cutting	284
9-4	Transverse (x-x) stress due to self-weight	284
11-1	Strand and concrete properties of experimental girders	328
11-2	Model vs. FE for maximum peeling stress condition	328
11-3	Model vs. FE for combined stress condition	328
11-4	Hoyer stresses end of specimen WN	328
11-5	Peeling stresses at end of specimen WN	328
11-6	Transverse splitting stresses and splitting crack data	329

LIST OF FIGURES

<u>Figure</u>	<u>page</u>
1-1 I-Girder highway bridge.....	29
1-2 Cross-section 54 in. deep Florida I-Beam.....	29
1-3 End region reinforcement.....	30
1-4 FIB-54 end region reinforcing detail	30
1-5 Confinement reinforcement.....	31
1-6 End region	31
1-7 End region strut-and-tie	31
1-8 Shear span	32
1-9 Transfer length	32
1-10 Development length	33
1-11 Strand debonding.....	33
2-1 End region strut-and-tie behavior	44
2-2 Bond-shear failure	44
2-3 Slitting crack	44
2-4 Confinement reinforcement.....	45
2-5 Splitting crack at prestress transfer	45
2-6 Transverse tie above bearing	46
2-7 End region strut and tie models.....	46
2-8 Flange cracking in girder with debonded strands concentrated below web	47
2-9 Confinement reinforcement as shear reinforcement.....	47
2-10 Shear-friction model.....	48
2-11 Hoyer Effect.....	49
3-1 Labeling scheme	60

3-2	Specimen labels and graphical descriptions	61
3-3	Cross-section FIB-54	62
3-4	Strand layout and prestressing details	62
3-5	Strand bond and shielding patterns.....	63
3-6	Reinforcement for girder H.....	64
3-7	Reinforcement for girder V.....	65
3-8	Reinforcement for girders W and F	66
3-9	Reinforcement for Girder D.....	67
3-10	Reinforcement and bearing plate details.....	68
3-11	Confinement reinforcement schemes.....	69
3-12	Cast-in-place deck reinforcement.....	69
3-13	Girder orientation during fabrication	70
3-14	Tension pattern and wire break locations	70
3-15	Reinforcement girder H.....	71
3-16	Reinforcement girder V	71
3-17	Reinforcement girder W	71
3-18	Reinforcement girder F	72
3-19	Reinforcement girder D.....	72
3-20	Concrete placement and internal consolidation phase 1	73
3-21	Concrete placement phase 2.....	73
3-22	Girder finished surface	74
3-23	Girders covered with tarps	74
3-24	Strand release patterns.....	75
3-25	Test girder lifted by crane	75
3-26	Girder resting on dunnage on stressing bed	76

3-27	Girder H on truck prior to transit	76
3-28	Deck Construction	77
3-29	Concrete placement	77
4-1	Test set-up.....	87
4-2	Support conditions.....	87
4-3	Test specimen and load frame	88
4-4	Coordinate system relative to load and supports.....	88
5-1	MS gage installation.....	93
5-2	XS gage installation	93
5-3	ES gage installations.....	94
5-4	V gage installation	95
5-5	Wire harness and plywood bulkhead	95
5-6	S gage installation	96
5-7	LVDT placement and labels.....	96
5-8	LVDT and support frame.....	97
5-9	Girder H and V strands monitored by LVDT	97
5-10	Wood frame and LVDTs	98
5-11	Girder W, F, and D strands monitored by potentiometer.....	98
5-12	Aluminum brackets and linear potentiometers on strands.....	99
5-13	Load cells below hydraulic actuators.....	99
6-1	Girders H and V strand cutting stages	133
6-2	Transverse Strain HC.....	133
6-3	Flange displaced shapes for specimen HC.....	134
6-4	Shear and moment during release, lifting, storage	134
6-5	Girders W and F strand cutting stages.....	135

6-6	Girders W and F strand bond patterns	135
6-7	Bearing plate strain	136
6-8	Flange displaced shapes specimens FN and FB.....	137
6-9	Displaced shapes specimen WB and WN.....	138
6-10	WB Confinement reinforcement strain at 2 in. and 9 in. from end of girder.....	139
6-11	WN Confinement reinforcement strain at 2 in. and 9 in. from end of girder.....	140
6-12	FB confinement reinforcement strain at 2in. and 9in. from end of girder	141
6-13	FN Confinement reinforcement strain at 2in. and 9in. for end of girder	142
6-14	Confinement reinforcement average strain at prestress release	142
6-15	Forces in reinforcement and plates after prestress transfer	143
6-16	Strain gages for measuring transfer length	144
6-17	Transfer length in girders H and V.....	144
6-18	Transfer length girder F	145
6-19	Web splitting and flange splitting cracks	145
6-20	Girder H and V cracks prior to load tests	146
6-21	Flange splitting crack intersecting outer strand.....	147
6-22	Web splitting cracks specimens H and V	147
6-23	Maximum crack widths girders H and V	148
6-24	Flange splitting crack data girders H and V	148
6-25	Girders W, F, & D web and flange splitting cracks	149
6-26	End of bottom flange covered by portion of steel bulkhead	150
6-27	Girder F flange splitting cracks	150
6-28	Flange splitting cracks girders W, F, and D	151
6-29	Maximum crack widths girders W, F, and D.....	151
6-30	Web splitting cracks girders W, F, and D	152

6-31	Girder D flange splitting cracks.....	152
7-1	Web-shear failure.....	186
7-2	Bond-shear failure.....	186
7-3	Lateral-splitting failure.....	187
7-4	Lateral-splitting failure mechanics.....	187
7-5	Specimen HC load test summary.....	188
7-6	Specimen HU load test summary.....	189
7-7	Specimen VC load test summary.....	190
7-8	Specimen VU load test summary.....	191
7-9	Specimen WN load test summary.....	192
7-10	Specimen WB load test summary.....	193
7-11	Specimen FN load test summary.....	194
7-12	Strut-and-tie behavior specimen FN.....	195
7-13	Longitudinal splitting cracks on bottom of specimen FN.....	195
7-14	Confinement reinforcement strain specimen FN.....	196
7-15	Specimen FB load test summary.....	197
7-16	Specimen DC load test summary.....	198
7-17	Specimen DM load test summary.....	199
7-18	Strain gage placement girders W, F, and D.....	200
7-19	Confinement stress at shear = 375 kip.....	200
7-20	Confinement stress at ultimate capacity.....	201
7-21	Transverse (x-x) stress profiles at bearing plate centerline.....	201
7-22	Strain gage placement girders H and V.....	202
7-23	Specimens HC and VC confinement reinforcement and bearing plate transverse (x-x) forces due to maximum applied load.....	203
7-24	Bearing plate stress due to applied load.....	204

7-25	Bearing plate force due to applied load.....	204
7-26	Percent of transverse force due to applied loads carried by bearing plate.....	205
7-27	Percent of transverse force carried by bearing plate in WB and FB	205
7-28	Maximum superimposed shear.....	206
7-29	Girder D bottom flange cracking.....	206
7-30	Relationship between strand quantity and end region capacity	207
7-31	Comparison of FB and WB	207
8-1	Coordinate system relative to load and supports.....	225
8-2	FE Model Configuration	225
8-3	Rigid shell and link elements	225
8-4	Bearing Pad.....	226
8-5	End Region Dimensions	226
8-6	FE Model Symmetry.....	227
8-7	FE Model Top View.....	227
8-8	Comparison of small beam test set-up, FE model details, and FE mesh.....	228
8-9	Bearing pad axial stiffness.....	229
8-10	Transverse strain (x-x) at end of beam for proposed and refined mesh.....	229
8-11	Small beam transverse (x-x) strain profile (V=15kip).....	230
8-12	Small beam load vs. deflection at load point.....	230
8-13	Small beam load vs. strain S5 (y-y).....	231
8-14	Small beam load vs. average of strain S11 and S12 (y-y)	231
8-15	Maximum principal tensile (P1) strain location.....	232
8-16	Sensitivity study maximum transverse (x-x) strain.....	232
8-17	FIB and rectangular section FE models	233
8-18	Location of maximum flexural strain	233

8-19	Bursting behavior	234
8-20	Normalized transverse (x-x) strain at end of FIB-8	234
8-21	Flexural behavior	235
8-22	Normalized transverse (x-x) strain at end of FIB-16	235
8-23	Normalized transverse (x-x) strain vs. bearing pad width.....	236
8-24	Normalized transverse (x-x) strain vs. bearing pad width, FIB.....	237
8-25	Normalized transverse (x-x) strain vs. bearing pad width, Rectangular Section.....	238
8-26	Normalized transverse (x-x) strain vs. bearing pad width, small beam.....	239
8-27	Steel bearing plate beam and model.....	240
8-28	Bearing Plate Discretization.....	241
8-29	Effect of bearing plate and bearing pad width on transverse (x-x) strain.....	241
8-30	Normalized transverse (x-x) strain vs. bearing pad width, FIB Section with steel bearing plate	242
8-31	Integration area for transverse force	243
8-32	Element (x-x) stress and y-z area.....	243
8-33	Transverse (x-x) force vs. bearing geometry	244
9-1	Coordinate system and free-body diagram of girder after prestress transfer	264
9-2	FE model details.....	265
9-3	Strand layout and element mesh.....	266
9-4	Verification study mesh densities	266
9-5	Verification study principal tensile stresses.....	267
9-6	Displaced shape.....	267
9-7	Comparison of experimental and FE model strains at cracks	268
9-8	Comparison of experimental and FE model transverse (x-x) strain.....	269
9-9	Comparison experimental and FE model longitudinal (y-y) strain.....	269

9-10	Comparison experimental and FE model vertical (z-z) strain.....	270
9-11	Integration area for lateral force.....	270
9-12	Element x-x stress and y-z area	271
9-13	Transverse (x-x) stress at stages of prestress transfer	272
9-14	Transverse force vs. % strands released.....	273
9-15	Transverse (x-x) stress distribution at stage 1	274
9-16	Transverse (x-x) stress distribution at stage 2	275
9-17	Transverse force vs. length of prestress transfer.....	276
9-18	Transverse stress distribution 17.5in. transfer length	277
9-19	Transverse stress distribution 42.5in. transfer length	278
9-20	Length of tension area vs. transfer length.....	279
9-21	Transverse (x-x) stress at MID section through bottom flange.....	279
9-22	Flange splitting cracks at girder end.....	280
9-23	Lines for stress calculations.....	280
9-24	FE model stresses at girder end.....	281
9-25	Transverse (x-x) stress at mid-flange line	281
9-26	Average transverse (x-x) stress at end of girder due to strand cutting	282
9-27	Transverse (x-x) stress due to self-weight	282
9-28	Transverse (x-x) stress due to self-weight	283
10-1	Local and general zones.....	297
10-2	Illustration of transverse and frictional forces caused by the Hoyer effect.....	297
10-3	Transverse tie force strut-and-tie models.....	298
10-4	Node layout	299
10-5	Strand anchorage force	299
10-6	Design model compared to nominal strength of experimental girders	300

10-7	Design model compared to experimental girders at maximum shear	300
10-8	Design model compared to experimental girders at maximum shear	301
11-1	Hoyer Effect.....	318
11-2	Flange tension due to outer strands	319
11-3	Camber due to prestress force	319
11-4	Self-weight reaction effects.....	320
11-5	Flange splitting in experimental girder.....	320
11-6	Strand cutting conditions.....	321
11-7	Strand physical analog.....	321
11-8	Calculated radial stress (p) distribution	322
11-9	Effect of cover distance on calculated radial stress (p)	322
11-10	Concrete stress distribution due to Hoyer Effect	323
11-11	Stresses at plane cut through strand and concrete	323
11-12	Bottom flange free body diagram	324
11-13	Analysis sections for FIB bottom flange.....	324
11-14	Strand bond and shielding pattern specimen WN	325
11-15	Transverse (x-x) splitting stress at end of specimen WN.....	325
11-16	Strand pattern CN, PT, and LB	326
11-17	Strand pattern SL.....	326
11-18	Calculated transverse splitting stress vs. experimental crack length	327
11-19	Calculated transverse splitting stress vs. experimental crack area	327

LIST OF ABBREVIATIONS

AASHTO	American Association of State Highway and Transportation Officials
ACI	American Concrete Institute
FDOT	Florida Department of Transportation
FEA	Finite Element Analysis
FE	Finite Element
FIB	Florida I-Beam
ES	Strain gage placed internally in concrete
LRFD	Load and resistance factor design
LVDT	Linear variable differential transformer
MCFT	Modified Compression Field Theory
MS	Strain gage placed on mild steel reinforcement
SG	Strain gage placed on concrete surface during load testing
VWG	Vibrating wire strain gage
XS	Strain gage placed on concrete surface during prestress transfer

Abstract of Dissertation Presented to the Graduate School
of the University of Florida in Partial Fulfillment of the
Requirements for the Degree of Doctor of Philosophy

FUNCTION AND DESIGN OF CONFINEMENT REINFORCEMENT IN
PRETENSIONED CONCRETE I-GIRDERS

By

Brandon E. Ross

August 2012

Chair: H.R. (Trey) Hamilton III
Cochair: Gary R. Consolazio
Major: Civil Engineering

Confinement reinforcement is placed near the end of pretensioned concrete I-girders to enclose prestressing strands in the bottom flange. Experimental and analytical test programs were conducted to investigate the function of confinement reinforcement, and to provide the basis for a confinement reinforcement design model. Five 54-in. deep Florida I-Beam (FIB-54) girders were fabricated and load tested in the experimental program. Each end of each girder had a different combination of variables, which resulted in ten unique test specimens. Variables included: presence or absence of embedded steel bearing plates, quantity and configuration of confinement reinforcement, strand bond pattern, strand quantity, and quantity of horizontal and vertical end region reinforcement. Data were collected during and after prestress transfer to evaluate the effects of test variables on bottom flange cracking. Load tests were then conducted on each specimen (end) to determine the effects of test variables on girder behavior and capacity. Specimens were loaded in three-point bending at a shear span-to-depth ratio of 2.0. Failure modes in the test program included web-shear, bond-shear, and lateral-splitting. Data from fabrication and load testing were used to

validate linear-elastic finite element models. Validated models were then used to investigate additional variables such as: Bearing pad geometry and stiffness, cross-section geometry, prestress release sequence, and strand transfer length. Building on the experimental and analytical results, serviceability and ultimate strength design models were created for the bottom flange of pretensioned I-girders. The serviceability model is specific to FIB cross-sections and can be used to evaluate transverse splitting stresses which cause bottom flange cracking. The ultimate strength model is general for any pretensioned I-girder cross-section and can be used to design bottom flange confinement reinforcement to mitigate lateral-splitting failure. Both the serviceability and ultimate strength models were found to be in good agreement with experimental data. Other primary outcomes of the research include an improved understanding of the function of confinement reinforcement during prestress transfer and at ultimate load, and an improved understanding the interaction between confinement reinforcement and the other test variables.

CHAPTER 1 INTRODUCTION

Motivation

Of the almost 12,000 bridges in Florida's public road system, approximately half utilize prestressed concrete as the structural system (FHWA, 2010). Simple-span pretensioned concrete I-girders are the most common type of prestressed concrete structures, and are ubiquitous in Florida's highway system (Figure 1-1). In 2009, the Florida Department of Transportation (FDOT) introduced the Florida I-Beam (FIB) (Figure 1-2) for use in highway bridges. The FIB girders "were developed to be more efficient to fabricate, safer to construct, and more cost effective when compared to the [previously] used prestressed beams" (FDOT 2009a).

To further improve the efficiency of FIB girders, it is desirable to investigate the feasibility of reducing reinforcement placed in the end region (Figure 1-3). End region reinforcement is specified by FDOT standard details (Figure 1-4), which are based on historic FDOT details, code requirements, and constructability considerations (Nolan 2009; Fallaha 2009). There is particular incentive to investigate confinement reinforcement, which is placed in the bottom flange around prestressing strands (Figure 1-3). The current use of confinement reinforcement is limited by the following:

- Confinement reinforcement approximately doubles the amount of time required to place reinforcement in I-girders (Magus 2010).
- Code provisions governing confinement reinforcement are based on limited experimental data. The interaction of confinement reinforcement and other end region design variables has not been studied.
- Code provisions governing confinement reinforcement are prescriptive and do not provide a rational model for design.

Previous research (discussed in the Chapter 2) has focused on the effects of confinement reinforcement but does little to address its function. For purposes of this document, the “function” of confinement reinforcement is defined as how, why, where, and when confinement reinforcement acts in the end region structure.

Research presented in this document made use of analytical and experimental methods to investigate the function of confinement reinforcement. Interaction between confinement reinforcement and other end region variables was also considered. One goal of the research was to provide a rational model for the design of confinement reinforcement. Experimental results coupled with a rational model may justify a reduction in the quantity of reinforcement in the end region, thereby improving the efficiency of pretensioned I-girders.

In addition to having sufficient strength pretensioned I-girders must also satisfy serviceability requirements. Bottom flange splitting cracks are a particular serviceability concern in girders with relatively slender bottom flanges such as the FIB. Accordingly, development of a serviceability design model for the bottom flange of FIB girders was part of the research program. Such a model can improve the efficiency of FIB girders by giving engineers a tool for designing bottom flanges that are less prone to splitting cracks.

Document Organization

This document begins with a summary of the literature and code provisions germane to confinement reinforcement. Chapters following the literature review describe the experimental and analytical research programs and present design models for confinement reinforcement. As relevant, chapters include background information

and conclusions specific to that chapter. The final chapter summarizes the work completed and presents overall conclusions and recommendations.

Original Contribution

Of the few studies that have been conducted investigating confinement reinforcement, most have focused on the effects of confinement reinforcement and provide little or no information on its function. The first goal of the presented research was to understand the function of confinement reinforcement. This means determining how, why, where, and when confinement reinforcement acts in the end region structure.

The end region of pretensioned concrete I-girders can have many design variations such as: placement and quantity of horizontal and vertical reinforcement, placement and shielding of prestressing strands, magnitude of prestress force, and diameter of prestressing strands; just to name a few. The second goal of this research was identification of the ways and means by which confinement reinforcement interacts with other variables in the end region.

Building on the outcome of the first two goals, the final goal was to create rational procedures for designing confinement reinforcement. Each of the goals represents an original contribution to the field of structural engineering.

Background

As with any technical subject, pretensioned concrete has specific jargon. This section discusses some of the terms, phrases, and concepts germane to the study of pretensioned concrete.

Confinement reinforcement. Confinement reinforcement is mild steel reinforcement placed around prestressing strands in the bottom flange of precast pretensioned concrete girders (Figure 1-5).

End region. The end region is loosely defined as the portion of a girder located within one and a half member depths from the girder end (Figure 1-6). The end region serves two critical functions: 1) Force transfer between the prestressing strands and concrete, and 2) Delivery of shear forces to the support. Mild reinforcement, including confinement reinforcement, is placed in the end region to aid in these functions.

Prestress transfer. In precast pretensioned concrete construction, concrete is cast around steel strands that have been preloaded in tension. After concrete is sufficiently cured tension force in the strands is released, thereby transferring force into the surrounding concrete. This event is referred to as prestress transfer. Flame cutting of the strands is a common method of releasing the prestress force. The effects of prestress transfer are important considerations in the design of end region reinforcement.

Strut-and-tie behavior. After cracking, the behavior of concrete members can be modeled by a truss analogy. In this analogy, concrete struts carry compressive forces, and steel ties carry tensile forces (Figure 1-7). Behavior modeled by the truss analogy is referred to as strut-and-tie behavior. Strut-and-tie modeling is one approach for designing of end region reinforcement.

Shear span. Shear span is the horizontal distance from the support to the point of load application (Figure 1-8). Shear span-to-depth ratio (or a/d ratio) is often used to describe the loading condition of concrete members. Shear behavior is, among other factors, a function of the shear span-to-depth ratio. Strut-and-tie modeling is generally appropriate for members loaded with relatively small shear span-to-depth ratios.

Transfer length. Transfer length is the length over which prestressing force is transferred from prestressing strands into the surrounding concrete (Figure 1-9).

Transfer length occurs within the end region. By design the prestress force in a strand is always less than ultimate capacity. Hence transfer length is not equivalent to the length required for full strand development.

Development length. Development length is the length of concrete embedment required to fully anchor prestressing strands. Strands with full development length can carry their ultimate tensile capacity (Figure 1-10). Development length is greater than transfer length.

Strand debonding (shielding). Stress in pretensioned concrete girders can be controlled by selectively preventing force transfer between strands and concrete. To prevent force transfer, strands are debonded (also called shielding), at the ends of the beam. Debonding is accomplished by placing a sleeve over the strand to prevent bond with the concrete. Debonding moves the transfer length of shielded strands away from the girder end (Figure 1-11).

Strand Slip. Strand slip is movement of prestressing strands relative to the surrounding concrete due to applied loads. Strand slip generally occurs after the formation of cracks within the strand development length. These cracks reduce the available bond length for developing the strands, thus leading to strand slip once load on the strands exceeds capacity along the reduced embedment length. Strands can still partially develop even after the onset of slip.



Figure 1-1. I-Girder highway bridge. (Photos courtesy of B.E. Ross)

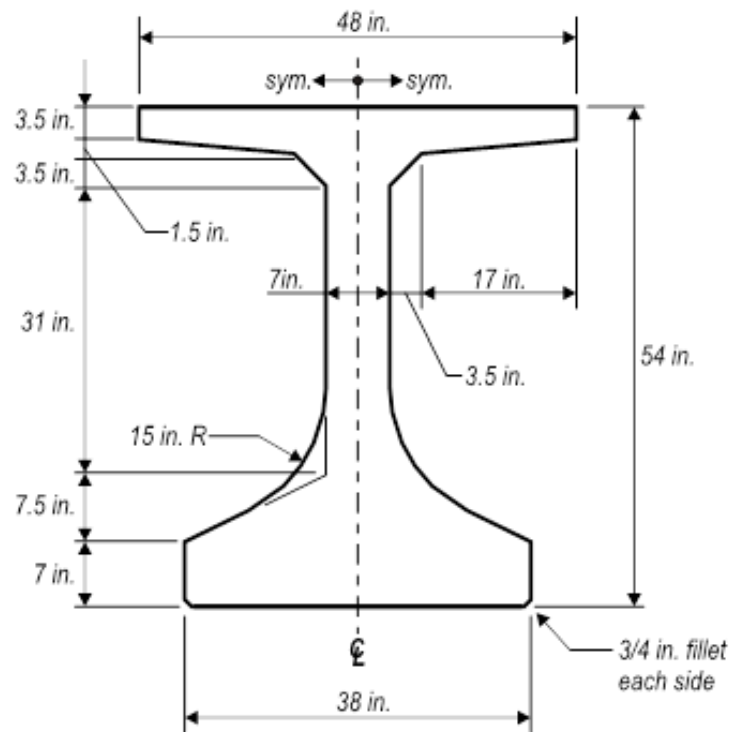


Figure 1-2. Cross-section 54 in. deep Florida I-Beam



Figure 1-3. End region reinforcement. (Photo courtesy of B.E. Ross)

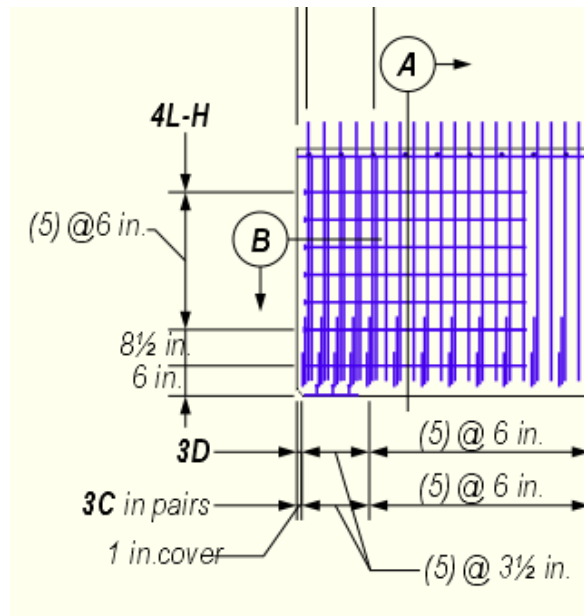


Figure 1-4. FIB-54 end region reinforcing detail. (Based on FDOT 2009b)

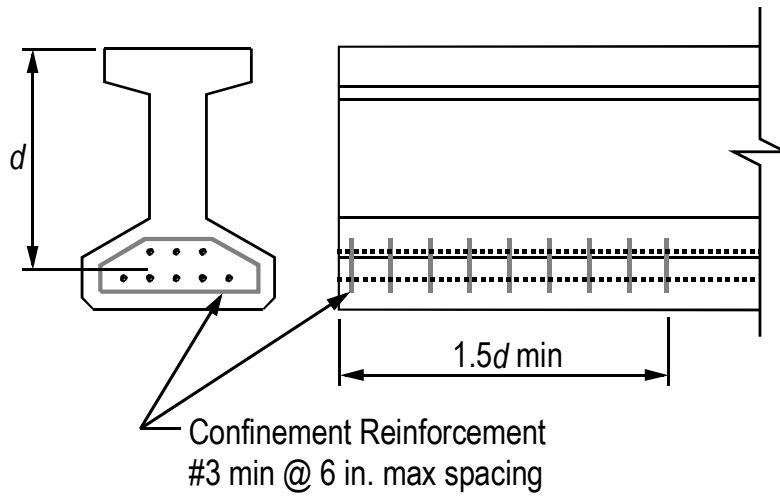


Figure 1-5. Confinement reinforcement

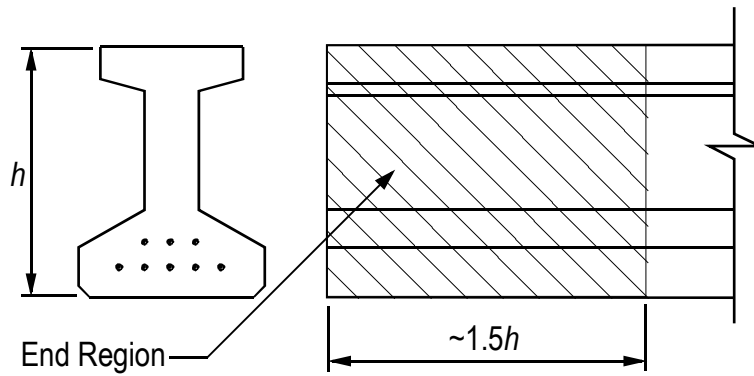


Figure 1-6. End region

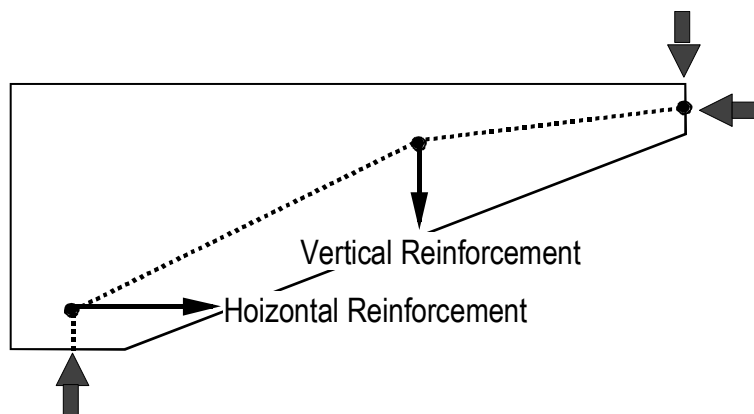


Figure 1-7. End region strut-and-tie

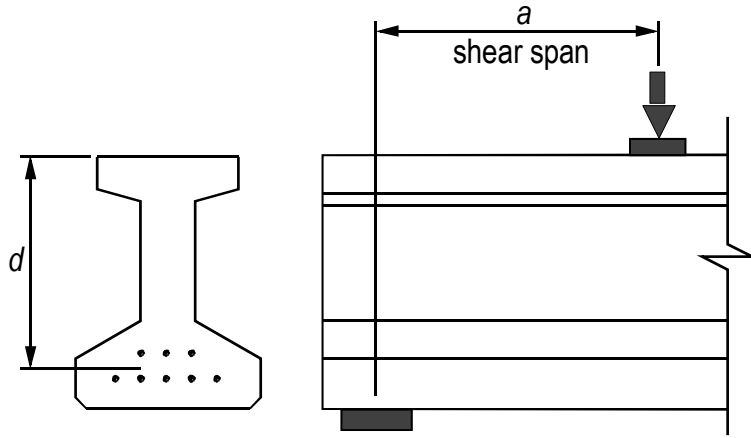


Figure 1-8. Shear span

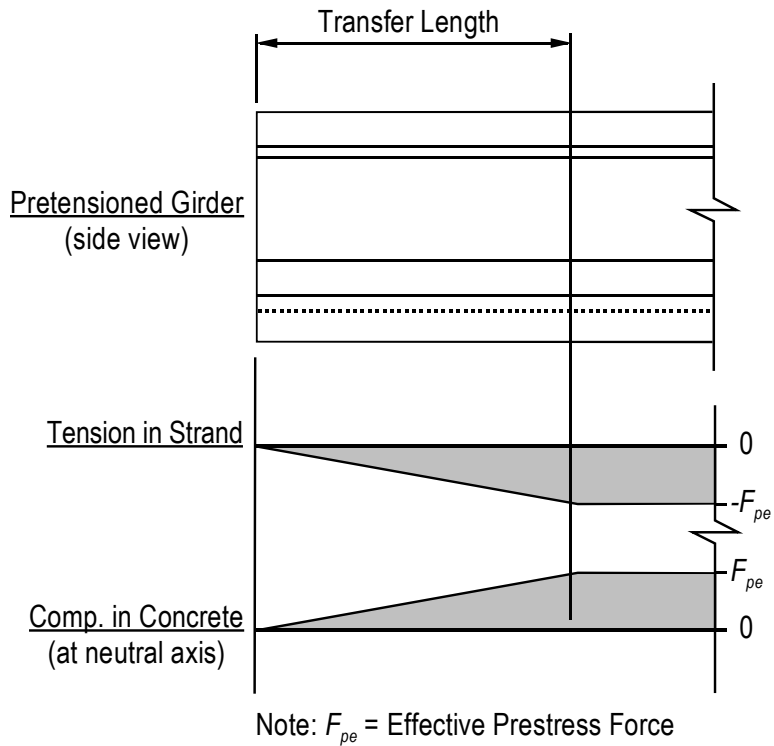


Figure 1-9. Transfer length

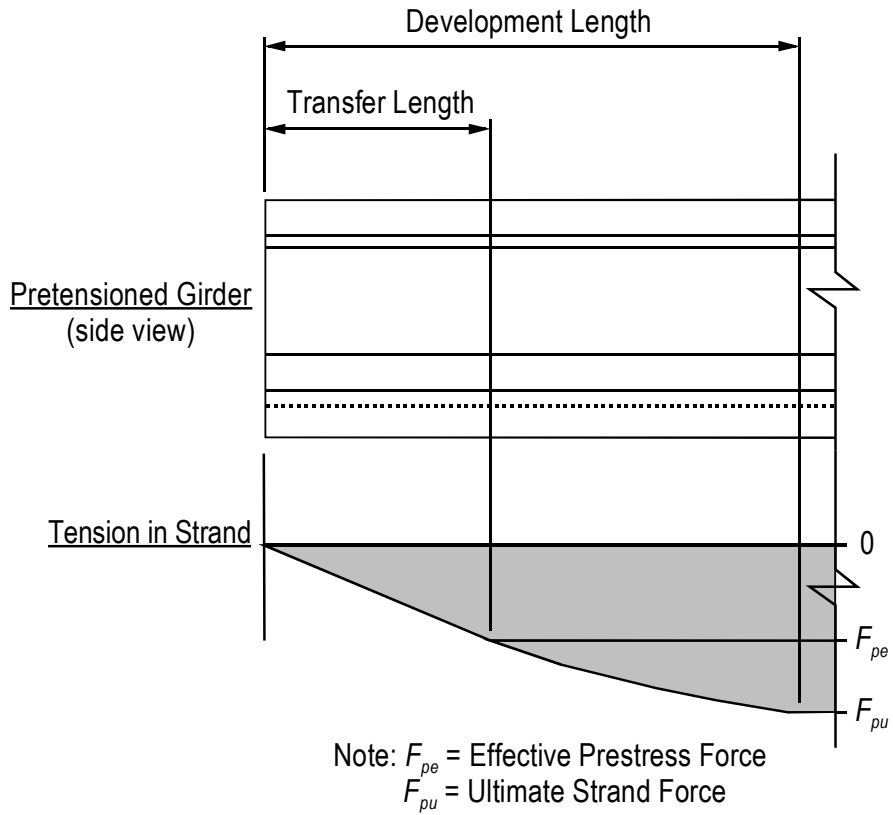


Figure 1-10. Development length

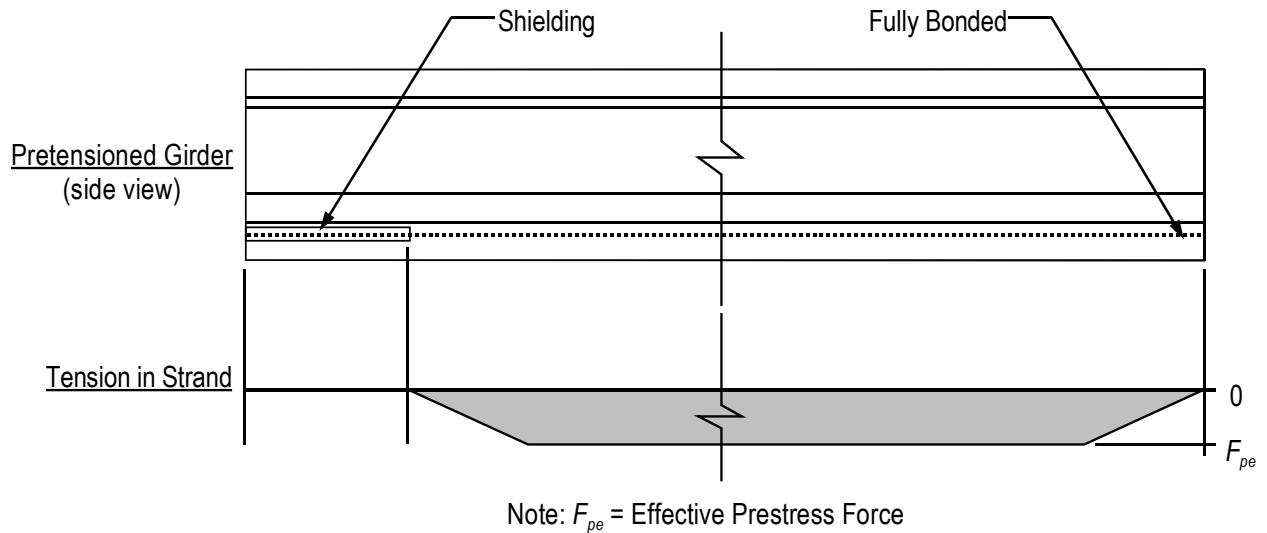


Figure 1-11. Strand debonding

CHAPTER 2 REVIEW OF LITERATURE

This chapter summarizes the work of other researchers regarding confinement reinforcement and other relevant topics. It is organized topically, beginning with a discussion of end region failure modes. Code requirements regarding confinement reinforcement and end region detailing are also summarized.

End Region Failure Modes

The end region of pretensioned girders can fail in modes other than basic “flexural failure” or “shear failure.” Two such failure modes are bond-shear failure and lateral-splitting failure. Both of these modes have been observed experimentally, and have relevance in the study of confinement reinforcement.

Bond-Shear Failure

After cracks form in the end region, load is carried by a strut-and-tie mechanism (Figure 2-1). If cracks form near the girder end then strand anchorage is interrupted, and the strands may slip (Figure 2-2). Bond-shear failure occurs when strands can no longer support load, or when the compression zone crushes due to the rotation allowed in-part by strand slip. This type of failure can be very sudden and has also been called “bond-tension failure” or “bond failure.” Bond-shear failure has been observed during load tests of girders without confinement reinforcement (Maruyama and Rizkalla 1988, Kaufman and Ramirez 1988, Englekirk and Beres 1994, Llanos et al. 2009), as well as during tests of girders with confinement reinforcement (Ross et al 2010, Deatherage et al. 1994, Barnes et al. 1999, Kuchma et al. 2008).

Lateral-Splitting Failure

As with bond-shear failure, lateral-splitting failure occurs after cracks form in the end region and the girder begins strut-and-tie behavior. In this failure mode, splitting cracks (Figure 2-3) form due to transverse stresses above the support (Ross et. al. 2010, Llanos et. al. 2009, Csagoly 1991). Splitting cracks can lead to strand slip relative to the surrounding concrete. In girders without confinement reinforcement the formation of splitting cracks and the associated strand slip can lead to sudden girder failure (Ross et al. 2010). Development of transverse forces and their relationship to confinement reinforcement are primary considerations of the research presented in this document.

Figure 2-3 shows a splitting crack forming at the centerline of the cross-section. Splitting cracks in the outer portion of the bottom flange have also been observed experimentally (Llanos et. al. 2009). Splitting cracks in the flange can also lead to sudden girder failure.

Code Requirements

Confinement reinforcement is required by AASHTO LRFD article 5.10.10.2 (AASHTO 2009). Figure 2-4 graphically presents the confinement reinforcement requirements. The requirements are prescriptive, meaning that confinement reinforcement is not designed, but is rather specified according to the strict “recipe.” The function of confinement reinforcement is not discussed in the code or in the associated commentary.

Strand shielding is addressed by AASHTO LRFD article 5.11.4.3. This article limits shielding to no more than 25% of strands in a girder. Limits are also placed on the percentage of shielded strands in a given row (40%) and the quantity strands that

can have shielding terminate at the same section (greater of 40% or four strands). Shielding is required to be symmetric about the cross-section centerline.

Article 5.8.3.5 addresses the amount of longitudinal steel required at any section, including sections near the supports. Requirements at the support are based on a strut-and-tie model similar to that shown in Figure 1-7. Sufficient steel must be provided to support the horizontal tie force above the bearing. To prevent bond-shear failures the article states that, “Any lack of full development shall be accounted for.”

Confinement Reinforcement during Prestress Transfer

In addition to design for ultimate loads, pretensioned girders must also be designed and detailed for serviceability criteria arising from fabrication, shipping, deck placement, and service. Loads from prestress transfer in particular can have negative consequences on performance and durability of girders. Llanos et al (2009) observed splitting cracks at prestress transfer (Figure 2-5) in the bottom flange of test girders. Splitting cracks formed due to a problematic strand-shielding pattern wherein fully bonded strands were placed in the outer portion of the flange and shielded strands were placed below the web. Splitting cracks were allowed to propagate because confinement reinforcement was not present. Other researchers (Russell and Burns 1996) recommended the use of confinement reinforcement to prevent splitting at prestress transfer.

Russell and Burns (1996) investigated transfer length for 0.5 and 0.6 in. diameter prestressing strands in girders with and without confinement reinforcement. The authors' state:

Overall, confining reinforcement had little or no effect in improving the transfer lengths...In fact, the measured transfer lengths for strands confined

by mild steel reinforcement were marginally longer than strands where confinement was not provided.

Other authors have reported similar findings for 0.7 in. diameter strands (Patzlaff et al. 2010, Akhnoukh 2010). None of the authors investigating transfer length in confined girders reported splitting cracks during prestress transfer. Each concluded that the negligible impact on transfer length was due to the inactivity of confinement reinforcement in the absence of cracking.

Work regarding confinement reinforcement in the anchorage zone of post-tensioned concrete members has been conducted by Breen et al. (1991) and Roberts (1990). These works, while useful for post-tensioned members, do not apply directly to the design of pretensioned members. In post-tensioned concrete, prestress force is transferred to the concrete in a relatively small local zone. In pretensioned concrete, however, the prestress force is transferred to the concrete over the relatively large strand transfer length. The local zone in post-tensioned members is analogous to an axially loaded column, and confinement reinforcement for the local zone can be designed using an approach similar to columns. As demonstrated in subsequent chapters of this document, confinement in the bottom flange of pretensioned I-girders is used to control cracks and to carry transverse tension forces. These functions are distinct from confinement reinforcement in columns and post-tensioned local zones, which provide confinement to axially loaded concrete.

Confinement Reinforcement during Loading

Confinement reinforcement has been shown to affect girder performance under applied loads. This section summarizes previous research investigating the effects of confinement reinforcement on girder strength and behavior during loading.

Shear Capacity

Csagoly (1991) tested 16 pretensioned girders, some with confinement reinforcement and some without. Confinement reinforcement improved shear capacity by an average of 13% relative to girders without confinement. Shahawy et al. (1993) and Ross et al. (2010) also tested girders with and without confinement reinforcement. Results from Shahawy et al. indicate that confinement reinforcement improved shear capacity by 10% to 17%. Ross et al. reported an average increase in shear capacity of 25%.

Transverse Reinforcement

In some cases, equilibrium of strut-and-tie systems requires the formation of tension ties in bottom flange in the transverse direction. If confinement reinforcement is not provided to act as the transverse tie, concrete must carry the tension force. This condition is undesirable, and has been found culpable in splitting cracks by Csagoly (1991), Llanos et al. (2009), and Ross et al. (2011a).

According to Csagoly, splitting cracks result from “the spreading of the reaction force above the bearing.” This concept is shown graphically in Figure 2-6. A transverse force “T” is formed to maintain static equilibrium as the reaction force is spread from the web to the bearing pad. Splitting cracks form when the transverse force exceeds the concrete tensile capacity.

Llanos et al. (2009) also observed splitting failures in load tests of full-scale girders, and likewise attributed these failures to transverse forces above the support. Mechanics leading to these transverse forces were different from the Csagoly model, and are described by Figure 2-7. Figure 2-7a is a model of a girder with bonded strands below the web. Inclined compressive forces travel through the web, arriving at a node

above the support. A tie resists the horizontal component of the inclined force. Because strands are fully bonded, they can act as the tie, and equilibrium is maintained. In contrast to Figure 2-7a, Figure 2-7b models the condition from the Llanos et al. test girders in which fully bonded strands were located at the edges of the flange. Because only the strands in the outside portion of the flange were bonded near the support, they were the only strands able to act as ties (Figure 2-7b). This resulted in a disruption of the node at the support point. Because of the offset between the strut in the web and the two ties (fully bonded strands) in the bottom flange, secondary struts formed to transfer the load laterally to the nodes at the ties. Additional secondary struts were essential between the support and the nodes at the ties to complete the load path to the support. Both pairs of secondary struts induced horizontal components that acted transverse to the beam.

Test beams had no reinforcement (such as confinement reinforcement) to support the transverse force, and edges of the bottom flange peeled or split away at failure (Figure 2-8). The authors speculate that “[confinement] reinforcement might have held the bulb together after cracking.”

Vertical Reinforcement

Another possible function of confinement reinforcement is that of vertical, or “shear” reinforcement. Csagoly (1991) proposed this function and included it in a strut-and-tie model of the end region. In the model, inclined cracks crossing confinement reinforcement mobilize the confinement steel, thereby generating a vertical force that contributes to the end region shear capacity (Figure 2-9).

Ductility

Load tests by Ross et al. (2011a) demonstrated that confinement reinforcement can have a positive effect on girder ductility. Six test girders with confinement reinforcement had an average of 157% more displacement ductility than did the six test girders without confinement. The improvement in ductility is attributed to the mitigation of lateral-splitting failure affected by the confinement reinforcement. Morcus et al. (2010) also noted an improvement in ductility in girders with confinement reinforcement.

Development Length

By restraining cracks, confinement reinforcement may reduce strand development length. To test this possibility, Patzlaff et al. (2010) load tested (6) pretensioned concrete T-beams with varying configurations of confinement reinforcement. In all cases, the girders failed in flexure, and at loads sufficient to fully develop the strands. Because the strands reached full development in all tests, no conclusions were made regarding the effect of confinement reinforcement on development length.

Akhnoukh (2010) investigated the effects of confinement reinforcement on development length by conducting pullout tests of 0.7 in. diameter strands embedded in 4 ft, 5 ft, and 6 ft long concrete prisms. Specimens also varied in the quantity and spacing of confinement reinforcement. Pullout tests were terminated when the strand ruptured or when the strand slipped relative to the concrete. The 4 ft specimens with (5) #3 confinement hoops always failed by strand rupture, whereas the majority of the 4 ft specimens with (3) #3 confinement hoops failed by strand slip. The author concluded that confinement reinforcement decreased the development length.

Shear Friction

Akhnoukh (2010) proposed a shear friction method for designing confinement reinforcement. Currently this is the only design method in the literature. The Akhnoukh method is based on an assumed crack running through a row of strands, which engages the confinement reinforcement thereby inducing normal and friction forces on the crack plane (Figure 2-10). Equilibrium is applied in the longitudinal direction to equate the friction force with the force in the strands, resulting in Equation 2-1. Akhnoukh applied this model to design confinement reinforcement for the strand pullout tests discussed previously. It was concluded that the shear-friction concept can be used to quantify the effect of confinement reinforcement on strand development.

$$A_{ts} = \frac{A_{ps} \cdot f_{ps}}{\mu \cdot f_{tsy}} \quad (2-1)$$

Where:

- A_{ts} = Area of transverse (confinement) reinforcement crossing crack (in²)
- A_{ps} = Total area of prestressing strand (in²)
- f_{tsy} = Yield strength of transverse (confinement) reinforcement (ksi)
- f_{ps} = Stress in prestressing strands at ultimate capacity (ksi)
- μ = Coefficient of friction

Hoyer Effect

The diameter of prestressing strands decreases due to the Poisson effect as strands are pretensioned (Figure 2-11). Upon release strand tension at the end of the member is relieved, and the strand diameter increases. The surrounding concrete resists the increase in diameter, resulting in tensile forces in the concrete and in mechanical bond between the strand and concrete. Radial strand expansion and concrete tensile stress are greatest at the member end. Radial strand expansion and the associate concrete tensile stresses are zero at the end of the transfer length. This

condition is referred to as the Hoyer Effect and is the primary contributor to strand-concrete bond capacity. This effect is named for Ewald Hoyer, the German Engineer who first discussed radial expansion of prestressing strands (Hoyer 1939).

Oh et al. (2006) derived a model for transfer length that accounts for the Hoyer effect. The Oh model is rigorous, utilizing equilibrium, material constitutive properties, and strain compatibility. The model can be used for calculating stresses at the strand-concrete interface and for calculating tensile concrete stresses. Building on the equilibrium-compatibility portion of the model, Oh then considers the effects of concrete cracking adjacent to the strands within the transfer length. The full model (including crack effects) was compared to experimental tests of transfer length and found to have good correlation.

Summary of Literature

The following conclusions are made based on the aggregate findings of the relevant literature. Results from two or more authors support each conclusion.

- The presence of confinement reinforcement does not prevent strand slip
- Confinement reinforcement is inactive until engaged by cracks in adjacent concrete
- Confinement reinforcement has negligible effect on transfer length in uncracked concrete
- Confinement reinforcement improves shear capacity and ductility of girders
- Transverse tensile forces forming above the bearing can lead to splitting cracks in concrete girders
- Transverse tensile forces form due to applied loads and the Hoyer effect

Based on limited treatment or complete absence in the literature, the following topics are deserving of additional attention:

- Function of confinement reinforcement at prestress transfer and ultimate strength
- Effect of confinement reinforcement on development length
- Optimal quantity and placement of confinement reinforcement
- Relationship between confinement reinforcement and splitting failure
- Effect of prestress force on bottom flange transverse tensile stress
- Effect of confinement reinforcement on strand-concrete bond capacity
- Interaction of confinement reinforcement with other end region variables
- Rational confinement reinforcement design methods

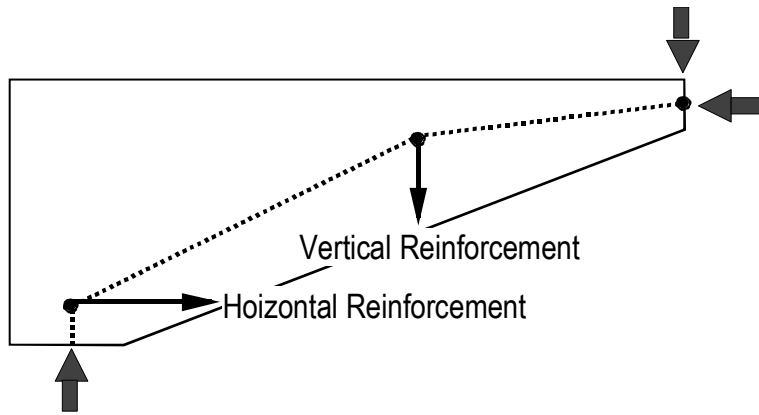


Figure 2-1. End region strut-and-tie behavior

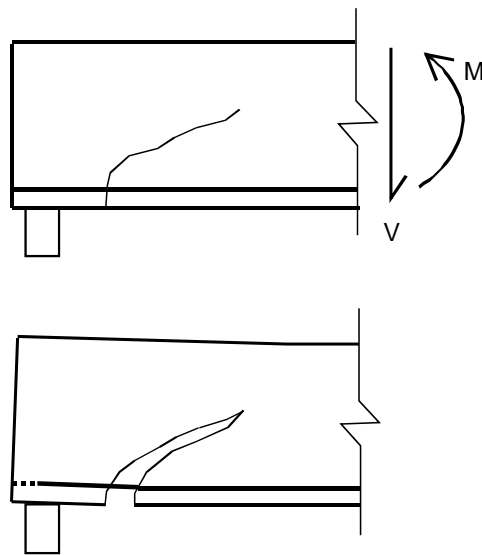


Figure 2-2. Bond-shear failure

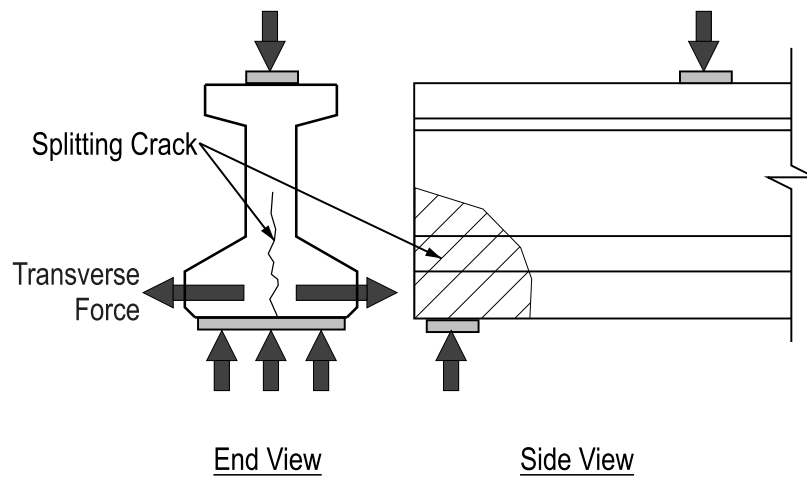


Figure 2-3. Slitting crack

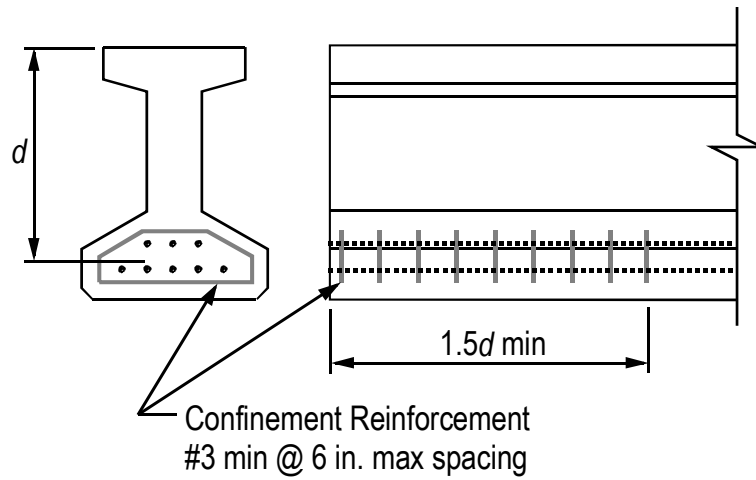


Figure 2-4. Confinement reinforcement. (Based on AASHTO 2007)

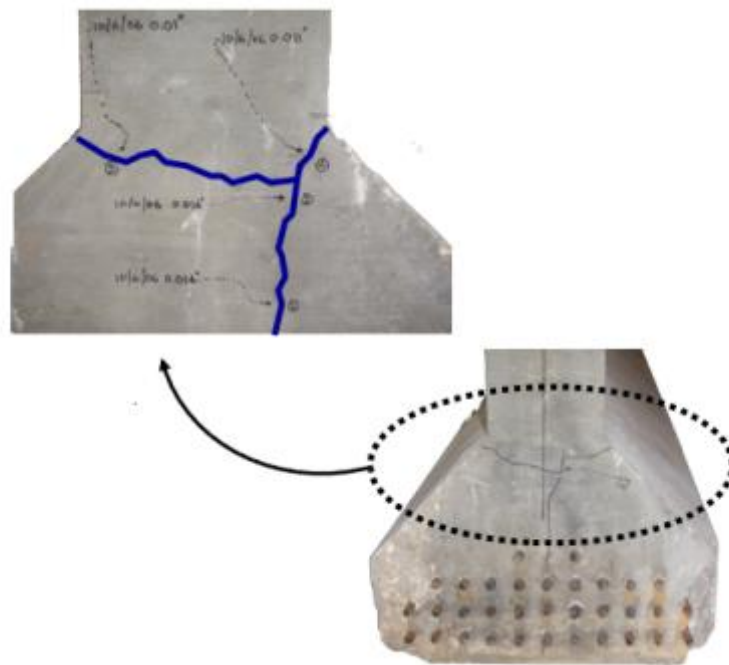


Figure 2-5. Splitting crack at prestress transfer. (Photos courtesy of B.E. Ross)

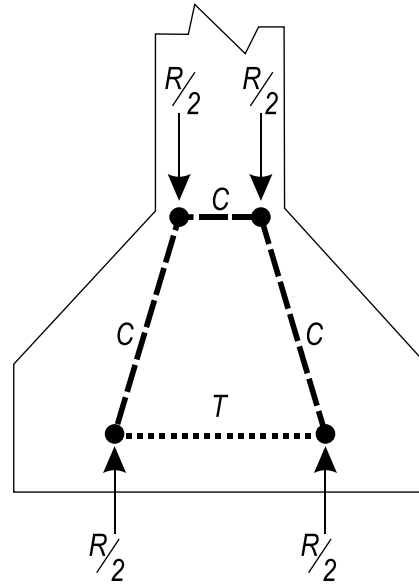


Figure 2-6. Transverse tie above bearing. (Based on Csagoly 1991)

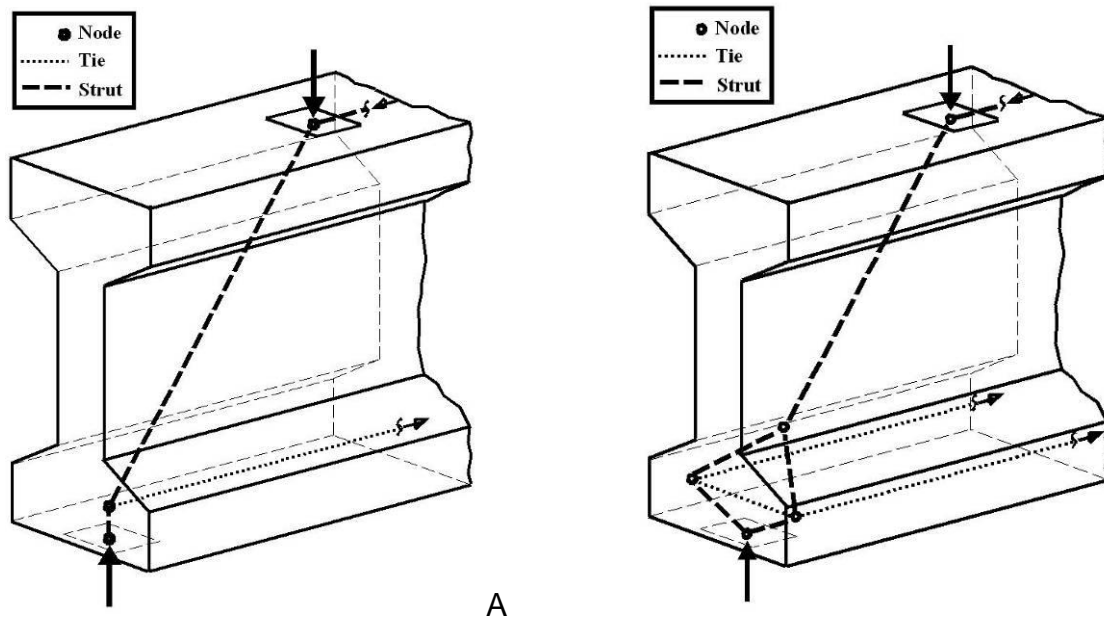


Figure 2-7. End region strut and tie models. A) Girders with fully bonded strands below web, B) Girder with debonded strands concentrated below web.

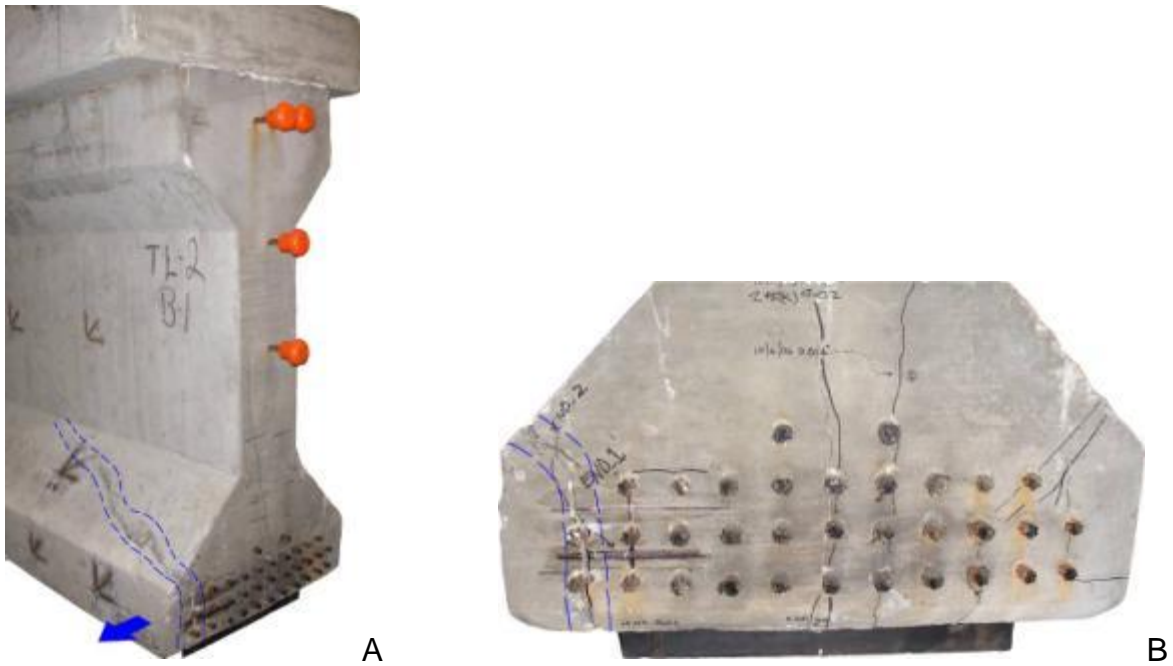


Figure 2-8. Flange cracking in girder with debonded strands concentrated below web. A) Side-end view, B) Close-up of end. (Photos courtesy of B.E. Ross)

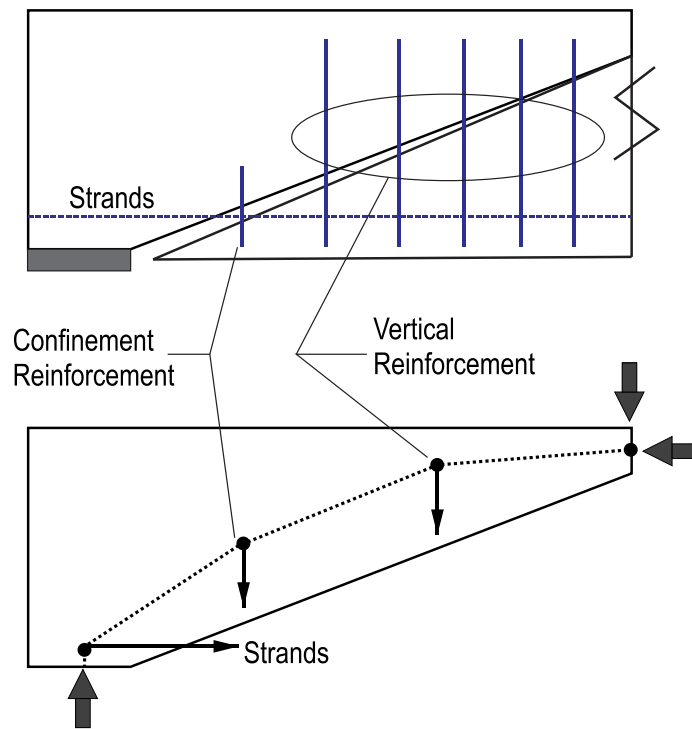


Figure 2-9. Confinement reinforcement as shear reinforcement

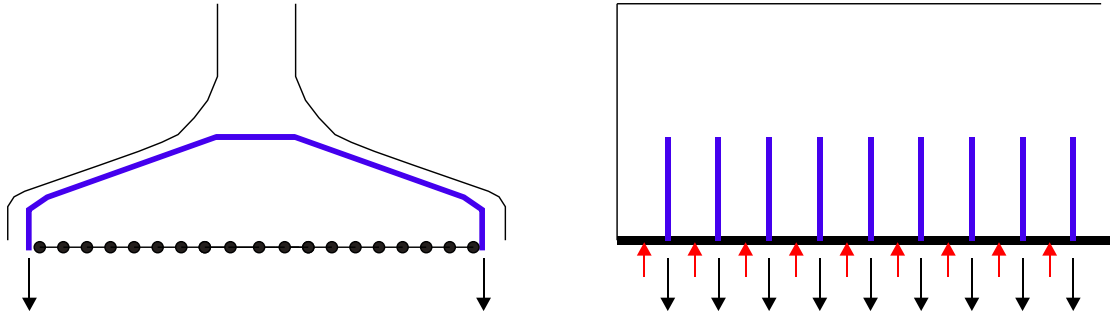


Figure 2-10. Shear-friction model (Based on Akhnoukh 2010)

A) Before Prestressing



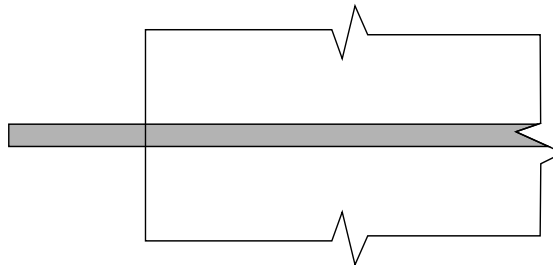
B) Prestressing

Strand elongates longitudinally and contracts transversely



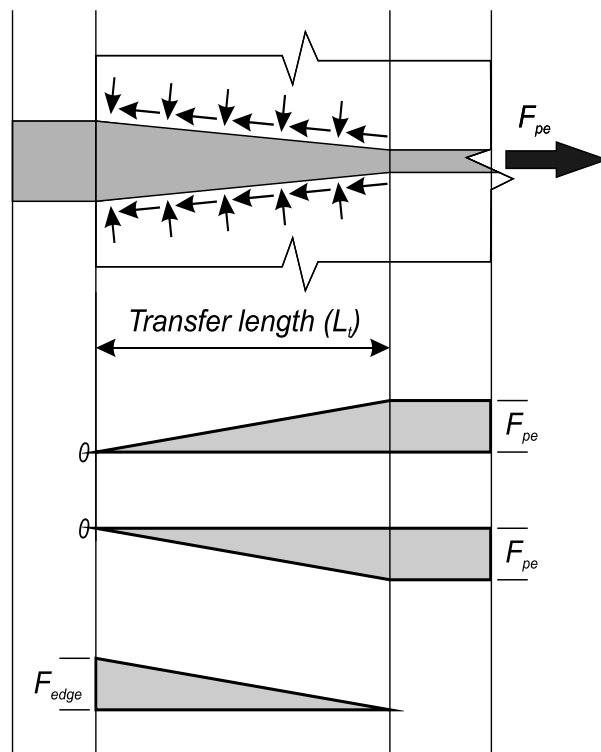
C) Concrete Cast

Concrete around deformed shape



D) Prestress Transfer

Strand expands transversely causing normal and frictional forces



Tension in strand

Compression in concrete

Normal stress at interface

Figure 2-11. Hoyer Effect. A) Strand before stressing, B) Strand after prestressing, C) Concrete cast around strand, D) Stresses and forces after transfer.

CHAPTER 3 TEST GIRDER DESIGN AND CONSTRUCTION

Five 54 in. deep Florida I-Beam (FIB-54) girders were fabricated and tested to evaluate the effects of end region detailing on girder behavior and capacity. Variables in the test program included: quantity of horizontal and vertical mild reinforcement in the end region, quantity or lack of confinement reinforcement, strand debonding pattern, and presence or lack of embedded steel bearing plates. This chapter presents details of the girders, construction procedures, and material properties. The labeling convention used to identify the different girders and specimens is also presented.

Test Girder Classification

Each end of each girder had a unique combination of variables. Because of the unique detailing, each end will be referred to as a separate “specimen” in this document. Figure 3-1 presents the nomenclature used to label specimens and girders. The first letter in the label identifies the girder and the second letter is used to designate the end. Both letters combine to form a specimen label. Letters used in the labels describe the key variables associated with each girder and specimen. A complete description of variables is contained in Table 3-1. Schematic representations of each specimen and the associated variables are shown in Figure 3-2.

Girders were constructed in two phases. The final column in Table 3-1 notes the construction phase for each test girder. Phase 1 girders were constructed at Dura-Stress Inc. in Leesburg, FL in August of 2010. Phase 2 girders were constructed at Standard Concrete Products in Tampa, FL in February of 2012.

Meetings were held with the FDOT, the project sponsor, prior to each construction phase to solicit input on test variables. Variables in phase I include the presence or

lack of confinement reinforcement and quantity of mild steel reinforcement in the end region. Variables tested in phase II include confinement reinforcement configuration, the presence or lack of steel bearing plates, and the strand bond pattern.

Test Girder Design

Test girder prototype design was based on girders used in an existing bridge in Clay County, FL, which had the FIB-54 cross-section (Figure 3-3) and spanned approximately 120 ft. The strand pattern and reinforcement for the prototype girder were designed based on these conditions. Due to laboratory space restrictions, the test girder length was reduced to 49.5 ft. The shorter length, however, still allowed for evaluation of the end region detailing, which was the primary focus of the research program.

The prototype design called for (52) 0.6-in. diameter prestressing strands in the bottom flange and (4) 3/8-in. diameter strands in the top flange (Figure 3-4) using the strand bond pattern designated as “design pattern” in Figure 3-5. While strand bond patterns were varied among the specimens as indicated in Figure 3-5, the strand diameter, positions, and total prestress force were constant. The design pattern had six partially shielded strands and seven fully shielded strands. Fully shielded strands in the test girders correspond to locations in the prototype with shielding lengths of 20 ft or 35 ft. Because test girders were shorter than the prototype, these shielding lengths resulted in fully shielded strands in the test girders.

Some strands in Figure 3-5 are denoted as “Shielded entire length”. This designation is not strictly accurate for girders W, F, and D. All strands in these girders were bonded to the concrete for at least 18 in. at the girder center span. This was done for safety reasons so that the strands would be restrained from dangerous whipping

movements during release of prestress forces. Bonding at the center 18 in. did not affect the end regions where load tests were conducted.

The “web pattern” and “flange pattern” (Figure 3-5) were designed to test the effect of strand placement on end region behavior and capacity. These patterns were created by partially shielding strands in select locations. Both patterns violate current AASHTO LRFD requirements for quantity and placement of shielding, but were useful for research purposes. The two outermost strands in each pattern were fully bonded so that confinement reinforcement could be secured to these strands during fabrication.

Mild reinforcement details (Figure 3-6 through Figure 3-9) were based on the prototype girder and on FDOT Florida-I 54-Beam Interim Standard Details (FDOT, 2008, 2010). Bar labels are similar to those used in FDOT standards. The numeric portion of each label indicates the size of bar (i.e. 5A is a #5 bar). Reinforcement bending and bearing plates details are shown in Figure 3-10. The different types of bars will be described in the following paragraphs.

5A. Bars placed longitudinally in the top flange and were continuous for the entire length of the girder. Splices of 5A bars were at least 36 in. long.

BP. Galvanized steel bearing plates with headed studs embedded in the concrete at the girder bearing. Plates in girders H and V had eight studs, whereas plates in girders W, F, and D had six studs. Changes in stud quantity and width were made to follow the FDOT bearing plate detail which changed after girders H and V were constructed. Changes to the FDOT bearing plate detail were unrelated to the current research program.

3C, 4C, 3D, 4E & 4F. Bars placed in the bottom flange as confinement reinforcement around the prestressing strands. Both FDOT and modified confinement schemes were used in the test program and are shown in Figure 3-11. The FDOT confinement scheme used #3 bars and the modified scheme used #4 bars. Fewer bars were used in modified scheme and all bars were placed directly above the bearing. The D and E bars in the modified scheme did not splice at the cross-section centerline as did the C bars in the FDOT scheme.

7G & 8G. Bars placed longitudinally in the top flange. These bars were included to control cracking in the top flange after prestress transfer, and are not specified in FDOT standards. The G bars did not extend into the end regions where load testing took place. Girders H and V had #7 G bars. Girders W, F, and D had #8 G bars.

5K & 5Ks. Bars were placed vertically in the web with hooks top and bottom. These bars protruded through the top flange to help develop composite action with the cast-in-place deck. They also acted as shear reinforcement. The bottom hook on 5K bars was 16 in. long to assist in constructability. The bottom hook on 5Ks bars was only 6 in. long. To eliminate any incidental confinement effects from the bottom hooks, 5Ks bars were used in lieu of 5K bars within the end region.

4L & 4L-H. Bars were placed horizontally in the end region of girder H. The 2008 FIB details specify that 4L bars extend beyond the girder end and hook into a cast-in-place end diaphragm. Test girders did not have end diaphragms. In the absence of a diaphragm to anchor the 4L bars, 4L-H bars with headed anchors were used in the web and bottom flange where development was critical. The 4L bars did not have headed anchors and were placed in the top flange. For reasons unrelated to the experimental

program the 2010 FDOT standard detail eliminated the use of end diaphragms and horizontal bars in the end region. Girders W, F, and D were designed using the 2010 detail and did not have 4L or 4L-H bars.

4M. Bars placed transversely in the top flange.

N-Strands. Strands placed in the top flange. These strands are sometimes called “dormant” strands. Their primary purpose is to support mild reinforcement during fabrication. They also provide a nominal amount of crack control to the top flange at prestress transfer.

5Y. Vertical bars bundled with 5Ks and 5Z bars at girder ends. These bars are used to control web splitting cracks that form due to prestressing.

5Z. Bars placed vertically within the end region to control web splitting cracks.

Cast-in-place concrete slabs were built on top of the test girders to mimic a bridge deck. The slab was 8-in. thick, 48-in. wide and was reinforced longitudinally and transversely (Figure 3-12).

Specified material properties matched FDOT standards. Specifications are listed in Table 3-2. Tested material properties will be discussed in a later section.

Girder Construction

Girders H and V were fabricated at Dura-Stress, Inc. in Leesburg, FL during the first phase of construction. Girders W, F, and D were fabricated in the second phase at Standard Concrete Products in Tampa, FL. The fabrication process was similar for both phases. Differences are specifically noted in the text in this section. Table 3-3 presents a summary of the construction events and dates for both phases.

Fabrication began with the placement prestressing strands and form bulkheads. Plywood bulkheads were used during phase one. Holes were cut in the plywood for

strands to pass through. Steel bulkheads were used in phase two. The steel bulkheads were installed in segments after the strands were tensioned.

A hydraulic jack was used to tension the strands. Jacking force was determined from pressure in the hydraulic line and was verified by measuring strand elongation. Girders were oriented on stressing beds as shown in Figure 3-13. Dormant strands in the top flange were tensioned first followed by strands in the bottom flange. The same tensioning pattern (Figure 3-14) was used for both phases.

Wire breaks occurred in three different strands during phase one (Figure 3-14). The wire breaks did not occur inside the test girders so the strand cross-section within the girders was not compromised. The jacking force of the strands with broken wires could not be checked by the elongation method, however the jacking force as determined by pressure in the hydraulic line was still within the specified range. No wires broke during the second construction phase.

After tensioning, mild steel reinforcement was placed. Select bars were instrumented with strain gages prior to placement in the girders. Figure 3-15 through Figure 3-19 show the reinforcement in each specimen.

Concrete was mixed at on-site batch plants. For phase one girders, concrete was placed in two lifts and was consolidated with internal and external vibrators after each lift (Figure 3-20). The internal vibrator was only used on the north side of the web to keep the vibrator away from internal strain gages which were primarily placed on the south side. A self-consolidating concrete mix was used for phase two (Figure 3-21) and vibration was not necessary. Test cylinders were taken by the fabricators and by the research team from each batch of concrete. The top surface of each girder was raked

to intentionally roughen the surface (Figure 3-22). Girders were covered with heavy tarps during curing (Figure 3-23).

Forms were removed six days after casting during phase one and three days after casting during phase two. Prestress was transferred to the girders the day after form removal. The time between form removal and prestress transfer was used to install bonded foil strain gages and to connect the data acquisition system.

Two 4x8 field cured cylinders were tested on the day of prestress transfer. The average compressive strength was 6880 psi for phase one and 7320 psi for phase two. Both values are above the specified release strength of 6500 psi.

Flame cutting was used in both phases to release the prestressing strands. Individual strands were cut simultaneously at points shown in Figure 3-13. Dormant strands in the top flange were cut first, followed by the bottom strands, which were cut from the outside-in and from bottom-to-top (Figure 3-24). This release pattern was selected because it is relatively easy to execute and because it is typical of precast girders in Florida. Strand cutting was stopped intermittently at multiple stages to obtain strain readings from the vibrating wire strain gages and to check the girders for cracking.

For safety reasons, the fully shielded strands in phase one were cut last and were released by a single cut between girders H and V. In some cases the fully shielded strands completely slipped out of the girders upon release. This was not an issue in phase two because each strand was at least partially bonded to each girder.

The girders in both phases shifted slightly (less than 1 in.) along the length of the stressing bed multiple times during prestress transfer. Movement events always

corresponded to strand cuts. A more pronounced shift occurred during phase one as the final bonded strand was cut. Just after the final bonded strand was cut, girders H and V each slid approximately 2 ft. along the stressing bed. After sliding, the gap between girders was approximately 7 ft-6in.

To investigate changes in strain due to lifting (Figure 3-25), girders H and V were lifted by crane immediately after prestress transfer was completed. Girders were supported by the crane momentarily and then placed on dunnage on the stressing beds (Figure 3-26). Strain data were collected during lifting and as girders were placed on dunnage. After the data were collected, the girders were taken to a storage yard to await shipping. Girders were examined for cracking periodically while in they were held in storage at the prestress fabrication facilities.

Girders were trucked to the Marcus H. Ansely FDOT structures laboratory in Tallahassee, FL for deck construction and load testing. Strain gages were used to monitor strain in girder H (phase one) during transport. Figure 3-27 shows girder H being transported. The black box on top of the girder in the picture housed the data acquisition system.

After unloading of the test girders in Tallahassee, forms were constructed and reinforcement was placed for the concrete deck. Wood forms were affixed to the top flange of the girders using pipe clamps (Figure 3-28). Concrete was prepared by a local ready mix plant.

Cast-in-place decks were poured inside the lab. Concrete was transported from the mix truck to the girders via a bucket and crane (Figure 3-29). Concrete was consolidated using hand-held and form-mounted vibrators. After consolidation and

screeding, the decks were troweled to a smooth finish. Cylinders of the concrete were taken for material testing.

Material Properties

Concrete, mild steel, and prestressing strand were detailed to match FDOT specifications. FDOT class VI concrete ($f'_c = 8500$ psi) was specified for the girders, and FDOT class II concrete ($f'_c = 4500$ psi) for the deck. Concrete compressive strength was tested using both 4x8 and 6x12 cylinders. Table 3-4 presents the tested concrete strengths.

Prestressing strands were Grade 270 low-relaxation, conforming to ASTM A416. Tested strand properties are shown in Table 3-5.

Bond capacity of phase one prestressing strands was tested in accordance with the proposed standard recommended by the North American Strand Producers (NASP 2009). This test method consists of pull-out tests of strand samples embedded in mortar. The method places tight requirements on flow and strength of the mortar. Flow must be between 100 and 124, and the strength at the time of the pull-out tests must be between 4500psi and 5000psi. The pull-out tests must be conducted between 22 and 26 hours after mixing and placing the grout. In spite of efforts to create a grout that would meet specifications, the grout used in the NASP tests failed to achieve the required strength. Table 3-6 lists the grout strengths. Low grout strength was the only deviation from the test method. Flow of the grout was 107.5. Table 3-7 lists results of the NASP tests. Because the grout strength was less than the value specified by the method, results from NASP tests are conservative when compared to tests that strictly meet the grout strength requirements.

Table 3-8 presents the tested material properties for mild steel reinforcement. All reinforcement was ASTM A615 grade 60, with the exception of the 4L-H headed bars placed in girder H. The supplier of the headed bars provided reinforcing bars that met ASTM A706. During phase one the #3 bars came from two separate suppliers; Table 3-8 presents values from both suppliers.

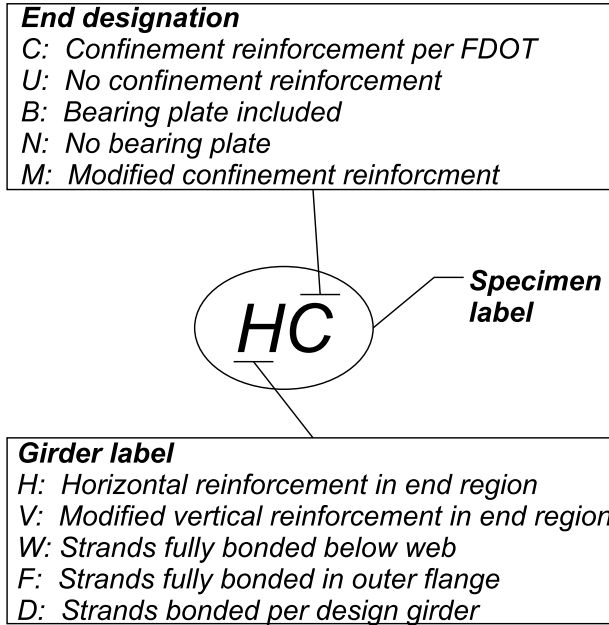


Figure 3-1. Labeling scheme

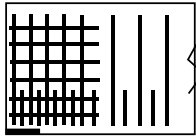
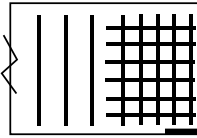
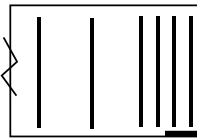
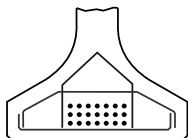
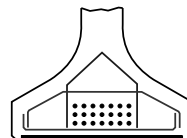
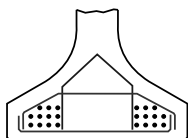
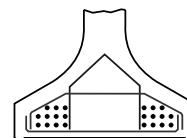
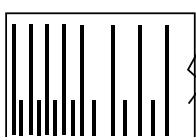
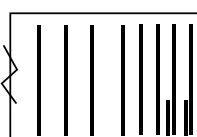
	<i>End 1</i>	<i>End 2</i>
<i>Girder H</i>	<p><i>HC</i></p> 	<p><i>HU</i></p> 
<i>Girder V</i>	<p><i>VC</i></p> 	<p><i>VU</i></p> 
<i>Girder W</i>	<p><i>WN</i></p> 	<p><i>WB</i></p> 
<i>Girder F</i>	<p><i>FN</i></p> 	<p><i>FB</i></p> 
<i>Girder D</i>	<p><i>DC</i></p> 	<p><i>DM</i></p> 

Figure 3-2. Specimen labels and graphical descriptions

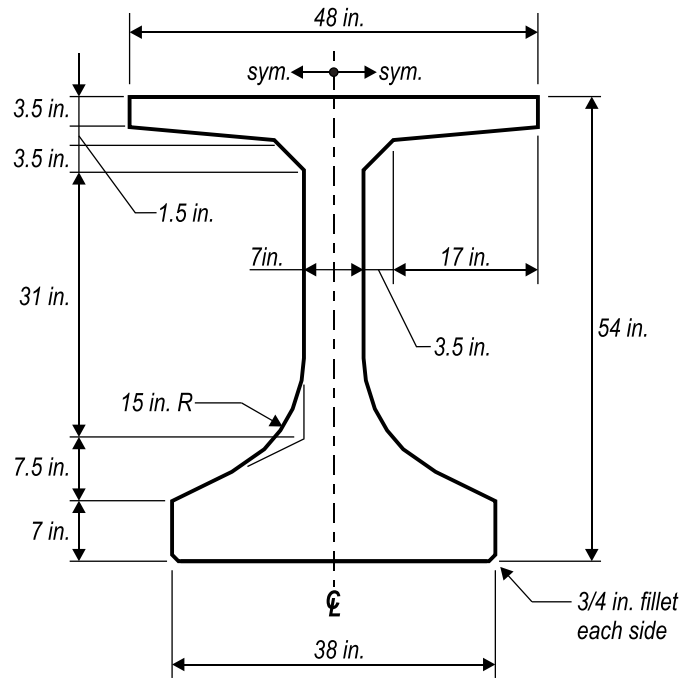


Figure 3-3. Cross-section FIB-54

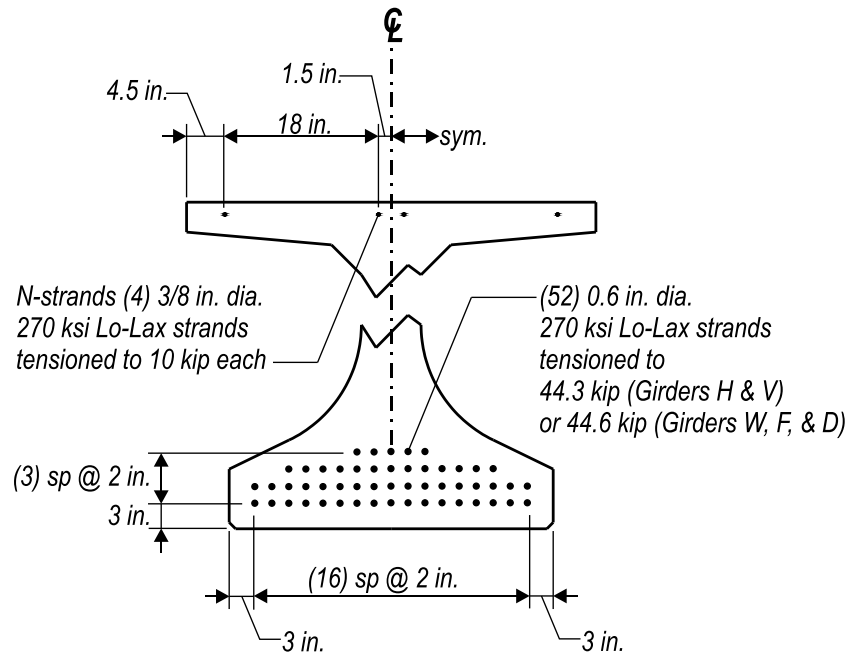
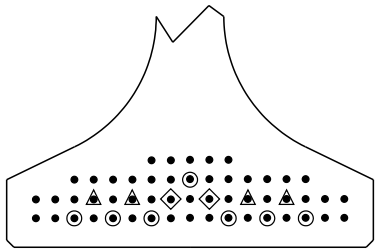
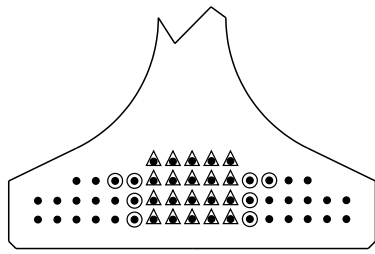


Figure 3-4. Strand layout and prestressing details

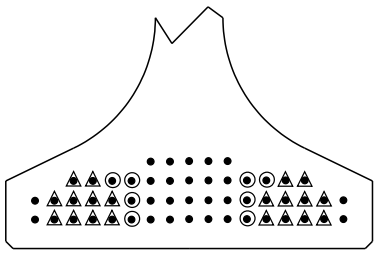
- Fully Bonded
- ⊙ Shielded entire length
- ▲ Shielded 10 ft
- ◊ Shielded 5 ft



Design Pattern



Flange Pattern



Web Pattern

Figure 3-5. Strand bond and shielding patterns

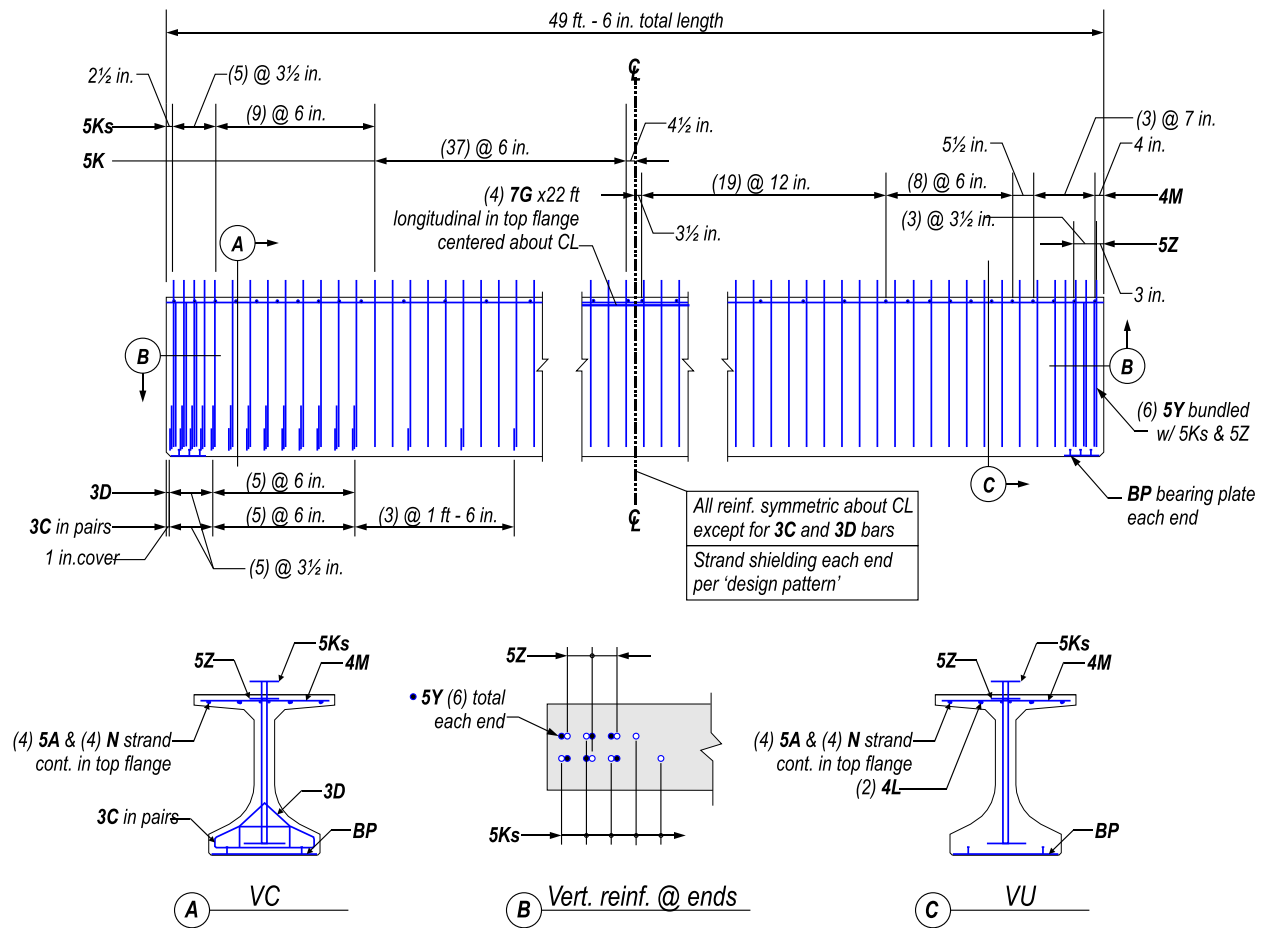


Figure 3-7. Reinforcement for girder V

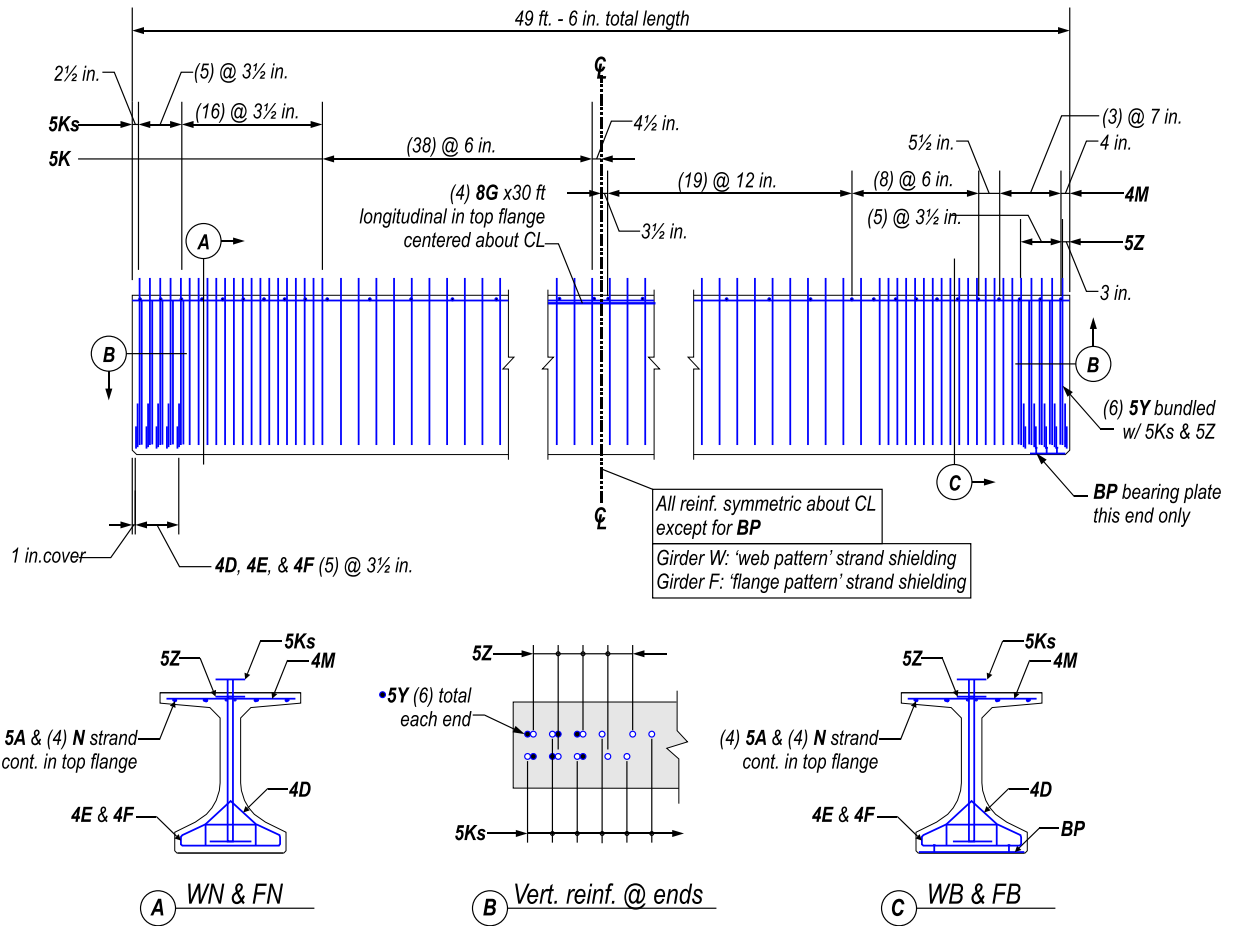


Figure 3-8. Reinforcement for girders W and F

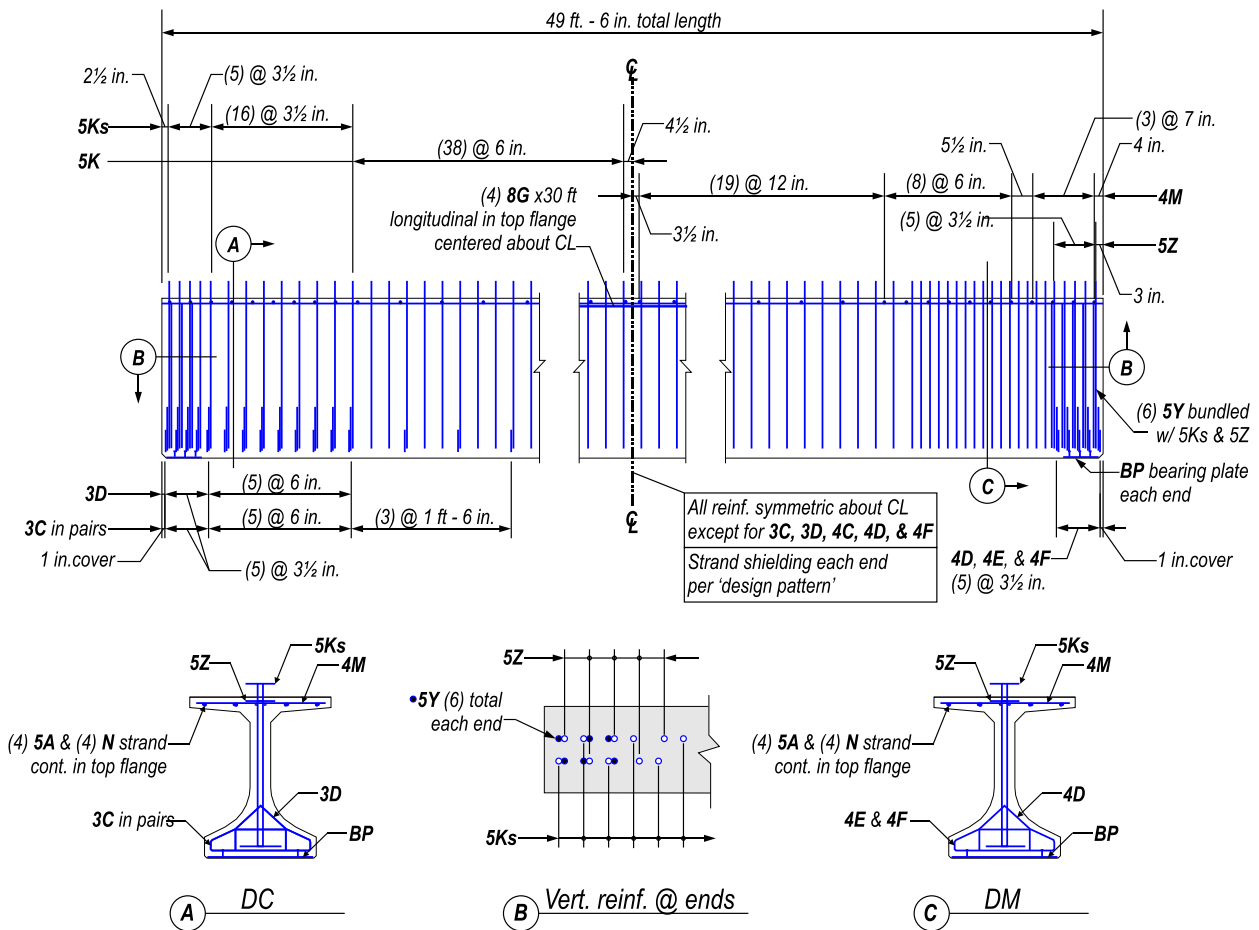


Figure 3-9. Reinforcement for Girder D

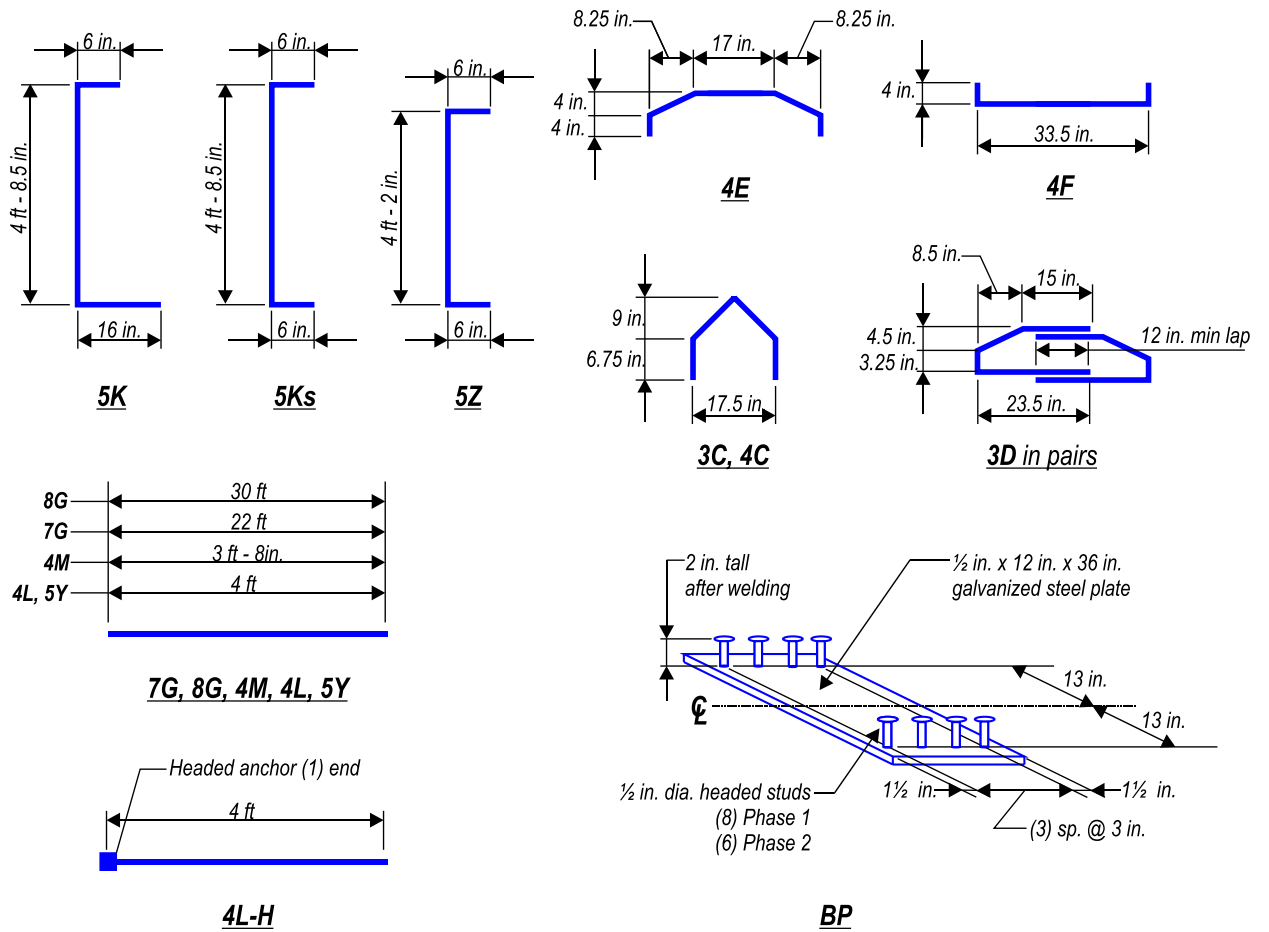


Figure 3-10. Reinforcement and bearing plate details

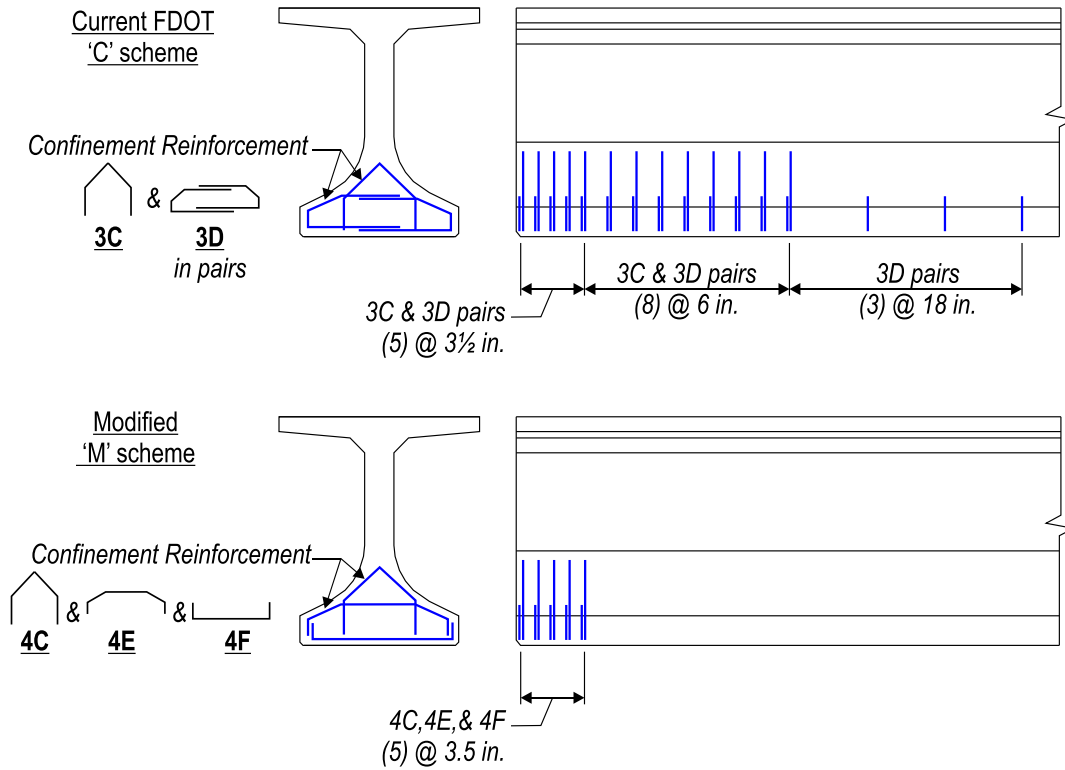


Figure 3-11. Confinement reinforcement schemes

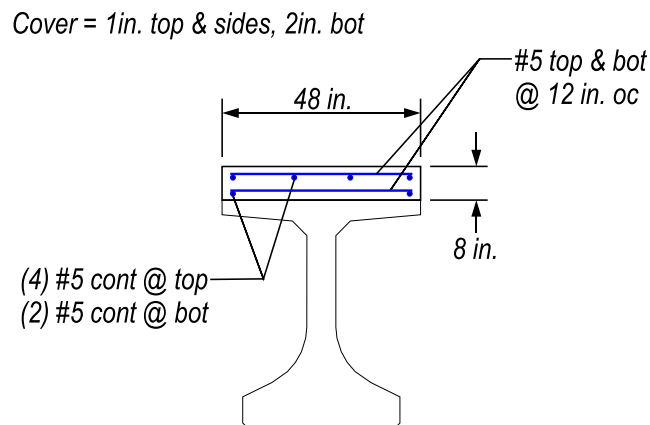


Figure 3-12. Cast-in-place deck reinforcement

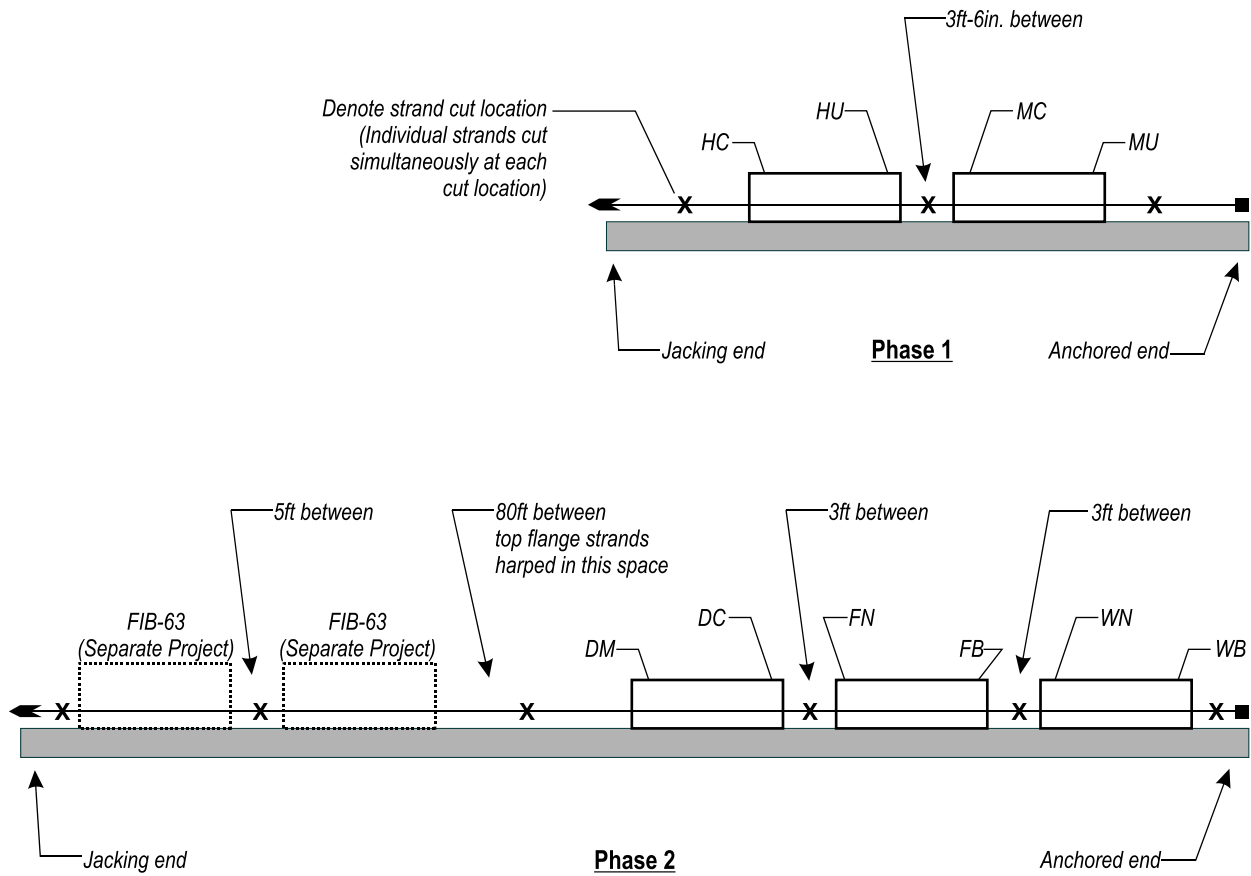


Figure 3-13. Girder orientation during fabrication

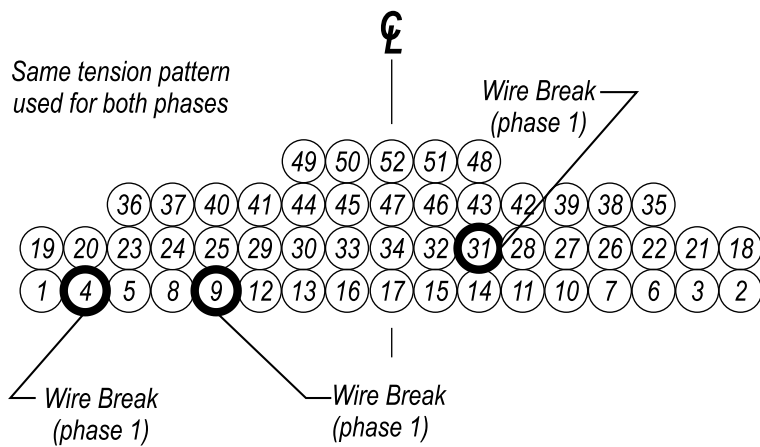


Figure 3-14. Tension pattern and wire break locations



A



B

Figure 3-15. Reinforcement girder H. A) Specimen HC, B) Specimen HU. (Photos courtesy of B.E. Ross)



A



B

Figure 3-16. Reinforcement girder V. A) Specimen VC, B) Specimen VU. (Photos courtesy of B.E. Ross)



A

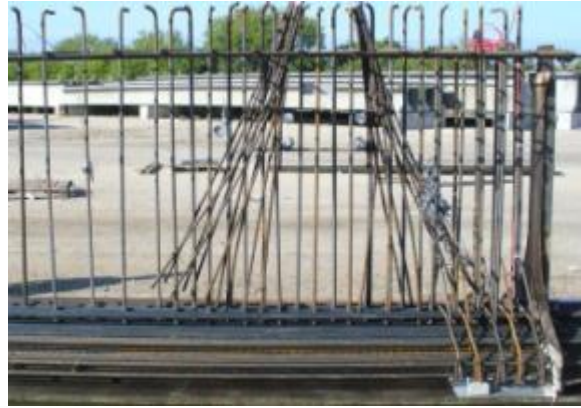


B

Figure 3-17. Reinforcement girder W. A) Specimen WN, B) Specimen WB. (Photos courtesy of B.E. Ross)



A



B

Figure 3-18. Reinforcement girder F. A) Specimen FN, B) Specimen FB. (Photos courtesy of B.E. Ross)



A



B

Figure 3-19. Reinforcement girder D. A) Specimen DC, B) Specimen DM. (Photos courtesy of B.E. Ross)



Figure 3-20. Concrete placement and internal consolidation phase 1. (Photo courtesy of B.E. Ross)



Figure 3-21. Concrete placement phase 2. (Photo courtesy of B.E. Ross)



Figure 3-22. Girder finished surface. (Photo courtesy of B.E. Ross)



Figure 3-23. Girders covered with tarps. (Photo courtesy of B.E. Ross)

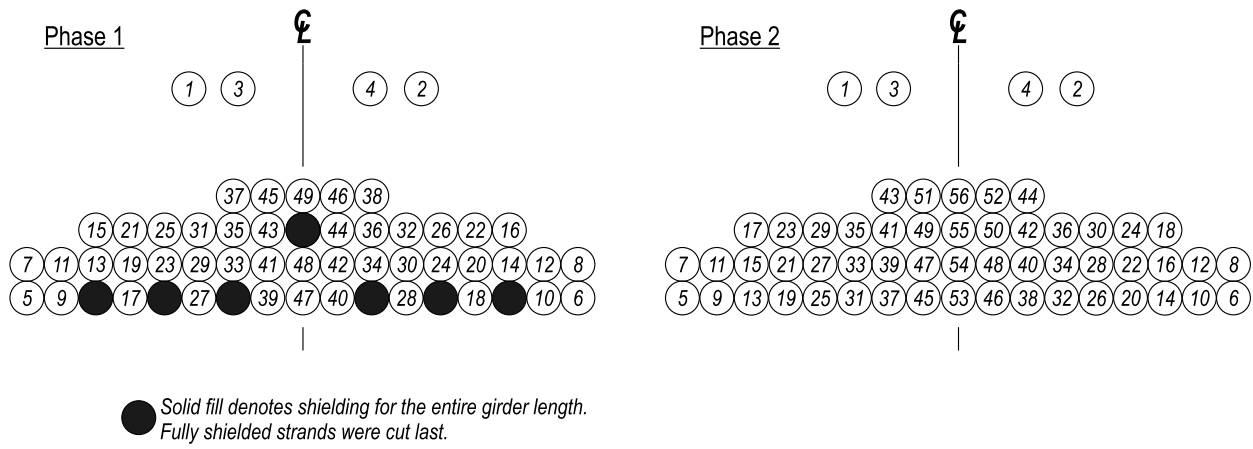


Figure 3-24. Strand release patterns



Figure 3-25. Test girder lifted by crane. (Photo courtesy of B.E. Ross)



Figure 3-26. Girder resting on dunnage on stressing bed. (Photo courtesy of B.E. Ross)



Figure 3-27. Girder H on truck prior to transit. (Photo courtesy of B.E. Ross)



A



B

Figure 3-28. Deck Construction. A) Reinforcement and formwork, B) Wood formwork.
(Photos courtesy of B.E. Ross)



A



B

Figure 3-29. Concrete placement. A) Bucket and chute, B) Bucket lifted by crane.
(Photos courtesy of B.E. Ross)

Table 3-1. Test girder and specimen variables

Test Girder	Specimen	Bearing plate	Mild reinforcement		Strand bond pattern	Confinement reinforcement	Phase
			Vertical	Horizontal			
H	HC	Yes	FDOT	Yes	Design	FDOT	1
	HU	Yes	FDOT	Yes	Design	No	1
V	VC	Yes	Mod	No	Design	FDOT	1
	VU	Yes	Mod	No	Design	No	1
W	WN	No	FDOT	No	Web	Mod	2
	WB	Yes	FDOT	No	Web	Mod	2
F	FN	No	FDOT	No	Flange	Mod	2
	FB	Yes	FDOT	No	Flange	Mod	2
D	DC	Yes	FDOT	No	Design	FDOT	2
	DM	Yes	FDOT	No	Design	Mod	2

FDOT: Detailed per FDOT design standards

Mod: Detailed with modifications to FDOT design standards

Web: Fully bonded strands placed below web

Flange: Fully bonded strands placed in outer portion of flange

Design: Strand pattern based on prototype design

Table 3-2. Specified material properties

Material	Specification
Girder Concrete	FDOT class VI 8500 psi 28-day compressive strength 6000 psi compressive strength at prestress transfer
Deck Concrete	FDOT class II 4500 psi 28-day compressive strength
Prestressing Strand	ASTM A416 270 ksi ultimate strength Low relaxation
Mild Reinforcement	ASTM A615 60 ksi yield strength

Table 3-3. Fabrication important dates

Event	Phase 1 Date	Phase 2 Date
Strands tensioned	August 30, 2010	February 13, 2012
Concrete poured	September 1, 2010	February 17, 2012
Concrete exceeds release strength	September 3, 2010	February 20, 2012
Forms removed	September 7, 2010	February 20, 2012
Prestress released	September 8, 2010	February 21, 2012
Moved to storage	September 8, 2010	February 22, 2012
Trucked to FDOT laboratory	February 23, 2011	April 30, 2012
Deck cast	April 6, 2011	May 7, 2012
Load testing	May 9, 2011 to May 17, 2011	May 23, 2012 to June 1, 2012

Table 3-4. Tested concrete compressive strengths

Material	Cast date	Test date	Average strength (psi)	Sample size	Testing agent*	Cure Method
Phase1 Girder Concrete	8-31-10	9-3-10	6400	(2) 4x8 cylinders	1	Wet
		9-8-10	6940	(2) 4x8 cylinders	1	Field
		9-8-10	6880	(3) 6x12 cylinders	2	Field
		9-29-10	9185	(3) 4x8 cylinders	1	Wet
		9-29-10	8235	(3) 6x12 cylinders	2	Field
		9-28-10	8790	(3) 4x8 cylinders	3	Wet
		5-10-11	10,950	(4) 6x12 cylinders	4	Wet
		5-17-11	11,610	(3) 4x7 cores girder FH	4	Core
Phase 1 Deck Concrete	4-6-11	5-4-11	6615	(3) 6x12 cylinders	4	Field
		5-18-11	6950	(3) 6x12 cylinders	4	Field
Phase 2 Girder Concrete	2-17-12	2-20-12	7050	(2) 4x8 cylinders	1	Wet
		2-21-12	7330	(2) 4x8 cylinders	1	Field
		3-02-12	8790	(2) 4x8 cylinders	1	Wet
		3-16-12	8250	(3) 6x12 cylinders	2	Wet
		3-16-12	9210	(3) 4x8 cylinders	1	Wet
Phase 2 Deck Concrete	5-7-12	5-30-12	10,520	(3) 6x12 cylinders	4	Field
		5-30-12	6400	(9) 6x12 cylinders	4	Field

- * 1. Tested by girder fabricator
 2. Tested by FDOT State Materials Office
 3. Tested by FDOT District Office
 4. Tested by FDOT Structures Research Center

Table 3-5. Prestressing steel properties

Material	Stress at 1% elongation	Ultimate stress	Elongation at ultimate stress	Testing agent*
Phase 1	259 ksi	285 ksi	5.47%	1
Prestressing Strand	271 ksi	284 ksi	4.59%	2
Phase 2	261 ksi	287 ksi	5.38%	1
Prestressing Strand	259 ksi	285 ksi	NA	2

- * 1. Strand supplier
 2. FDOT State Materials Office (average of 4 samples)

Table 3-6. Grout strength for NASP Tests

Time of test (Time zero at mixing of grout)	Grout Strength* (average of (3) cubes)
22 hr	4210 psi
23 hr	4380 psi
24 hr	4030 psi
25 hr	4280 psi
26 hr	4340 psi

* Test method requires a strength between 4500 and 5000 psi

Table 3-7. NASP Test Results

Test Number	Load at 0.1 in. strand slip
1	22.08 kip
2	22.80 kip
3	24.09 kip
4	22.93 kip
5	22.98 kip
6	22.57 kip
Average	22.91 kip

Table 3-8. Steel reinforcement properties

Material	Yield Stress	Ultimate Stress	Elongation at Ultimate Stress	Testing agent*
Phase 1 #4 Headed rebar	68.8 ksi	90.8 ksi	19%	1
Phase 1 #3 confinement rebar	64.6 ksi	89.6 ksi	18%	2
	72.9 ksi	114.8 ksi	11%	1
	78.6 ksi	121.3 ksi	9%	1
	69.5 ksi	106.2 ksi	9%	2
Phase 1 #5 vertical rebar	66.1 ksi	100.7 ksi	17%	1
	68.6 ksi	105.7 ksi	9 %	2
Phase 2 #3 confinement rebar	73.6 ksi	113.3 ksi	12%	1
	85.2 ksi	115.4 ksi	12%	2
Phase 2 #4 confinement rebar	70.0 ksi	109.1 ksi	11%	1
	76.4 ksi	106.8 ksi	11%	2
Phase 2 #5 vertical rebar	64.5 ksi	103.2 ksi	11%	1
	63.2 ksi	103.5 ksi	13%	2

- * 1. Rebar supplier
 2. FDOT State Materials Office (average of 2 samples minimum)

CHAPTER 4 SETUP AND TEST PROCEDURES

Data Collection during Fabrication

Strain and crack data were collected during various stages of fabrication including: prestress transfer, lifting, storage, trucking, and deck construction. This section describes the procedures used to collect data during each stage of construction.

Data from strain gages were monitored and logged using a computerized data acquisition system powered by portable generators. Data from vibrating wire strain gages were monitored using an electronic readout box and logged manually. Crack data were collected through visual observation and using a microscope.

Instrumentation details are presented in Chapter 5.

Prestress transfer. Data were collected from each girder during prestress transfer. Prior to transfer girders were examined for cracks and null readings were taken from all gages. For girders H and V, the acquisition system and generator were secured to the top of the girders. For girders F, W, and D the acquisition system was placed in a van adjacent to the stressing bed. Strand cutting was paused at various times during prestress transfer to allow for visual evaluations and to take readings from the vibrating wire gages. Visual evaluations and vibrating wire readings were also conducted after prestress transfer was complete. Crack widths were measured by microscope at few locations on each specimen. Crack locations were marked with a crayon or marker and documented by photograph.

Lifting. Data were collected during lifting of girders H and V only. Immediately following the conclusion of prestress transfer, girder H and V were lifted by crane, held in place for approximately four minutes, and then placed onto dunnage. Strain data

were collected throughout this process. The data acquisition systems and generators were strapped to the top of the girders to secure them during lifting. Vibrating wire gage readings were taken and visual crack evaluations were conducted during each step.

Storage. All girders received periodic visual evaluations while they were in storage at the precast facilities. Cracks were marked then documented by photograph. Crack widths were measured by microscope at few locations on each specimen. Dates of visual evaluations are listed in Table 3-3. Vibrating wire gage data were also collected while the girders were in storage.

Trucking. Internal and external strain gages were used to monitor concrete strains in girder H during trucking from the precast facility to the laboratory. The data acquisition system and generator were strapped to the top of the girder to secure them during transport. Vibrating wire readings were taken before and after trucking. A visual evaluation was given to all girders upon arrival at the laboratory.

Deck construction. All girders were visually evaluated for cracks before and after construction of the cast-in-place decks. Vibrating wire gage readings were also taken before and after deck construction.

Material properties. Samples of reinforcement, strand, and concrete were taken during each construction phase and were tested to determine the associated material properties. Documentation regarding material properties was also obtained from the supplier of each material.

Load Test Setup and Procedures

Load tests were conducted at the FDOT M. H. Ansley Structures Research Center in Tallahassee, FL. Test dates are listed in Table 4-1. Load tests were conducted on

both ends of each girder. After the first end was tested, the supports and load point were moved and the opposite end was tested.

For purposes of this document each end will be referred to as a separate specimen. Each specimen was loaded at least twice. The first loading simulated the service load. The simulated service load was approximately 300kip and was determined from the prototype girder that was used as a basis for the test girder designs. Once the service load was reached, the load was held constant and cracks were identified and marked. After the cracks were marked the load was removed. The second loading determined the specimen's ultimate strength. A load-displacement plot was monitored real-time during the ultimate load test. Load was applied until it was apparent from the load-displacement plot that a peak load had been reached. Cracking was documented after the ultimate load test was complete.

Load and support geometry are shown in Figure 4-1. Each support consisted of a 10 in. x 32 in. reinforced bearing pad. Pads were "Type E" pads constructed according to FDOT design interim design standards (FDOT 2009d). The bearing pad at the near support was centered below the embedded steel bearing plate (Figure 4-2). Load was applied to the specimen using side-by-side hydraulic actuators. The load rate was controlled by adjusting a pump that pressurized the hydraulic system. The combined load rate varied from 0.1 kip/sec to 0.6 kip/sec, with the typical rate being approximately 0.4 kip/sec. Load was spread from the actuators to the girders through steel plates and a 10 in. x 30 in. reinforced neoprene bearing pad. A reaction frame was used to transmit load from the actuators to the strong floor (Figure 4-3).

Load, displacement, strand slip, and strain data were continuously collected during the service and ultimate load tests. Strain from the vibrating wires strain gages was collect at discrete points during load testing. Concrete samples were tested in conjunction with the load tests to determine compressive strength at the time of load testing.

Coordinate System

A consistent coordinate system is used throughout this document. The system is used to define instrumentation locations and to identify the direction of strains, stress, and forces. The origin for the coordinate system is placed at the centerline of the cross-section, at the bottom of the girder, and at the girder end (Figure 4-4). The z-direction is vertical, the x-direction is horizontal across the width of the girder, and the y-direction is horizontal along the span length. The support nearest the origin is denoted as the near support, and the opposite end is denoted as the far support.

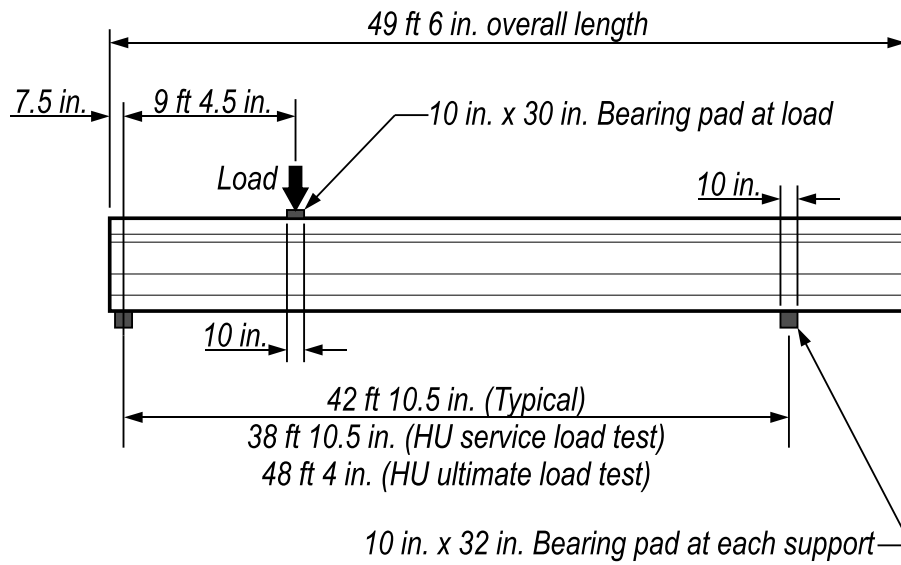


Figure 4-1. Test set-up



A



B

Figure 4-2. Support conditions. A) Bearing, B) Load point. (Photos courtesy of B.E. Ross)



Figure 4-3. Test specimen and load frame. A) Looking at top of girder, B) Looking at side-end of girder. (Photos courtesy of B.E. Ross)

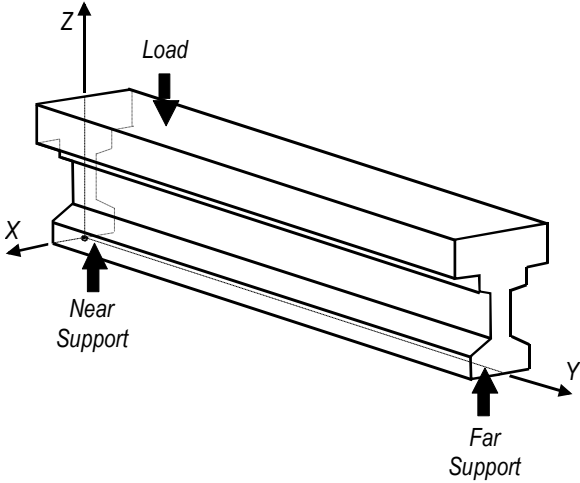


Figure 4-4. Coordinate system relative to load and supports

Table 4-1. Load test dates

Specimen	Service load test	Ultimate strength test
HC	May 11, 2011	May 11, 2011
HU	May 9, 2011	May 10, 2011
VC	May 13, 2011	May 13, 2011
VU	May 17, 2011	May 17, 2011
WN	May 23, 2012	May 23, 2012
WB	May 25, 2012	May 25, 2012
FN	May 29, 2012	May 29, 2012
FB	May 30, 2012	May 30, 2012
DC	May 31, 2012	May 31, 2012
DM	June 1, 2012	June 1, 2012

CHAPTER 5 INSTRUMENTATION

Strain, displacement, force, and crack data were collected during fabrication and load testing. This chapter describes the instrumentation used to collect data and the labeling scheme that was used to identify the various instruments.

Types and Descriptions

Data were collected using load cells, LVDTs, linear potentiometers, variable resistance strain gages and vibrating wire strain gages. Table 5-1 lists the different types of instrumentation and the associated labels. With the exception of the vibrating wire strain gages, all data were logged electronically. Vibrating wire gage data were logged manually from an electronic readout box.

MS strain gages were attached to select mild reinforcement and to bearing plates prior to placement in the test girders (Figure 5-1). MS gages had a gage length of 5mm and were used to monitor strain during prestress transfer and load testing.

XS strain gages (Figure 5-2) were attached to the surface of test girders immediately after formwork was removed. These gages were used to measure concrete strains during prestress transfer, lifting, and trucking. XS gages had a 60mm gage length.

ES gages were embedded in the test girders and were used to monitor concrete strain during all phases of fabrication and load testing. ES gages had a gage length of 60mm. Figure 5-3 shows ES gage installations prior to concrete placement.

V series gages were vibrating wire strain gages which were embedded in the test girders. These gages had a gage length of 152mm and were used to measure concrete strain during all phases of fabrication and load testing. Figure 5-3 shows a V

series gage installation prior to concrete placement. Because vibrating wire gages do not experience electronic drift over time, they were particularly useful in monitoring long term prestress losses.

Wire leads were collected into harnesses after all internal instrumentation (MS, ES, and V series gages) had been placed in the girders. Harnesses in girders F and V were routed to the ends of the girders and exited through holes in the wood bulkheads (Figure 5-5). Harnesses in girders F, W, and D were routed to the top of the girders. Wire harnesses were covered with a rubber sleeve and duct tape to protect the wires during concrete casting. A label was placed at the end of each wire lead for identification purposes.

Prior to load testing S and R series strain gages were installed at discrete locations on girder surfaces (Figure 5-6). These gages had 60mm gages lengths. R series gages were strain rosettes built-up from three individual strain gages.

L series instruments were LVDTs used to monitor vertical displacement during load tests. Labels and locations of the LVDTs measuring vertical displacement are shown in Figure 5-7. LVDTs were mounted to fixed support structures as shown in Figure 5-8.

LVDTs were also used to monitor strand slip for girders H and V. Monitored strands are shown in Figure 5-9. LVDTs for monitoring strand slip were mounted to a wooden bracket affixed to the girder end (Figure 5-10). This set-up was unreliable because cracking in the concrete caused the LVDT frame to shift during load testing.

Rather than LVDTs, P series variable resistant potentiometers were used to measure strand slip for girders F, W, and D. Instrumented strands are shown in Figure

5-11. P series instruments were mounted directly to the strands using custom-machined aluminum brackets and set-screws (Figure 5-12). This set-up did not have the problems associated with the wooden frame used for girders H and V.

Load cells (Figure 5-13) were used to measure the force applied during the load tests. A hydraulic system was used to apply the loads, and a pressure transducer was used to measure pressure in the hydraulic line during testing. Both force and pressure data were logged electronically, along with displacement and strain data from the other instruments.

Strain Gage Coordinates

Figures in this document that present strain data typically also contain information regarding the location of gage(s) from which the data were collected. Information in the figures gives a general idea of the gage orientation and position but doesn't always give specific coordinates. Table 5-2 through Table 5-11 give specific coordinates of gages referenced in this document. Coordinates are based on the system defined in Figure 4-4. Many gages used in the experimental program are not specifically referred to in this document. Additional information regarding these instruments will be available in a forthcoming report for the FDOT (Ross et al., in preparation).

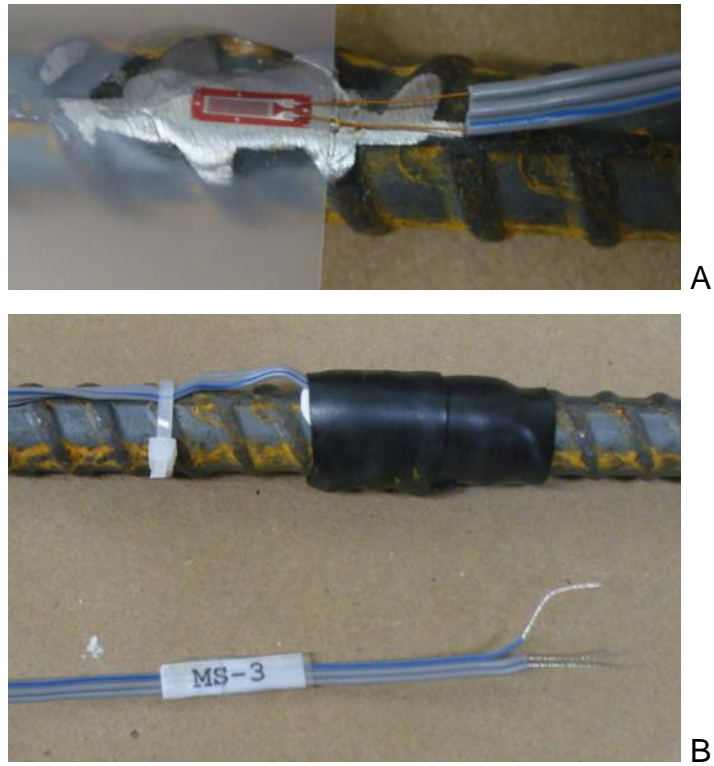


Figure 5-1. MS gage installation. A) Gage before protective covering, B) Protective cover and label. (Photos courtesy of B.E. Ross)

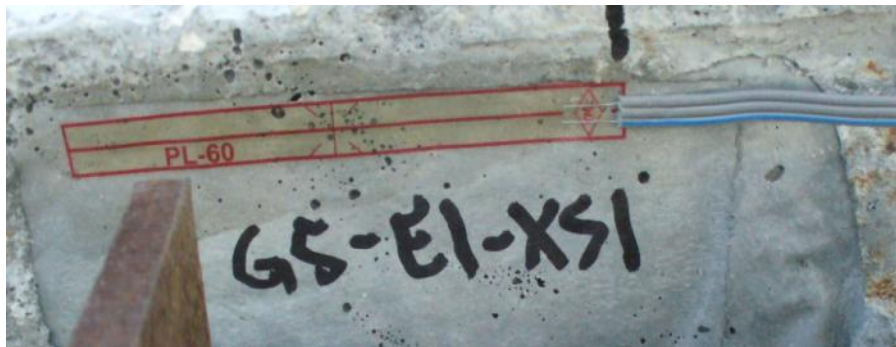


Figure 5-2. XS gage installation. (Photo courtesy of B.E. Ross)



A



B

Figure 5-3. ES gage installations. A) Gage installed vertically, B) Gage installed transversely. (Photos courtesy of B.E. Ross)



Figure 5-4. V gage installation (looking down). (Photo courtesy of B.E. Ross)



Figure 5-5. Wire harness and plywood bulkhead. (Photo courtesy of B.E. Ross)

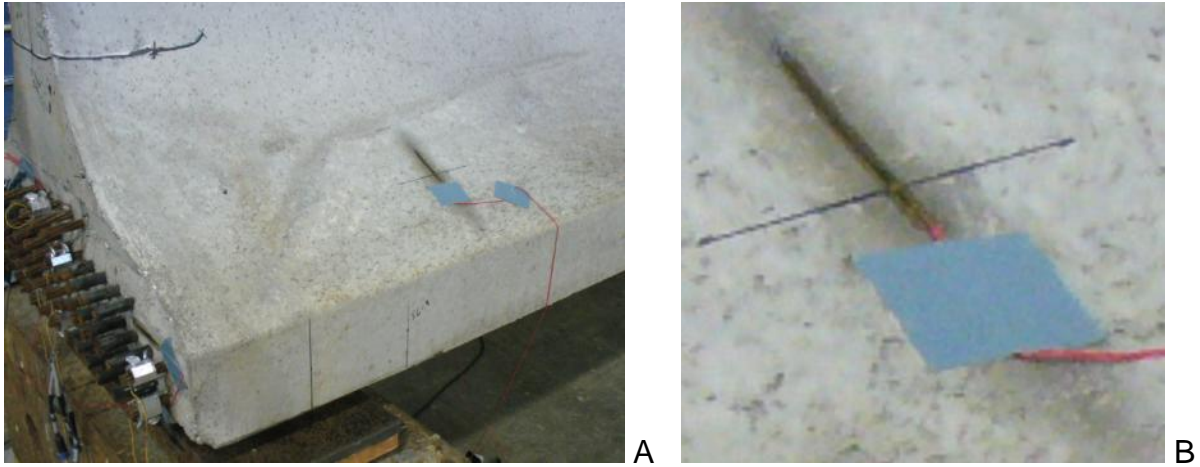


Figure 5-6. S gage installation. A) Gage on top of bottom flange, B) Close-up of gage. (Photos courtesy of B.E. Ross)

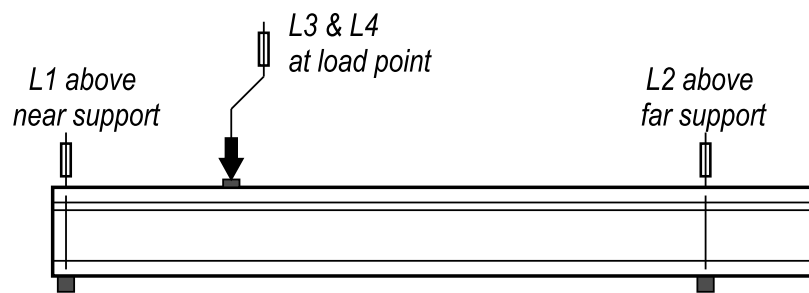


Figure 5-7. LVDT placement and labels



Figure 5-8. LVDT and support frame. (Photo courtesy of B.E. Ross)

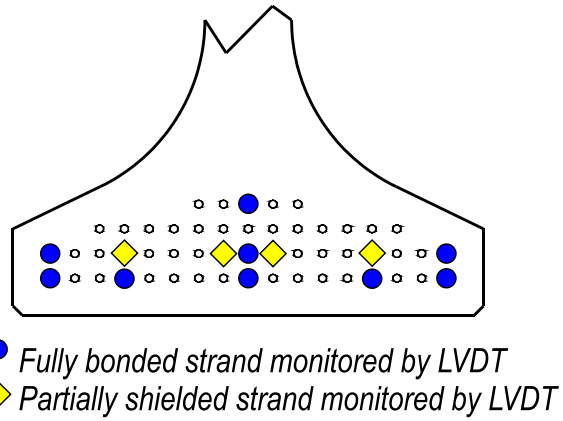


Figure 5-9. Girder H and V strands monitored by LVDT



Figure 5-10. Wood frame and LVDTs. (Photo courtesy of B.E. Ross)

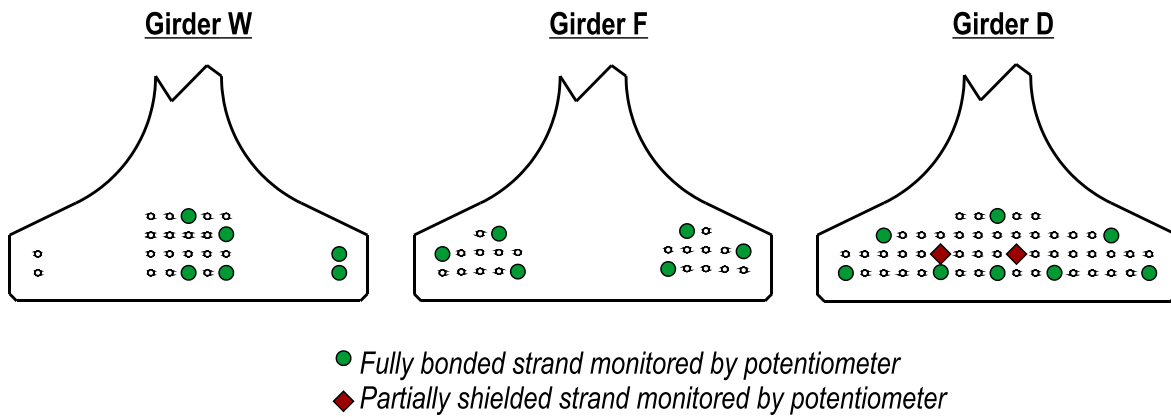


Figure 5-11. Girder W, F, and D strands monitored by potentiometer

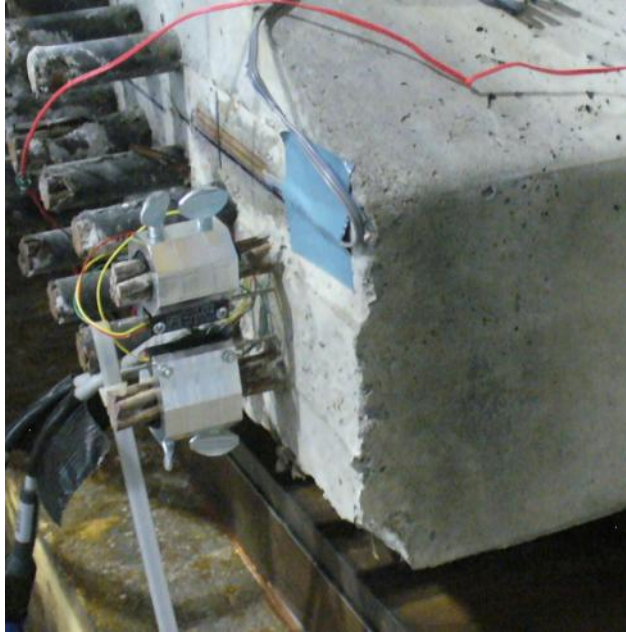


Figure 5-12. Aluminum brackets and linear potentiometers on strands. (Photo courtesy of B.E. Ross)



Figure 5-13. Load cells below hydraulic actuators. (Photo courtesy of B.E. Ross)

Table 5-1. Instrumentation types and labels

Label	Type	Placement
MS	Foil strain gage	Reinforcement & bearing plates
XS	Foil strain gage	Concrete surface
ES	Embedded strain gage	Concrete interior
V	Vibrating wire strain gage	Concrete interior
S	Foil strain gage	Concrete surface
R	Foil strain rosette	Concrete surface
L	Linear variable displacement transducer (LVDT)	Load point, supports, & strands
P	Linear potentiometer	Strands
--	Load Cell	Load point

Table 5-2. Specimen HC strain gage coordinates

Instrument	X (in.)	Y (in.)	Z (in.)	Orientation	Reference(s)
XS1	0.5	0	36	Z	Figure 9-10
XS2	0	0	24	Z	Figure 9-7
XS3	0	0	12	X	Figure 6-2, Figure 9-7, Figure 6-3 Table 6-2
XS5	-19	18	6	Y	Figure 6-17, Figure 9-9
XS6	-19	30	6	Y	Figure 6-17, Figure 9-9
XS7	-19	36	6	Y	Figure 6-17, Figure 9-9
XS8	-19	42	6	Y	Figure 6-17, Figure 9-9
XS9	-19	48	6	Y	Figure 6-17, Figure 9-9
XS10	-19	54	6	Y	Figure 6-17, Figure 9-9
XS11	19	18	6	Y	Figure 6-17, Figure 9-9
XS12	19	54	6	Y	Figure 6-17, Figure 9-9
ES1	0	5	35	Z	Figure 9-10
ES2	-3	27	8	X	Figure 6-2, Table 6-2
ES3	-3	47	8	X	Figure 6-2, Table 6-2
MS1	-0.5	2	0.5	X	Figure 7-22
MS2	0	13	0.5	X	Figure 7-22
MS10	0	2	10	X	Figure 7-22
MS14	0	2	2	X	Figure 7-22
MS15	-1	2	16	X-Z	Figure 7-22
MS20	0	8	10	X	Figure 7-22
MS24	-13	8	2	X	Figure 7-22
MS25	-1	9	16	X-Z	Figure 7-22
MS30	0	22	10	X	Figure 7-22
MS34	0	22	2	X	Figure 7-22
MS35	-1	22	16	X-Z	Figure 7-22
MS40	0	66	10	X	Figure 7-22
MS44	0	66	2	X	Figure 7-22
MS45	-1	67	16	X-Z	Figure 7-22
MS51	0	2	0	X	Figure 7-22
MS52	0	13	0	X	Figure 7-22
V2	0	2	8	X	Figure 9-8

Table 5-3. Specimen HU strain gage coordinates

Instrument	X (in.)	Y (in.)	Z (in.)	Orientation	Reference(s)
XS3	0	0	12	X	Figure 6-3, Table 6-2
XS5	-19	18	6	Y	Figure 6-17, Figure 9-9
XS6	-19	30	6	Y	Figure 6-17, Figure 9-9
XS7	-19	36	6	Y	Figure 6-17, Figure 9-9
XS8	-19	42	6	Y	Figure 6-17, Figure 9-9
XS9	-19	48	6	Y	Figure 6-17, Figure 9-9
XS10	-19	54	6	Y	Figure 6-17, Figure 9-9
XS11	19	18	6	Y	Figure 6-17, Figure 9-9
XS12	19	54	6	Y	Figure 6-17, Figure 9-9
ES1	0	5	35.5	Z	Figure 9-10
ES2	3	27	8	X	Figure 6-2, Table 6-2
ES3	3	48	8	X	Figure 6-2, Table 6-2
MS1	0	2	0.5	X	Figure 7-22
MS2	0	13	0.5	X	Figure 7-22
MS51	0	2	0	X	Figure 7-22
MS52	0	13	0	X	Figure 7-22
V2	0	2	8	X	Figure 9-8

Table 5-4. Specimen VC strain gage coordinates

Instrument	X (in.)	Y (in.)	Z (in.)	Orientation	Reference(s)
XS3	0	0	12	X	Figure 6-3 Table 6-2
XS5	-19	18	6	Y	Figure 6-17, Figure 9-9
XS6	-19	30	6	Y	Figure 6-17, Figure 9-9
XS7	-19	36	6	Y	Figure 6-17, Figure 9-9
XS8	-19	42	6	Y	Figure 6-17, Figure 9-9
XS9	-19	48	6	Y	Figure 6-17, Figure 9-9
XS10	-19	54	6	Y	Figure 6-17, Figure 9-9
XS11	19	18	6	Y	Figure 6-17, Figure 9-9
XS12	19	54	6	Y	Figure 6-17, Figure 9-9
ES1	0	5	35.5	Z	Figure 9-10
ES2	-3	29	8	X	Figure 6-2, Table 6-2
ES3	-3	48	8	X	Figure 6-2, Table 6-2
MS1	-0.5	2	0.5	X	Figure 7-22
MS2	0	13	0.5	X	Figure 7-22
MS10	0	2	10	X	Figure 7-22
MS14	0	2	2	X	Figure 7-22
MS15	-1	3	16	X-Z	Figure 7-22
MS20	0	8	10	X	Figure 7-22
MS24	-13	8	2	X	Figure 7-22
MS25	-1	8	16	X-Z	Figure 7-22
MS30	0	22	10	X	Figure 7-22
MS34	0	22	2	X	Figure 7-22
MS35	-1	22	16	X-Z	Figure 7-22
MS40	0	64	10	X	Figure 7-22
MS44	0	64	2	X	Figure 7-22
MS45	-1	64	16	X-Z	Figure 7-22
MS51	0	2	0	X	Figure 7-22
MS52	0	13	0	X	Figure 7-22
V2	0	2	8	X	Figure 9-8

Table 5-5. Specimen VU strain gage coordinates

Instrument	X (in.)	Y (in.)	Z (in.)	Orientation	Reference(s)
XS3	0	0	12	X	Figure 6-3, Table 6-2
XS5	-19	18	6	Y	Figure 6-17, Figure 9-9
XS6	-19	30	6	Y	Figure 6-17, Figure 9-9
XS7	-19	36	6	Y	Figure 6-17, Figure 9-9
XS8	-19	42	6	Y	Figure 6-17, Figure 9-9
XS9	-19	48	6	Y	Figure 6-17, Figure 9-9
XS10	-19	54	6	Y	Figure 6-17, Figure 9-9
XS11	19	30	6	Y	Figure 6-17, Figure 9-9
XS12	19	54	6	Y	Figure 6-17, Figure 9-9
ES1	0	5	34.5	Z	Figure 9-10
ES2	3	27	8	X	Figure 6-2, Table 6-2
ES3	3	48	8	X	Figure 6-2, Table 6-2
MS1	0	2	0.5	X	Figure 7-22
MS2	0	13	0.5	X	Figure 7-22
MS51	0	2	0	X	Figure 7-22
MS52	0	13	0	X	Figure 7-22
V2	0	2	8	X	Figure 9-8

Table 5-6. Specimen WN strain gage coordinates

Instrument	X (in.)	Y (in.)	Z (in.)	Orientation	Reference(s)
MS10	-1	2.5	17.5	XZ	Figure 6-11, Figure 7-18
MS11	0	2.5	10	X	Figure 6-11, Figure 7-18
MS12	0	2	2	X	Figure 6-11, Figure 7-18
MS20	-1	9	18	XZ	Figure 6-11, Figure 7-18
MS21	0	9	10	X	Figure 6-11, Figure 7-18
MS22	0	10	2	X	Figure 6-11, Figure 7-18
MS30	-1	16.5	17.5	XZ	Figure 6-11, Figure 7-18
MS31	0	16.5	10	X	Figure 6-11, Figure 7-18
MS33	0	16	2	X	Figure 6-11, Figure 7-18

Table 5-7. Specimen WB strain gage coordinates

Instrument	X (in.)	Y (in.)	Z (in.)	Orientation	Reference(s)
MS3	0	0.5	0.5	X	Figure 6-9, Figure 7-18
MS4	0	7.5	0.5	X	Figure 6-9, Figure 7-18
MS5	0	13.5	0.5	X	Figure 6-9, Figure 7-18
MS10	1.5	2.5	18	XZ	Figure 6-10, Figure 7-18
MS11	0	2	10.5	X	Figure 6-10, Figure 7-18
MS12	0	2	2	X	Figure 6-10, Figure 7-18
MS20	1.5	9	18	XZ	Figure 6-10, Figure 7-18
MS21	0	9	10.5	X	Figure 6-10, Figure 7-18
MS22	0	8	2	X	Figure 6-10, Figure 7-18
MS30	1.5	16	18	XZ	Figure 6-10, Figure 7-18
MS31	0	15.5	10.5	X	Figure 6-10, Figure 7-18
MS33	0	15	2	X	Figure 6-10, Figure 7-18

Table 5-8. Specimen FN strain gage coordinates

Instrument	X (in.)	Y (in.)	Z (in.)	Orientation	Reference(s)
XS1	19	14.5	6.25	Y	Figure 6-18
XS2	19	23	5.25	Y	Figure 6-18
XS3	19	30	6.25	Y	Figure 6-18
XS4	19	121	6.5	Y	Figure 6-18
XS5	19	128	6	Y	Figure 6-18
XS6	19	135.5	6.5	Y	Figure 6-18
XS7	19	142.5	6.5	Y	Figure 6-18
MS10	-1	2	18	XZ	Figure 6-13, Figure 7-18
MS11	0	2	10.5	X	Figure 6-13, Figure 7-18
MS12	0	3	2	X	Figure 6-13, Figure 7-18
MS20	-1	9	18.5	XZ	Figure 6-13, Figure 7-18
MS21	0	9	10.5	X	Figure 6-13, Figure 7-18
MS22	0	7	2	X	Figure 6-13, Figure 7-18
MS30	-1	16	18.5	XZ	Figure 6-13, Figure 7-18
MS31	0	15.5	10.5	X	Figure 6-13, Figure 7-18
MS33	0	14.5	2	X	Figure 6-13, Figure 7-18

Table 5-9. Specimen FB strain gage coordinates

Instrument	X (in.)	Y (in.)	Z (in.)	Orientation	Reference(s)	
XS1	19	14	5.5	Y	Figure 6-18	
XS2	19	22	6	Y	Figure 6-18	
XS3	19	29.5	5.25	Y	Figure 6-18	
XS4	19	119	6	Y	Figure 6-18	
XS5	19	127	6.25	Y	Figure 6-18	
XS6	19	135	6	Y	Figure 6-18	
XS7	19	142	6.25	Y	Figure 6-18	
MS3	0	0.5	0.5	X	Figure 6-8	
MS4	0	7	0.5	X	Figure 6-8	
MS5	0	13.5	0.5	X	Figure 6-8	
MS10	0.5	2	17	XZ	Figure 6-12	Figure 7-18
MS11	0	2	10	X	Figure 6-12	Figure 7-18
MS12	0	1.5	2	X	Figure 6-12	Figure 7-18
MS20	1	9	18	XZ	Figure 6-12	Figure 7-18
MS21	0	8.5	10	X	Figure 6-12	Figure 7-18
MS22	0	7.5	2	X	Figure 6-12	Figure 7-18
MS30	0.5	16.5	17.5	XZ	Figure 6-12	Figure 7-18
MS31	0	16	10	X	Figure 6-12	Figure 7-18
MS33	0	14	2	X	Figure 6-12	Figure 7-18

Table 5-10. Specimen DC strain gage coordinates

Instrument	X (in.)	Y (in.)	Z (in.)	Orientation	Reference(s)
MS3	0	3	0.5	X	Figure 7-18
MS4	0	9	0.5	X	Figure 7-18
MS5	0	15	0.5	X	Figure 7-18
MS10	1	2	18	XZ	Figure 7-18
MS11	0	1.5	10.5	X	Figure 7-18
MS12	0	2	3	X	Figure 7-18
MS20	1	9	18	XZ	Figure 7-18
MS21	0	9	10	X	Figure 7-18
MS22	0	8.5	3	X	Figure 7-18
MS30	2	16	18	XZ	Figure 7-18
MS31	0	16.5	10.5	X	Figure 7-18
MS33	0	16	3	X	Figure 7-18

Table 5-11. Specimen DM strain gage coordinates

Instrument	X (in.)	Y (in.)	Z (in.)	Orientation	Reference(s)
MS3	0	2.5	0.5	X	Figure 7-18
MS4	0	8	0.5	X	Figure 7-18
MS5	0	15	0.5	X	Figure 7-18
MS10	3	2.5	18	XZ	Figure 7-18
MS11	0	2.5	10	X	Figure 7-18
MS12	0	3	2.5	X	Figure 7-18
MS20	3	9.5	18	XZ	Figure 7-18
MS21	0	9	10.5	X	Figure 7-18
MS22	0	8	2.5	X	Figure 7-18
MS30	3	16	18.5	XZ	Figure 7-18
MS31	0	16	10	X	Figure 7-18
MS33	0	15	2.5	X	Figure 7-18

CHAPTER 6 RESULTS AND DISCUSSION: FABRICATION

Strain and crack data were collected during multiple stages of fabrication including: prestress transfer, lifting, storage, trucking, and deck placement. Data were collected to analyze the effects of fabrication events on end region behavior. The effects of end region detailing, particularly confinement reinforcement, were also of interest. Strain data are presented and discussed first followed by crack data.

Strain Data

Concrete Strain

Concrete strain data were primarily collected from girders H and V. These girders had the same strand shielding pattern, instrumentation scheme, material properties, and timing of construction events. To facilitate review of the strain-time history, the strand flame-cutting sequence is divided into the stages shown in Table 6-1. Stages A through D listed in Table 6-1 are graphically depicted in Figure 6-1.

General trends in the strain-time history for specimen HC (Figure 6-2) are representative of the other specimens in girders H and V. Any differences between the specimens were in the strain magnitudes, which are discussed later.

Strands in the top flange were the first to be cut; this stage is denoted A in Figure 6-2. Data indicate that the transverse strain change was negligible when the top strands were cut. Cutting the bottom strands (stages B, C, and D) had significant impact on transverse tensile strain. The largest measured transverse tensile strain in specimen HC was 406 microstrain reported by gage XS3. This gage was located on the end of the girder, at the cross-section centerline, 3in. above the strands. The maximum strain occurred at the beginning of stage D after all strands in the outer flange

had been cut and before any of the strands below the web had been cut. For this chapter, strands in the outer portion of the flange are referred to as “outer strands” and strands below the web are referred to as “inner strands”.

Transverse strain at gage XS3 decreased as inner strands were cut during stage D. The strain-time history from gage XS3 can be understood by considering the strand release pattern (Figure 6-1) and the resulting deformed shapes (Figure 6-3). As the outer strands were cut during stage B, the outside edges of the bottom flange deformed as shown in Figure 6-3. This deformed shape corresponded with the formation of tensile strains at the location of XS3. After the inner strands were cut, deformation of the bottom flange was more uniform and the tensile strain at XS3 was partially relieved. Once all of the strands were cut (stage E), the reported tensile strains at XS3 settled to approximately 25 microstrain.

Concrete strain was monitored for all specimens in girders H and V using gages placed at the same location as XS3 on specimen HC. Results from these gages are summarized in Table 6-2. While the overall behavior of the other specimens in girder H and V were similar to that shown in Figure 6-2, the magnitudes of the reported strains differed.

Several observations can be made from the strain data in Table 6-2. First, although cracks were not visually observed during prestress transfer, the strain magnitudes suggest that cracks had likely formed in each specimen, with the possible exception of specimen VC. Expected rupture strain for the concrete used in the specimens is approximately 132 microstrain. This value of expected rupture strain was derived from empirical equations for concrete elastic and rupture moduli from ACI 318

(2011). Second, the average maximum tensile strain in the unconfined specimens (HU and VU) was 3.4 times greater than the average maximum tensile strain in the confined specimens (HC and VC). Cracks forming in the unconfined ends would not have been impeded by confinement reinforcement, resulting in greater maximum transverse strains than in the confined ends. Finally, the average concrete tensile strain during stage E (all strands cut) was 2.6 times greater in the specimens without confinement reinforcement. The presence of confinement reinforcement significantly reduced the concrete tensile strain at the end of specimens HC and VC relative to specimens HU and VU.

Internal concrete strain gages (ES2 and ES3 in Figure 6-2) reported increases in tensile strain as prestress force was transferred. In contrast to gage XS3, the tensile strain reported by these gages increased as the inner strands were cut during stage D. Based on this observation and the location of the internal gages, it is concluded that the bending behavior captured by gage XS3 only occurred at or near the end of specimen HC. ES gages in HU, VC, and VU confirmed similar behavior in those specimens. In each specimen strain magnitudes reported by ES gages (Table 6-2) suggest that concrete near the internal gages remained linear-elastic (i.e. no cracking) during prestress transfer.

Confinement reinforcement did not affect the magnitude of concrete strain at the ES gages. Similar strain magnitudes were reported by specimens with and without confinement reinforcement (Table 6-2). Gages ES2 and ES3 were placed approximately 2ft and 4ft from the specimen ends, respectively. It is concluded that

confinement reinforcement only affected concrete strain at the end of the test specimens.

Stage F on Figure 6-2 denotes lifting of girder H. Figure 6-4 shows the supports conditions, loading, shear, and moment diagrams for the girders before, during, and after lifting. The change in support conditions had negligible effect on strain in the end region. None of the gages in the end region of girders H or V reported more than a 25 microstrain change during lifting and placement on dunnage.

Confinement Reinforcement and Bearing Plate Strain

Girders W and F were fabricated during phase 2 and had the same material properties, instrumentation scheme, and timing of construction events. Instrumentation was designed to capture confinement reinforcement and bearing plate behavior. To facilitate discussion of data, strand cutting events were broken into the stages listed in Table 6-3. Strand cutting events listed in Table 6-3 are keyed to the strand cutting pattern shown in Figure 6-5.

The strand bond patterns in girders W and F (Figure 6-6) had significant influence on the observed strain behavior. Girder W had fully bonded strands placed primarily below the web and partially shielded strands placed in the outer portion of the flange. Girder F had fully bonded strands in the outer portion of the flange and partially shielded strands below the web.

Three strain gages were placed on the bearing plates in specimens FB and WB. Gages were oriented to monitor the transverse ($x-x$) strain during prestress transfer. Gage locations and strain data are shown in Figure 6-7. Gage MS3 in specimen FB malfunctioned during prestress transfer and data from this gage is not shown in figure.

Strain at MS4 in specimen FB grew in tension as the outer strands were cut during stage K. Outer strands were fully bonded in specimen FB and caused the flange and plate to bend as shown in Figure 6-8. Strain in the plate was fairly constant after stage K. This is because no strands were cut during stage L and because the strands released during stage M were shielded in specimen FB. The difference in strain between gages MS4 and MS5 indicates in-plane bending of the plate due to the eccentric prestress force.

Data from gages on the plate in specimen WB also indicate in-plane bending during and after strand cutting. The direction of plate bending in specimen WB changed when the strands below the web were cut during stage M. This behavior is attributed to the strand bond pattern in specimen WB, which placed a few fully bonded strands in the outer portion of the flange and many fully bonded strands below the web. This pattern is thought to have caused the deformations and internal forces shown schematically in Figure 6-9. Release of the outermost strands at the beginning of stage K led to tension in the bearing plate at MS3 and compression in the bearing plate at MS5. The strain sense in the bearing plate reversed after the inner strands were released during stage M. After all strands were released (stage N) the bearing plate was in compression at MS3 and tension at MS5. The net strain in the plate after all strands were cut was approximately 32 microstrain tension, as calculated from the average of gages MS3, MS4, and MS5. The average strain from these gages is also equal to the strain reported at MS4, indicating that the strain reported by MS4 is also a reasonable measure of net strain.

Transverse forces in the bearing plates were calculated by multiplying the net bearing plate strains by the plate cross-sectional area and elastic modulus. Assuming that the net bearing plate strain is equal to the strain at MS4 (center of plate) the net plate strain at stage N was 32 microstrain tension for specimen WB and 79 microstrain tension for specimen FB. Accordingly, net tensile stresses in the plates were 0.9ksi, and 2.3ksi, and the net tensile forces in the plates were 5.2kip and 13.6kip for specimens WB and FB, respectively.

Select confinement reinforcement assemblies were instrumented with strain gages to monitor confinement reinforcement strain during prestress transfer. A confinement assembly is defined as the reinforcing bars placed together at the same y-ordinate (Figure 6-10). One strain gage was placed on each of the three reinforcement layers in each assembly.

Figure 6-10 shows confinement reinforcement strain from specimen WB. Reinforcement nearest to the end of the girder ($y=2\text{in.}$) was initially in tension due to release of the outermost strands during stage K. The strain later became compressive as the inner strands were released during stage M. This strain behavior is similar to the bearing plate strain in WB and is also attributed to flange bending behavior described in Figure 6-9. Confinement reinforcement placed 9in. from the end had very little strain until the innermost strands were released at the end of stage M. General strain behavior from the confinement assembly at 9 in. is representative of the strain behavior reported by gages on the confinement assembly placed 15 in. from the end (not shown).

Specimen WN had the same strand bond pattern as WB. The only significant difference in strain data between WN (Figure 6-11) and WB was that the confinement

reinforcement located 2in. from the end of specimen WN did not move all the way into compression during stage M. This difference may have been due to the absence of a bearing plate in specimen WN. Without a bearing plate there was less confinement in specimen WN and tensile strains were not relieved during stage M.

Specimen FB had fully bonded strands in the outer flange, all of which were cut during stage K. As such, confinement strain in FB (Figure 6-12) increased during stage K. No fully bonded strands were cut after stage K and the strain did not change in the subsequent stages. Confinement reinforcement was in tension throughout and after the strand cutting process.

Specimen FN had the same strand bond pattern as FB with fully bonded strands located in the outer portion of the flange. Strain behavior in specimen FN (Figure 6-13) was similar to FB up until the inner strands were released during stage M. During stage M the strain increased rapidly in the bottom (MS12) and middle (MS11) layers of confinement reinforcement. The strain magnitude during stage M suggests that cracking occurred in the nearby concrete. This result is puzzling because inner strands in specimen FB were shielded for 10ft from the specimen end. It appears that the shielded strands may have induced stresses in the concrete as they expanded after being cut. The thin plastic used to shield the strands may have been insufficient to absorb the strand expansion and prevent normal stresses at the strand-concrete interface. These stresses could have caused the strain changes at gages MS12 and MS11 that occurred during stage M.

Strain data at the end of stage N (all strands cut) is listed in Table 6-4 for each specimen. Several observations can be made by averaging the stage N strain data

(Figure 6-14). First, strain was greatest in the bottom layer of reinforcement for each test specimen. On average strain in the bottom layer was 1.4 times greater than the middle layer strain and almost 3 times greater than the top layer strain. Second, the largest confinement reinforcement strain occurred in specimens FN and FB in the confinement assemblies 2 in. from the member ends. Confinement reinforcement strain at 2in. from the end of FN and FB was almost 4 times greater on average than confinement strain at 9in. This is due to the bending behavior of the FN and FB described in Figure 6-8. Third, confinement strain in specimen FN was typically larger than in FB. The average confinement strain was over 2 times larger in specimen FN than FB. The difference in strain magnitude is attributed to the bearing plate in FB which carried transverse forces thereby reducing the strain in the confinement reinforcement. Finally, the maximum confinement strains in FN and FB were larger than the maximum confinement strains in WN and WB. On average the maximum strain in the FX specimens was 2.6 times greater than the WX specimens

Strain data were used to estimate the total force in each confinement reinforcement assembly after all strands had been cut (stage N). Forces were calculated by multiplying strains from Table 6-4 by the reinforcement area and steel elastic modulus. Two of five assemblies in specimens WB and FB were not monitored with strain gages. Strains in these assemblies were determined using linear interpolation. In specimens WN and FN three of five confinement assemblies were not monitored. Strains in the unmonitored assemblies were interpolated using the available strain data, or were extrapolated using the available data as well as the relationships between assemblies in specimens WB and FB. Results for each specimen are shown

in Figure 6-15 along with the estimated forces in the bearing plates. Only the x-direction force component in the inclined top layer of reinforcement was included in the results shown in the figure.

Total transverse force in the confinement reinforcement and bearing plate (where present) was 63% larger on average in specimens FB and FN than in specimens WB and WN. The additional force is attributed to the strand bond pattern in specimens FB and FN, which placed fully bonded strands in the outer portion of the flange. These fully bonded strands led to additional tension at ends of FN and FB. Most outer strands in specimens WB and WN were partially shielded and did not affect tension at the specimen ends. Transverse forces are compared to the jacking forces in Table 6-5. Combined transverse forces were equal to 0.6% to 1.7% of the jacking force in the fully bonded strands. Once again, due to the strand bond pattern, the relationship of transverse force to jacking force was larger for FN and FB than for WN and WB.

Data were not collected to estimate confinement reinforcement and bearing plate forces in specimens DC and DM. Strands in these specimens were placed in the 'design' strand bond pattern. Fully bonded strands were evenly distributed throughout the bottom flange in this pattern, placing it somewhere between the Wx and Fx specimens in terms of transverse tensile behavior. The transverse force in specimens with the design pattern would likely be smaller than Fx specimens because inner strands in the design pattern relieved tension due to the outer strand. Also, specimens with the design pattern likely had greater transverse force than the Wx specimens because the design pattern included outside strands.

Transfer Length

Longitudinal strains in the bottom flange of I-girders increase through the transfer length as prestress force is transferred from strands to concrete. At locations beyond the transfer length longitudinal strain is approximately constant. Transfer length in the test girders was experimentally determined by identifying the location at which longitudinal strain in the bottom flange transitioned to constant strain. This was accomplished using strain gages placed at intervals along the bottom flange (Figure 6-16).

When sufficient data are available, the 95% Average Maximum Strain (AMS) Method is a well-established method for determining transfer length from experimental strain data (Russell and Burns 1993). The available strain data in the current study were insufficient to apply the AMS method, but were still sufficient to estimate the transfer length by other means.

Figure 6-17 presents strain gage data from the bottom flange of girders H and V immediately after prestress transfer. Blue markers on the figure indicate the strain values reported by individual gages. Values reported by the gages were effectively constant (with some experimental scatter) for the monitored positions along the specimen lengths. This indicates that the gages were placed too far from the end of the girder to capture strain in the transfer length. A bi-linear curve representing the apparent strain profile is also shown in Figure 6-17. The apparent profile shows that the strain must be zero at the end of the girder and must increase to the experimental values recorded at 18in. Beyond 18in. the experimental strains and apparent strain were approximately constant. Thus the transition to constant strain occurred prior to

18in. and it is concluded that the transfer length is not greater than 18in. for girders H and V.

Figure 6-18 shows experimental strain data from girder F. As before, the blue markers on the figure are data points from individual gages. A piecewise linear curve representing the apparent strain profile is also shown in the figure. Girder F had fully bonded strands in the outer portion of the flange. Strands below the web were shielded for 10ft from the end. Gages were placed near the end of the girder and 10ft from the end in order to evaluate the transfer length of both fully bonded and partially shielded strands.

Gages placed near the ends of girder H reported increasing strain indicative of the transfer length. Beyond 30in. the strain was approximately constant until 120in. at which point the partially shielded strands began to transfer prestress force. Thus the change to constant strain occurred approximately 30in. from the girder end indicating that transfer length for the fully bonded strands was also approximately 30in.

Gages placed between 120in. and 144in. from the end reported increasing strain along the girder length. This indicates that they were within the transfer length of the partially shielded strands. Data were not available beyond 144in. and the transition to constant strain was not observed. As such transfer length of the partially shielded strands cannot be obtained directly from the available data. Transfer length can be estimated by assuming linear-elastic behavior of the concrete and strands. The 24 fully bonded strands affected a microstrain of 575 at the end of their transfer length. The 20 partially shielded strands should have added a proportional amount of strain, resulting in 1054 microstrain at the end of their transfer length. Slope of the apparent strain profile

is based on the available data points. Extending the strain profile along this slope shows that the apparent strain intersects 1054 microstrain at a distance 220in. from the member end. Prestress transfer of the partially shielded strands is thus estimated to have occurred between 120in. and 220in. from the member end. The estimated strand transfer length is 100in. This is significantly longer than the transfer length of the fully bonded strands. Additional data are necessary, though unavailable, for making a more accurate determination of transfer length in the partially shielded strands.

Transfer length was not measured in the other phase two girders (W and D) due to constraints with the data acquisition system. The transfer lengths in girders W and D were likely similar to girder F because the same strand and concrete materials were used for all phase two girders.

Measured transfer length for girders H and V was different from girder F. This difference is attributed to the different strand and concrete materials used in phase one (girder H and V) and phase two (girder F). Measured transfer lengths for fully bonded strands in both phases were less than the AASHTO LRFD calculated transfer length of 36in. Differences between experimental and code values may partially be due to the fact that strain data collected immediately after prestress transfer were used to determine the experimental transfer lengths. Barnes et al. (1999) observed that the transfer length grows by 10% to 20% in the weeks following prestress transfer.

Gages used to measure transfer length were placed at the outside edge of the bottom flange. Longitudinal strain at this location occurred due to axial shortening of the girder and due to shear lag from prestressing forces in the outer stands. Because of the shear lag component, the apparent transfer lengths measured by the gages were likely

somewhat longer than the effective transfer length. This effect would be greatest near the end of the girder. Barnes et al. (1999) used finite element modeling to quantify the effect of shear lag on transfer length measurements in AASHTO Type I girders. For fully bonded stands and an apparent transfer length of 18in. Barnes et al. calculated that the effective transfer length would be 16.5 in. For the test girders, the shear lag component of the strain will be affected by the relatively slender and wide bottom flange of the FIB. Thus the correction due to shear lag in the test girders would likely be slightly larger than calculated by Barnes et al.

Crack Data

Girders were inspected periodically during the time between form removal and load testing. When observed crack lengths and widths were measured and documented. Cracks widths were determined using a microscope that was precise to ± 0.001 in. Crack lengths were determined by visual inspection with the naked eye.

Three types of cracks were observed in the test girders:

- Top flange flexural cracks
- Web splitting cracks
- Flange splitting cracks

Top flange cracking was due to flexural stresses generated by the vertically eccentric prestressing and is outside the scope of this end region research. Web splitting (Figure 6-19) cracks were also due to eccentricity of prestressing. Vertical tension stress formed in the web at the end of the specimens as the prestress force was distributed to the cross-section. Flange splitting cracks are of primary interest in the current investigation of confinement reinforcement and were caused by horizontal eccentricity of prestressing, Hoyer expansion of strands, and self-weight reaction of the

test girders. Transverse tensile stress formed in the bottom flange as prestressing forces were distributed through the cross-section from eccentric strands in the outer portion of the flange. Additional tensile stresses formed due to the Hoyer effect, in which strand expansion after cutting was restrained by the concrete. Self-weight caused tensile stresses above the support due to Poisson and flange bending effects. Cracks in the top flange, web, and bottom flange occurred when the tensile stresses described above exceeded the concrete strength.

Presentation of crack data is divided according to the two phases of construction. This was done because the materials properties, construction procedures, and curing conditions varied between the construction phases. Within each phase, crack data were further divided between flange splitting cracks and web splitting cracks.

Cracking was quantified and compared in terms of total crack length, total crack area, and maximum crack width. Total crack length was calculated by summing the length of individual cracks for a specimen. Total crack area was calculated by summing the length of each crack multiplied by its representative width. Representative widths were determined from microscope measurements taken at selected points along cracks. Maximum crack width was determined from the microscope readings.

As part of an NCHRP research project, Tadros et al. (2010) recommended criteria for acceptance, repair, and rejection of girders with web splitting cracks. Criteria are based on laboratory data and from field data from Nebraska and Virginia. More stringent criteria may be warranted in aggressive environments such as along Florida coasts. Nevertheless, the recommendations shown in Table 6-6 and were used as a benchmark for evaluating crack widths in the test specimens.

In general, cracking behavior differed between the two phases of construction. Cracks were first observed in phase one girders (H and V) in the days following prestress transfer, whereas cracks were first observed in phase two girders (W, F, and D) during prestress transfer. Another difference was that cracks in the phase one girders typically did not grow after they were first observed. Cracks in the phase two girders continued to grow in length during the weeks after they were first observed.

Girders H and V

Girders H and V were fabricated together during the first phase of construction. Girders were inspected for cracking ten times between form removal and load testing (Table 6-7). Figure 6-20 shows web and flange splitting cracks observed during inspections. Flexural cracking in the top flange cracking is not shown in the figure.

Cracks were first observed in girders H and V nine days after prestress transfer. The day that cracks formed is unknown because girders H and V were not inspected during the days immediately following prestress transfer. Web splitting cracks were observed in each specimen. Flange splitting cracks were only observed in specimens without confinement reinforcement (HU and VU). At the end of these specimens the flange cracks intersected with the outermost strand in the third row (Figure 6-21). Strands at this location had 2.5 in. of clear cover to the top surface of the flange, which was the least amount of top cover for any strand in the test girders.

Cracks in specimens H and V changed little after they were first observed. An additional web splitting crack was observed in specimen HC during an inspection fifteen days after prestress transfer. No other significant changes in crack quantity, width or length were observed during subsequent inspections of girders H and V.

Web splitting cracks in specimens with the greater amount of end region reinforcement (HC and HU) were an average of 72% longer than the cracks in specimens with less reinforcement (VC and VU)(Figure 6-22). One possible reason that web cracks were longer in HC and HU was that horizontal bars at the ends of these specimens created a path where horizontal cracks could form and propagate. Web cracks in HC and HU always occurred at the location of horizontal bars.

Although the additional reinforcement increased the total web crack length, it was also more effective in controlling web crack widths. The maximum web splitting crack width was 0.008in. in specimens HC and HU, whereas maximum crack widths were 0.012in. and 0.02 in. in VC and VU, respectively (Figure 6-23). The additional vertical bars in specimens HC and HU appear to have increased the post-cracking stiffness thereby reducing maximum crack width relative to VC and VU.

For girders H and V the maximum crack widths were typically less than 0.012 in., which according to the criteria in Table 6-6 do not require repair. Only specimen VU had a crack with a width greater than 0.012 in. One of the web splitting cracks in this specimen had a maximum width of 0.02 in. According to the criteria in Table 6-6 this crack would require repair by filling with cementitious material and application of a sealant to the girder end.

Total crack area (Figure 6-22) was derived from both length and width data, and provides a quantitative comparison of end cracking. Web cracks in specimens HC and HU were longer but narrower than web cracks in VC and VU. Because of this, there is less variation in total web crack area than was observed in total web crack length and

maximum web crack width. Variation in total web crack area varied by 24% between HX and VX specimens.

Flange splitting cracks only occurred in specimens HU and VU, which did not have confinement reinforcement. The total length and area of flange cracks were similar between HU and VU (Figure 6-24). The maximum width of flange splitting cracks was 0.004 in (Figure 6-23). Presumably, confinement reinforcement in HC and VC controlled the formation and propagation of flange cracks in those specimens.

Girders W, F, and D

Girders W, F, and D were fabricated together during the second phase of construction. Construction events, inspection dates, and notes from girders W, F, and D are listed Table 6-8. Flange and web splitting cracks were first observed in these girders after the outer strands had been cut during prestress transfer. Cracks grew in quantity and length in the days and weeks following prestress transfer. Figure 6-25 shows the web and flange splitting cracks observed prior to load testing. Flexural cracks in the top flange are not shown.

Steel bulkheads were used during construction of girders W, F, and D. A portion of the bulkhead covering the end of the bottom flange (Figure 6-26) remained with each test girder for approximately two weeks after prestress transfer. Bottom flange ends covered by the bulkheads were inspected for the first time 30 days after transfer. Cracks were observed at the girder ends during this inspection. Because the ends were previously covered, it is not known when splitting cracks at the end of the bottom flanges first formed.

The location of cracks shown in Figure 6-25 can be understood by considering the strand bond patterns in the test specimens. For example, specimens WN and WB had

flange splitting cracks located 10ft from their ends. These cracks formed within the transfer length of partially shielded strands. Strands in WN and WB were 45% partially shielded, with all shielding located in the outer portion of the flange. It is believed that the flange cracks in WN and WB occurred due to Hoyer stresses and lateral-splitting stresses associated with the partially shielded strands.

Strands in specimens FN and FB were also 45% shielded, with all shielding located below the web and all shielding terminating 10ft from the specimen ends. This pattern placed fully bonded strands in the outer portion of the flange and led to tensile stresses in the bottom flange as illustrated by Figure 6-8. Flange splitting cracks formed when tension stresses at the end of the flange exceeded the concrete tensile strength. Flange cracks at the ends of FN and FB intersected strands (Figure 6-27) suggesting that the Hoyer effect also contributed to the tensile stresses and crack formation. Flange splitting cracks in FN and FB were greater in total length and in total area than all other specimens (Figure 6-28). The maximum width of flange splitting cracks was also greater for FN and FB (Figure 6-29) than other specimens.

Specimens DC and DM had the largest number of fully bonded strands (39) in the phase 2 test girders. As such the web stresses and web splitting cracks were greatest in DC and DM. All other specimens had only 24 fully bonded strands. The total length of web splitting cracks in specimens DC and DM were 132 in. and 179 in., respectively (Figure 6-30). The maximum width of web splitting cracks was 0.008 in. specimens DC and DM (Figure 6-29).

Specimens DC and DM had flange splitting cracks (Figure 6-31) in addition to web cracks. At the end of these specimens the flange splitting cracks intersected strands,

suggesting that the Hoyer effect contributed to crack formation. In specimen DC the cracks intersected the outermost strands in the second and third rows.

The maximum crack width in girders W, F, and D was 0.008 in. This width does not warrant repair using the criteria from Table 6-6.

Variable Comparison and Discussion

This section compares crack behavior across specimens and variables. Trends identified in the test specimens will be useful in detailing end regions to prevent and control cracking during and after prestress transfer.

Flange splitting cracks (Figure 6-24) formed in phase one specimens without confinement reinforcement (HU and VU) but not in specimens with confinement (HC and VC). This result suggests that confinement reinforcement controls flange splitting cracks that form due to prestressing. It is presumed that confinement reinforcement in HC and VC prevented flange splitting cracks from opening and propagating.

The quantity of bonded strands affected the total length and area of web splitting cracks. This is evident from Figure 6-30 which compares specimens DC and DM (39 strands each) with specimens WN, WB, FN, and FB (24 strands each). On average the total crack length and total crack area were 78% and 168% larger, respectively, in specimens with 39 fully bonded strands than in the specimens with only 24 strands. The maximum web crack width was twice as large in specimens with 39 fully bonded strands as in those with 24. These results indicate that reducing the quantity of fully bonded strands through partial shielding can successfully control the length, area, and maximum width of web splitting cracks.

The location of shielded strands within the bottom flange (inner flange or outer flange) was not a factor in length, area, or maximum width of web splitting cracks. Web

splitting cracks in specimens with shielded strands placed in the outer portion of the flange (WN and WB) had similar total length, total area (Figure 6-30), and maximum width (Figure 6-29) as comparable specimens with shielded strands placed below the web (FN and FB).

The effect of confinement reinforcement and bearing plates on web splitting cracks is not obvious from the test data. Comparing total crack areas for girder H and V (Figure 6-22), it can be seen that specimens with confinement reinforcement had similar crack area but longer lengths than specimens without confinement. Specimens WN and FN without bearing plates had more crack length and area (Figure 6-29 and Figure 6-30) as specimens WB and FB with bearing plates. One possible explanation for the greater amount of cracking in FB and WB is that bottom flange confinement provided by the bearing plates resulted in shorter transverse lengths and higher end stresses than in specimens without bearing plates.

Specimens FN and FB had the worst flange cracking and had all bonded strands placed in the outer portion of the flange. Severity of flange cracking specimens FN and FB is attributed to this strand bond pattern. The total length and total area (Figure 6-28) of flange cracks in FX specimens were both on 2.5 times greater on average than the same metrics in the other phase 2 specimens. Similarly, the maximum flange crack width (Figure 6-29) was twice as large in FX specimens as in the other phase 2 specimens. Based on these results it is recommended that strands be placed as near to the centerline of the bottom flange as practical in order to maximize cover and minimize flange splitting cracks.

Six of the ten specimens had flange splitting cracks at the member end. In five of the six with flange cracks at the end, flange cracking intersected the outermost strand in the third row (Figure 6-21). Strands at this location had only 2.5 in. of clear cover to the top of the bottom flange. This was the least amount of cover of any strand in the test specimens. It is recommended that this location be avoided when designing strand patterns. Furthermore it is recommended that strand patterns be designed with the maximum amount of top cover.

Flange cracks were observed within the transfer length of the partially shielded strands in specimens WB and WN. Approximately 45% of strands in these specimens were partially shielded, and all shielding terminated at the same section 10ft from the specimen ends. Both the overall shielding percentage and the termination of shielding violated AASHTO LRFD requirements. Flange cracks were not observed within the transfer length of partially shielded strands in specimens that complied with the AASHTO requirements.

Similar to specimens WB and WN, specimens FB and FN also violated the AASHTO requirements for total percentage of shielded strands and quantity of strand shielding that terminated at a section. Unlike specimens WB and WN, however, specimens FB and FN had partially shielded strands placed below the web and did not have flange cracks within the transfer length of the partially shielded strands. This demonstrates that the overall percentage of shielded strands was not a factor in flange cracking. The location of shielding was more critical to flange cracking than was the percentage of strand shielding that terminated at a given section.

Flange cracking in specimen end regions extended up to 30in. from the member end. This length is 6 in. shorter than the code calculated transfer length of 36in. The similarity between these values suggests that code specified transfer length may be a good estimate of flange splitting crack lengths and that the code transfer length is a reasonable guideline for placement of confinement. The correlation between flange splitting crack length and transfer length is attributed in-part to the Hoyer effect which causes tensile splitting stresses within the transfer length.

Embedded steel bearing plates were excluded from specimens WN and FN. Absence of a bearing plate in specimen FN led to 64% greater total crack flange crack length and 76% greater total crack area when compared to specimen FB which had a bearing plate. Both specimens had fully bonded strands placed only in the outer portion of the flange.

Absence of a steel bearing plate did not adversely affect cracking in specimen WN relative to WB which had a bearing plate. Neither specimen had flange cracks at the member end. Thus presence of a bearing plate had the beneficial effects of reducing crack length and area, but only in specimens with fully bonded strands placed in the outer portion of the flange.

Configuration of confinement reinforcement can be compared using results from specimens DC and DM. Specimen DC had #3 confinement reinforcement as currently specified by FDOT. DM had #4 confinement reinforcement but had fewer total confinement bars than DC. Specimen DC had 151% greater total flange crack length, and 113% greater total flange crack area than did specimen DM. Average flange crack width was not significantly different between the specimens. These results suggest that

the modified confinement reinforcement performed better at controlling flange splitting cracks than the FDOT configuration. This is attributed to the fact that specimen DM had more reinforcement placed closer to the end than did specimen DC.

Summary and Conclusions

Cracking and strain data were collected in pretensioned FIB girders during multiple stages of construction including: prestress transfer, lifting, storage, transport, and deck construction. Each end of each girder had a different set of variables. Variables included: the quantity or lack of confinement reinforcement, the presence or lack of a steel bearing plate, and the strand bond pattern. Two of the tested strand bond patterns were intentionally designed to violate current AASHTO LRFD requirements. Strain data from the reinforcement and bearing plates were used to estimate the transverse forces developed during prestress transfer. The following conclusions are made based on results from the strain data:

- Transverse tensile strains were observed in the bottom flange, confinement reinforcement and embedded bearing plates during and after prestress transfer. Tensile strains are attributed to prestressing forces, the Hoyer effect and girder self-weight and are thought to have caused flange splitting cracks.
- Transverse tensile strains are greatest in sections with fully bonded strands placed only in the outer portions of the bottom flange. Bonded strands in the outer flange are eccentric with the resultant internal force, thereby inducing bending in the bottom flange and associated transverse tension at the girder end.
- Transverse tensile strains are smaller in sections with fully bonded strands placed below the web than in sections without fully bonded strands below the web. This is because prestress forces from the inner (below the web) strands counteract the transverse tension caused by prestress forces from strands in the outer portions of the flange.
- Confinement reinforcement can be effective in controlling transverse tensile strain and associated splitting cracks in the bottom flange during and after prestress transfer. Specimens without confinement reinforcement had average transverse tensile strains in the bottom flange concrete that were 3.4 times greater than specimens with confinement reinforcement.

- The greatest strain in confinement reinforcement typically occurs in the lowest layer of reinforcement. In the test specimens, the bottom layer of confinement had strains 1.4 times greater on average than the middle layer.
- Confinement strains are largest near the end in members with fully bonded strands placed in the outer portion of the flange. In test specimens with fully bonded outer strands the strain was 4 times larger in bars 2in. from the end than in bars 9in. from the end.
- Transverse tensile forces in confinement reinforcement and bearing plates were approximately 50% larger on average in members with bonded strands in the outer flange only, as compared to members with bonded strands in the inner flange only.
- The combined transverse tensile force in confinement reinforcement and bearing plate was estimated (based on strain data) to be between 0.6% and 1.7% of the total jacking force in fully bonded stands. These values represent lower and upper bounds for extreme strand bond patterns.
- Lifting of test girders and placement on dunnage had little effect on the transverse and vertical strain in the end region. The maximum change in strain during this process of 25 microstrain.

Cracking was monitored in test specimens from the time forms were removed until the time of load testing. The following conclusions are made based on results from the crack data:

- In some cases web and flange splitting cracks occur during and immediately following prestress transfer. In other cases cracking occurs during the days or weeks following transfer.
- Length and width of web and flange cracks are affected by detailing of the end region, even in specimens having the same cross-section.
- Flange splitting cracks in test specimens had maximum widths between 0.002 in. and 0.008 in. These cracks widths do not warrant repair according to the criteria set forth by Tadros et al. (2010).
- Flange splitting cracks extended up to 30in. from the test specimens ends. This length is comparable to the code calculated transfer length of 36 in. (30 strand diameters). This result suggests that the code transfer length is a reasonable extent for the placement of confinement reinforcement to control flange splitting cracks.

- Confinement reinforcement appears to have effectively controlled flange splitting cracks in specimens HC and VC. Splitting cracks were observed in comparable specimens (HU and VU) without confinement reinforcement.
- Absence of a steel bearing plate affected the lengths and widths of flange splitting cracks in specimens with fully bonded strands placed only in the outer portion of the flange. For example, the total flange crack length was 64% greater and total flange crack area 76% greater in specimen FN (no plate) than in specimen FB (with plate).
- The total length and area of flange splitting cracks were dependent on the strand bond pattern. Specimens with bonded strands placed only in the outer flange had 2.5 times greater total flange crack length and area than specimens with bonded strands distributed throughout the bottom flange. Splitting cracks did not occur in the end region in specimens where bonded strands were placed only in the inner portion of the flange.
- Flange splitting cracks formed within the transfer length of partially shielded strands in two specimens. These cracks were affected by the placement of shielded strands in the outer portion of the flange, and the quantity of shielding that terminated at a same section. The total percentage of shielded strands did not affect cracking.
- Flange splitting cracks were not observed in the transfer length of shielded strands in specimens complying with AASHTO LRFD requirements for quantity of shielding that can terminate at a given section.
- Splitting cracks in the bottom flange typically intersected the outermost strand in the third row from the bottom. This strand location had the least amount of top cover of any location in the test girders.
- Length and area of web splitting cracks was a function of the quantity of fully bonded strands. Web splitting cracks in specimens with 39 fully bonded strands were 78% longer and had 168% more area than web cracks in specimens with 24 fully bonded strands.
- Position of fully bonded strands in the bottom flange did not affect the length, area, or width splitting cracks in the web.

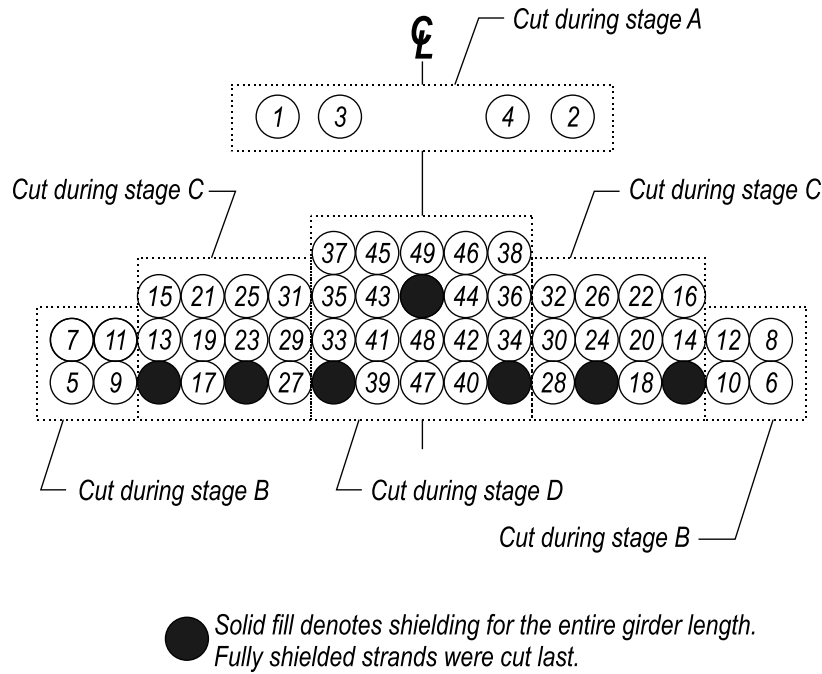


Figure 6-1. Girders H and V strand cutting stages

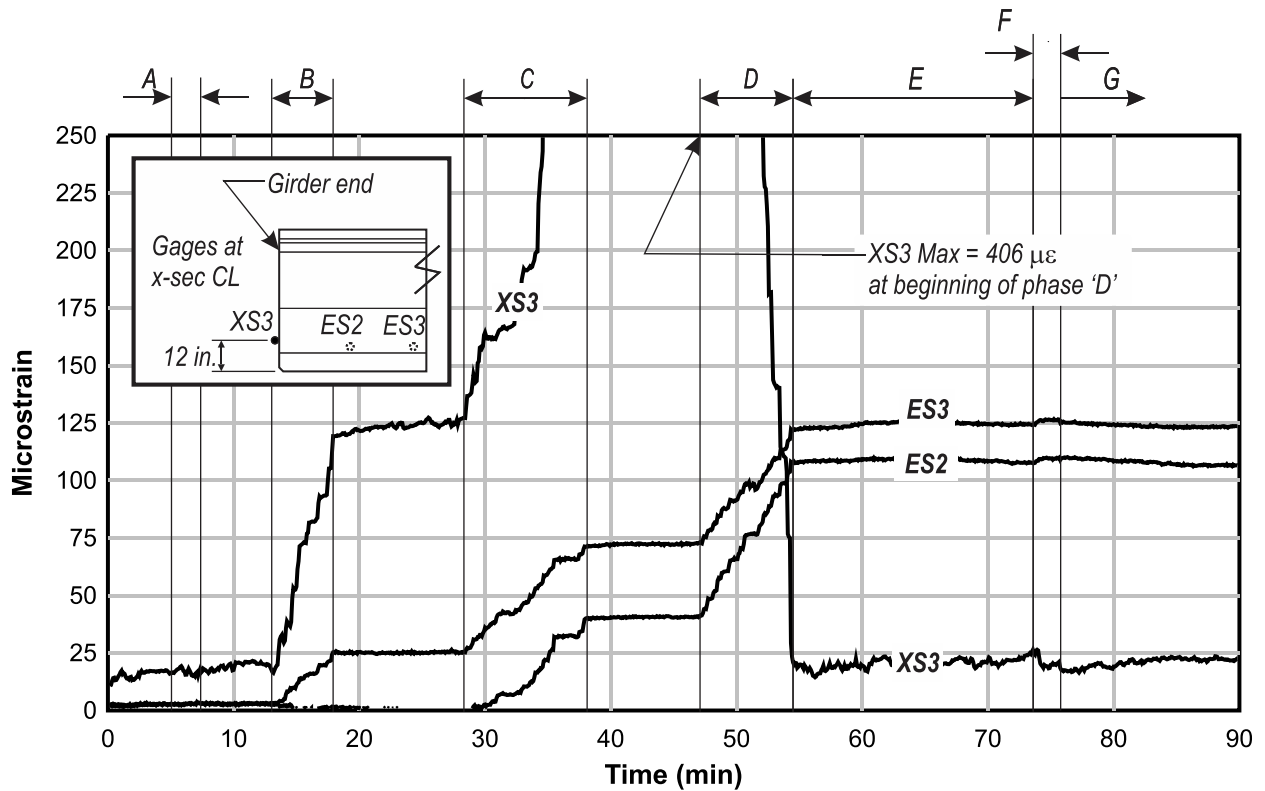


Figure 6-2. Transverse Strain HC

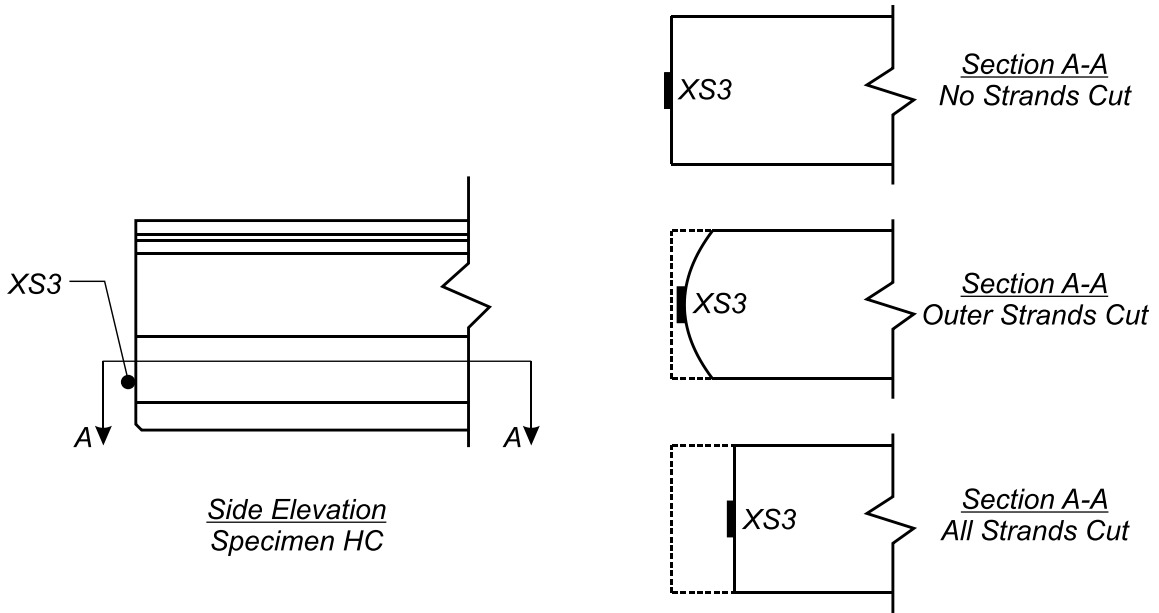


Figure 6-3. Flange displaced shapes for specimen HC

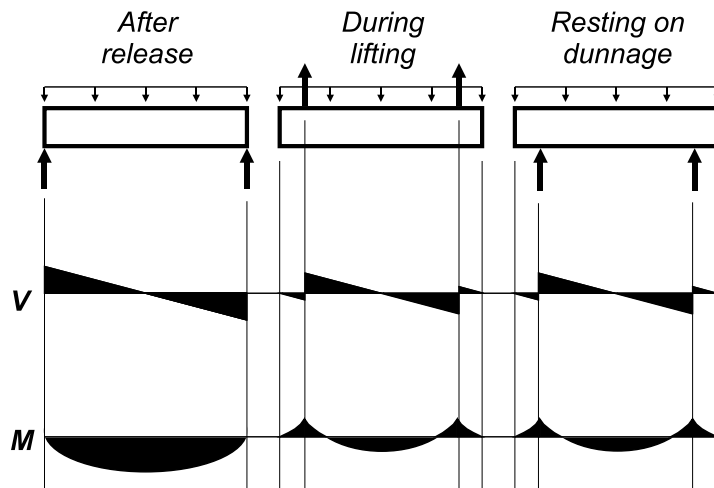


Figure 6-4. Shear and moment during release, lifting, storage (prestressing not shown)

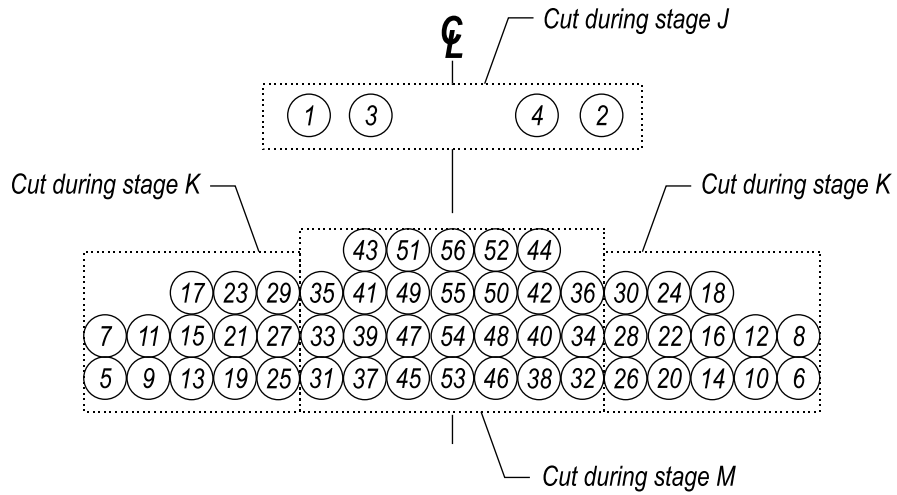


Figure 6-5. Girders W and F strand cutting stages

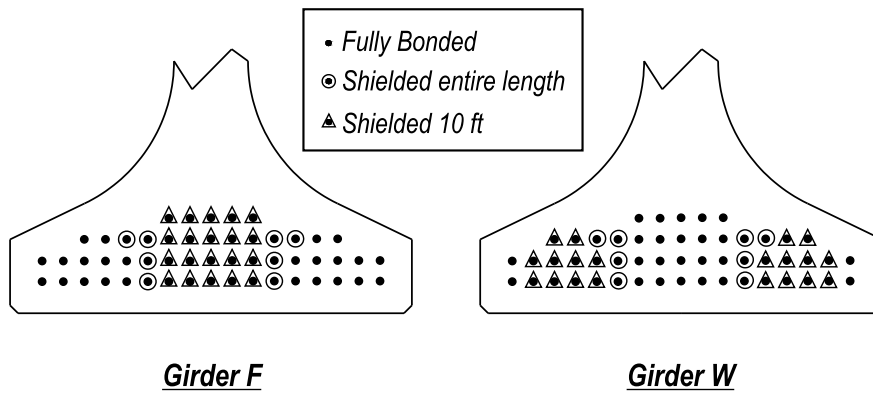
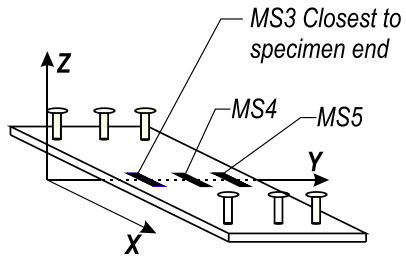


Figure 6-6. Girders W and F strand bond patterns



Specimen WB

Specimen FB

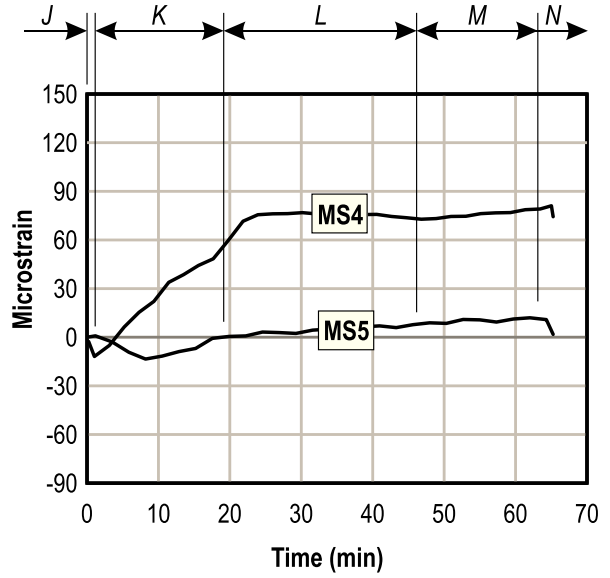
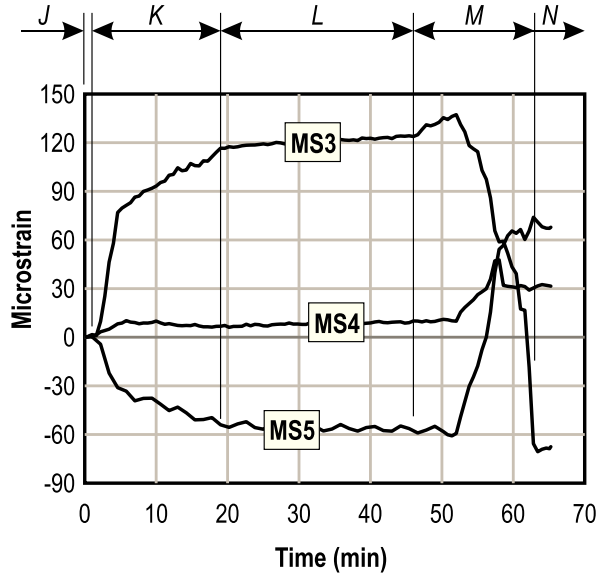


Figure 6-7. Bearing plate strain

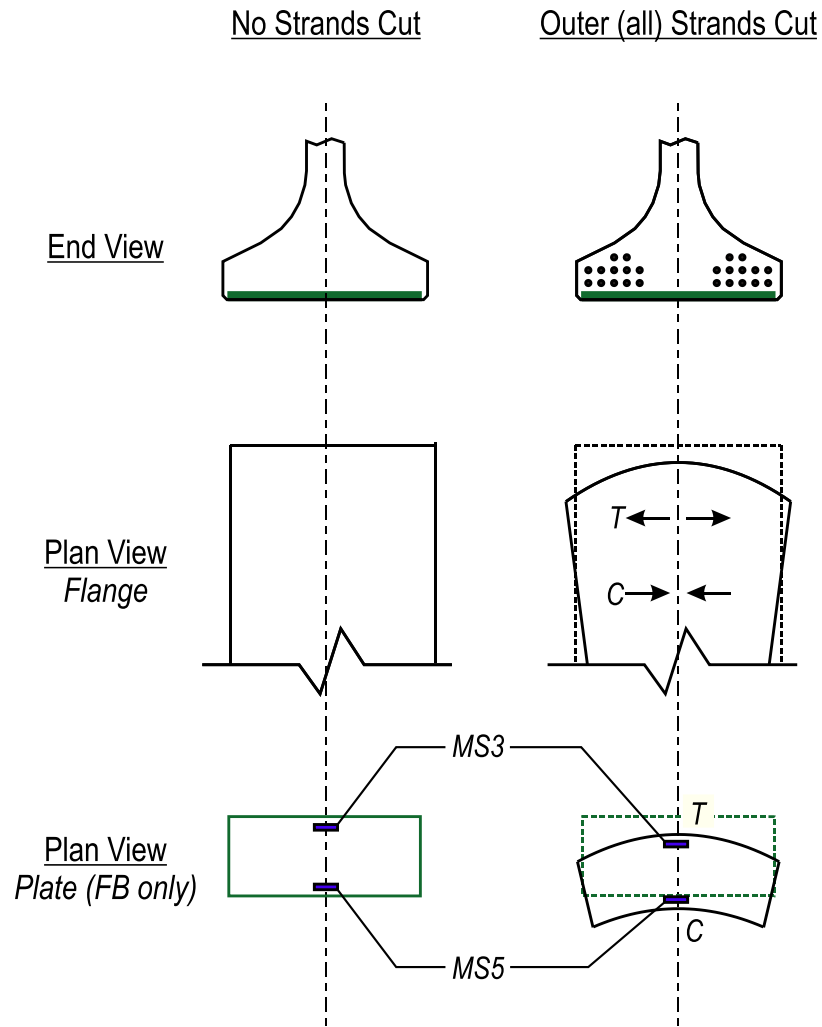


Figure 6-8. Flange displaced shapes specimens FN and FB

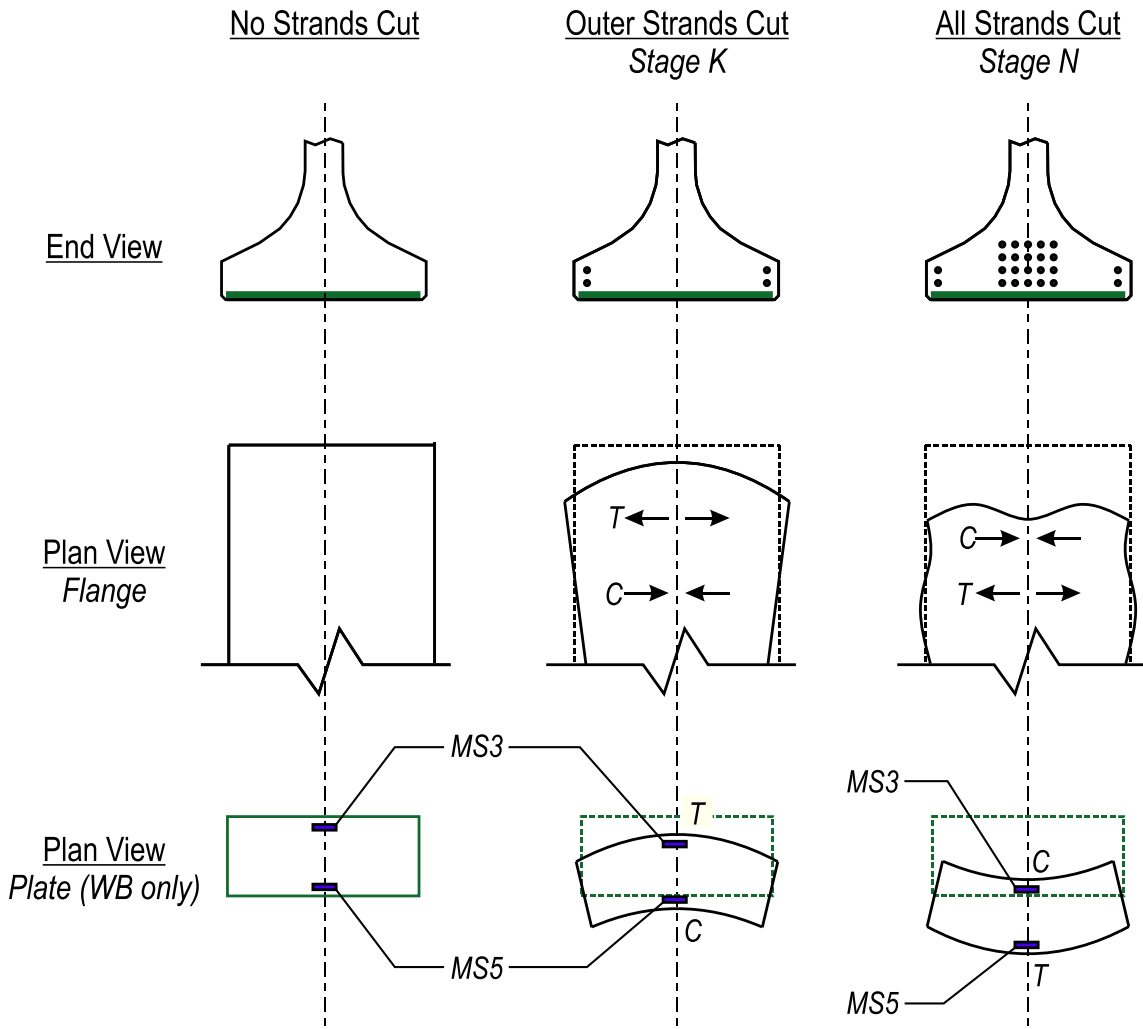


Figure 6-9. Displaced shapes specimen WB and WN

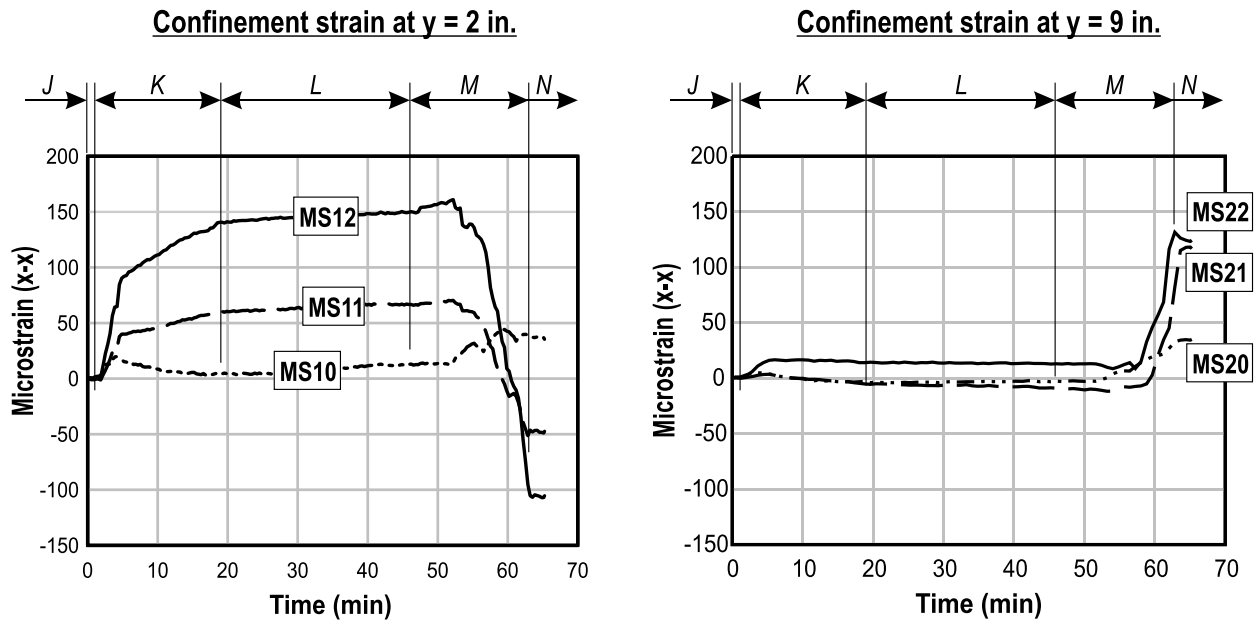
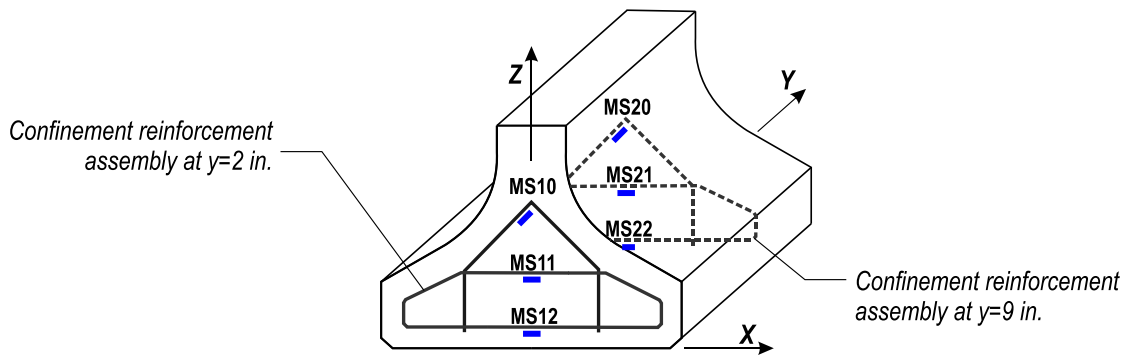


Figure 6-10. WB Confinement reinforcement strain at 2 in. and 9 in. from end of girder.

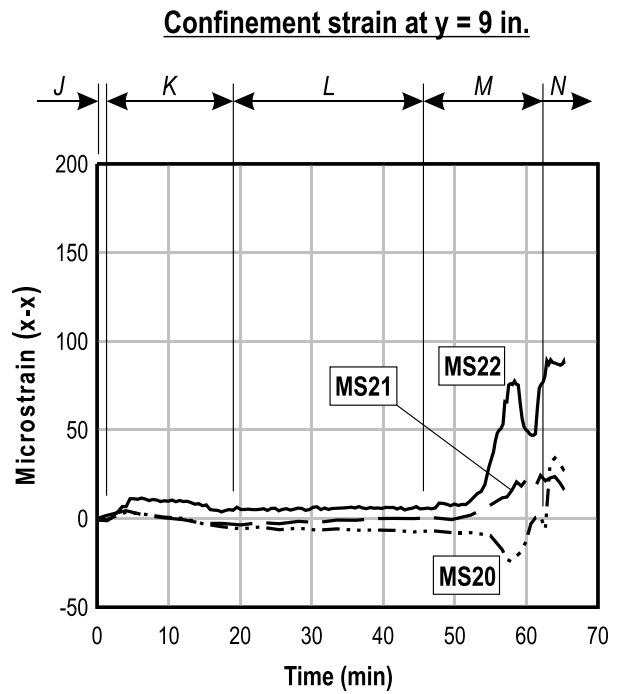
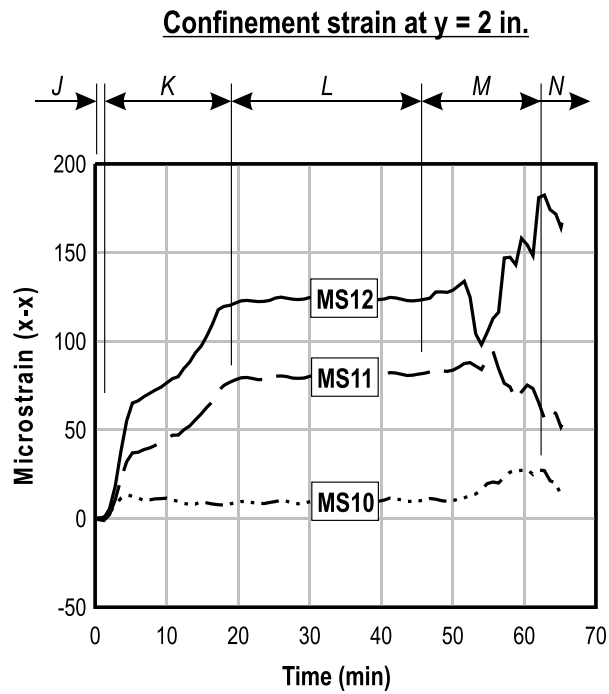
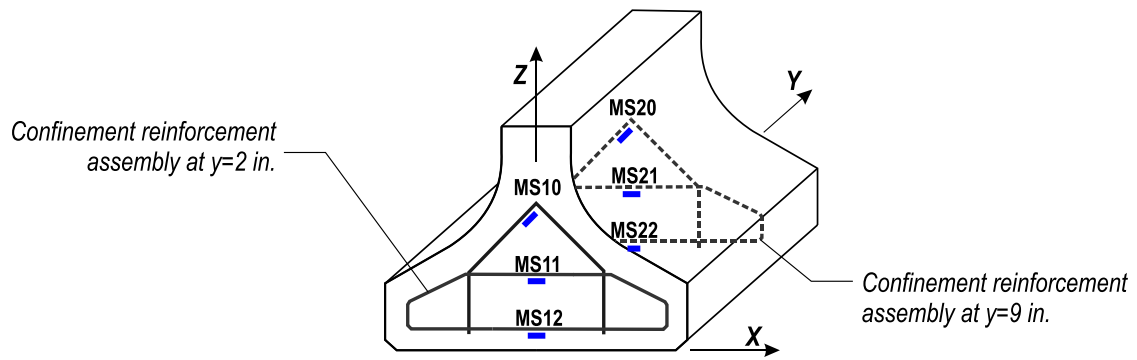


Figure 6-11. WN Confinement reinforcement strain at 2 in. and 9 in. from end of girder

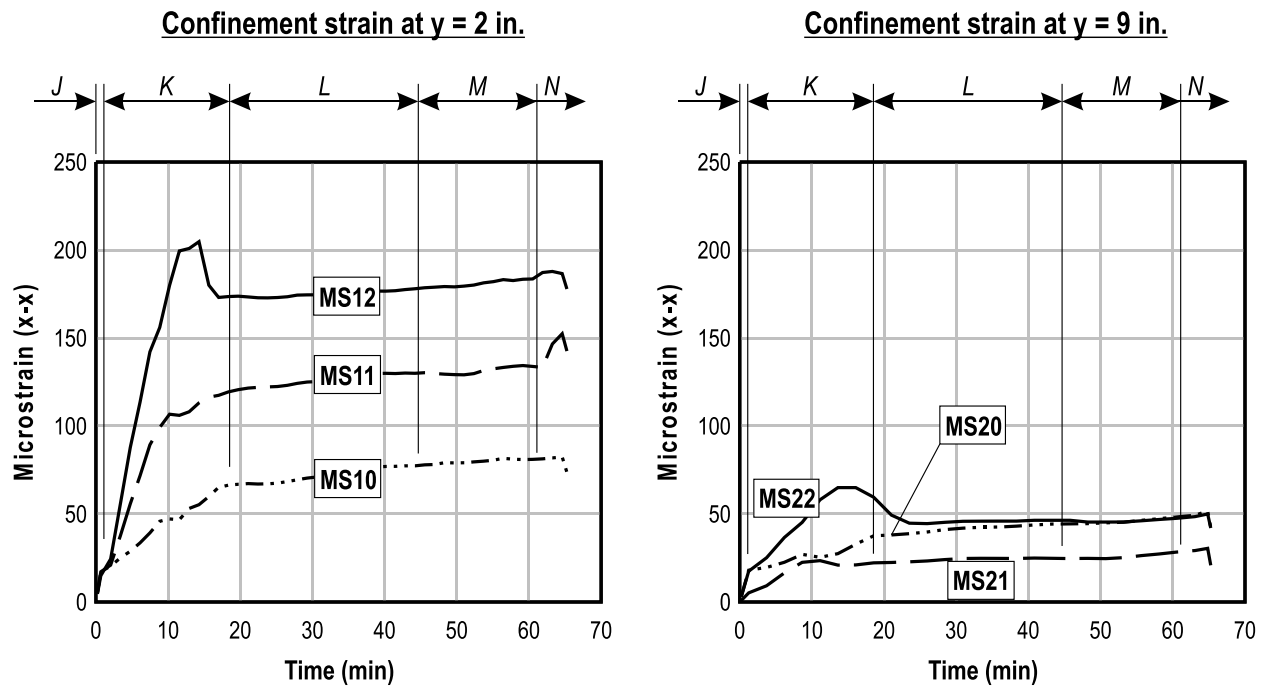
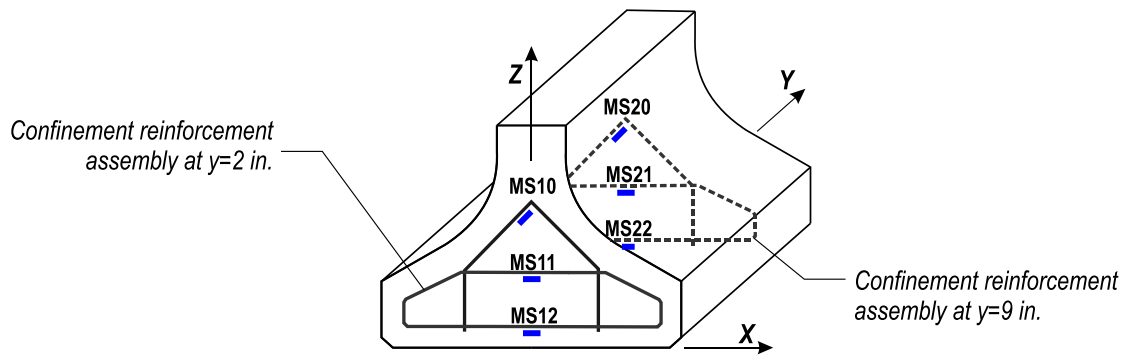


Figure 6-12. FB confinement reinforcement strain at 2in. and 9in. from end of girder

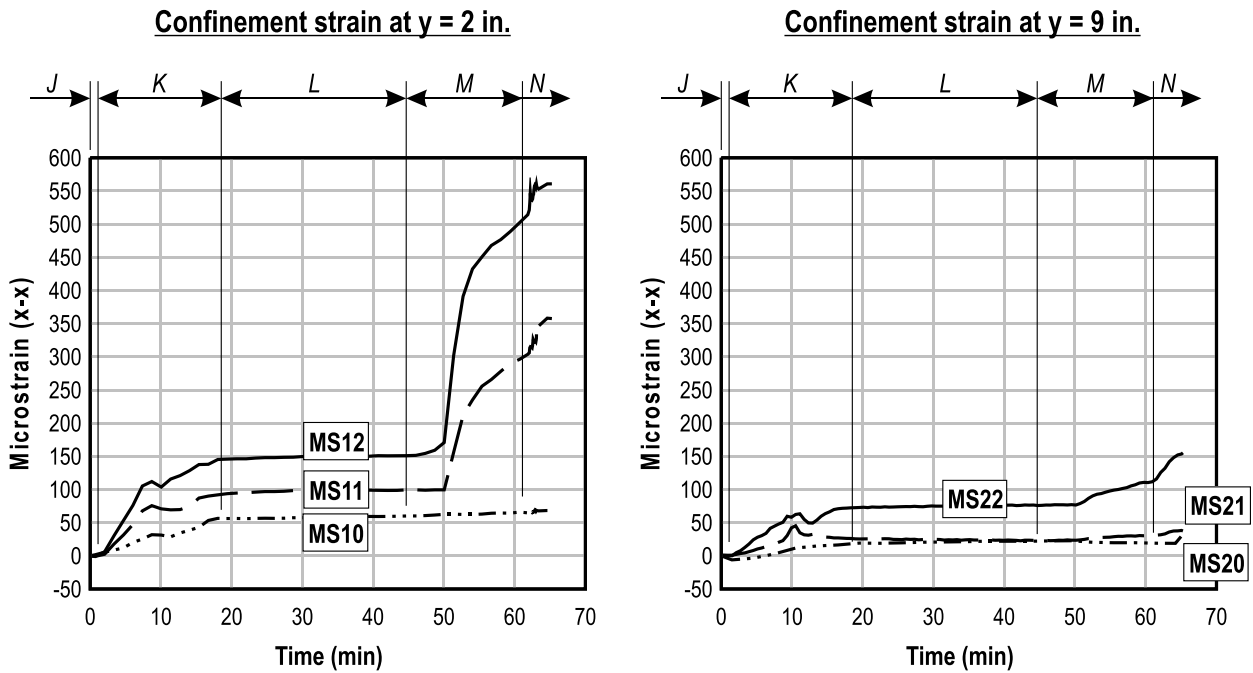
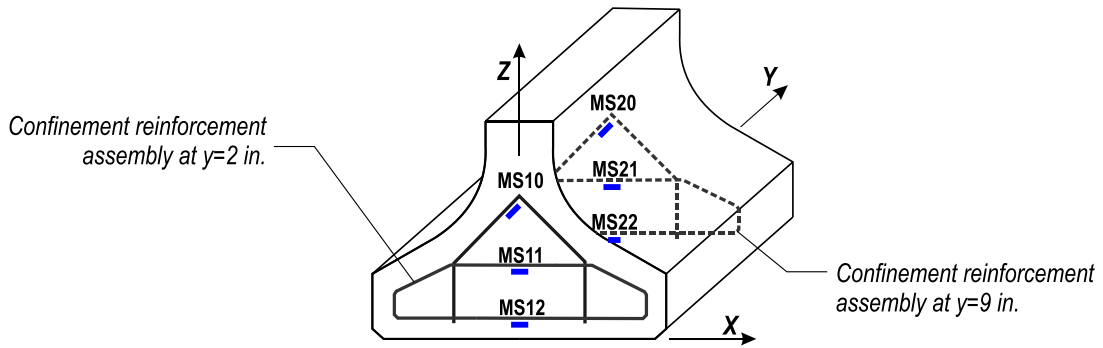


Figure 6-13. FN Confinement reinforcement strain at 2in. and 9in. for end of girder

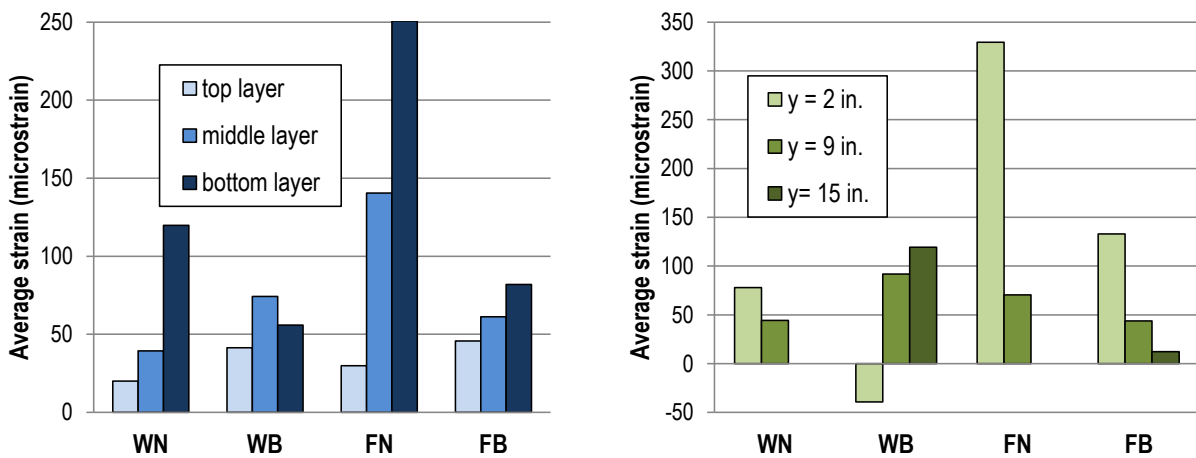


Figure 6-14. Confinement reinforcement average strain at prestress release

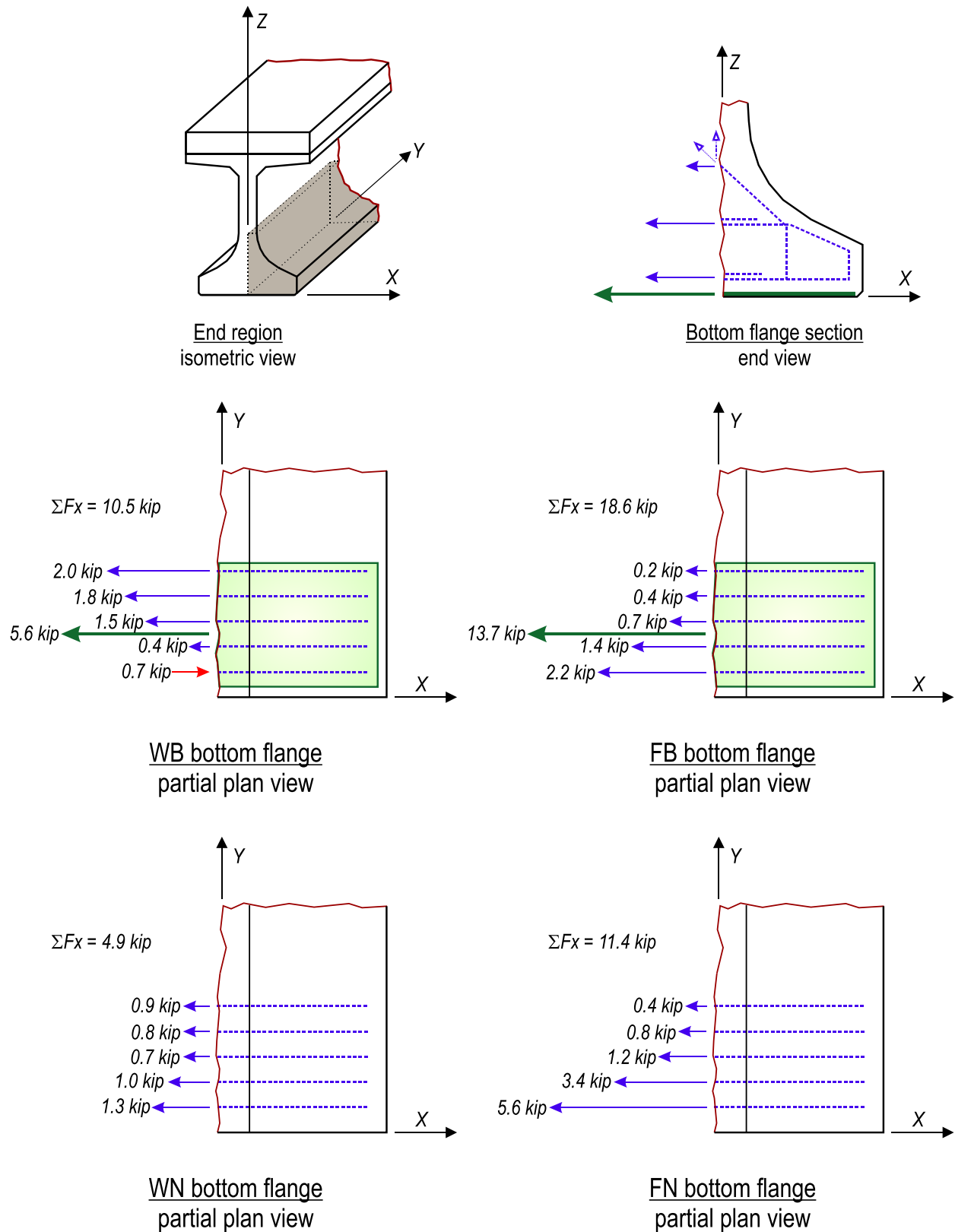


Figure 6-15. Forces in reinforcement and plates after prestress transfer



Figure 6-16. Strain gages for measuring transfer length. (Photo courtesy of B.E. Ross)

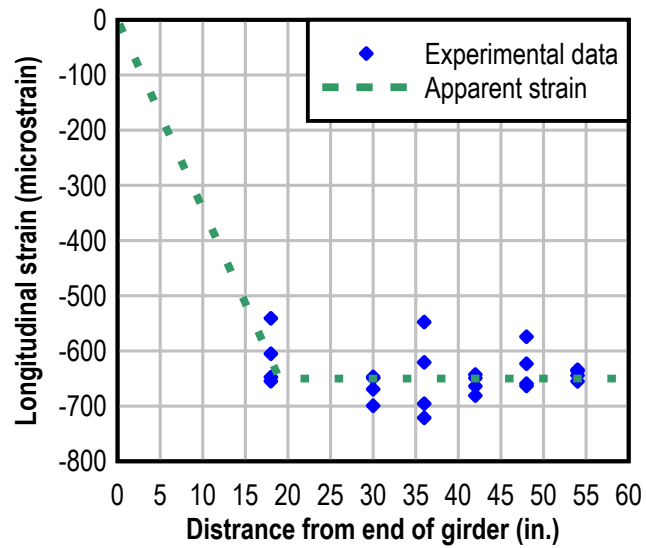


Figure 6-17. Transfer length in girders H and V

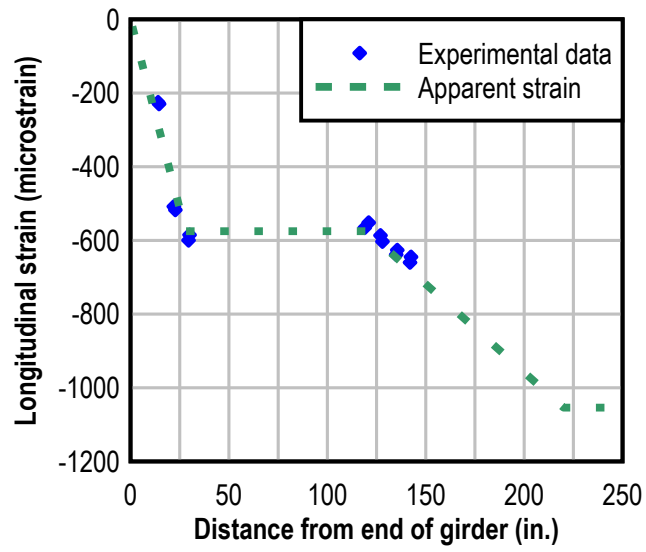


Figure 6-18. Transfer length girder F



Figure 6-19. Web splitting and flange splitting cracks. (Photo courtesy of B.E. Ross)

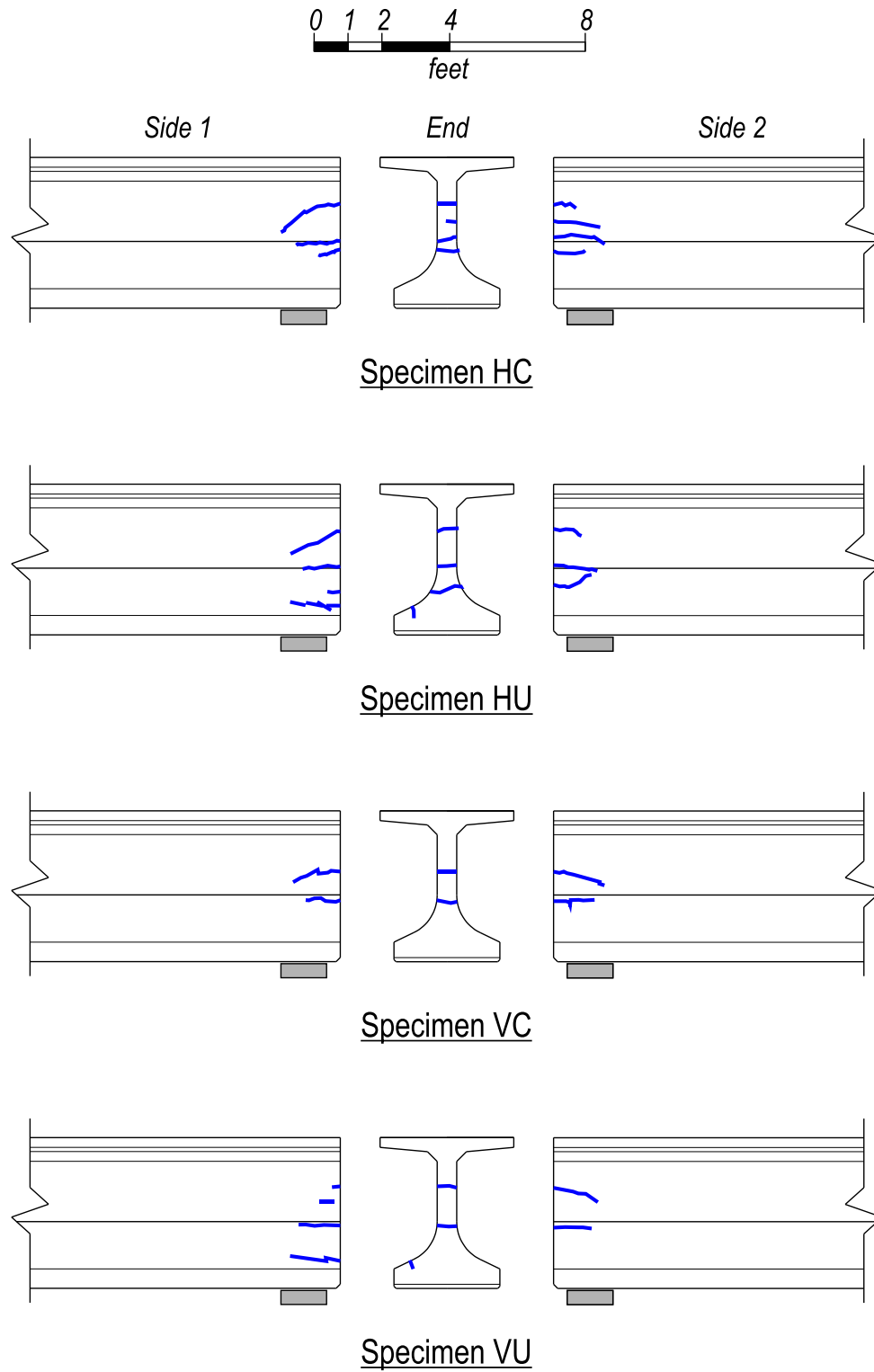


Figure 6-20. Girder H and V cracks prior to load tests

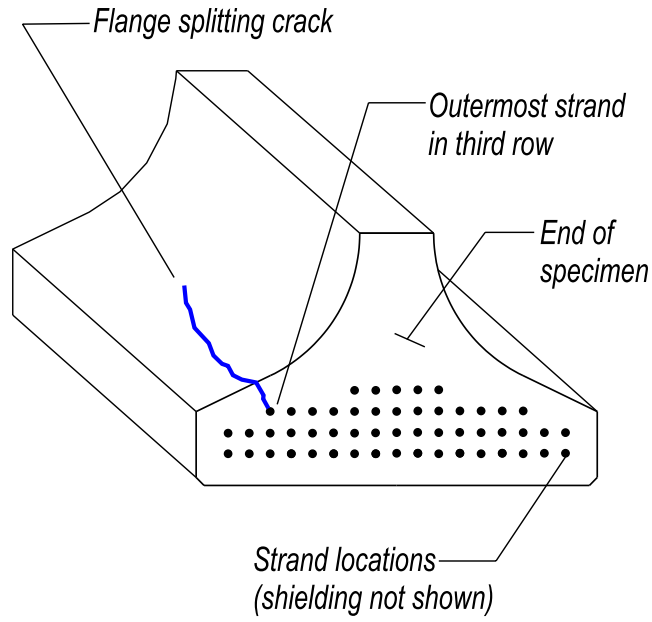


Figure 6-21. Flange splitting crack intersecting outer strand

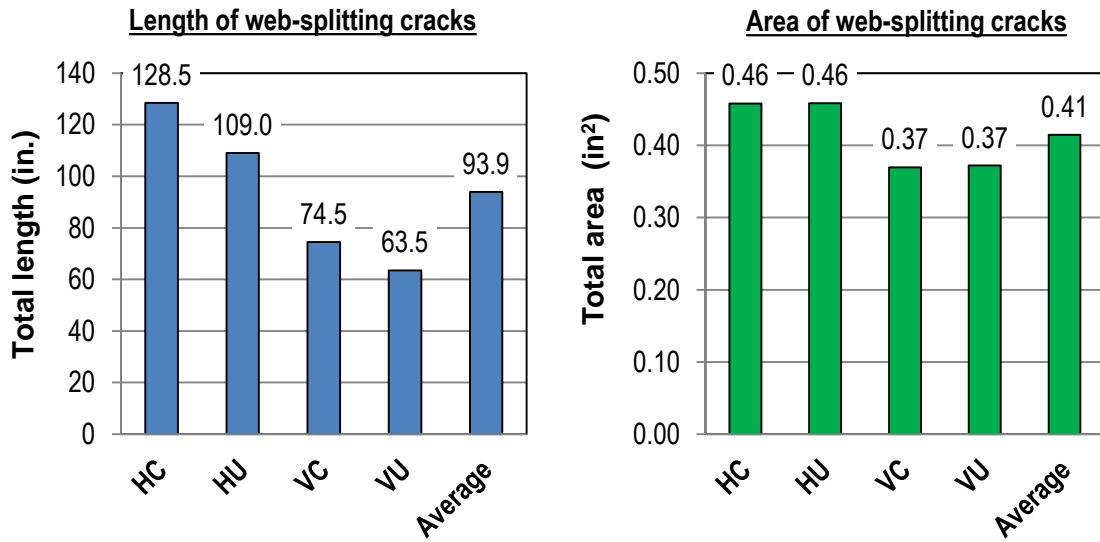


Figure 6-22. Web splitting cracks specimens H and V

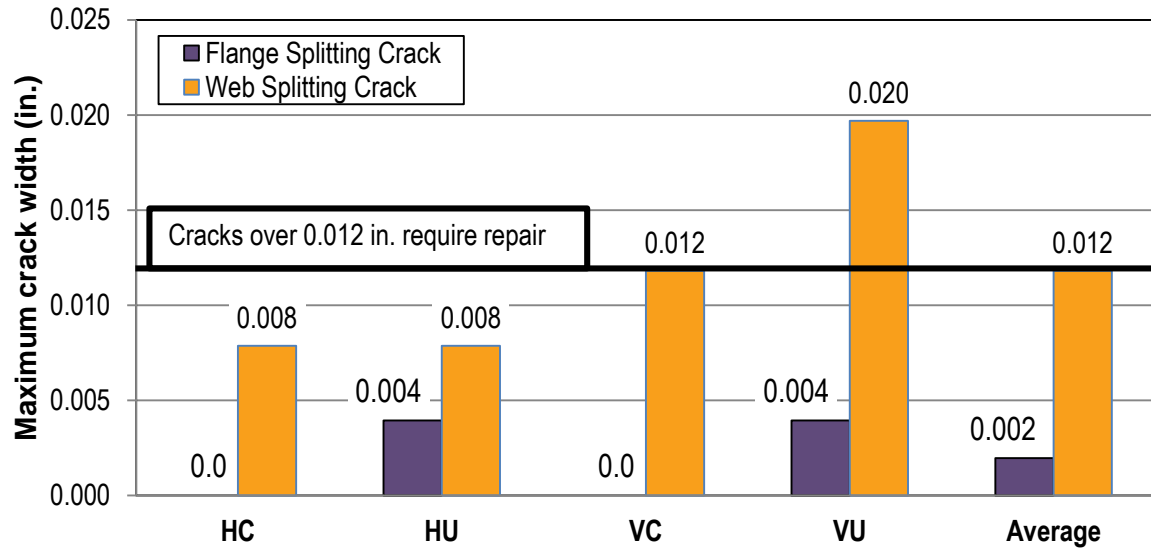


Figure 6-23. Maximum crack widths girders H and V

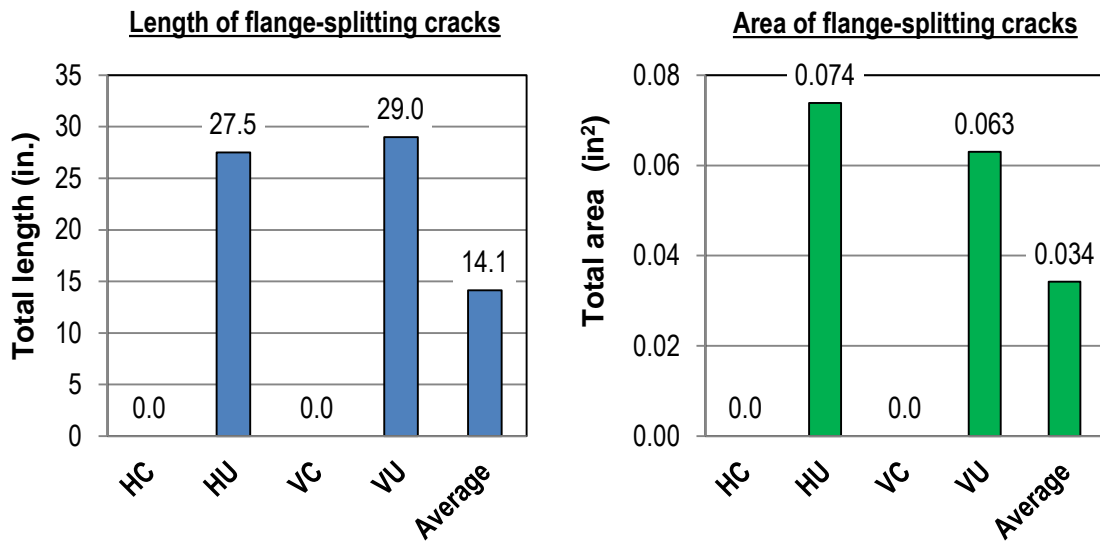


Figure 6-24. Flange splitting crack data girders H and V

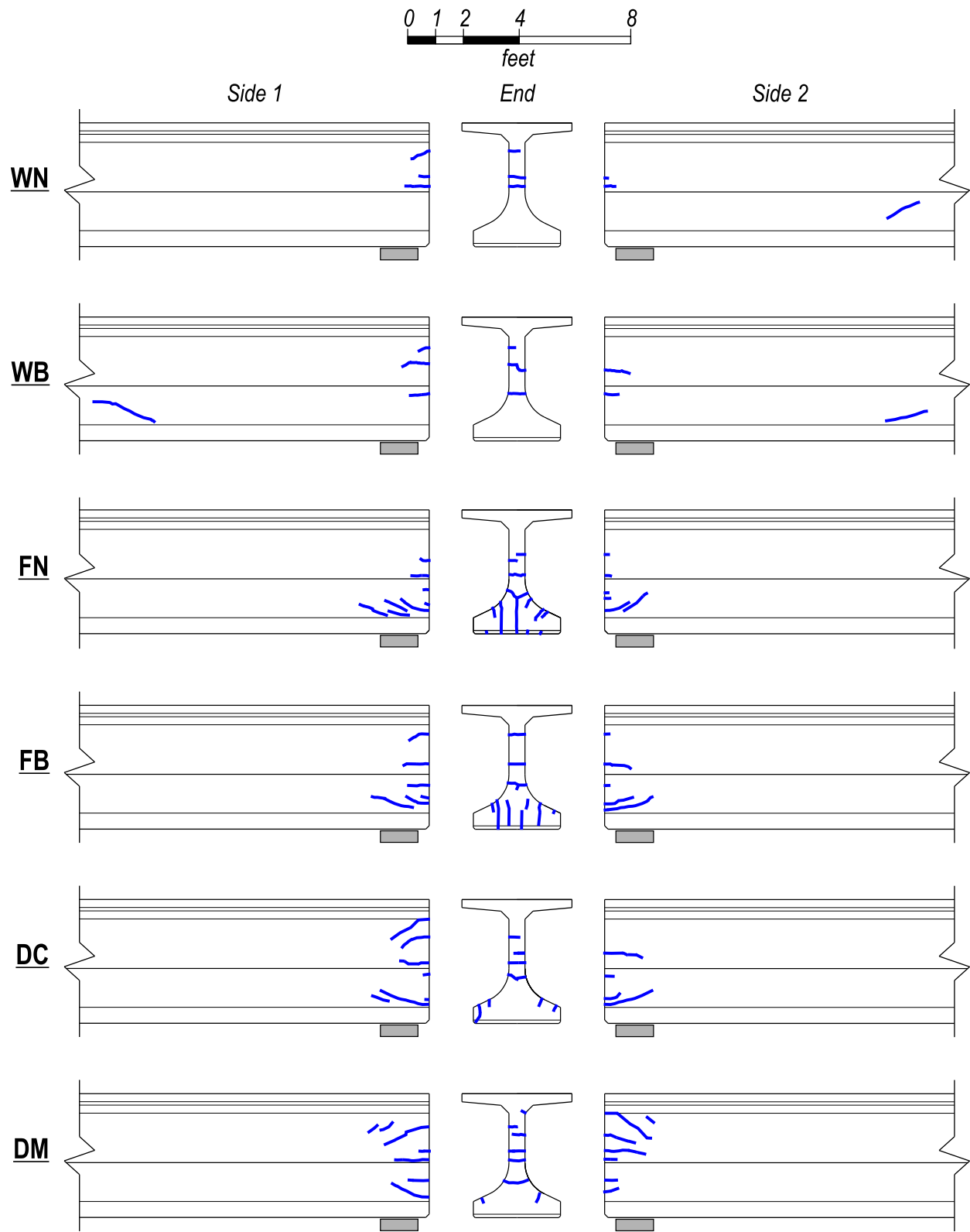


Figure 6-25. Girders W, F, & D web and flange splitting cracks



Figure 6-26. End of bottom flange covered by portion of steel bulkhead. (Photo courtesy of B.E. Ross)



A



B

Figure 6-27. Girder F flange splitting cracks. A) Specimen FN, B) Specimen FB. (Photos courtesy of B.E. Ross)

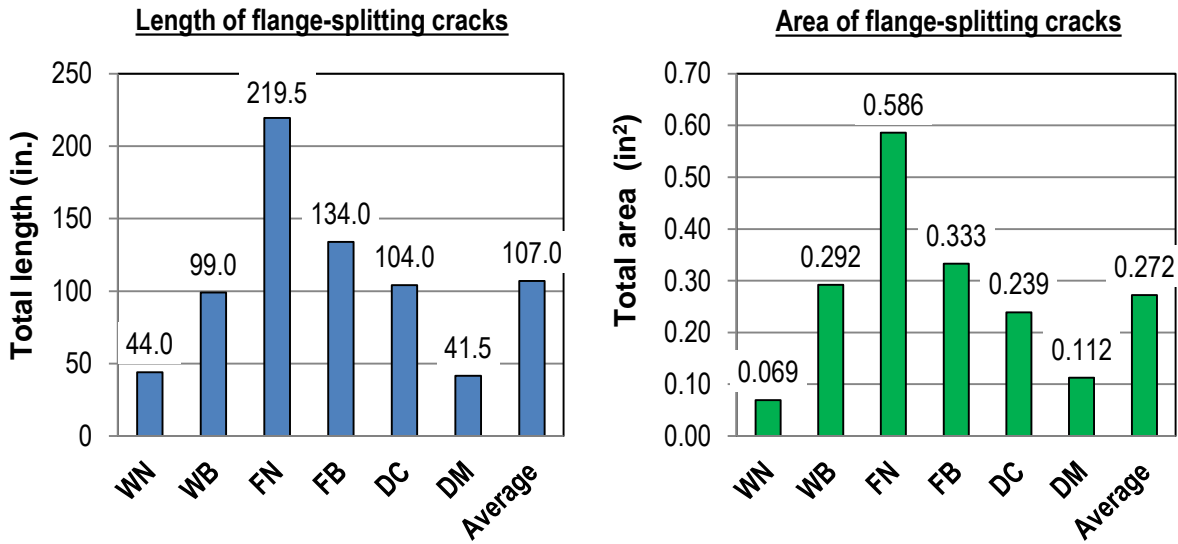


Figure 6-28. Flange splitting cracks girders W, F, and D

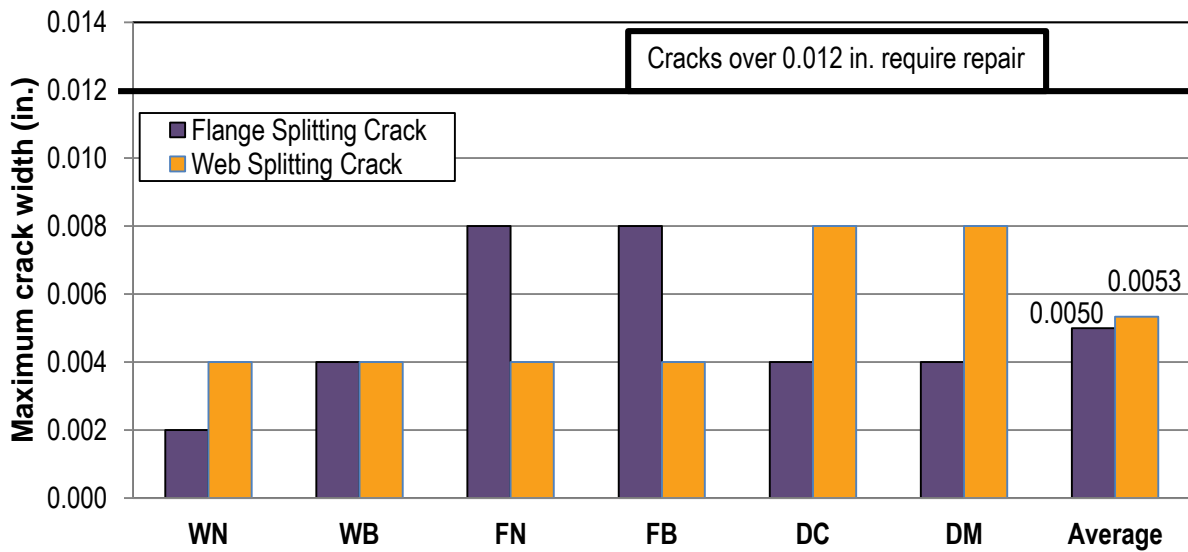


Figure 6-29. Maximum crack widths girders W, F, and D

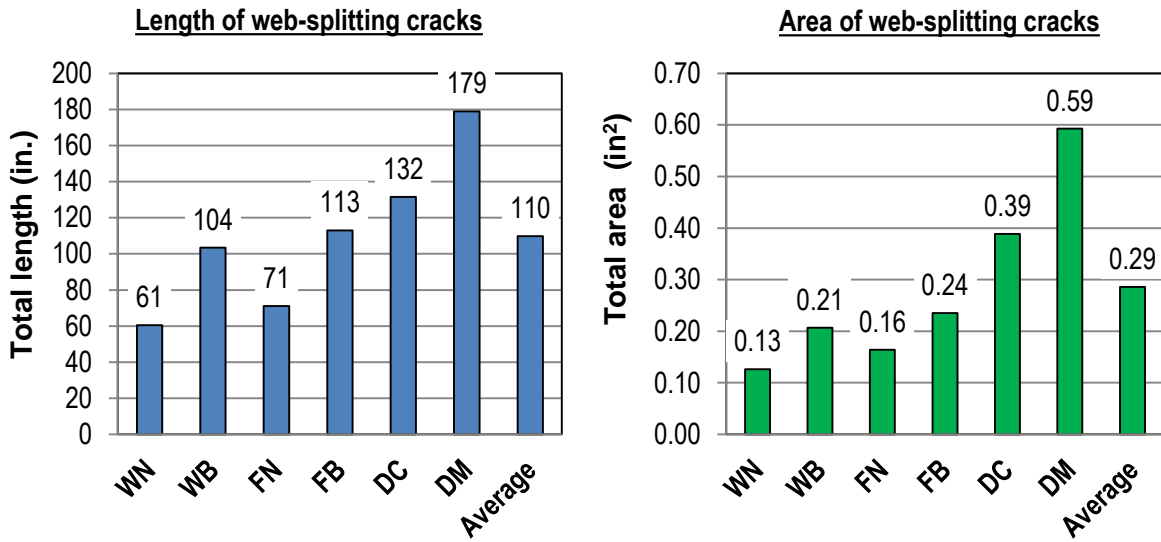


Figure 6-30. Web splitting cracks girders W, F, and D

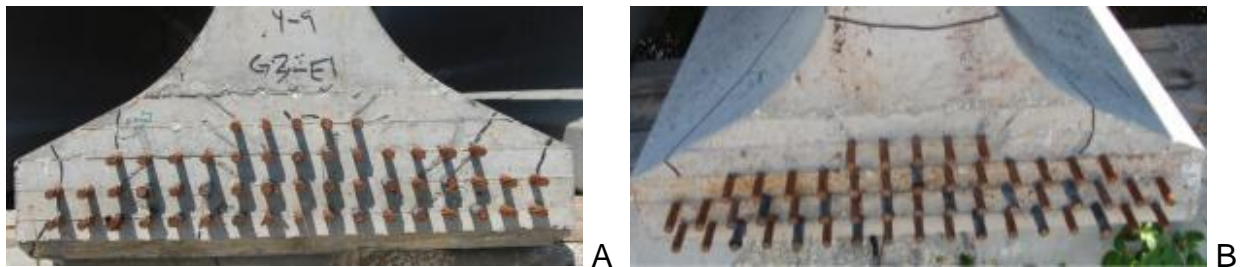


Figure 6-31. Girder D flange splitting cracks. A) Specimen DC, B) Specimen DM. (Photos courtesy of B.E. Ross)

Table 6-1. Girders H and V fabrication events and stages

Stage	Event
A	strands 1-4 cut
B	strands 5-12 cut
C	strands 13-32 cut
D	strands 33-49 cut
E	All bonded strands cut, girder resting on bed
F	Girder held aloft by lifting loops
G	Girder resting on dunnage

Table 6-2. Tensile strain girders H and V

Gage	Strain in specimens with confinement reinforcement (microstrain)		Strain in specimens without confinement reinforcement (microstrain)	
	HC	VC	HU	VU
X3 maximum tensile strain	406	177	724	1258
X3 Stage E (all strands released)	25	15	60	45
ES2 Stage E	109	113	100	135
ES3 Stage E	125	88	111	105

Table 6-3. Girders W and F fabrication stages

Stage	Event
J	strands 1-4 cut
K	strands 5-30 cut
L	Pause
M	strands 30-56 cut
N	all strands cut

Table 6-4. Confinement reinforcement strain after prestress transfer

Specimen	Confinement reinforcement layer	Confinement strain (microstrain)		
		y = 2in.	y = 9in.	y = 15in.
WN	Top	7	19	not recorded
	Middle	47	28	not recorded
	Bottom	160	87	not recorded
WB	Top	37	34	53
	Middle	-49	117	155
	Bottom	-106	124	150
FN	Top	70	18	not recorded
	Middle	358	38	not recorded
	Bottom	560	155	not recorded
FB	Top	81	51	5
	Middle	134	30	20
	Bottom	184	50	12

Table 6-5. Confinement and plate forces

Specimen	Confinement reinforcement transverse force	Bearing plate transverse force	Combined force in reinforcement and plate	Jacking force in fully bonded strands	Transverse force / jacking force
WN	6.2 kip	--	6.2 kip	1070 kip	0.6%
WB	4.3 kip	5.6 kip	9.9 kip	1070 kip	0.9%
FN	11.1 kip	--	11.1 kip	1070 kip	1.0%
FB	4.9 kip	13.7 kip	18.6 kip	1070 kip	1.7%

Table 6-6. Recommended action for web splitting cracks (Tadros et al. 2010)

Crack Width (in.)	Required Action
Less than 0.012	None
0.012 to 0.025	Fill cracks with cementitious material and apply surface sealant to end 4 ft of girder
0.025 to 0.05	Fill cracks with epoxy and apply surface sealant to end 4 ft of girder
Greater than 0.05	Reject girder unless shown by detailed analysis that structural capacity and long-term durability are sufficient

Table 6-7. Girders H and V construction events and inspection dates

Event	Date	Days after prestress transfer	Notes
Form Removal	September 7, 2010	--	No cracks observed
Prestress Transfer	September 8, 2010	0	No cracks observed
Lifting and setting on dunnage	September 8, 2010	0	No cracks observed
Girders in storage	September 17, 2010	9	Splitting cracks observed (all specimens)
Girders in storage	September 23, 2010	15	Additional web splitting crack observed (HC)
Girders in storage	October 10, 2010	49	No additional cracks
Girders in storage	January 7, 2011	121	No additional cracks
Trucking	February 23, 2011	167	No additional cracks
Casting deck	April 6, 2011	204	No additional cracks
Begin load tests	May 5, 2011	237	No additional cracks

Table 6-8. Girders W, F, & D construction events and inspection dates

Event	Date	Days after prestress transfer	Notes
Form Removal	February 20, 2012	--	No cracks observed
Prestress Transfer	February 21, 2012	0	First cracks observed after outer strands released.
In storage immediately after lifting	February 22, 2012	1	Additional splitting cracks and extension of previous cracks observed.
In storage	February 23, 2012	2	Additional splitting cracks and extension of previous cracks observed.
In storage	February 24, 2012	3	Additional splitting cracks and extension of previous cracks observed.
In storage	March 6, 2012	14	Additional splitting cracks and extension of previous cracks observed.
In storage	March 22, 2012	30	Additional splitting cracks and extension of previous cracks observed.
In storage	April 9, 2012	48	Bottom flange at ends examined for first time. Previously the bulkhead plates were covering the flange end. Additional splitting cracks and extension of previous cracks observed.
Trucking	April 30, 2012	69	Additional splitting cracks and extension of previous cracks observed.
Casting deck	May 7, 2012	76	No additional cracking observed.
Begin load testing	May 23, 2012	92	Bottom of girder inspected for first time. Flange splitting cracks observed prior to load tests.

CHAPTER 7 RESULTS AND DISCUSSION: LOAD TESTS

This chapter presents the results of load testing conducted on ten FIB-54 specimens. Test results are presented in terms of superimposed shear, which is referred to as shear in this chapter. Superimposed shear is defined as the shear force due to the applied load acting at the support nearest the load point. Self-weight is not included in the superimposed shear.

Displacement results are presented as the vertical displacement occurring at the load point. Displacement at the load point was calculated as the average of the displacements reported by LVDTs that were placed on either side of the load. The effect of bearing pad displacement has been removed.

Strand slip data are presented as the average slip from all monitored fully bonded strands. Displacement data from partially shielded strands are not included. Locations of monitored strands are presented in Chapter 5.

Failure Modes

Three different modes of failure were observed in the test program: Web-shear, lateral-splitting and bond-shear. This section defines each type of failure and discusses the characteristics associated with each failure mode.

Web-shear failure is distinguished by crushing of the concrete web at peak load. This type of failure is controlled by the capacity of the web to carry diagonal compression between the top and bottom flanges. A post-peak characteristic of web-shear failure includes sliding of the top portion of the girder relative to the bottom along a shear plane through the web (Figure 7-1). This type of failure mode is considered in the shear design provisions of AASHTO LRFD and ACI 318.

Lateral-splitting failure is characterized by longitudinal cracks in the bottom flange and by peeling (outward) movement at the edges of the bottom flange (Figure 7-3.) Peeling movement of the bottom flange is caused by eccentricity between prestressing forces in the outer flange and the resultant equal and opposite force centered in the web (Figure 7-4.) This condition creates a moment which opens bottom flange cracks, and peels the edges of the bottom flange outward. In specimens with sufficient bottom flange confinement, peeling movement and longitudinal cracks are restrained, and peeling failure is mitigated.

Strand slip is observed in some specimens failing in lateral-splitting mode. Flange splitting cracks are a precursor to strand-slip in lateral-splitting failures. Once strands start to slip cracks open wider and capacity is lost in a sudden manner.

Longitudinal cracking along the specimen bottom (Figure 7-3) is also a characteristic of lateral-splitting failure. Cracks on the bottom are another manifestation of lateral-splitting cracks on the top surface of the bottom flange.

Bond-shear failure is characterized by strand-slip at peak load. This type of failure is governed by concrete-strand bond capacity and by specimen propensity for cracking within the strand development length. Cracking in the development length is always a precursor to strand slip (Figure 7-2). Cracks interrupting strand development reduce the embedment length to the distance between the crack and the girder end. After strands start slipping the cracks opened wider and new cracks form. An abrupt slip event occurs at peak load followed by a subsequent loss of capacity. Longitudinal splitting cracks can also be observed on the bottom of specimens that failure in bond-shear (Figure 7-2).

As described above, similar characteristics are associated with lateral-splitting and bond-shear failures. One subtle difference between these failure modes is the cause of cracking in the bottom flange. In lateral-splitting failures bottom flange cracking is caused by shear forces and transverse tensile forces due to eccentric prestressing. Bottom flange cracking in bond-shear failures are caused primarily by shear forces. Magnitude of strand slip is a more obvious distinction between bond-shear and lateral-splitting failures. In the test program, specimens failing in bond-shear reported maximum average strand slip over 0.25in. When slip was observed in specimens failing in later-splitting maximum the average slip was less than 0.1in.

Load Test Results

HC

Detailing of specimen HC (Figure 3-6) was effectively identical to the 2008 FDOT Interim Design Standards (FDOT, 2008). Variables in specimen HC included FDOT specified confinement reinforcement and bearing plate in the bottom flange, horizontal reinforcement in the end region, and the 'design' strand bond pattern (Figure 3-5) which had (39) fully bonded strands. Specimen HC failed in web-shear mode. Shear-displacement and crack pattern are shown in Figure 7-5.

Cracks in HC were first observed during the service load test at a shear of 225 kip. Inclined web cracks between the load point and support were the first to be observed. The service load test reached a peak shear of 244kip. Cracks partially closed during the unloading stage of the service load test. Web cracks in specimen HC had a maximum width of 0.004 in. at a shear of 244kip, and 0.002 in. after load was removed.

Following service load testing specimen HC was loaded to ultimate capacity. Stiffness decreased gradually as load increased beyond the level of the service load

tests. Because flexural cracks were not observed, loss in stiffness is attributed to formation and growth of diagonal cracks. Ultimate capacity was signaled by web crushing followed immediately by sliding movement of the specimen's top portion relative to the bottom. Sliding movement occurred along the inclined cracks in the web. This type of failure is classified as a web-shear failure. Loss of capacity after the web-shear failure was abrupt. Specimen HC supported a maximum shear of 766 kip, the most of any specimen in the test program.

Strand slip data are not presented in Figure 7-5. LVDT data indicate that strand slip was negligible at lower loads. At higher loads cracks caused shifting of the frame holding the LVDTs thereby compromising the strand slip data. Specimens DC and DM used the same strand bond pattern as HC, but used different strand slip instrumentation that did not shift during testing. Slip data from the DC and DM suggest that strand slip was not a factor in the failure mode of specimens (such as HC) with the design strand pattern. The lack of slip observed in the specimens with this pattern is attributed to the relatively large quantity of fully bonded strands.

HU

Detailing of specimen HC (Figure 3-6) was effectively identical to the 2008 FDOT Interim Design Standards (FDOT, 2008), with the exception that no confinement reinforcement was placed in the bottom flange. Specimen HU had a bearing plate in the bottom flange, horizontal reinforcement in the end region, and the 'design' strand pattern (Figure 3-5) which included (39) fully bonded strands. Shear-displacement and crack pattern are shown in Figure 7-6.

Cracks in HU were first observed during the service load test at a shear of 215 kip. The first crack to be observed was a web crack inclined between the load point and

support. Web cracks in specimen HU had a maximum width of 0.004 in. at a shear of 230kip, and partially closed to 0.002 in. after load was removed.

Following service load testing specimen HU was loaded to ultimate capacity. Stiffness decreased gradually as load increased beyond the level of the service load tests. Loss in stiffness is attributed to formation and growth of diagonal cracks. Web cracks that formed at lower loads were observed to spread into the bottom flange during the latter stages of testing. Flexural cracks were not observed.

Peak load in specimen HU corresponded to lateral-splitting failure in the bottom flange, which resulted in an abrupt loss of load. Specimen HU supported a maximum shear of 666 kip.

Strand slip data are not shown in Figure 7-6. LVDT data indicate that strand slip was negligible at lower loads. At higher loads cracks caused shifting of the frame holding the LVDTs thereby compromising the strand slip data. Data from specimens with similar strand bond patterns and better instrumentation suggest that strand slip was not a contributing factor to in the failure of in specimens with the 'design' strand bond pattern.

VC

Detailing of specimen VC (Figure 3-7) was similar to the 2008 FDOT Interim Design Standards (FDOT, 2008), with the exceptions that fewer vertical bars and no horizontal bars were placed in the end region. Other variables in specimen VC included FDOT specified confinement reinforcement and bearing plate in the bottom flange, and the 'design' strand bond pattern (Figure 3-5) which included (39) fully bonded strands. Specimen VC failed in a web-shear failure mode. Shear-displacement and crack pattern are shown in Figure 7-7.

Cracking in VC was first observed during service load testing at a shear of 240 kip. An inclined web crack between the load point and support was the first to be observed. Cracks in specimen VC partially closed during the unloading stage of the service load test. Web cracks in VC had a maximum width of 0.014 in. at a shear of 290kip, and 0.002 in. after load was removed.

Following the service load testing specimen VC was loaded to ultimate capacity. Stiffness decreased gradually as load increased beyond the level of the service load tests. Because flexural cracks were not observed, the loss in stiffness is attributed to formation and growth of diagonal cracks. Ultimate capacity was signaled by web crushing followed immediately by movement of the portion of the specimen above the inclined cracks relative to that below the inclined crack. This type of failure is classified as a web-shear failure. Loss of capacity after the web-shear failure was abrupt. Specimen VC supported a maximum shear of 698 kip.

Strand slip data are not shown in Figure 7-7. LVDT data indicate that strand slip was negligible at lower loads. At higher loads cracks caused shifting of the frame holding the LVDTs thereby compromising the strand slip data. Data from specimens with similar strand bond patterns and better instrumentation suggest that strand slip was not a contributing factor to in the failure of in specimens with the 'design' strand bond pattern.

VU

Specimen VU (Figure 3-7) had the least amount of reinforcement of any specimen in the test program. Variables in specimen VU included no confinement reinforcement, no horizontal reinforcement and reduced vertical reinforcement in the end region. Specimen VU had a bearing plate in the bottom flange and had the 'design' strand bond

pattern (Figure 3-5) which included (39) fully bonded strands. Shear-displacement and crack pattern are shown in Figure 7-8.

Cracks in VU were first observed during the service load test at a shear of 243 kip. The first crack to be observed was a web crack inclined between the load point and support. Web cracks in specimen VU had a maximum width of 0.001 in. at a shear of 243kip, and did not change in width as load was removed after the service load test.

Following service load testing specimen VU was loaded to ultimate capacity. Stiffness decreased gradually as load increased beyond the level of the service load tests. Loss in stiffness is attributed to formation and growth of diagonal cracks. Web cracks that formed at lower loads were observed to spread into the bottom flange during the latter stages of testing. Flexural cracks were not observed.

Peak load in specimen HU corresponded to lateral-splitting failure in the bottom flange, which resulted in an abrupt loss of load. Specimen VU supported a maximum shear of 635 kip.

Strand slip data are not shown in Figure 7-8. LVDT data indicate that strand slip was negligible at lower loads. At higher loads cracks caused shifting of the frame holding the LVDTs thereby compromising the strand slip data. Data from specimens with similar strand bond patterns and better instrumentation suggest that strand slip was not a contributing factor to in the failure of in specimens with the 'design' strand bond pattern.

WN

The primary features of specimen WN (Figure 3-17) were the lack of an embedded bearing plate and the 'web' strand bond pattern (Figure 3-5) that placed (20) fully bonded strands below the web. Four additional strands were fully bonded at the edges

of the flange, resulting in a total of (24) fully bonded strands. Other variables in WN included no horizontal bars in the end region and modified confinement reinforcement. The modified confinement scheme had fewer, but larger, bars than specified by the FDOT. Shear-displacement, shear-slip and crack pattern results for specimen WN are shown in Figure 7-9.

Cracking in WN was first observed during service load testing at a shear of 198 kip. An inclined web crack between the load point and support was the first to be observed. Cracks widths in specimen WN partially closed during the unloading stage of the service load test.

Following service load testing specimen WN was loaded to ultimate capacity. Stiffness decreased gradually as load increased beyond the level of the service load tests. Loss of stiffness is attributed primarily to flexural cracks which were first observed at a shear of 435 kip. Strand-slip initiated at approximately the same load. Popping sounds indicative of strand slip were heard with increasing frequency as the load approached a peak shear of 507 kip. At peak shear, the strands slipped suddenly resulting in opening of the crack in front of the bearing pad and a subsequent loss of load. Capacity of WN was limited by strand-concrete bond, and failure of WN is labeled as a bond-shear failure.

WB

The primary feature of specimen WB (Figure 3-17) was the 'web' strand bond pattern (Figure 3-5) that placed (20) fully bonded strands below the web. Four additional strands were fully bonded at the edges of the flange, resulting in a total of (24) fully bonded strands. Other variables in WN included presence of an embedded bearing plate, and modified confinement reinforcement. The modified confinement

scheme had fewer, but larger, bars than specified by the FDOT. Shear-displacement, shear-slip and crack pattern results for specimen WB are shown in Figure 7-10.

Cracking in WB was first observed during service load testing at a shear of 175 kip. An inclined web crack between the load point and support was the first to be observed. Cracks widths in specimen WB partially closed during the unloading stage of the service load test.

Following service load testing specimen WB was loaded to ultimate capacity. Stiffness decreased gradually as load increased beyond the level of the service load tests. Loss of stiffness is attributed primarily to flexural cracks which were first observed at a shear of 380 kip. The first flexural crack occurred below the load and intersected cracks in the flange that had formed prior to load testing due to prestress transfer. Additional flexural cracks were observed at a shear of 494 kip.

Specimen WB had the greatest ductility and reached the largest displacement of any test specimen. The displacement at peak load was approximately 1.05in. Peak shear for WB was 612 kip. At peak shear the strands slipped abruptly and the crack in front of the bearing pad opened suddenly. Strand slip and cracking resulted in a sudden loss of load.

The bearing plate and confinement reinforcement in specimen WB maintained the structural integrity of the bottom flange above the bearing throughout load testing. Because the bottom flange held together above the bearing, the strand-concrete bond was also maintained at high load levels in WB. Capacity of the WB was governed by strand-concrete bond, and failure of WB is labeled as a bond-shear failure.

FN

The primary features of specimen FN (Figure 3-18) were lack of an embedded bearing plate and the 'flange' strand bond (Figure 3-5) pattern that placed (24) fully bonded strands in the outer portions of the bottom flange. Other variables in FN included no horizontal bars in the end region and modified confinement reinforcement. The modified confinement scheme had fewer, but larger, bars than specified by the FDOT. Shear-displacement, shear-slip and crack pattern results for specimen FN are shown in Figure 7-11.

Cracking in FN was first observed during service load testing at a shear of 174 kip. An inclined web crack between the load point and support was the first to be observed. Additional inclined cracks formed and intersected splitting cracks in the bottom flange that had formed prior to load testing due to prestress transfer. Shear in the service load test reached 237kip, but for safety reasons the load was immediately removed and cracks were marked after the specimen was unloaded. The concern with specimen FN was that the strand bond pattern and lack of a bearing plate could affect a sudden failure. Cracks widths in specimen FN partially closed during the unloading stage of the service load test.

Following service load testing specimen FN was loaded to ultimate capacity. Stiffness decreased as load increased beyond the level of the service load tests, but not to the degree observed with other specimens. Loss of stiffness is attributed to formation and growth of diagonal cracks. Web cracks that formed at lower loads were observed to spread into the bottom flange during the latter stages of testing. Flexural cracks were not observed.

Specimen FN reached a peak shear of 375 kip. This was the smallest peak of any specimen in the test program. At peak shear the strands slipped suddenly and the crack in front of the bearing opened. Slip and cracking was accompanied by a subsequent drop in load. Failure of specimen FN is labeled as a lateral-splitting failure because failure occurred in large part due to transverse splitting cracks in the bottom flange.

Failure of specimen FN can be understood by considering the strut-and-tie model shown in Figure 7-12. During latter stages of the ultimate load test, shear load was carried through the web into the bottom flange by concrete compression struts. Once in the bottom flange the load split into three separate load paths. The two outer paths connected to nodes at the fully bonded outer stands. The inner path was in the same plane as the web and connected to an inner node above the centerline of the bearing pad. At outer nodes equilibrium in the y-direction was maintained by tie forces in the strands. Y-direction equilibrium at the inner node was maintained by tension force in the concrete. At peak load strands at the outer nodes slipped and the crack in front of the bearing pad propagated into the center of the bottom flange thereby cutting the concrete tie (Figure 7-13).

The strut-and-tie concept shown in Figure 7-12 is supported by strain data from the confinement reinforcement which formed the transverse tie between the outside nodes. Strain in the confinement reinforcement increased after peak load. Once the concrete tension tie failed at peak load, force from the inner load path transferred to the outer load paths. Accordingly, additional force was generated in the confinement reinforcement to maintain x-direction equilibrium at the outer nodes. This additional

force is responsible for the post-peak increase in strain observed in the confinement reinforcement (Figure 7-14).

FB

The primary features of specimen FB (Figure 3-18) were an embedded bearing plate and the 'flange' strand bond pattern (Figure 3-5) that placed (24) fully bonded strands in the outer portions of the bottom flange. Other variables in FB included no horizontal bars in the end region and modified confinement reinforcement. The modified confinement scheme had fewer, but larger, bars than specified by the FDOT. Shear-displacement, shear-slip and crack pattern results for specimen FB are shown in Figure 7-15.

Cracking in FB was first observed during service load testing at a shear of 158kip. An inclined web crack between the load point and support was the first to be observed. Cracks widths in specimen FB partially closed during the unloading stage of the service load test.

Following service load testing specimen FB was loaded to ultimate capacity. Specimen FB reached a peak shear of 409 kip. Failure of FB is categorized as a later-splitting failure. Circumstances and failure behavior of specimen FB were the same as those reported for specimen FN. As such, a detailed description of the failure mode is not repeated here.

DC

Specimen DC (Figure 3-19) was detailed according to the 2010 FDOT Interim Design Standards (FDOT, 2010). Variables in specimen DC included FDOT specified confinement reinforcement and bearing plate in the bottom flange, no horizontal reinforcement in the end region, and the 'design' strand pattern (Figure 3-5) which had

(39) fully bonded strands. Shear-displacement, shear-slip, and crack pattern are shown in Figure 7-16.

Cracks in DC were first observed during the service load tests at a shear of 174 kip. Inclined web cracks between the load point and support were the first to be observed. Cracks partially closed during the unloading stage of the service load test.

Following service load testing specimen DC was loaded to ultimate capacity. Stiffness decreased gradually as load increased beyond the level of the service load tests. Because flexural cracks were not observed, the loss in stiffness is attributed to formation and growth of diagonal cracks.

Ultimate capacity was signaled by web crushing followed immediately by movement of the portion of the specimen above the inclined cracks relative to that below the inclined crack. This failure is classified as a web-shear failure. Loss of capacity after the web-shear failure was abrupt. Specimen HC supported a maximum shear of 753 kip.

Figure 7-16 shows that strand slip in specimen DC was negligible prior to the peak load. Strand slip reported in the figure after peak load was likely exaggerated by cracking of the bottom flange at the end of the load test. Lack of slip observed in DC and other specimens with the 'design' strand bond pattern is attributed to the relatively large quantity of strands.

DM

Detailing of specimen HC (Figure 3-19) was effectively identical to the 2010 FDOT Interim Design Standards (FDOT 2010), with the exception that the modified confinement reinforcement scheme was used in the bottom flange. Modified confinement had fewer, but larger, bars than specified by the FDOT. Other variables in

specimen DM included a bearing plate in the bottom flange, no horizontal reinforcement in the end region, and the 'design' strand pattern (Figure 3-5) which had (39) fully bonded strands. Shear-displacement, shear-slip and crack pattern results for specimen DM are shown in Figure 7-17.

Cracks in DM were first observed during the service load tests at a shear of 166 kip. Inclined web cracks between the load point and support were the first to be observed. Cracks partially closed during the unloading stage of the service load test.

Following service load testing specimen DM was loaded to ultimate capacity. Stiffness decreased gradually as load increased beyond the level of the service load test. Because flexural cracks were not observed, the loss in stiffness is attributed to formation and growth of diagonal cracks.

Failure of specimen DM was a hybrid between lateral-splitting and web-shear. At peak load one of the inclined cracks had a suddenly increased in width. The load dropped approximately 5 kip after the crack opened. Opening of the crack and loss in load occurred in-part due to peeling movement of the bottom flange. Loading continued for approximately 15 sec until the web crushed and the load fell abruptly. After web crushing the top portion of the specimen slid along the cracking plane relative to the lower portion. Concrete spalled away from the web on both sides of the specimen during the web failure. Specimen DM supported a maximum shear of 703 kip. Longitudinal splitting cracks were observed on the bottom of DM after testing, indicative of lateral-splitting failure.

Figure 7-17 shows that strand slip in specimen DM was negligible prior to the peak load. Strand slip reported in the figure after peak load was likely exaggerated by

cracking of the bottom flange at the end of the load test. Lack of slip observed in DM is attributed to the relatively large quantity of strands.

Confinement Reinforcement and Bearing Plates

Strain gages were used to monitor bearing plates and select confinement reinforcement assemblies during load testing. Strain data were then used to calculate stresses and forces in the confinement reinforcement and bearing plates. Stresses and forces were calculated at a shear of 375 kip and at each specimen's maximum capacity. Analyses were conducted at a shear of 375 kip because this force corresponds to the maximum capacity of specimen FN. It is also near the factored shear force in the prototype bridge from which some the specimens were designed.

Girders W and F

Confinement reinforcement strain in specimens WN, WB, FN, and FB was monitored during prestress transfer and during load testing. Bearing plate strain was also monitored in WB and FB. Strain from prestress transfer and load testing were superimposed to determine total strain in the confinement reinforcement and bearing plates. It was assumed that strain did not change between prestress transfer and load testing. Although it is unlikely that strain was constant, it is necessary to make this assumption in order to estimate total strain.

Specimens WN, WB, FN, and FB each had the modified confinement reinforcement scheme (Figure 3-11) which placed five assemblies of confinement reinforcement above the bearing. Three of the five assemblies in each specimen were instrumented with gages (Figure 7-18). Gages were placed to measure the transverse (x-x) strain.

Combined strain from prestress transfer and load testing was multiplied by the steel modulus of elasticity to determine stress in the confinement reinforcement. Data indicate that confinement stresses were typically less than yield stress. One bar in specimen FN and one bar in WN had reached yield stress as ultimate load. Average stresses for each specimen at a shear force of 375 kip are shown in Figure 7-19. Figure 7-20 shows average stresses at ultimate capacity.

The largest stresses occurred in specimens WN and FN, which did not have bearing plates. At a shear of 375 kip, the average confinement stress in WN and FN was 3.5 times greater than the average stress in the specimens with bearing plates (WB and FB). At ultimate load the average stress in WN and FN was 2.5 times greater than WB and FB. These differences in stress are attributed to the presence of the steel bearing plate in WB and FB. The stiffness of the plate attracted transverse forces thereby reducing the forces (and stress) in the confinement reinforcement.

Average confinement stress varied according to the reinforcement layer. Average stresses in the middle and bottom layers were 6 to 8 times greater than stress in the top layer. It is believed that tension formed in the bottom flange as shear was delivered from the relatively narrow web to the wider bearing pad. This tension was likely the cause of the greater stress in the bottom and middle layers of confinement. Analytical modeling is presented in Chapter 8 to explore this effect.

Stress distribution in the confinement reinforcement also varied in the y-direction. For specimens with fully bonded strands placed below the web (WN and WB) the average stress in reinforcement at 8in. and 15in. was 1.6 to 2.1 times greater than the stress in reinforcement at 2in. The opposite trend was observed in specimens with fully

bonded strands placed in the outer flange (FN and FB). Average stress in reinforcement 2in. from the end of FN and FB was typically 2 times greater than average stress in reinforcement placed at 15in. Similar trends were noted in confinement behavior at prestress transfer as discussed in Chapter 6. The mechanics presented in Figure 6-8 and Figure 6-9 are believed to be culpable in the stress changes observed in stress in the y-direction. Discussion of these mechanics can be found in Chapter 6 and are not repeated here.

Strand bond pattern also affected the magnitude of the average stresses. At a shear of 375 kip, confinement reinforcement in specimens FN and FB had an average stress that was 2.5 times greater than the average stress in WN and WB. The additional stress in FN and FB is attributed to strand bond pattern which placed fully bonded strands in the outer portion of the flange. This pattern caused transverse tension as described in Figure 7-4.

Transverse forces in confinement reinforcement and bearing plates (WB and FB only) were estimated by multiplying transverse stresses by the respective cross-sectional areas. Linear interpolation was used to estimate forces in the confinement assemblies that were not monitored with gages. Results are presented in Table 7-1. Forces from reinforcement with compressive stress were not included in the results. Only the x-direction components of forces in the top layer were included.

Total transverse force between specimens WN and WB was consistent, suggesting that the presence of a bearing plate did not change the transverse force demand in these specimens.

Transverse forces in specimens FN and FB were not consistent. The bearing plate specimen (FB) had approximately 50% less transverse force. The difference in force between FB and FN is attributed to the bearing plate mechanics in specimen FB. Experimental data indicate that the bearing plate in FB carried an in-plane bending moment during loading. This behavior resulted in tensile and compressive forces in the bearing plate (Figure 7-21). The causes of the in-plane moment are the force and eccentricity of the outside strands (Figure 7-4). By carrying in-plane moment, the plate reduced the magnitude of transverse forces typically associated with the outer strands. In-plane bending of the plate in Specimen WB was not observed.

Girders H and V

Strain gages were placed on confinement reinforcement and bearing plates in specimens HC and VC to monitor strain during loading (Figure 7-22). Stresses and forces in these elements were estimated in the same manner as was done for specimens in girders W and F. Forces at ultimate load are shown in Figure 7-23, and are due to applied load only. Confinement strain data were not collected during prestress transverse in specimens VC and HC, and the effects of transfer are not included in Figure 7-23. In calculating the forces it was assumed the total strain in the confinement and plates was less than the yield strain. This assumption appears valid for HC and VC because yielding was only reached in two of the 36 bars that were monitored in girders W and F, and because the yielded bars occurred in specimens without bearing plates.

The estimated tensile force carried by all confinement reinforcement was 25.7 kip and 30.3 kip for specimens HC and VC, respectively. These forces equate to approximately 4% of the reaction at ultimate load. The largest confinement

reinforcement forces occurred near the end of the specimens. At locations farther away from the end, the confinement reinforcement carried compressive forces, thus confirming the theoretical behavior presented in Figure 7-4.

The transition from tensile to compressive action in the confinement reinforcement is estimated to have occurred at distances approximately 40in. and 50in. from the specimen ends (Figure 7-23). The flexural depth (d) of the non-composite member was 49in. Comparing the distribution of confinement forces with the flexural depth shows that all tension in the confinement reinforcement occurred within d of the member end. Current AASHTO LRFD requirements specify that confinement reinforcement must extend at least $1.5d$ from the member end. The experimental results suggest that this requirement is conservative, and that more effective placement of confinement reinforcement is possible. Other researchers (Tadros et al. 2010) have also suggested that the required distribution of confinement reinforcement should be reduced to less than $1.5d$.

Bearing Plates

Eight of the ten experimental specimens had embedded steel bearing plates. Strain in each bearing plate was monitored during load testing. Average stresses in the bearing plates were calculated by multiplying the average experimental strain by the elastic modulus. Bearing plate stresses due applied load (effects of prestress transfer not included) are presented in Figure 7-24. At ultimate load the average stresses ranged from 2.4 ksi (FB) to 10.6 ksi (VU). The relatively low average stress in specimen FB was due to in-plane bending of the plate as discussed previously.

Bearing plate forces were calculated by multiplying the average stresses by the cross-section areas (Figure 7-25). Net tension force in the bearing plates at ultimate

load ranged from 96.2 (VU) to 16.5 kip (FB). The average tension force at ultimate load was 62.9 kip.

Tension forces in the bearing plates are compared to the total transverse force in Figure 7-26. For this figure the total transverse force is defined as the combined transverse force in the bearing plate plus confinement reinforcement. Forces in Figure 7-26 are due to applied loads only. On average the bearing plates carried 60% to 71% of the total transverse force due to the applied load.

The portion of transverse force carried by the bearing plates at prestress transfer was evaluated using data from specimens WB and FB. As shown in Figure 7-27, contribution of the bearing plate at prestress transfer was affected by the strand bond pattern. The bearing plate in specimen FB (bonded strands in outer flange) carried almost 77% of the total transverse force at prestress transfer, whereas the plate in specimen WB (inner strands bonded) carried 52% of the transverse force at transfer.

Experimental data presented in this section indicate that bearing plates in FIB girders will typically carry more than 50% of transverse splitting forces. Thus for purposes of designing confinement reinforcement it is conservative to assume that the bearing plate will carry no more than 50% of transverse force.

Variable Comparisons

Maximum superimposed shear for each specimen are reported in Figure 7-28 and Table 7-2. Values ranged from a high of 766 kip (HC) to a low of 375 kip (FN), with an average of 612 kip. The large degree of variation in these results is a testament to the effect that detailing can have on end region behavior and capacity, even for members having the same cross-section and materials properties. Effects of the variables are discussed below and are summarized in Table 7-3.

Horizontal Reinforcement

The 2008 FDOT interim standard for FIB-54 girders (FDOT 2008) called for horizontal bars to be placed in girder end regions. For reasons unrelated to the current test program, this detail was changed such that the 2010 FDOT interim design standard (FDOT 2010) eliminated horizontal bars. Effects of the horizontal reinforcement can be evaluated using results from specimens HC and DC. Specimens HC and DC were effectively identical with the exception of horizontal reinforcement placed in HC. Failure loads of these specimens were within 2% of each other, and both specimens failed in a web-shear mode. This result suggests that the relatively small amount of horizontal reinforcement placed in specimen HC had negligible effect on behavior or capacity.

Previous research by the author (Ross et al. 2011b) has shown that horizontal reinforcement improves ductility in girders having a critical failure mode of bond-shear. Specimens HC and DC failed in web-shear, thus indicating that horizontal reinforcement had negligible impact when web-shear was the critical failure mode.

Embedded Steel Bearing Plate

FDOT details call for embedded steel plates to be placed at the end of I-girders above the bearing location. Inclusion of the plates in the FDOT detail was based on recommendations by Cook and Reponen (2008), and was implemented to prevent cracks at the bottom corner of girders during fabrication. Embedded steel bearing plates were included as a variable in the current test program to evaluate the effects of bearing plates on bottom flange confinement.

Specimens WB and WN had identical detailing with the exception of the bearing plate which was excluded from specimen WN. Specimen WB had a bearing plate and a capacity of 612 kip. This was 21% greater than the 507 kip capacity of WN. Both

specimens failed in bond-shear mode. The additional capacity in specimen WB is attributed to the confining effect of the bearing plate that helped maintain structural integrity of the bottom flange above the bearing. Because the bottom flange held together, strand-concrete bond in WB was maintained at loads beyond which specimen WN (no bearing plate) lost strand-concrete bond.

Specimens FB and FN also had identical detailing with exception of the bearing plate which was excluded from FN. Specimen FB had a bearing plate and a capacity of 409 kip. This was 9% larger than the 375 kip capacity of specimen FN. Both specimens failed in laterally-splitting mode. The additional capacity of specimen FB is attributed to the bearing plate, however the effect of the bearing plate was not as pronounced as the effect between specimens WN and WB.

Confinement Reinforcement

Three different confinement reinforcement schemes (Figure 3-11) were used in the test specimens. The current FDOT confinement scheme was used in specimens HC, VC, and DC. A modified confinement scheme was used in specimens WN, WB, FN, FB, and DM. The modified confinement scheme had fewer but larger bars than the FDOT scheme. Specimens HU and VU had the final scheme, in which confinement reinforcement was totally omitted.

FDOT vs. No Confinement. Specimens HC, VC, HU, and VU contained comparable variables and can be used to evaluate FDOT confinement relative to specimens with no confinement. HC and VC had FDOT confinement reinforcement and failed in a web-shear mode. The capacity of HC and VC was on average 13% larger than the capacity of HU and VU which had no confinement reinforcement. HU and VU failed in a later-splitting mode. Thus omission of confinement reinforcement

allowed lateral-splitting failure of the bottom flange and decreased capacity by 13%. Or, conversely, the presence of confinement reinforcement forced failure away from the bottom flange, thereby increasing capacity by an average of 13%.

FDOT vs. Modified Confinement. Detailing of specimens DC and DM (Figure 3-9) was identical with the exception of confinement reinforcement. DC had FDOT confinement reinforcement and a capacity of 753 kip, whereas DM had modified confinement reinforcement and a capacity of 703 kip. Failure mode was different between these specimens. In specimen DC the FDOT confinement reinforcement was sufficient to prevent lateral-splitting failure, thereby forcing a web-shear failure. Confinement reinforcement in DM was insufficient to prevent lateral-splitting of the bottom flange. Thus the current FDOT detail for confinement provides more effective confinement at ultimate load than the modified scheme. One reason that the FDOT scheme was superior is because it placed confinement bars in front of the bearing where they can act as stirrups. Confinement reinforcement as stirrups was postulated by Csagoly (1991) (Figure 2-9). Confinement bars were not provided away from the bearing in the modified scheme. This allowed propagation of cracks in front of the bearing of specimen DM (Figure 7-29).

Strand Quantity

Strand quantity had a greater effect on specimen capacity than any other variable in the test program. Average capacity of specimens with (39) fully bonded strands was 48% greater than the average capacity of specimens with only (24) fully bonded strands. The relationship between strand quantity and experimental capacity is described in Figure 7-30. The figure shows a linear trend line that was fit to the

experimental data. The trend line has an R^2 value of 0.69, indicating a reasonable degree of correlation between experimental capacity and strand quantity.

Current AASHTO LRFD requirements limit the quantity of partially shielded strands to 25% of the total strand count. Providing limits on strand shielding is considered good practice in light of the experimental results. Based on experimental data, every strand that was shielded resulted in a roughly proportional decrease in capacity. The data also suggest, however, that the means by which AASHTO LRFD limits strand shielding can be improved. Rather than limiting shielding to an arbitrary percentage, it is more rational to limit shielding according to the total number of bonded strands required to provide the necessary end region capacity. If sufficient strands are available to support the required capacity, then shielding of the remaining strands can reasonably be permitted. As will be discussed later, the minimum longitudinal reinforcement requirements of AASHTO section 5.8.3.5 can be employed to determine the necessary strand quantity for a given load demand.

Strand Placement

Strand placement can be evaluated using results from WN, WB, FN, and FB. Fully bonded strands in WN and WB were placed primarily in the center of the bottom flange below the web. In FN and FB, fully bonded strands were placed in the outer portions of the flange (Figure 3-5). Specimens WN and WB (strands below the web) failed in a bond-shear failure mode and at an average load that was 43% greater than specimens FB and FN (fully bonded strands in the outer flange). Specimens FB and FN failed in lateral-splitting mode. Crack patterns associated with the different strand patterns and failure modes are shown in Figure 7-31.

To maximize end region capacity and prevent lateral-splitting failures it is desirable to place strands as close to the cross-section centerline as practical. Doing so minimizes the horizontal eccentricity between prestressing forces and the equal but opposite internal force. This in-turn reduces the propensity for lateral-splitting in the bottom flange.

Code Comparisons

Experimental moments and shears in this section include both the applied load *and* self-weight of the specimens. Experimental moment is denoted as M_{exp} and is defined as the maximum moment occurring during testing at the section below the point load. Experimental shear is denoted as V_{exp} and is defined as the maximum shear occurring during testing at the near support.

Nominal capacities were calculated using the material properties listed in Table 7-4. These values are representative of the tested properties of materials in the experimental girders. The following paragraphs explain the calculation procedures used to determine nominal capacities.

Nominal Moment Capacity. None of the experimental specimens failed in flexure; however nominal moment capacities were still calculated for reference purposes. Capacity was calculated using principals of strain compatibility and equilibrium. Typical assumptions for concrete in flexure were applied. Nominal moment capacity is denoted as M_n . Shear associated with nominal moment is denoted as V_{Mn} .

AASHTO LRFD Nominal Shear Capacity. Concrete contribution to shear capacity was calculated using the General Procedure from section 5.8.3.4.2 of AASHTO LRFD (2007). This procedure is based on the modified compression field theory

(MCFT). Steel contribution was calculated using AASHTO LRFD Equation 5.8.3.3-4. AASHTO LRFD nominal shear capacity is denoted as V_{nLRFD} .

ACI Nominal Shear Capacity. Concrete contribution was calculated using section 11.3.3 of ACI 318 (2011). Provisions in this section are commonly referred to as the ACI detailed method. Steel contribution was calculated using the provisions of section 11.4.7. ACI nominal shear capacity is denoted as V_{nACI} .

Nominal Tie Capacity (Minimum longitudinal reinforcement). Nominal tie capacity calculations are based on the minimum longitudinal steel requirement in AASHTO LRFD 5.8.3.5. Equation 5.8.3.5-2 requires that sufficient longitudinal reinforcement be provided to carry tie forces at the bearing. Bond-shear failure is likely when the tie is insufficient. Procedures from Ross et al. (2011b) were used to calculate the shear force that accompanies the nominal tie capacity. These procedures encompass the AASHTO LRFD requirements, but were derived for application to test specimens. Shear associated with nominal tie capacity is denoted as V_{nT} . In making the tie calculations, a required development length of 72in. was assumed for the prestressing strands. The available tie force in the strands was reduced proportionally to the assumed available development of 22in.

For each specimen the experimental moment was less than the calculated nominal moment capacity (Table 7-5). This result is in agreement with experimental specimens, in which no flexural failures were observed. Most specimens carried experimental moments that were between 60% and 75% of their nominal moment capacity.

Nominal and experimental shear capacities are compared in Table 7-6. The AASHTO LRFD and ACI nominal shear capacities are based on web-shear failure, which was only observed in four of ten specimens. Bond-shear failure, the assumed failure mode of the AASHTO tie capacity, was only observed in two of the ten specimens. Because of inconsistencies between code-assumed and experimentally observed failure modes, the comparisons shown in Table 7-6 are useful for relative comparisons only.

Although inconsistent with failure modes, calculated nominal capacities were typically conservative relative to the experimental results. ACI shear calculations were the most conservative, and resulted in nominal capacities 34% less on average than the experimental results. AASHTO shear and AASHTO tie nominal capacities were 12% and 6% less on average, respectively, than the experimental results.

Specimens FN and FB were the only specimens with calculated nominal capacities greater than the experimental shear forces. These specimens failed in lateral-splitting. This type of failure is not explicitly considered in ACI or AASHTO code provisions. Because ACI and AASHTO codes do not account for lateral-splitting failure, code-based capacities for specimens FN and FB were unconservative (i.e. greater than experimental capacity). This result demonstrates the need for code provisions that account for lateral-splitting failure.

The nominal tie method was the most accurate for calculating end region capacity of the experimental specimens. Capacities calculated by the nominal tie method were 6% smaller on average than the experimental capacities. It must be noted, however, that nominal capacity calculated by the tie method is highly dependent on the values

that are assumed for the required and available development lengths. The AASHTO LRFD code does not give specific requirements for selecting these values. Rather the code states, “Any lack of full development length shall be accounted for.” In spite of the ambiguity in code language, the agreement shown between experimental and nominal tie capacities demonstrate the utility of this method for designing I-girder end regions. In particular, this method is useful in selecting strand quantities that are unlikely to result in bond-shear failures.

Summary and Conclusions

Ten uniquely detailed FIB-54 specimens were load tested in three-point bending at a shear span-to-depth (a/d) ratio of 2.0. Variables in the test program included:

- Presence/absence of confinement reinforcement
- Quantity and configuration of confinement reinforcement
- Presence/absence of horizontal reinforcement
- Quantity of vertical reinforcement
- Presence/absence of embedded steel bearing plates
- Strand quantity
- Strand placement

The following conclusions are made:

- Differences in detailing have significant effect on the end region capacity, even for members having the same cross-section. All test specimens used the FIB-54 cross-section, yet experimental capacities ranged from a maximum of 766 kip to a minimum of 375 kip.
- Horizontal reinforcement in the end region has negligible effect on the capacity of members failing in web-shear. The test specimen with horizontal reinforcement had no significant increase in capacity relative a comparable specimen without horizontal reinforcement.
- Embedded steel bearing plates provide confinement to the bottom flange, thereby improving end region capacity. Test specimens with bearing plates had 9% to 21% greater capacity relative to comparable specimens without bearing plates.
- Confinement reinforcement can be used to mitigate lateral-splitting failure, thereby improving end region capacity. Test specimens with confinement reinforcement

per current FDOT specifications failed in web-shear mode and at an average load 13% higher than comparable specimens without confinement. Specimens without confinement failed in lateral-splitting.

- To mitigate lateral-splitting failure confinement reinforcement must have sufficient quantity and effective placement. Lateral-splitting failure was observed in specimens with confinement reinforcement placed only above the bearing. A comparable specimen with confinement placed throughout the strand transfer length failed in web-shear and at a 7% higher load.
- Bearing plates carry a significant portion of transverse splitting forces. Up to 79% of the transverse tension was carried by bearing plates in the test program.
- For purposes of designing confinement reinforcement it is conservative to assume that bearing plates carry 50% or less of the transverse splitting force.
- Girders with fully bonded strands in the outer flange have greater transverse splitting forces than due girders with fully bonded strands placed below the web. In the test program, transverse force in confinement reinforcement was up to 2.5 times larger in specimens with strands in the outer flange relative to those with strands below the web.
- Strand quantity had the greatest effect on end region capacity of any variable in the test program. Specimens with 39 fully bonded strands had an average capacity that was 43% greater than specimens with 24 fully bonded strands.
- There was a reasonable degree of correlation ($R^2=0.69$) between quantity of fully bonded strands and experimental end region capacity. As such, design of strand shielding based on longitudinal tie capacity appears to be a rational design approach. This approach may give better results than the arbitrary shielding limits imposed by current AASHTO LRFD specifications.
- There is need for code provisions that explicitly address lateral-splitting failure. Current shear and longitudinal tie provisions resulted in nominal capacities that were unconservative (too large) for some specimens failing in lateral-splitting.

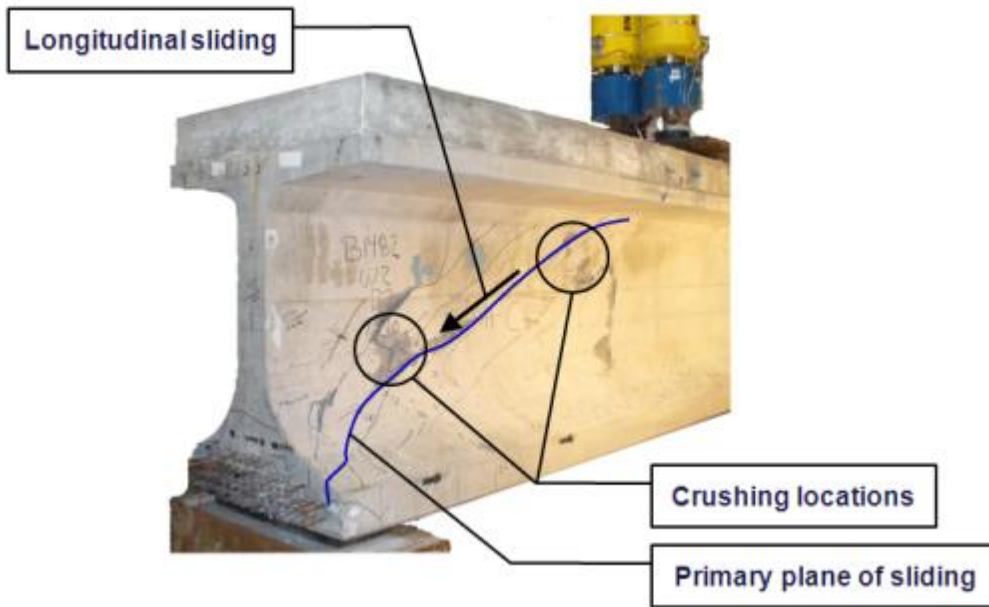


Figure 7-1. Web-shear failure. (Photo courtesy of B.E. Ross)

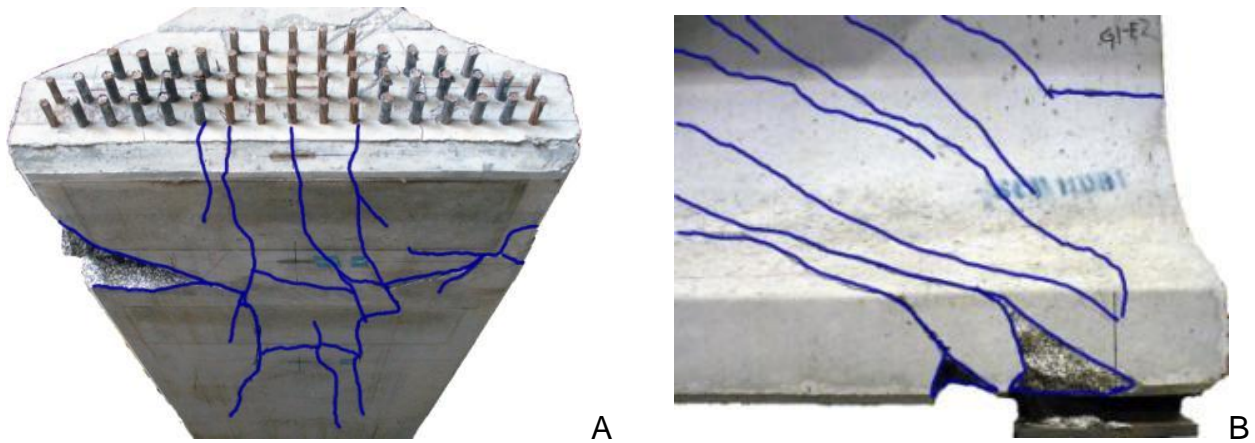


Figure 7-2. Bond-shear failure. A) Bottom view, B) Side view. (Photos courtesy of B.E. Ross)

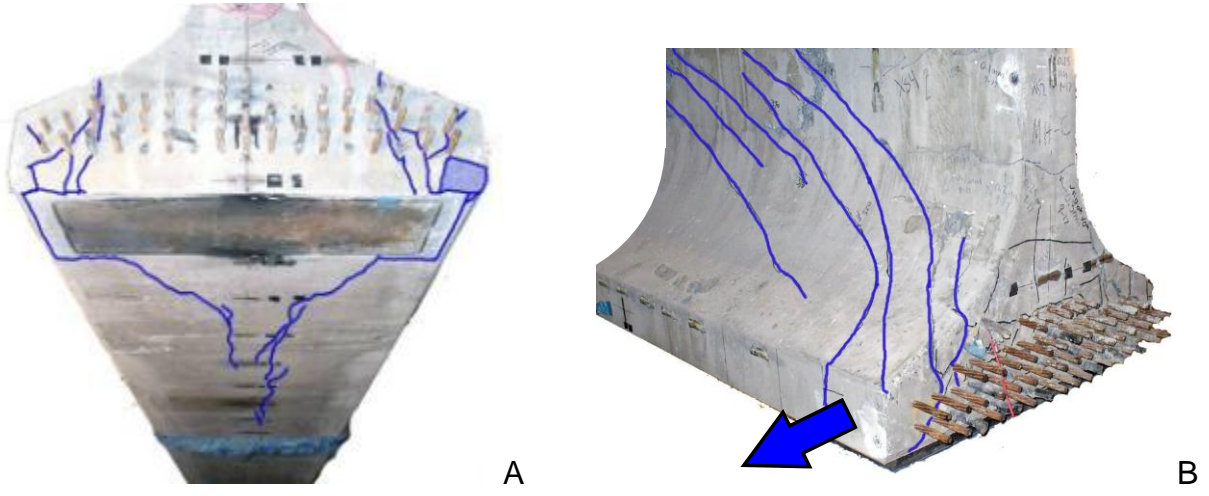


Figure 7-3. Lateral-splitting failure. A) Bottom view, B) Side-end view. (Photos courtesy of B.E. Ross)

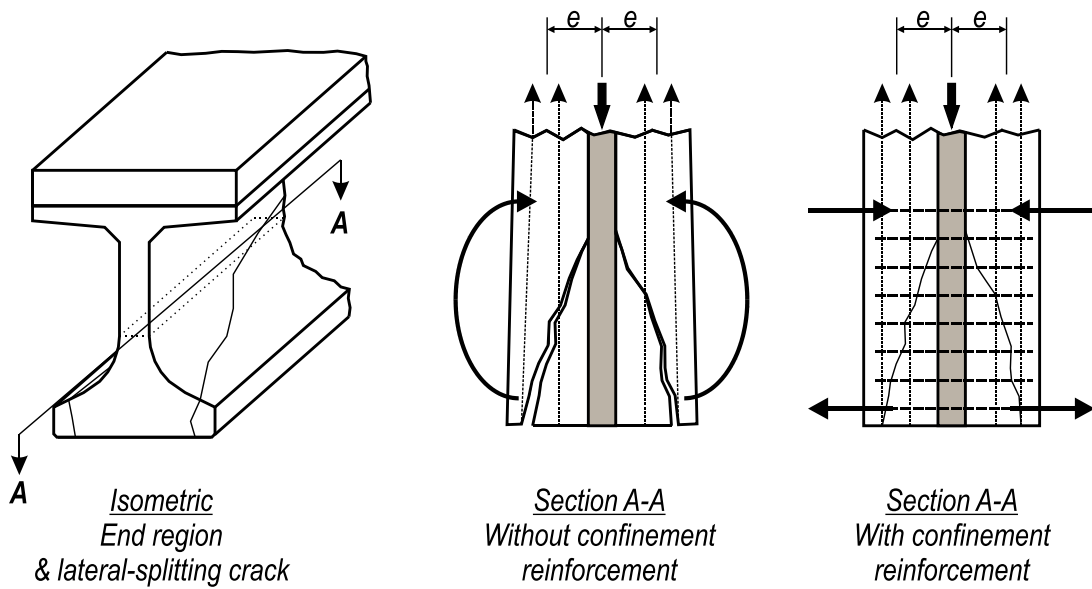
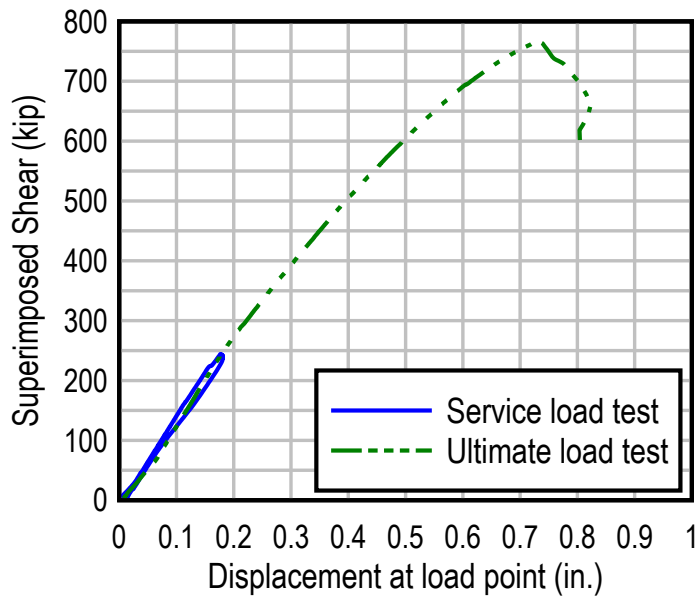
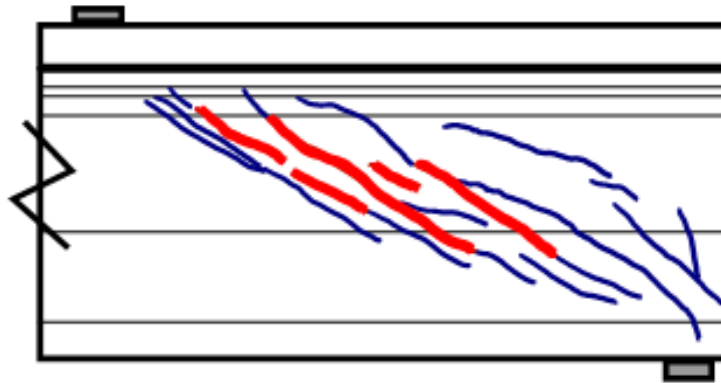


Figure 7-4. Lateral-splitting failure mechanics



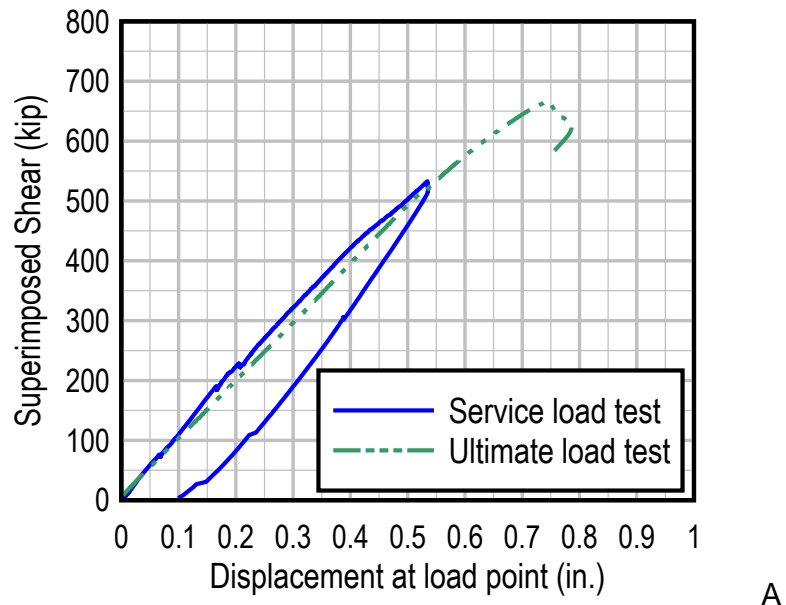
A

Release cracks not shown.
 Initial cracks shown bold in red
 Final cracks shown blue.



B

Figure 7-5. Specimen HC load test summary. A) Shear-displacement, B) Crack pattern.



Release cracks not shown.
 Initial crack shown bold in red
 Final cracks shown blue.

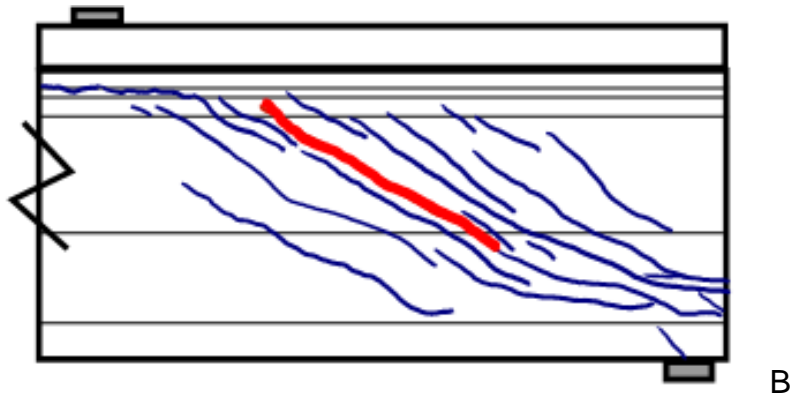
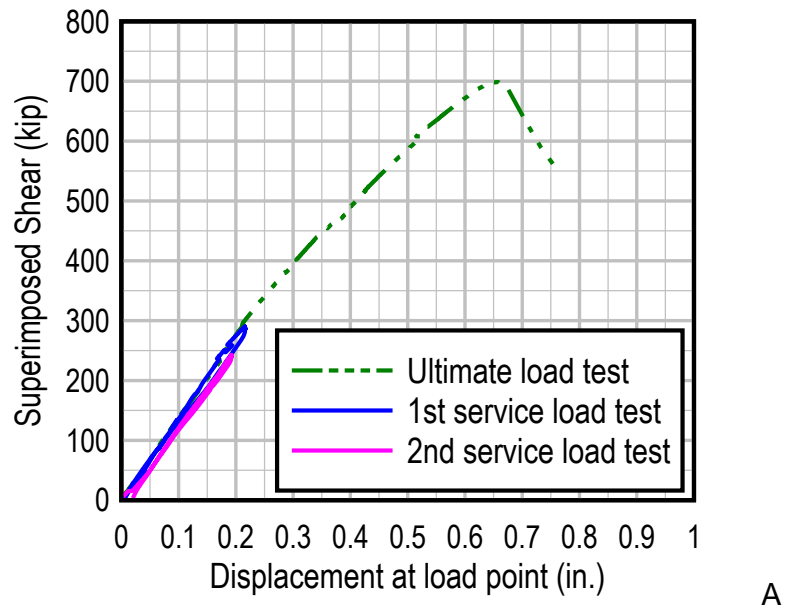


Figure 7-6. Specimen HU load test summary. A) Shear-displacement, B) Crack pattern.



Release cracks not shown.
 Initial crack shown bold in red.
 Final cracks shown blue.

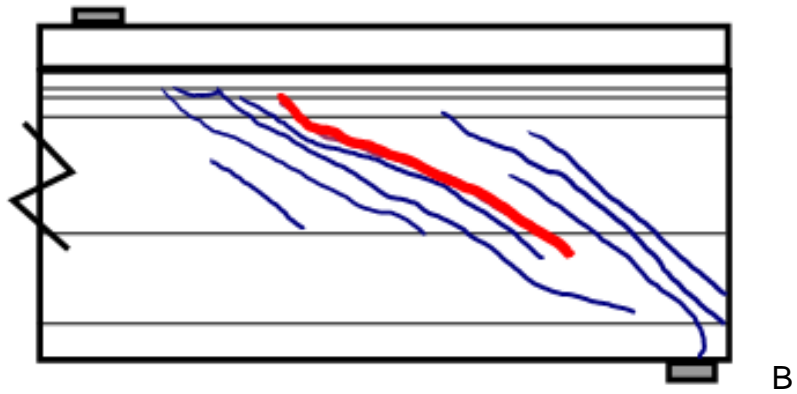
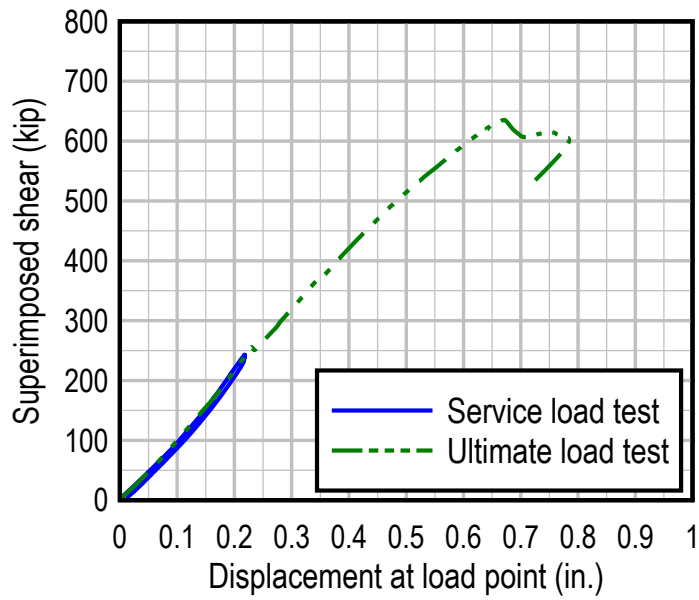


Figure 7-7. Specimen VC load test summary. A) Shear-displacement, B) Crack pattern.

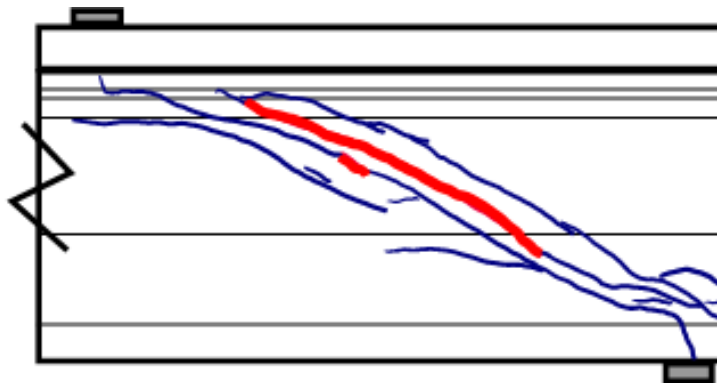


A

Release cracks not shown.

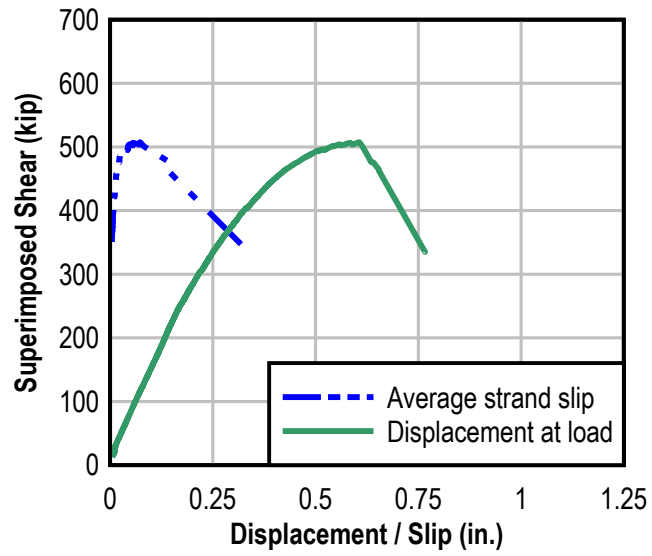
Initial cracks shown bold in red.

Final cracks shown blue.



B

Figure 7-8. Specimen VU load test summary. A) Shear-displacement, B) Crack pattern.

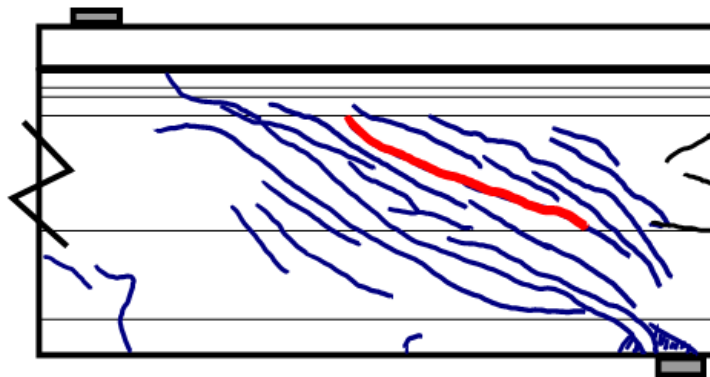


A

Release cracks shown black.

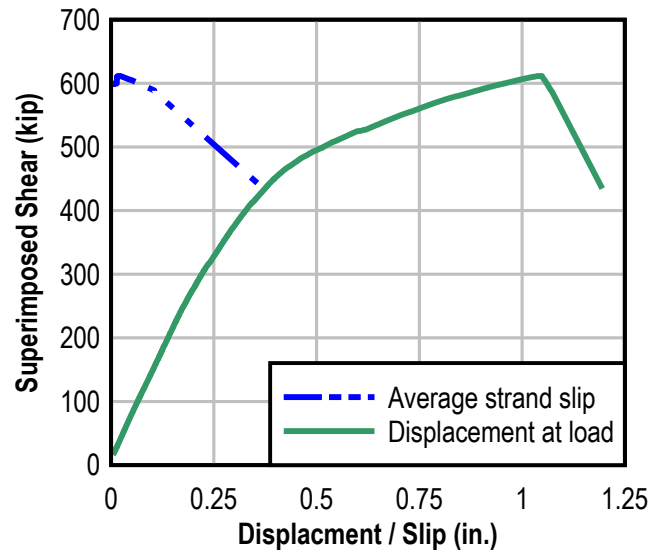
Initial crack shown bold in red.

Final cracks shown blue.



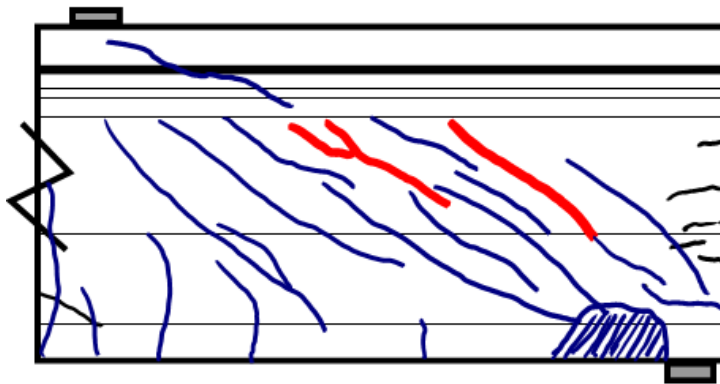
B

Figure 7-9. Specimen WN load test summary. A) Shear-displacement/slip, B) Crack pattern.



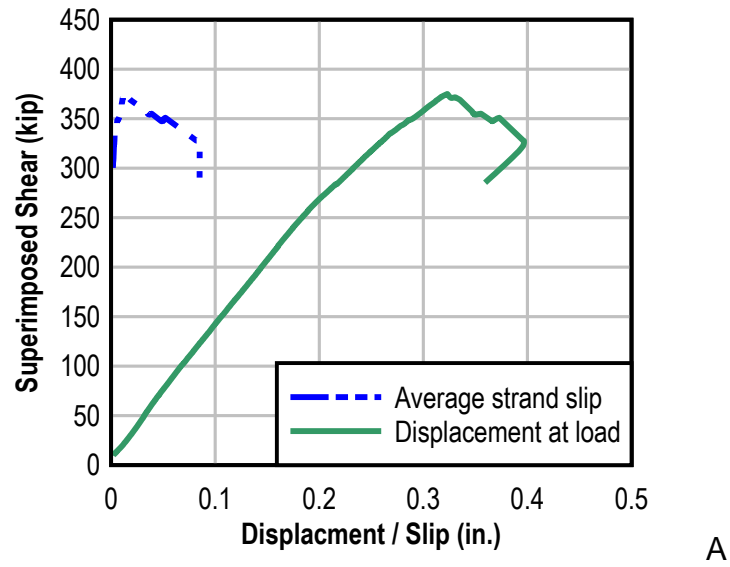
A

Release cracks shown black.
 Initial crack shown bold in red.
 Final cracks shown blue.



B

Figure 7-10. Specimen WB load test summary. A) Shear-displacement/slip, B) Crack pattern.



Release cracks shown black.
 Initial crack shown bold in red.
 Final cracks shown blue.

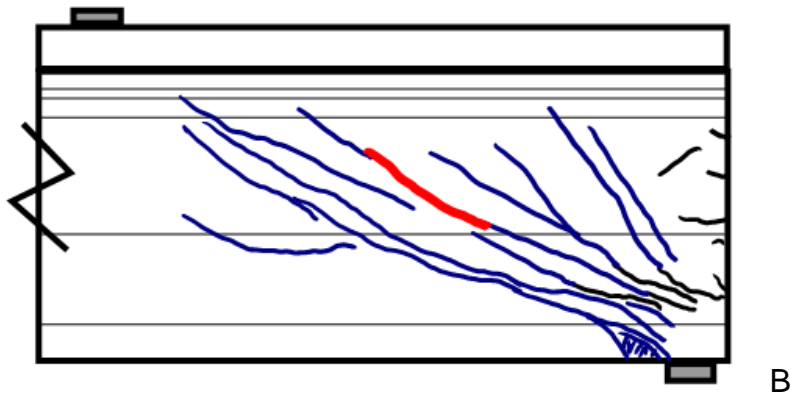


Figure 7-11. Specimen FN load test summary. A) Shear-displacement/slip, B) Crack pattern.

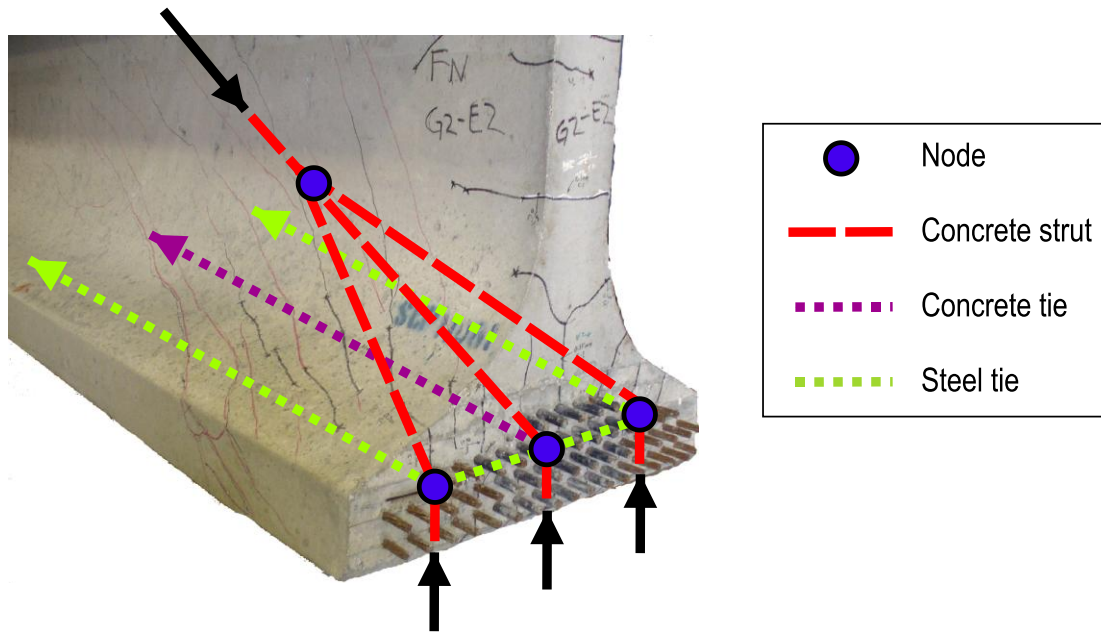


Figure 7-12. Strut-and-tie behavior specimen FN. (Photo courtesy of B.E. Ross)

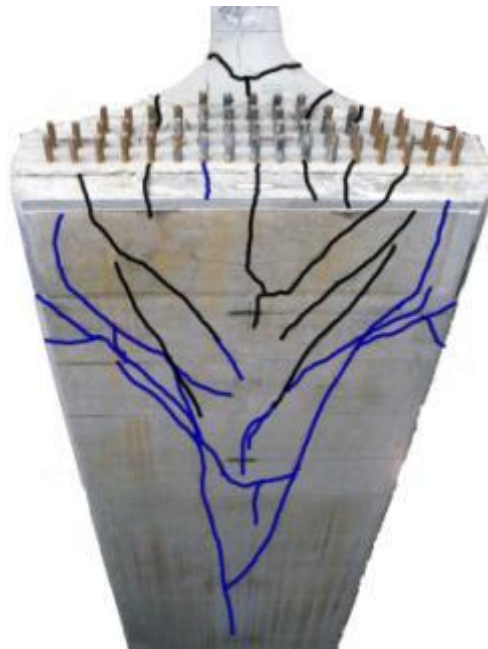


Figure 7-13. Longitudinal splitting cracks on bottom of specimen FN. Release cracks shown black. Final cracks shown blue. (Photo courtesy of B.E. Ross)

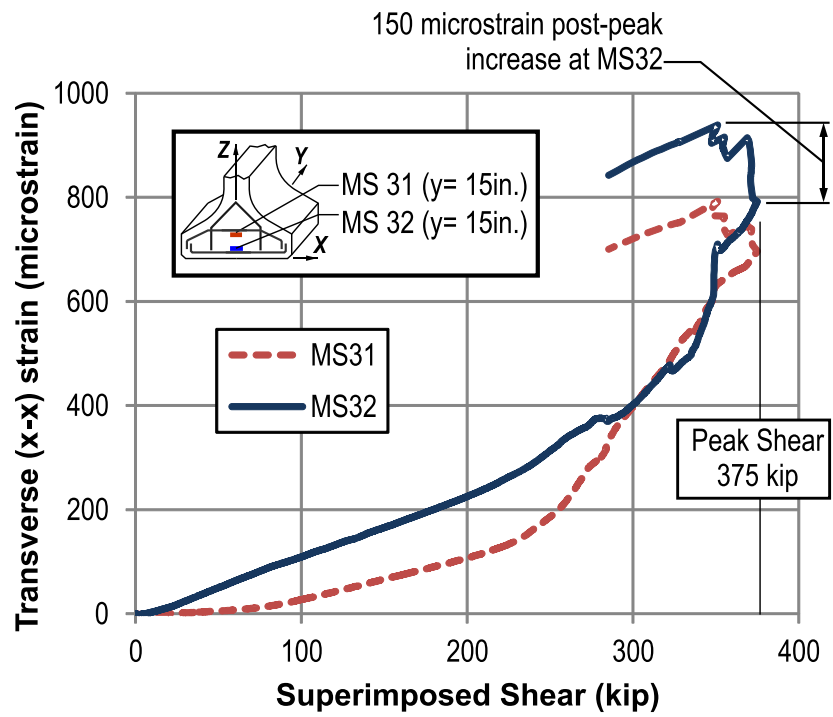
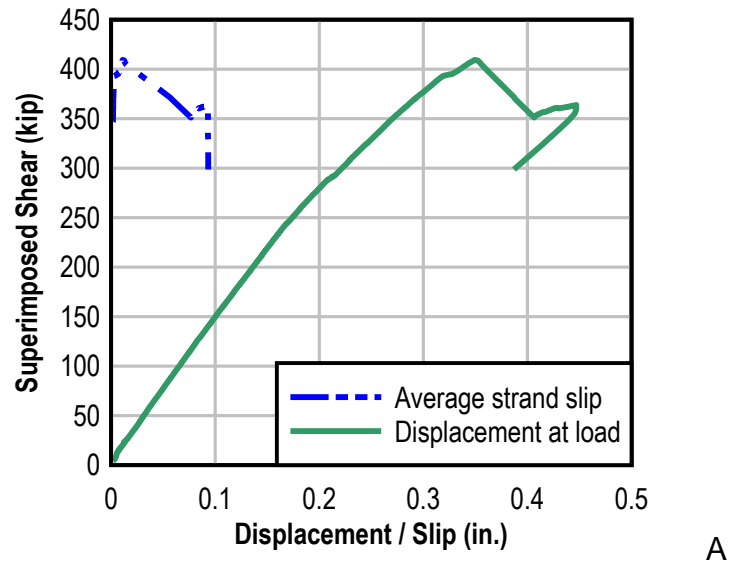


Figure 7-14. Confinement reinforcement strain specimen FN



Release cracks shown black.
 Initial crack shown bold in red.
 Final cracks shown blue.

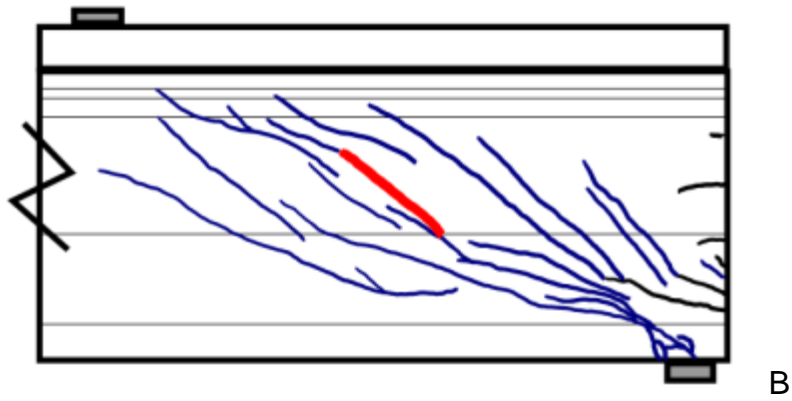
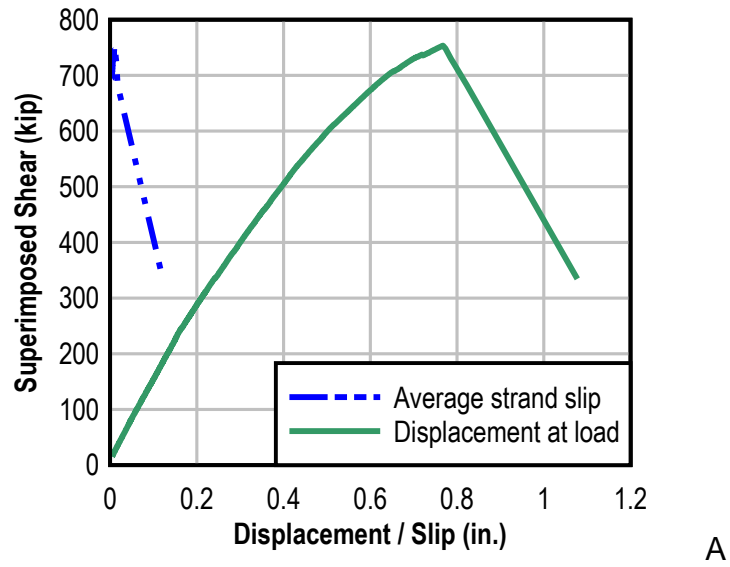


Figure 7-15. Specimen FB load test summary. A) Shear-displacement/slip, B) Crack pattern.



Release cracks shown black.
 Initial crack shown bold in red.
 Final cracks shown blue.

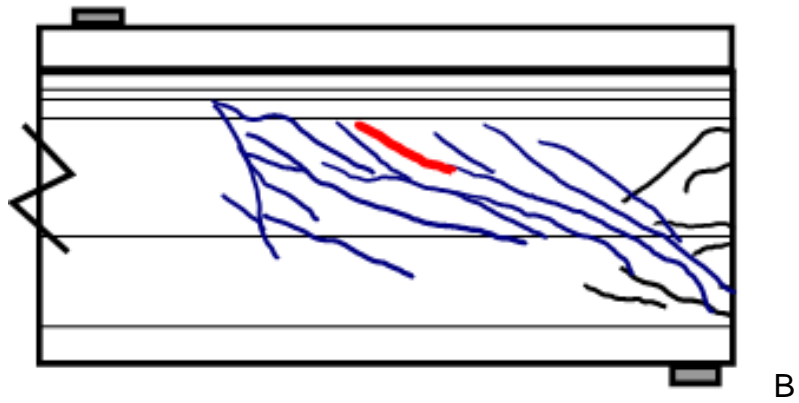
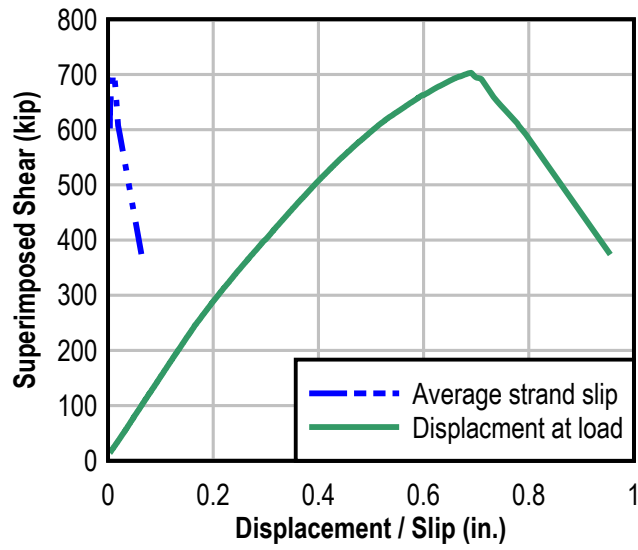
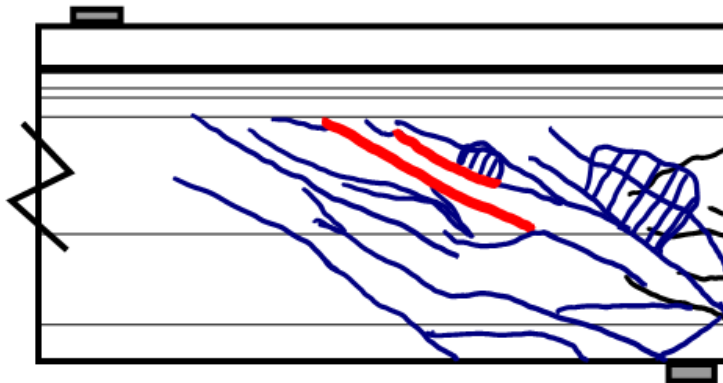


Figure 7-16. Specimen DC load test summary. A) Shear-displacement/slip, B) Crack pattern.



A

Release cracks shown black.
 Initial crack shown bold in red.
 Final cracks shown blue.



B

Figure 7-17. Specimen DM load test summary. A) Shear-displacement/slip, B) Crack pattern.

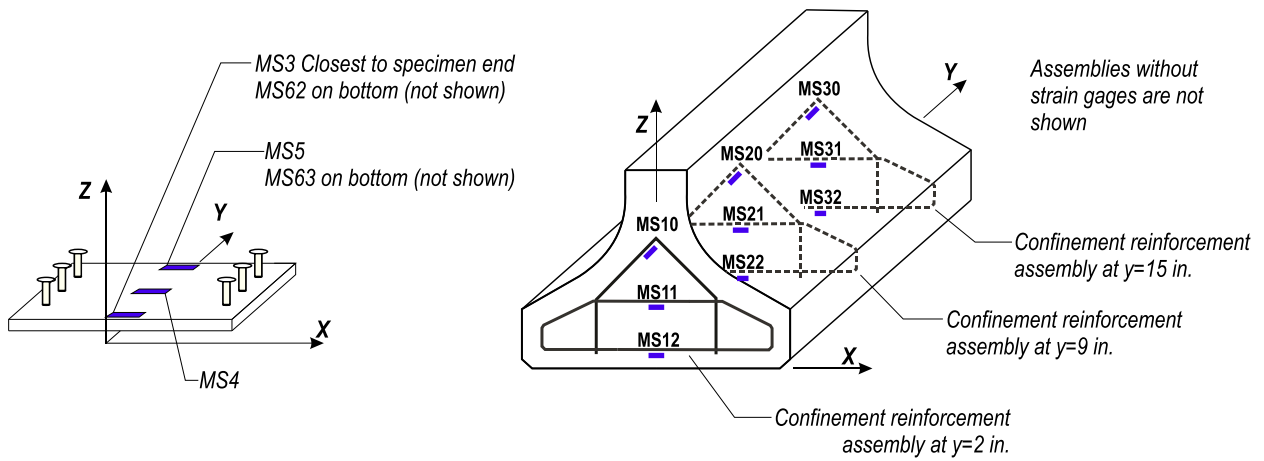


Figure 7-18. Strain gage placement girders W, F, and D

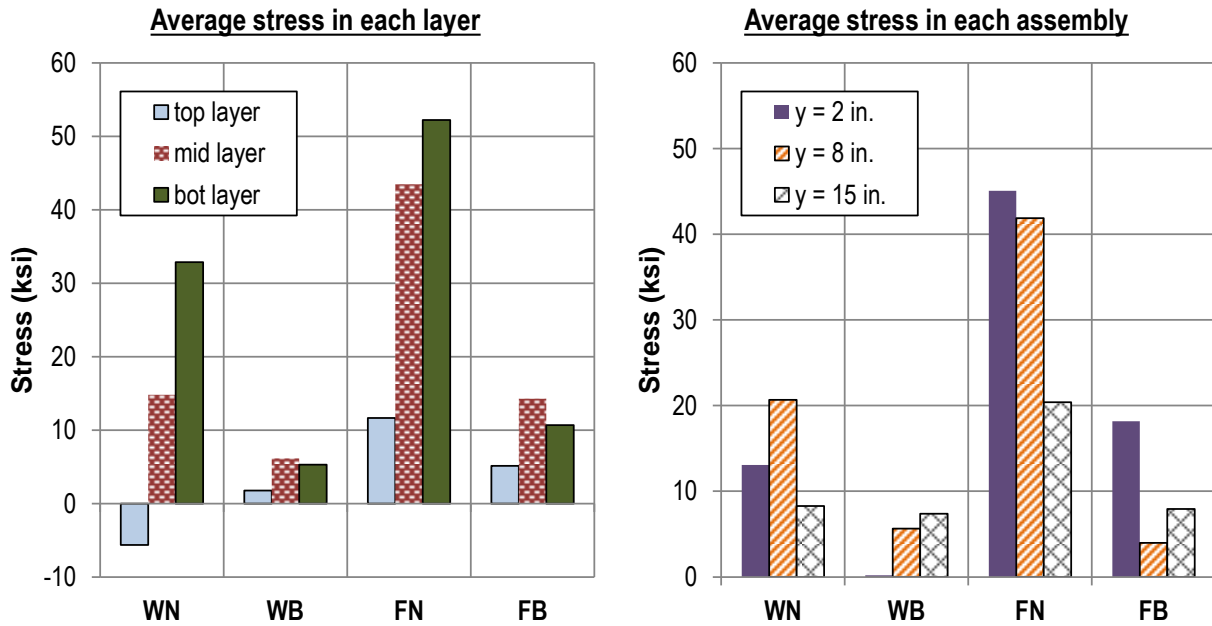


Figure 7-19. Confinement stress at shear = 375 kip

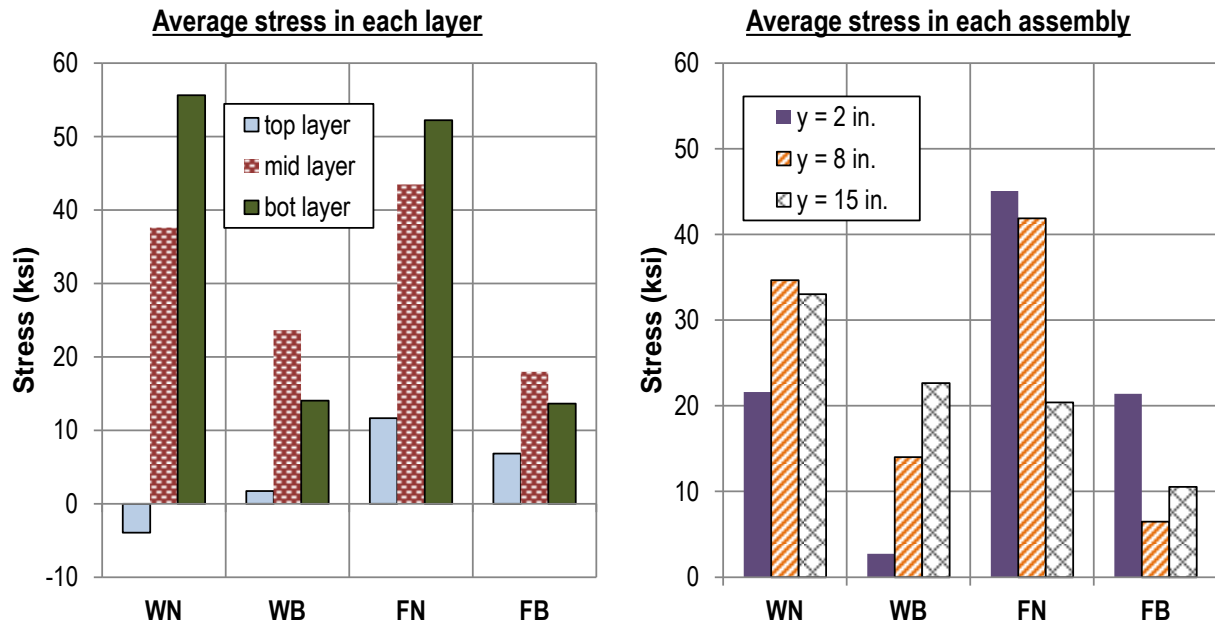


Figure 7-20. Confinement stress at ultimate capacity

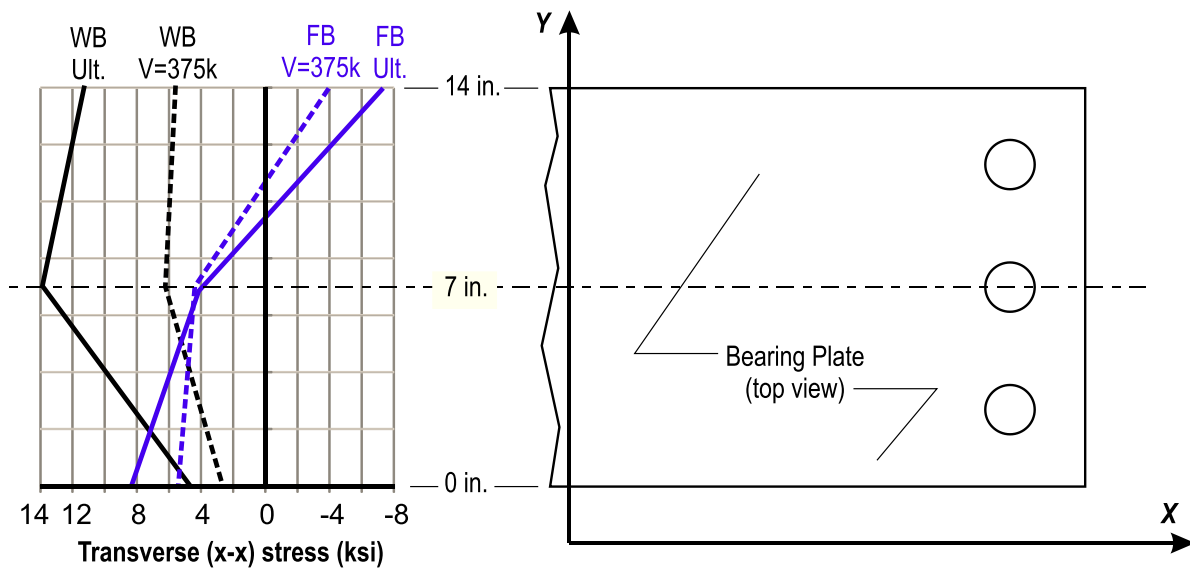


Figure 7-21. Transverse (x-x) stress profiles at bearing plate centerline

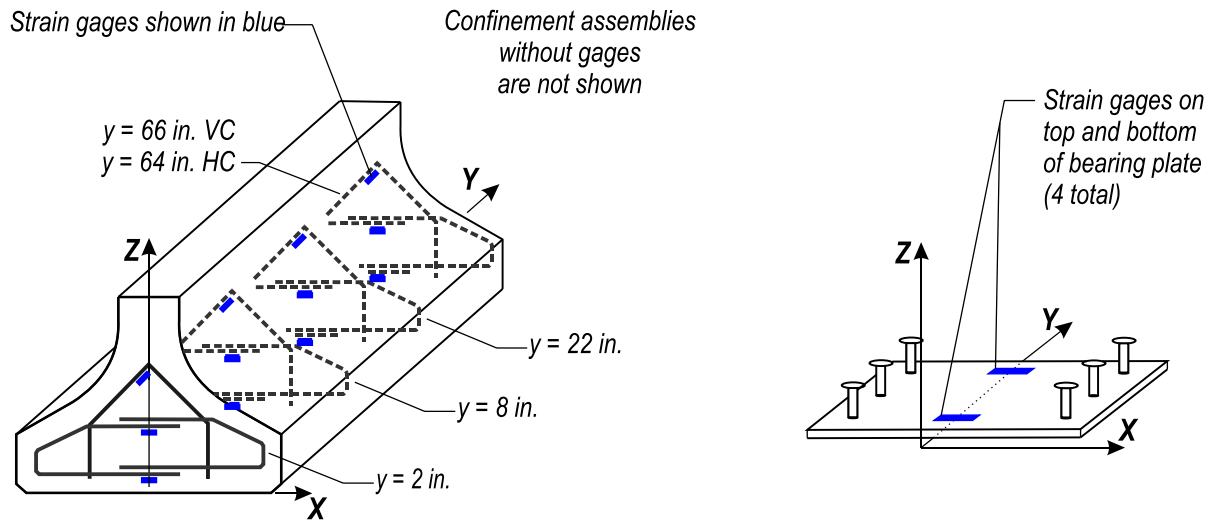
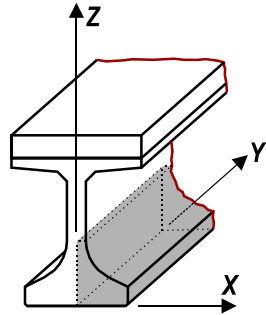
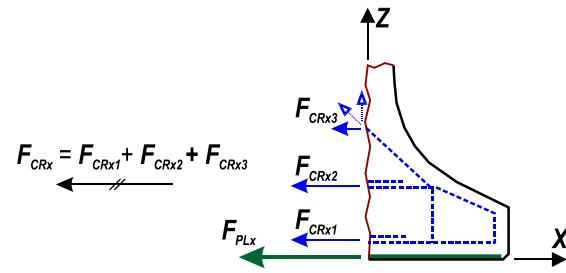


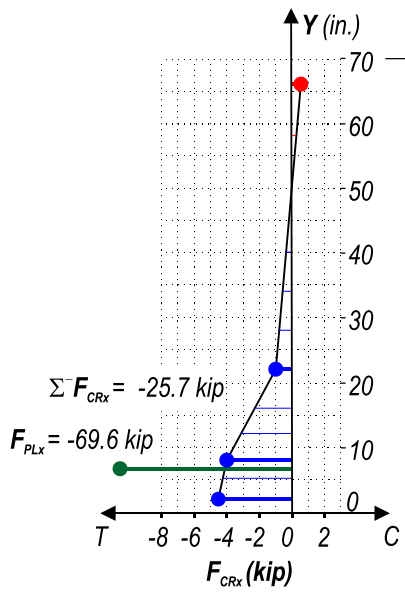
Figure 7-22. Strain gage placement girders H and V



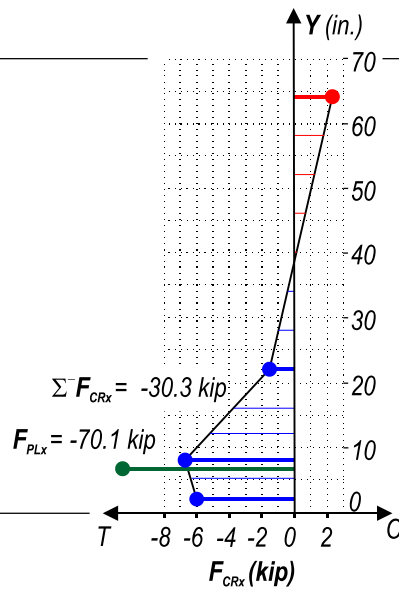
End region
isometric view



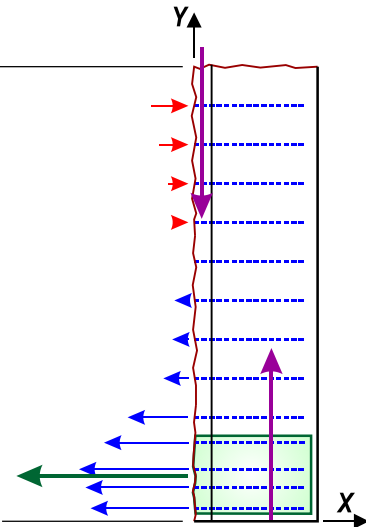
Bottom flange section
end view



Bottom flange forces
specimen HC



Bottom flange forces
specimen VC



Bottom flange section
partial plan view

Figure 7-23. Specimens HC and VC confinement reinforcement and bearing plate transverse (x-x) forces due to maximum applied load

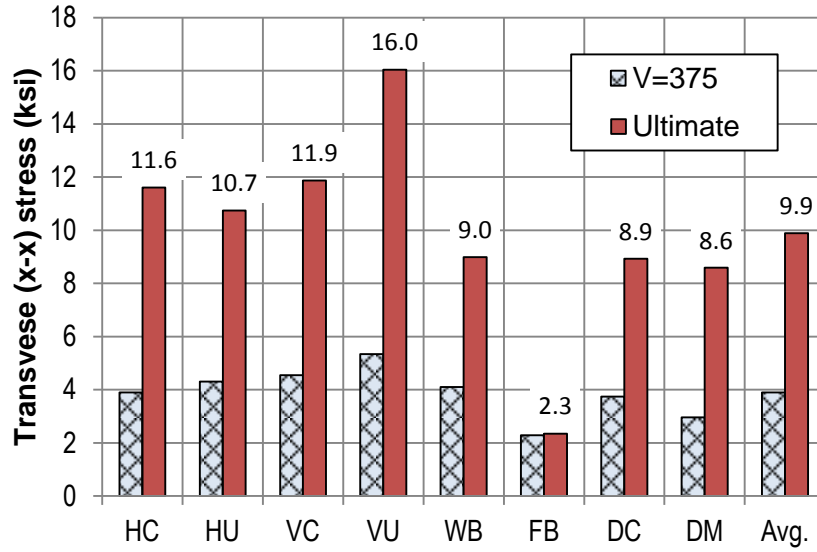


Figure 7-24. Bearing plate stress due to applied load

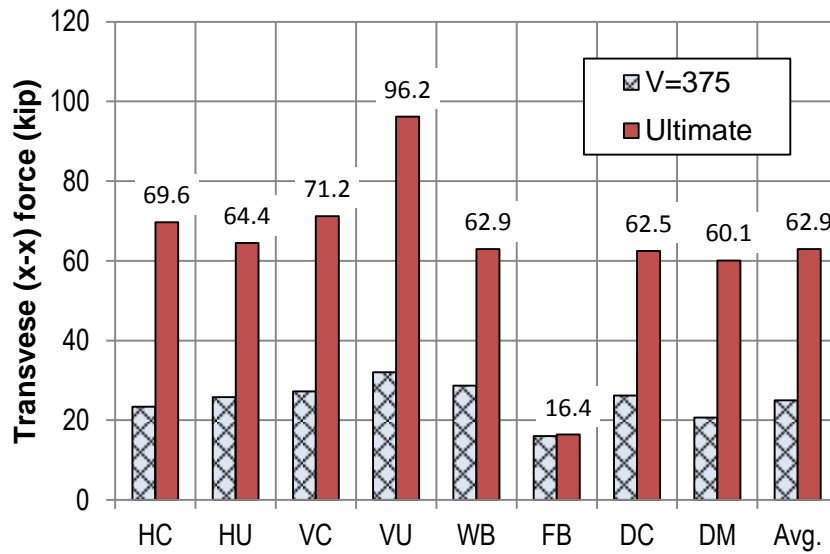


Figure 7-25. Bearing plate force due to applied load

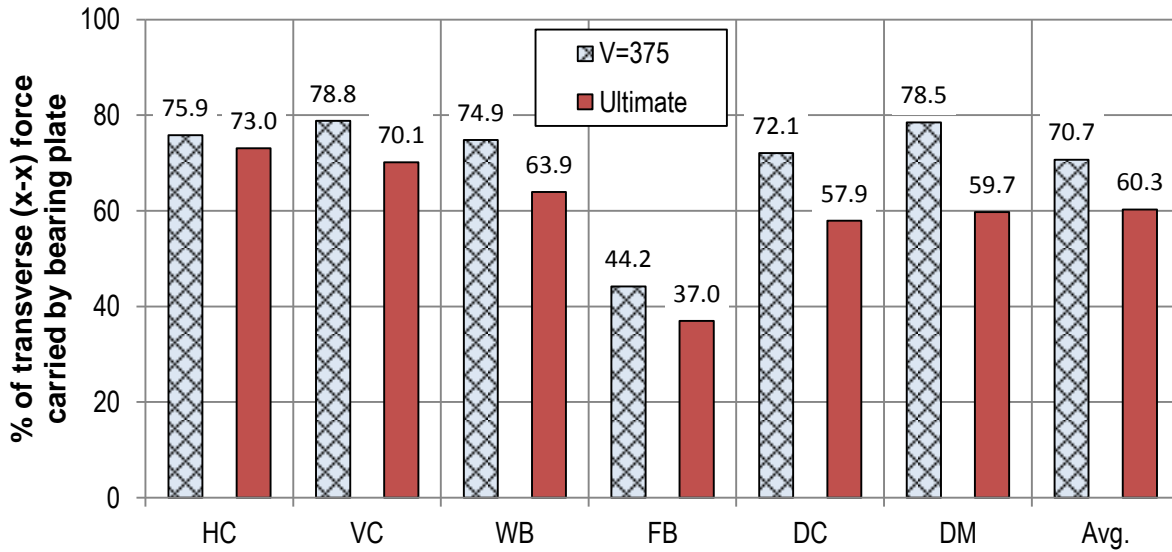


Figure 7-26. Percent of transverse force due to applied loads carried by bearing plate

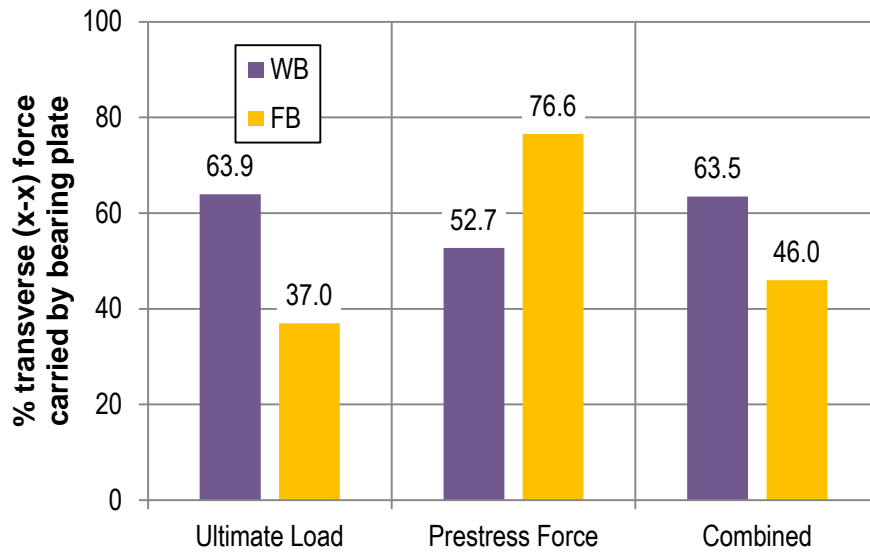


Figure 7-27. Percent of transverse force carried by bearing plate in WB and FB

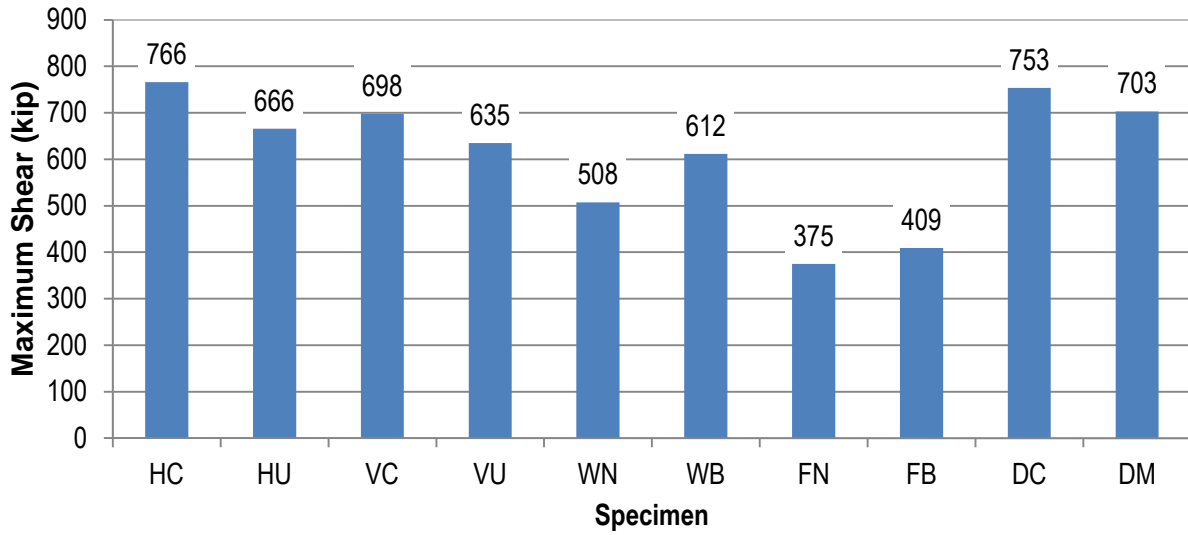


Figure 7-28. Maximum superimposed shear

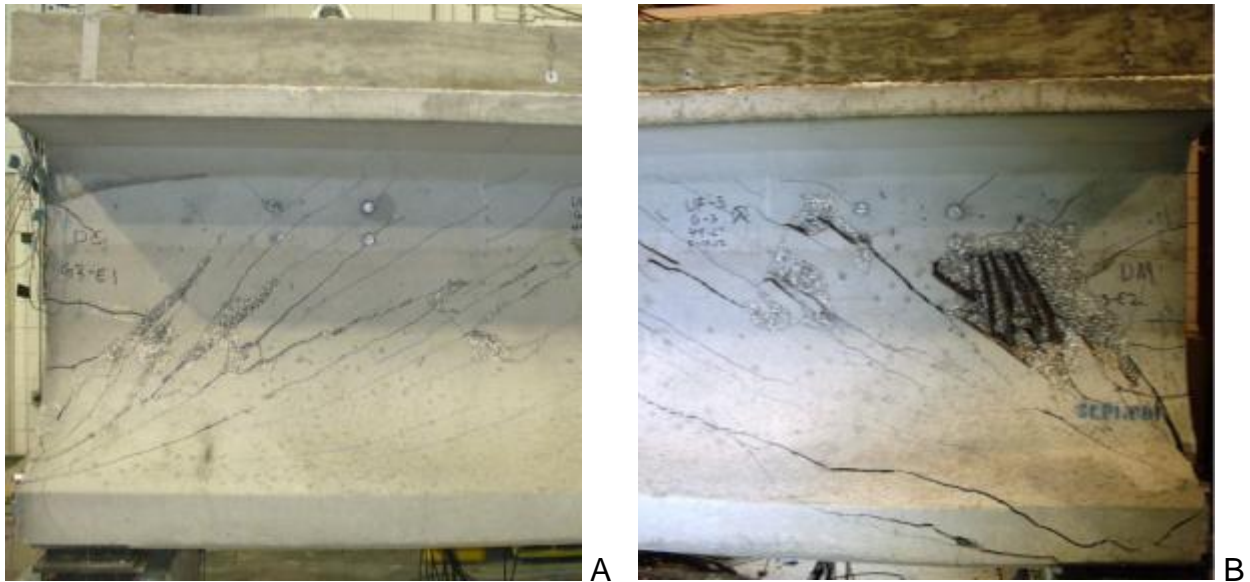


Figure 7-29. Girder D bottom flange cracking. A) Specimen DC with limited bottom flange cracking in front of bearing, B) Specimen DM with severe bottom flange cracking in front of bearing. (Photos courtesy of B.E. Ross)

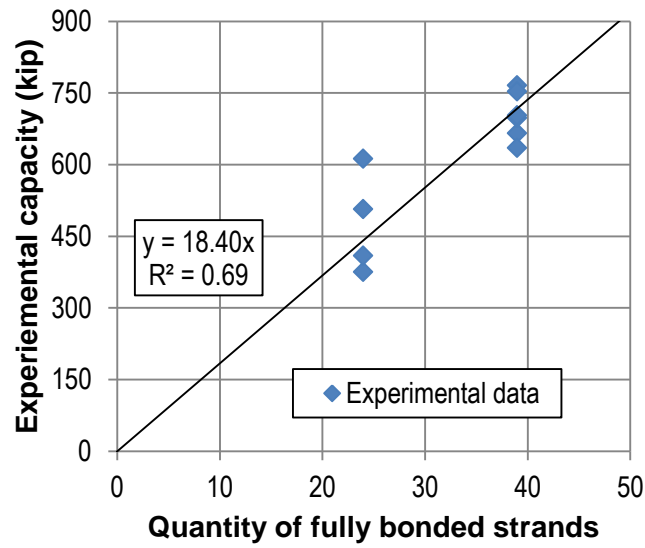


Figure 7-30. Relationship between strand quantity and end region capacity

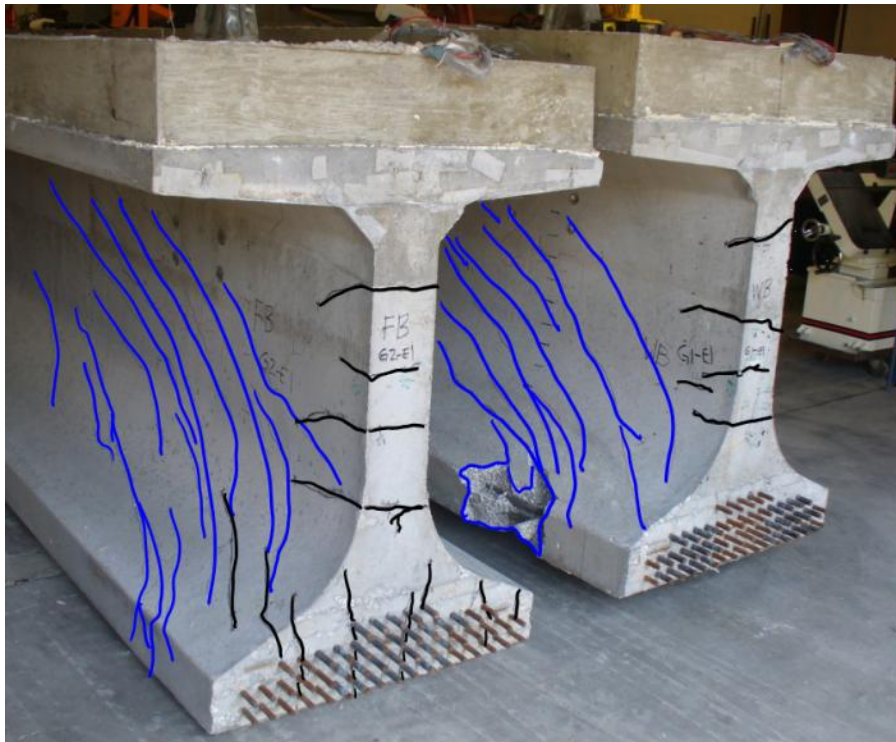


Figure 7-31. Comparison of FB (left) and WB (right). Release cracks shown black. Final cracks shown blue. (Photos courtesy of B.E. Ross)

Table 7-1. Transverse forces in W and F specimens

		WN (kip)	WB (kip)	FN (kip)	FB (kip)
Shear of 375 kip	Confinement reinforcement	50	15	107	27
	Bearing plate	0	36	0	30
	Total	50	51	107	58
Ultimate load	Confinement reinforcement	95	40	107	35
	Bearing plate	0	70	0	30
	Total	95	111	107	65

Table 7-2. Maximum superimposed shear

Specimen	Maximum superimposed shear (kip)	Maximum shear / average shear
HC	766	1.25
HU	666	1.09
VC	698	1.14
VU	635	1.04
WN	507	0.83
WB	612	1.00
FN	375	0.61
FB	409	0.67
DC	753	1.23
DM	703	1.15
Average	612	1.00

Table 7-3. Variable comparisons

Variable	Relevant specimens	Result
Horizontal reinforcement	HC, DC	Negligible effect on end region capacity in specimens failing in web-shear
Bearing plate	WN, WB, FN, FB	9% to 21% capacity increase from bearing plate
FDOT vs. no confinement reinforcement	HC, HU, VC, VU	13% capacity increase from FDOT confinement reinforcement
FDOT vs. modified confinement reinforcement	DC, DM	7% capacity increase from FDOT confinement reinforcement
Strand quantity	All	Average capacity increase of 18.4 kip / bonded strand
Strand placement	WN, WB, FN, FB	43% capacity increase for strands placed near centerline relative to strands placed in outer flange

Table 7-4. Material properties for capacity calculations

Property	Value
Prestressing strands ultimate strength	285 ksi
Vertical reinforcement yield strength	68 ksi
Concrete deck compressive strength	6500 psi
Concrete girder compressive strength	11000 psi

Table 7-5. Experimental moments and nominal moment capacities

Specimen	M_{exp} (kip-ft)	M_n (kip-ft)	V_{exp} (kip)	V_{Mn} (kip)	M_{exp}/M_n
HC	7384	10295	793	1098	0.72
HU	6478	10295	697	1098	0.63
VC	6746	10295	725	1098	0.66
VU	6155	10295	662	1098	0.60
WN	4954	6570	534	700	0.75
WB	5939	6570	639	700	0.90
FN	3716	6720	402	716	0.55
FB	4035	6720	436	716	0.60
DC	7262	10295	780	1098	0.71
DM	6793	10295	730	1098	0.66

Table 7-6. Experimental shear and nominal shear capacities

Specimen	V_{exp} (kip)	AASHTO Shear		ACI Shear		AASHTO Tie	
		V_{nLRFD} (kip)	V_{exp} / V_{nLRFD}	V_{nACI} (kip)	V_{exp} / V_{nACI}	V_{nT} (kip)	V_{exp} / V_{nT}
HC	793	590	1.34	490	1.62	678	1.17
HU	697	590	1.18	490	1.42	678	1.03
VC	725	590	1.23	490	1.48	657	1.10
VU	662	590	1.12	490	1.35	657	1.01
WN	534	528	1.01	454	1.18	507	1.05
WB	639	528	1.21	454	1.41	507	1.26
FN	402	528	0.76	454	0.89	514	0.78
FB	436	528	0.83	454	0.96	514	0.85
DC	780	590	1.32	490	1.59	657	1.19
DM	730	590	1.24	490	1.49	657	1.11
Average			1.12		1.34		1.06

CHAPTER 8 ANALYTICAL EVALUATION OF GIRDERS UNDER APPLIED LOADS

FE modeling was conducted to 1) provide a better understanding of the elastic behavior of the end region prior to cracking and 2) to evaluate the effects of bearing pad stiffness and width on end region elastic stresses. The FEA program Adina (R&D 2009) was used to conduct all modeling and analysis. All models were linear elastic. Strain gage and displacement data from experimental work conducted on pretensioned concrete beams (Ross et al. 2011a) were used to validate the FEA model. Hereafter the beams tested by Ross et al. are referred to as the “small beams.”

Model Configuration

The FE model was configured to be computationally efficient, yet able to capture the overall behavior of the beam as well as the local behavior of the end region. The ability of the model to capture the distribution of transverse tensile strain in the end region was of particular interest. The model was also designed such that the geometric and material properties could be adjusted to evaluate the sensitivity of the end region behavior to such parameters.

The coordinate system defined in Chapter 4 was also used in the FE models (Figure 8-1). The origin was located at the end of the beam nearest the point load, at the centerline of the cross-section, and at the bottom of the beam. The X axis was oriented horizontally across the cross-section, the Y direction was oriented horizontally along the length of the beam, and the Z direction was oriented vertically.

Figure 8-2 shows the model configuration. The shear span (distance from the load to the near support) and a small distance beyond the shear span were modeled with 27-node 3D solid elements on a primarily rectangular mesh. The remainder of the beam

was modeled with 1D beam elements, with the transition from beam to solid elements made using rigid 2D shell elements and 1D rigid links. Rigid shell and link elements (Figure 8-3) coupled the displacements of the 3D solid elements with the displacements and rotations of the 1D beam elements. Transitioning to beam elements reduced the computation demand of the model while still modeling the global beam behavior and boundary conditions. Beam elements were placed at the centroid of the cross-section and were assigned cross-sectional properties equivalent to the physical beam. At the far support, a rigid link was provided to connect the beam elements to the physical location of the bearing pad at the bottom of the beam.

Axial and shear stiffness of the bearing pad at the far support were modeled with 1D springs in the Z and Y directions respectively. At the near support, the axial and shear stiffness of the bearing pad was modeled with multiple spring elements in each of the X, Y, and Z directions. Position and quantity of spring elements matched the discretization of the solid elements used to model the beam (Figure 8-4). Stiffness was assigned to each spring in proportion to the tributary area represented by the spring.

Figure 8-5 defines key geometric variables of the model end region. Geometric variables were set-up to allow variation of features such as shear span-to-depth ratio, bearing pad size and location, span length, and the location of the applied load. Additional geometric variables are defined on the cross section shown in Figure 8-6.

The cross-section, boundary conditions and load were symmetrical about the Y-Z plane, allowing for only half of the beam to be considered in the FE model (Figure 8-6). A top view of the model, shown in Figure 8-7, gives the position of the model relative to the physical geometry of the beam.

Concrete modulus of elasticity for each model was 5300ksi, and the Poisson's ratio was 0.2. The modulus of elasticity value was chosen to match the tested material properties from the physical beams used for model validation.

The typical model configuration described above was validated by comparison with experimental data, and was then used in more general investigations of the stress and strain state in the end region. Details of the validation and general investigations are contained in the proceeding sections.

Small Beam Model

The configuration described above was used to model the small beams tested by Ross et al. (2011). Dimensions, elements sizes, and spring properties of the model are listed in Table 8-1. Variables in this table are defined in Figure 8-5 and Figure 8-6. The experimental test set-up being modeled, element types, and element density are shown in Figure 8-8. Stiffness values for the springs in the Z direction were based on experimental load-displacement data from LVDTs located over the bearing pads on the small beam tests (Figure 8-9). From these data, a representative axial stiffness of 1150 kip/in was chosen. At the far support, the full axial stiffness was assigned to the single spring at the bearing point. At the near support the axial stiffness was distributed to the springs based in proportion to tributary area. Stiffness of springs at both the near and far supports in the pad shear directions (X & Y) were based on properties reported for similar sized bearing pads (Yura et al. 2001).

Model Validation and Verification

Prior to comparing FE results with experimental data, convergence of the FE solution was verified by comparing the proposed model with a model containing a more refined mesh. Figure 8-10 shows the transverse (x-x) strain in the bottom bulb at the

near support for the proposed and refined mesh densities. Note that the section geometry and strain values were symmetric about the Y-Z plane, and that only half of the bottom bulb is shown in the figure. The strain values and strain distributions were similar for both models, with the maximum transverse strain occurring at the centerline of the beam directly above the bearing pad ($Z=0$, $X=0$). The refined model reported a maximum strain that was only 0.1% greater than the maximum value from the proposed model. Based on the degree of correlation with the refined mesh, element sizes used in the proposed model were considered appropriate.

Comparison with experimental data indicated that the FE model did an adequate job of capturing both the global and local linear elastic behavior of the physical test beams. Global behavior is compared in the load-displacement plot in Figure 8-12. Displacement in the figure (both experimental and analytical) is the vertical displacement at the load point, and was corrected to remove displacement due to deformation of the bearing pads. Within the elastic range, the FE model stiffness was 23% less stiff than the average experimental beam stiffness, but was still within the scatter of the experimental data.

The profile of the transverse ($x-x$) strain at the near end of the beam is shown in Figure 8-11. Strain profiles were compared at a load of 15kip, as this load was well within the elastic range for each of the test beams. Experimental data came from strain gages mounted at the end of the beams 5in. above the beam bottom. Shape of the strain profile was consistent between experimental data and the FE model, with the peak occurring at the centerline of the beam. Magnitudes of the strains calculated by

the FE model were larger than the average of the experimental data, but were still within the scatter of the data.

Figure 8-13 shows the load versus strain relationship for gage S5 which was located longitudinally on the bottom of the beam directly below the applied load. Experimental data from gage S5 was very consistent between tests. At the location of S5, the slope of the load-strain curve from the FE model was 20% less than the average slope of the experimental data.

Figure 8-14 shows the load versus strain relationship for gages S11 and S12. These gages were located on the top of the beam on either side of the applied load. Values from gages S11 and S12 were averaged to form the curves for the individual tests. Values reported by the FE model at the locations of S11 and S12 were identical because the FE model employed symmetry about the Y-Z plane. The slope of the load-strain curve reported by FE model was 5% greater than the average slope of the experimental data.

Finally, the maximum principal tensile strain was evaluated over the region shown in Figure 8-16. The maximum principle tensile strain occurred at the intersection of the web and the bottom bulb (Figure 8-15). The strain concentration at the web-bulb interface correlates with the location of cracks observed during testing.

The proposed FE model captured the general behavior of the physical beam, as well as the local behavior of the end region. In most cases the FE results were within the scatter of the experimental data. Based on the correlations presented above, the proposed FE model was considered adequate for conducting more general evaluations of the concrete girder end region.

Parametric Studies

The FE model configuration presented previously was used to evaluate parameters affecting the strain state in the end region including: bearing pad stiffness, cross-section geometry, steel bearing plates and bearing pad geometry.

Bearing Pad Stiffness

Four additional models were created to evaluate sensitivity of the end region strains to changes in bearing pad stiffness. In these models, the axial or shear stiffness of the bearing pad was either doubled or halved relative to the stiffness of the original model. By using half or double the stiffness properties of the original small beam model, the additional models cover the range of stiffness values for similar sized bearing pads reported by Yura et al. (2001). Details and results from the additional models are presented in Table 8-2. Information regarding the original model is also included in the table for reference.

Strain results were evaluated over the region shown in Figure 8-16. For each model, the maximum transverse tensile strain was located at the centerline of the beam directly above the bearing pad (Figure 8-16). Changes to bearing pad shear stiffness (K_v) had negligible effect on maximum transverse (x-x) strain over the range of values tested. However, changes to the axial stiffness (K_a) of the bearing pads did affect the maximum transverse strain. For the region considered, doubling the axial stiffness resulted in a 2.7% reduction in maximum transverse strain whereas halving the axial stiffness resulted in a 1.5% increase in maximum transverse strain.

Bearing Pad Geometry

To evaluate the effect of bearing pad width on the transverse strain in the end region, FE models of the Florida I-Beam (FIB) and a rectangular cross-section (Figure

8-17) were created using the modeling configuration described previously. Details of the models are given in Table 8-3. The bearing pad width, W_b , was varied from of 8.55 in. to 16.15 in. Because half-symmetry models were used, the bearing pad width, W_b , is equal to half of the total bearing pad width. Thus the FE model with W_b of 16.15 in. corresponded to a total bearing pad width of 32.3 in. This dimension is similar to the 32 in. width specified in the FDOT design standards (FDOT 2009c).

For convenience, models were assigned a label based on cross-section shape and nominal W_b dimension. For example, the label FIB-10 was assigned to the model with the FIB cross-section and a bearing pad width of 10.45 in. The label R-15 was given to the model with the rectangular cross-section and a bearing with of 15.20 in.

Stiffness and spacing of the individual springs comprising the bearing pad at the near support were held constant even as the bearing pad width varied. However, the total stiffness of the bearing pad changed as additional springs were added or removed to change the width of the bearing pad. The individual spring stiffness, as well as the total bearing pad stiffness, are listed in Table 8-4. In each model, total the stiffness of the far support matched the stiffness of the near support.

Transverse (x-x) strain results from the models were normalized by the maximum flexural ($\varepsilon_{y,max}$) tensile strain from the FIB model. The maximum flexural strain was located at the bottom of the beam below the load point (Figure 8-18). The value of $\varepsilon_{y,max}$ was slightly different for the FIB and rectangular cross-sections, however for a given section it did not vary as the bearing pad width changed. For a half-symmetry applied load of 67 kip (experimental load of 134 kip), $\varepsilon_{y,max}$ was 91 microstrain for the FIB

model, and for the same load, was 61 microstrain for the rectangular section model.

The transverse strains for each model were normalized by $\varepsilon_{y,\max}$ from the FIB model.

For the FIB cross-section, two types of behavior were observed as the bearing pad width was adjusted. First, when the pad width was narrow, the transverse strains were distributed in a bottle shape between the bearing pad and the bottom of the web (Figure 8-19). This is denoted as ‘bursting’ behavior. The mechanics of bursting behavior are similar to a split cylinder test, with transfer tensile strain forming perpendicular to compressive loads. The maximum transverse strain occurred above the bearing pad, as shown in Figure 8-20. As the pad width increased, flexural strains increased at the bottom edge of the flange as the load spread to the far edge of the bearing pad (Figure 8-21). This is denoted as ‘flexural’ behavior. For ‘flexural’ behavior, the maximum transverse strain occurred at the bottom of the section as shown in Figure 8-22.

To further investigate the relationship between transverse strain and bearing pad width, strain at three points on the end of the beam were plotted against the bearing pad width (Figure 8-23). Points were located at the end of the beam ($Y=0$ in.) along the plane of symmetry ($X=0$ in.) at Z coordinates of 0 in., 5 in., and 9 in. Looking first at the point $Z = 0$ in., it can be seen that the maximum transverse strain increased as the bearing pad width also increased. This condition was a consequence of flange-bending behavior. For the point at $Z= 9$ in., the transverse strain increased as the bearing pad width decreased. Thus the strain at $Z = 9$ in. was maximum when the beam experienced bursting behavior, and was smaller when flange bending dominated the behavior. The strain at $Z = 5$ in. remained fairly constant as the pad width changed. The optimum bearing pad width, i.e. the width that minimized the transverse strain, was

approximately 21 in. This is also the width where the behavior changed from bursting to flexural behavior.

Figure 8-24 shows the normalized transverse strains in the end region for four models with different bearing pad widths. Variations in the transverse strain between the different models only occurred in portions of the beam adjacent to the bearing pad. In these portions of the beam, the 'bursting' and 'flexural' behavior were evident in both the Z-Y and Z-X planes. Regardless pad width, the greatest transverse strains always occurred that the end of the beam.

Transverse strain distributions in the end region of the rectangular section are shown in Figure 8-25 for models with four different bearing pad widths. As previously noted, the transverse strains were normalized by $\varepsilon_{y,max}$ from the FIB model. The scale and color contours are different from earlier figures of the FIB section. The figure shows that the magnitudes of the strains in the rectangular section were considerably less than for the FIB section. For instance, the maximum normalized transverse strain in the R-8 model was only 38% of the maximum from the FIB-8 model. For R-16, the maximum normalized transverse strain was only 14% of the maximum from model FIB-16.

The greatest strain in the rectangular section models occurred in the model with the narrowest bearing pad. Conversely, the transverse strains were least in the model with the greatest pad width. Although the transverse strain varied as the pad width changed, the location of the maximum transverse strain always occurred at the end of the beam.

A parametric study of bearing pad width was also conducted using the small beam FE model (Figure 8-26). Results were similar to the FIB model. Regardless of bearing

pad width, maximum transverse strains always occurred at the end of the beam. Under the flexural mode, maximum transverse strain occurred at the end of the beam at bottom of the section. For the bursting mode, maximum strain occurred at the end of the beam and at a distance of approximately 60% of the flange depth above the bearing pad. The transition between bursting and flexural behavior occurred when the bearing pad width was approximately twice the web width. This pad width also corresponded to the lowest value of peak transverse strain.

Effect of Steel Bearing Plate

The FDOT standard detail for the FIB end region specifies (FDOT 2009c) a ½ in. thick x 12 in. x 36 in. steel bearing plate be embedded where the beam contacts the bearing pad. The bearing plate protects concrete in the region of high bearing stresses, and can be configured to aid in the constructability of skewed and/or sloped girders. Due to the location of the plate, its effect on the transverse (x-x) strain was of interest. To evaluate the effects of the bearing plate, the plate was added to the FIB models used in the previous section. The bearing plate was modeled with 4 node 2D shell elements positioned at the bottom of the beam (Figure 8-27). The bearing plate discretization was double that of the adjacent 27 node solid elements, thus each node from the plate elements aligned with a node from the adjacent solid element (Figure 8-28). Full composite behavior between the bearing plate and the concrete was assumed in the model. The parametric study of bearing pad width presented in the previous section was repeated for the model with the bearing plate.

Figure 8-29 shows the normalized transverse strain at the end of the beam vs. the bearing pad width for models with and without the steel bearing plate. As was done previously, the strain values in the figure were normalized by the maximum flexural

tensile strain ($\varepsilon_{y,max}$) (Figure 8-18) below the load point. Figure 8-29 shows that the presence of the steel bearing plate reduced the transverse strain at point Z=0. At a bearing pad width of 17 in., the model with the bearing plate reported 20% less transverse strain at point Z=0 than the model without the bearing plate. The reduction in strain was more pronounced at greater pad widths. For example, the bearing plate model reported 33% less transverse strain at a bearing pad width of 32 in. Results also indicated that the influence of the bearing plate was limited to those portions of the beam closest to the plate. At point Z =9, the presence of the bearing plate had insignificant effect on transverse strain.

Figure 8-30 shows the transverse strain distribution for models with different bearing pad widths. Similar to the FIB model that did not include the bearing plate, Figure 8-30 shows that the bearing plate models also experienced 'bursting' and 'flexural' behavior for narrow and wide bearing pad widths respectively.

When compared to the model without the bearing plate, the reduction of transverse strain is attributed to the additional confinement provided by the plate. This effect was most significant when the bearing pad width was widest, and when the maximum transverse strains occurred closest to the plate. The models only evaluated the effect of the plate in the range of elastic behavior, and did not consider contributions that the bearing plate may make after cracking and at ultimate strength.

Bearing Pad Width Effect on Transverse Force

Small beam, FIB, and FIB with bearing plate FE models developed in previous sections were used to evaluate the relationship between bearing pad width and

transverse force. As with all models in this chapter, the analysis was linear-elastic and considered the effects of applied loads only.

Transverse force was calculated by integrating transverse stress over the area shown in Figure 8-31. Boundaries of the integration area were selected to capture those portions of the girder near the bearing pad subjected to steep strain/stress gradients due to the reaction force, and to include portions of the bottom flange where confinement reinforcement is placed to carry transverse tension. Stress distributions beyond the integration area were not significantly affected by changes in bearing pad width. Analyzing transverse forces over the selected area gave a broad picture of pad width effects in the end region, whereas analysis of strain data in previous sections only looked at maximum effects and effects at discrete points.

The integration area used in transverse force calculation was located at the centerline of the considered cross-section. Dimensions of the integration area were determined as a function of the bottom flange width (W_f) so that similar integration calculations could be conducted on beams with different geometries.

Discrete normal (x-x) stress values from center nodes in the integration area were multiplied by the associated y-z areas to obtain the transverse (x-x) force (Figure 8-32). Total transverse tensile force was taken as the sum of all element tensile forces. Compressive forces (when they occurred) were ignored in calculations of the total transverse force. I.e. total tensile force is equal to the gross tension and was not reduced by compressive forces. This approach was taken because it was assumed that transverse compressive forces would be supported by concrete, and that confinement reinforcement would be designed to carry tensile forces. The magnitude of tension

force in the reinforcement was assumed unaffected by compression forces carried by concrete.

Figure 8-33 presents the variation in transverse force as a function of the bearing pad width in the FE models. For the considered models and geometries, the transverse force was equal to 13% to 28% of the reaction force. Transverse force was smallest relative to the reaction force when the bearing pad width was approximately 60% of the flange width. This ratio of bearing-to-flange width also corresponded to the change in behavior between bursting and flexural behavior as discussed in previous sections. For bearing pad-to-flange width ratios greater than 0.5, the FIB with bearing plate model had the lowest normalized transverse force. This is attributed to the stiffness of the bearing plate which attracted transverse force when the bearing pad width approached the flange width. Transverse force in the bearing plate was not included in the data presented in Figure 8-33.

FDOT design standards (FDOT 2009c) for FIB girders result in a bearing pad-to-flange width ratio of 0.84. For this ratio, the calculated transverse tensile force in the bottom flange was equal to approximately 25% of the reaction force in the model without a plate, and approximately 17% of the reaction force in the model with a plate. These relationships reflect linear-elastic behavior and would likely change after cracks form in the bottom flange.

Parametric Study Conclusions

Linear-elastic FE models were used to evaluate the effects of applied load on I-beam and rectangular shaped end regions. Variables in the models included bearing pad width, bearing pad stiffness, cross-section shape, and the presence of embedded steel bearing plates. The following conclusions are based on results of the evaluations:

- The location of maximum transverse strain always occurs at the end of the beam regardless of bearing conditions or cross-section.
- Due to Saint Venant's principle, changes to the bearing conditions have little effect beyond those portions of the beam nearest to the bearing.
- For the range of stiffness values reported for neoprene bearing pads, variations in pad shear stiffness have negligible effect on the transverse strain in the end region. However, variations in pad axial stiffness can change the transverse strain by +/- 3%.
- Depending on the width of the bearing pad, two types of strain distributions (behaviors) occur in the end region I-girders. A behavior denoted as 'bursting' occurs when the bearing pad width is narrow, and the transverse strain is distributed in a bottle-shaped manner. However, 'flexural' behavior occurs when the pad width is large, and transverse strain is dominated by flexural strains in the flange.
- When 'flexural' behavior occurs, the transverse strain increases as the bearing pad width increases.
- When 'bursting' behavior occurs, the transverse strain increases as the bearing pad width decreases.
- The transition between 'bursting' and 'flexural' behavior occurs when the bearing pad width is approximately equal to three times the web width. This pad width also corresponds to the optimal width for minimizing transverse tensile strain.
- The magnitude of transverse strains in rectangular sections are only 14% to 38% of the transverse strains in similarly dimensioned I-shaped flanged sections. This reduction in transverse strain is one of the benefits of using end blocks on girders with I-shaped sections.
- When the bearing pad width is less than the web width (as in the rectangular models), the transverse strains increase as pad width decreases.
- Steel bearing plates reduce the magnitude of transverse strain in the concrete nearest to the plate location. Bearing plates have greatest effect when the bottom flange is acting in the 'flexural' mode.
- Transverse force in the bottom flange above the bearing pad and due to applied load is minimized when the bearing pad width is approximately equal to 60% of the flange width.
- For typical FIB girders and bearing conditions, transverse force in the bottom flange above the bearing pad due to applied load can be estimated by multiplying the reaction force by 25%.

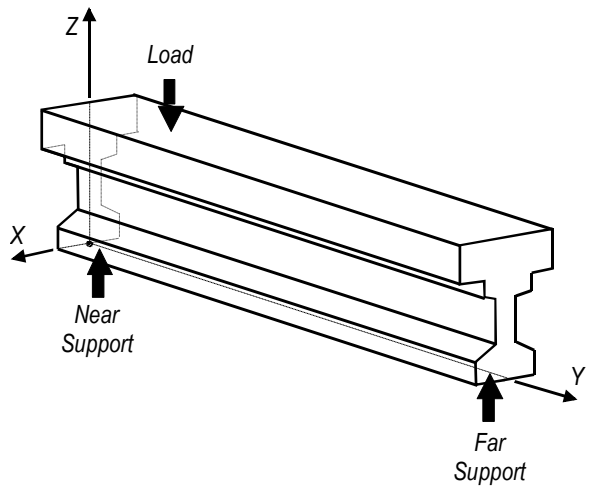


Figure 8-1. Coordinate system relative to load and supports

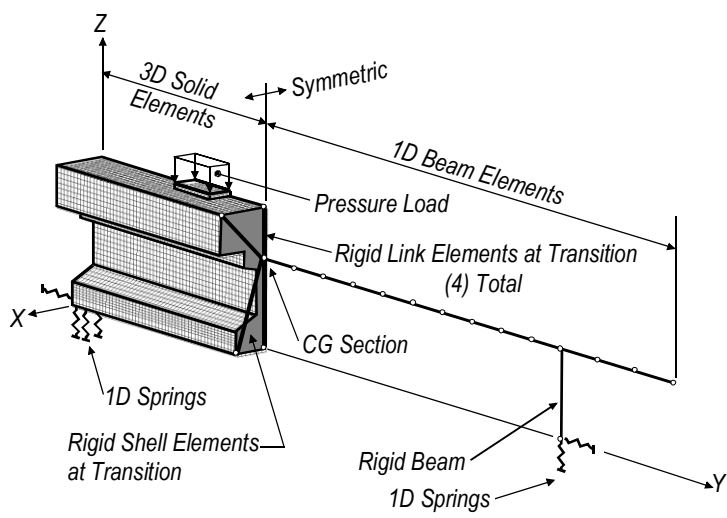


Figure 8-2. FE Model Configuration

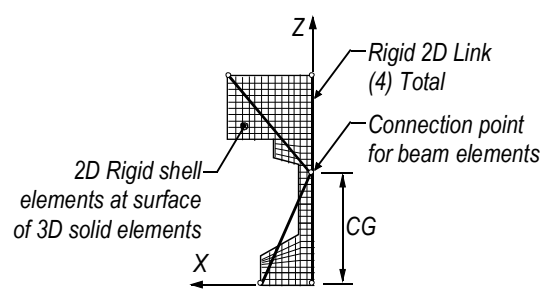


Figure 8-3. Rigid shell and link elements

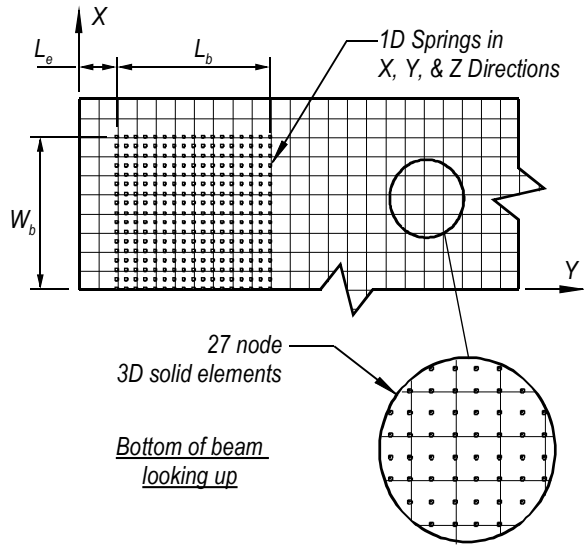


Figure 8-4. Bearing Pad

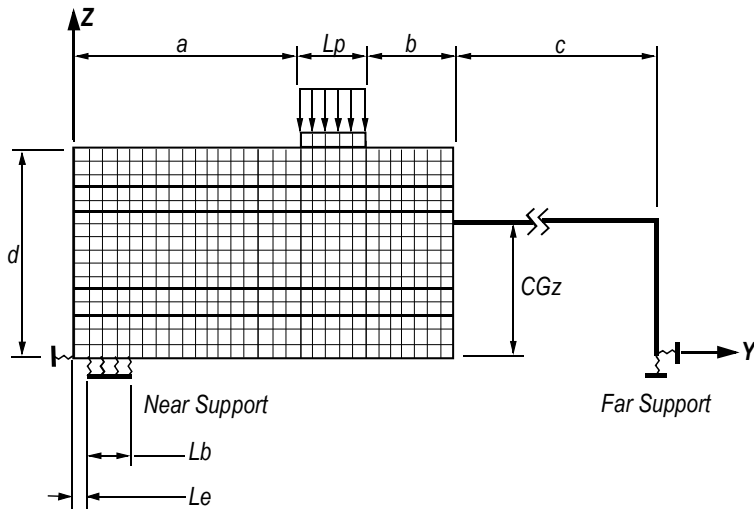


Figure 8-5. End Region Dimensions

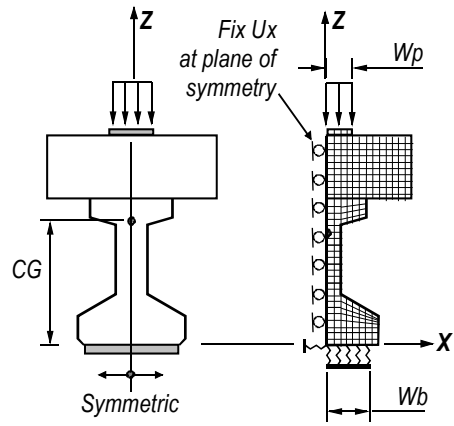


Figure 8-6. FE Model Symmetry

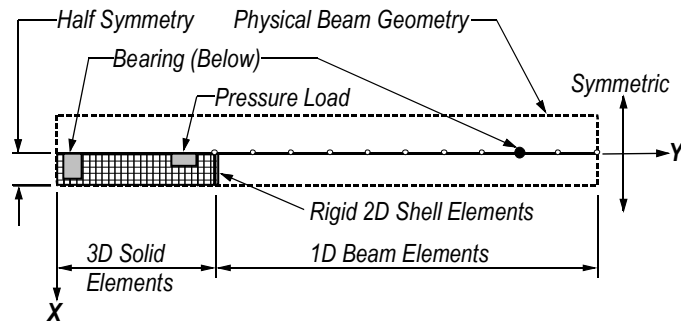


Figure 8-7. FE Model Top View

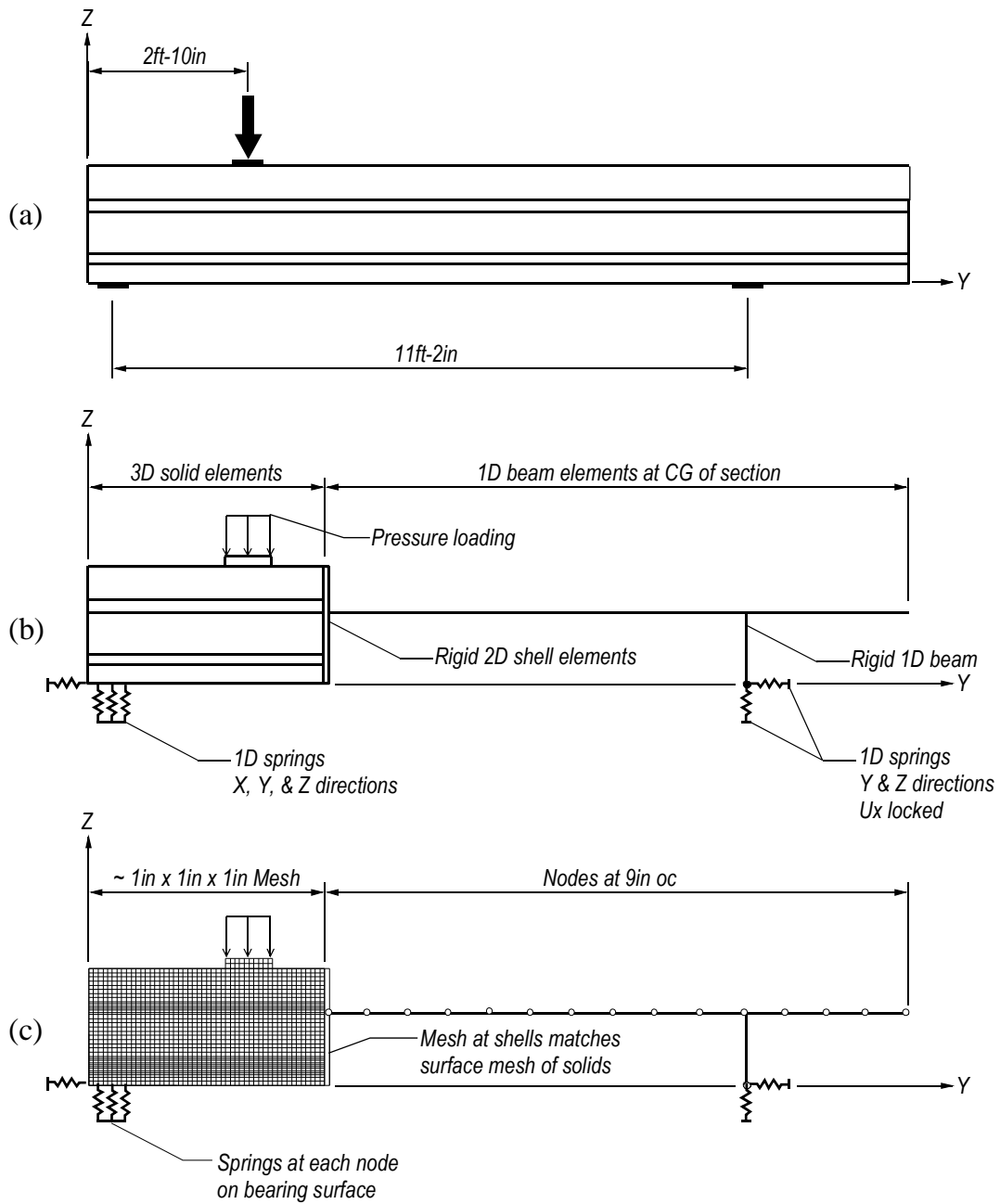


Figure 8-8. Comparison of small beam test set-up, FE model details, and FE mesh

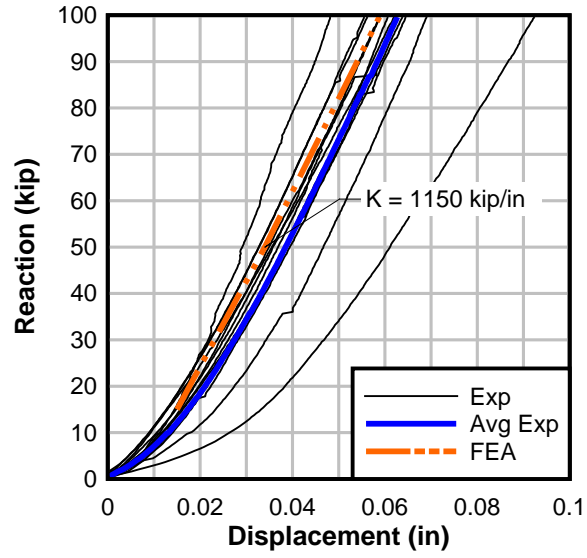


Figure 8-9. Bearing pad axial stiffness

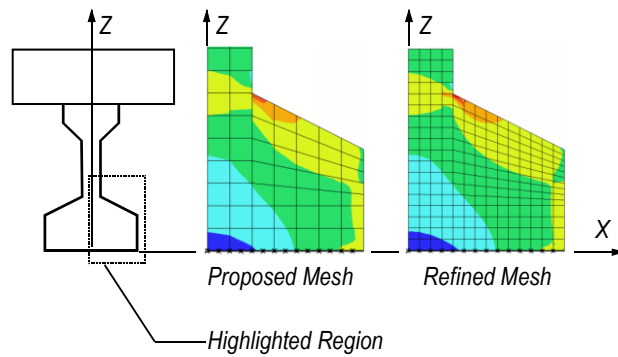


Figure 8-10. Transverse strain (x-x) at end of beam for proposed and refined mesh

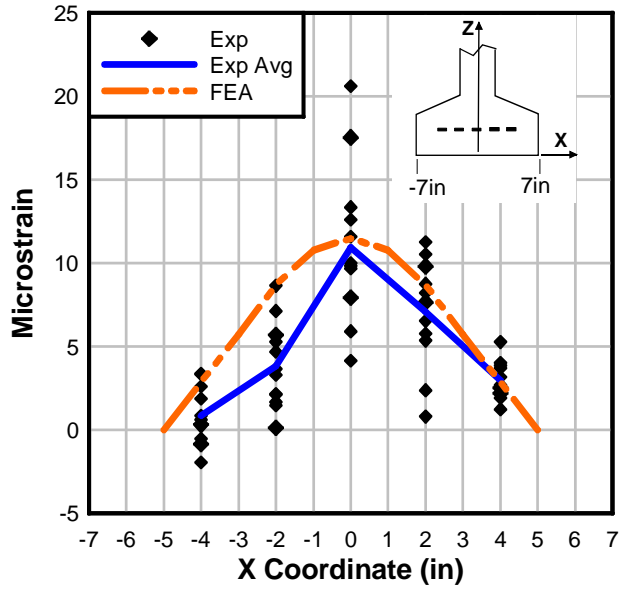


Figure 8-11. Small beam transverse (x-x) strain profile (V=15kip)

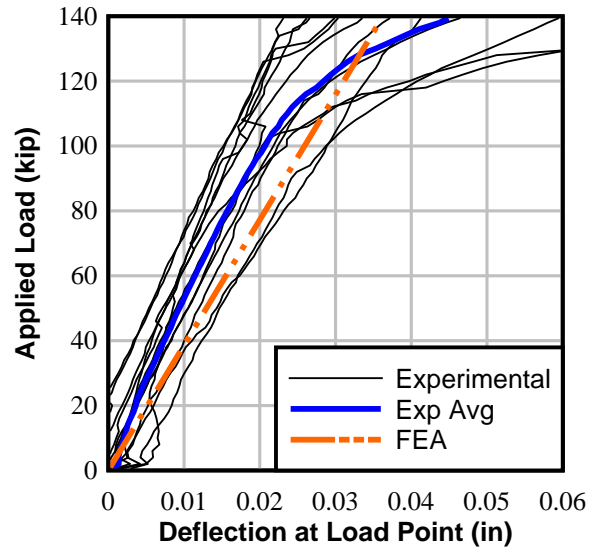


Figure 8-12. Small beam load vs. deflection at load point

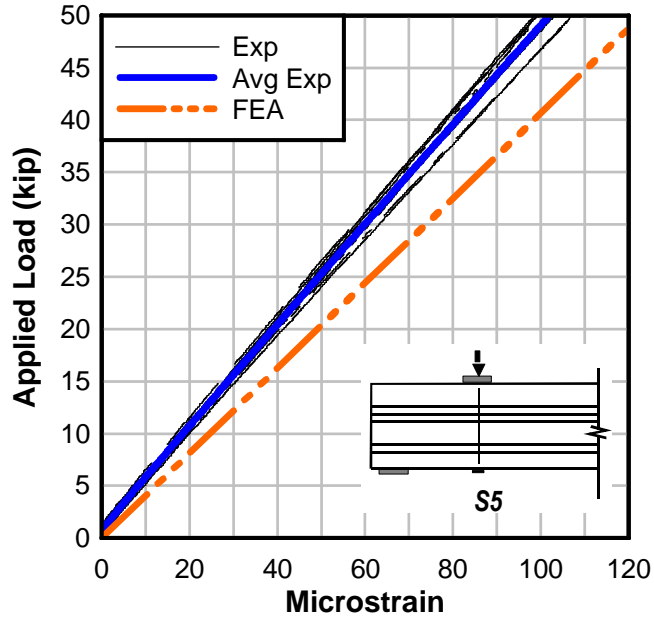


Figure 8-13. Small beam load vs. strain S5 (y-y)

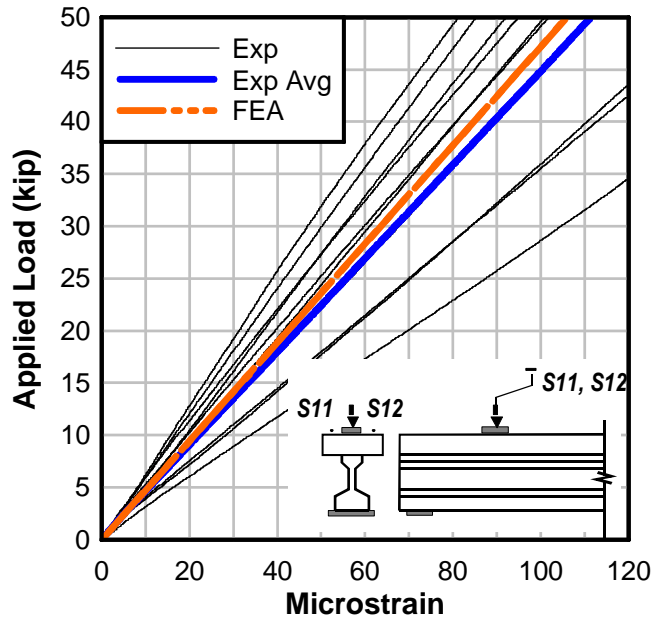


Figure 8-14. Small beam load vs. average of strain S11 and S12 (y-y)

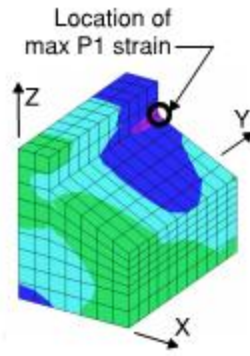


Figure 8-15. Maximum principal tensile (P1) strain location

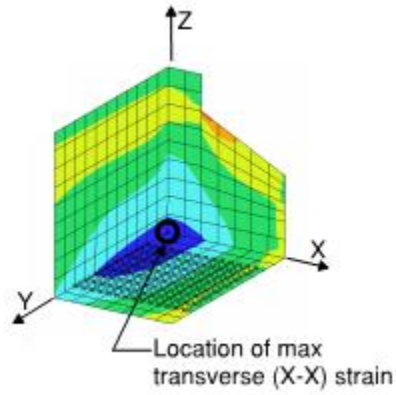


Figure 8-16. Sensitivity study maximum transverse (x-x) strain

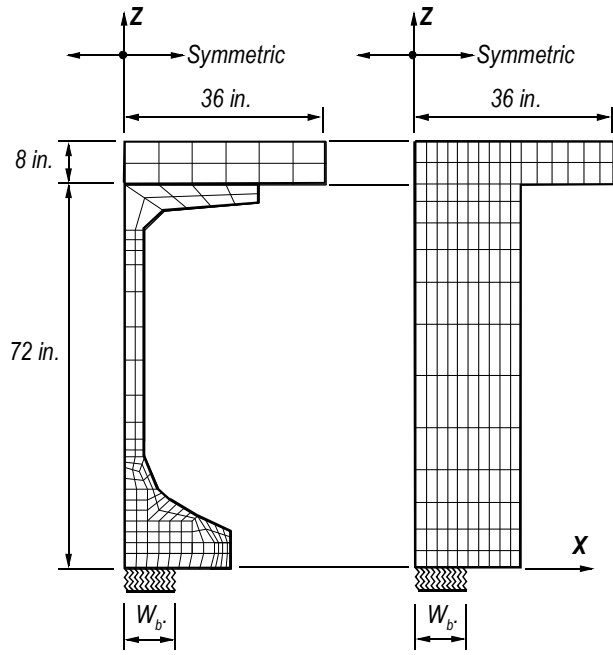


Figure 8-17. FIB and rectangular section FE models

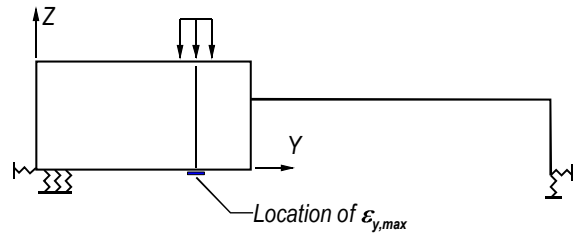


Figure 8-18. Location of maximum flexural strain (normalizing strain)

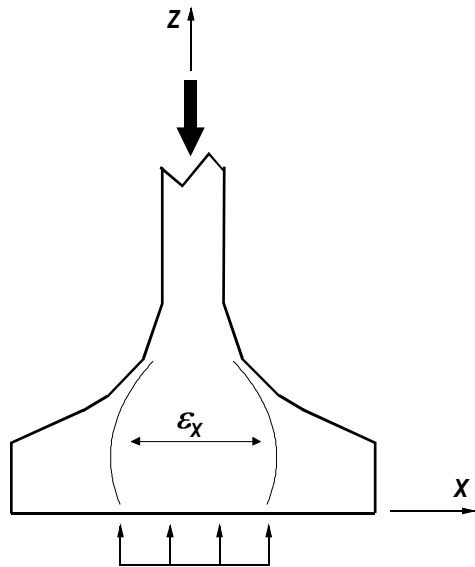


Figure 8-19. Bursting behavior

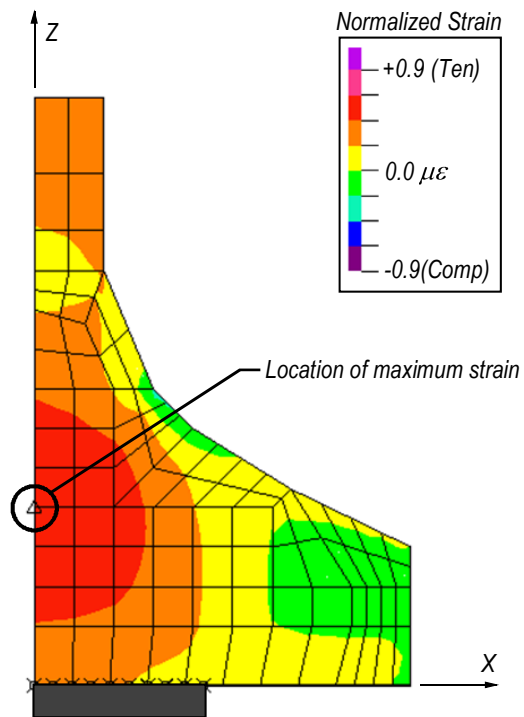


Figure 8-20. Normalized transverse (x-x) strain at end of FIB-8

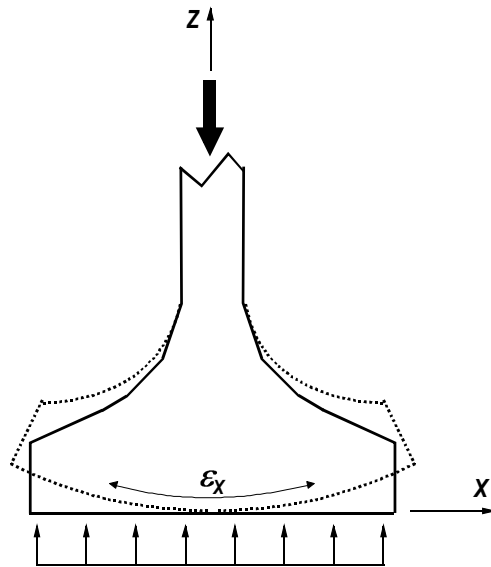


Figure 8-21. Flexural behavior

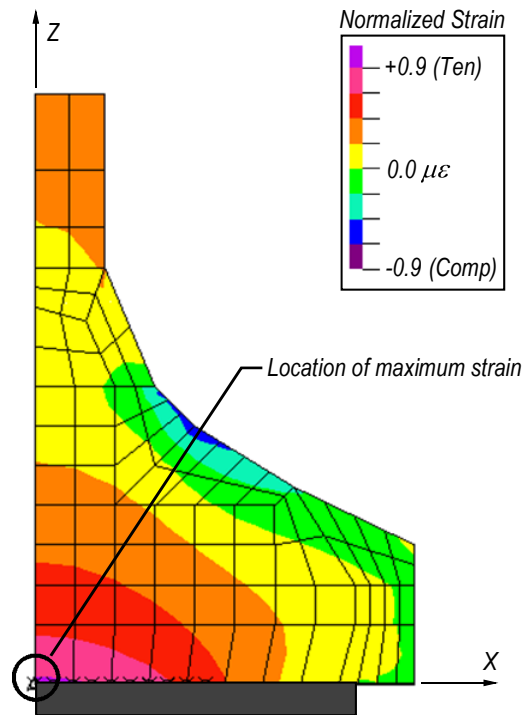


Figure 8-22. Normalized transverse (x-x) strain at end of FIB-16

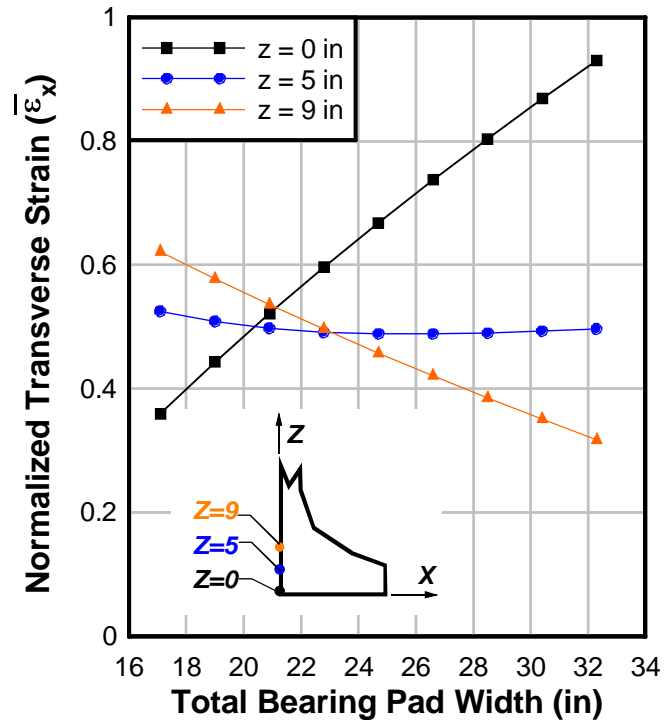


Figure 8-23. Normalized transverse (x-x) strain vs. bearing pad width

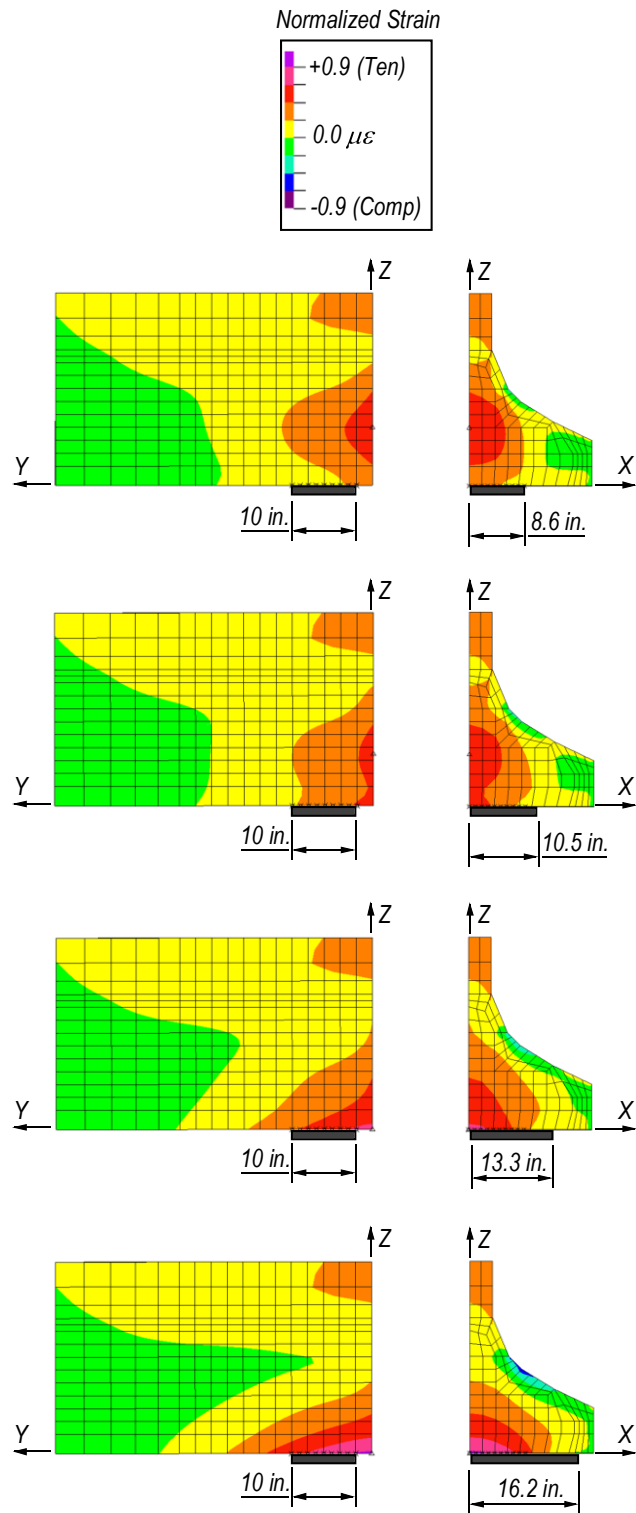


Figure 8-24. Normalized transverse (x-x) strain vs. bearing pad width, FIB

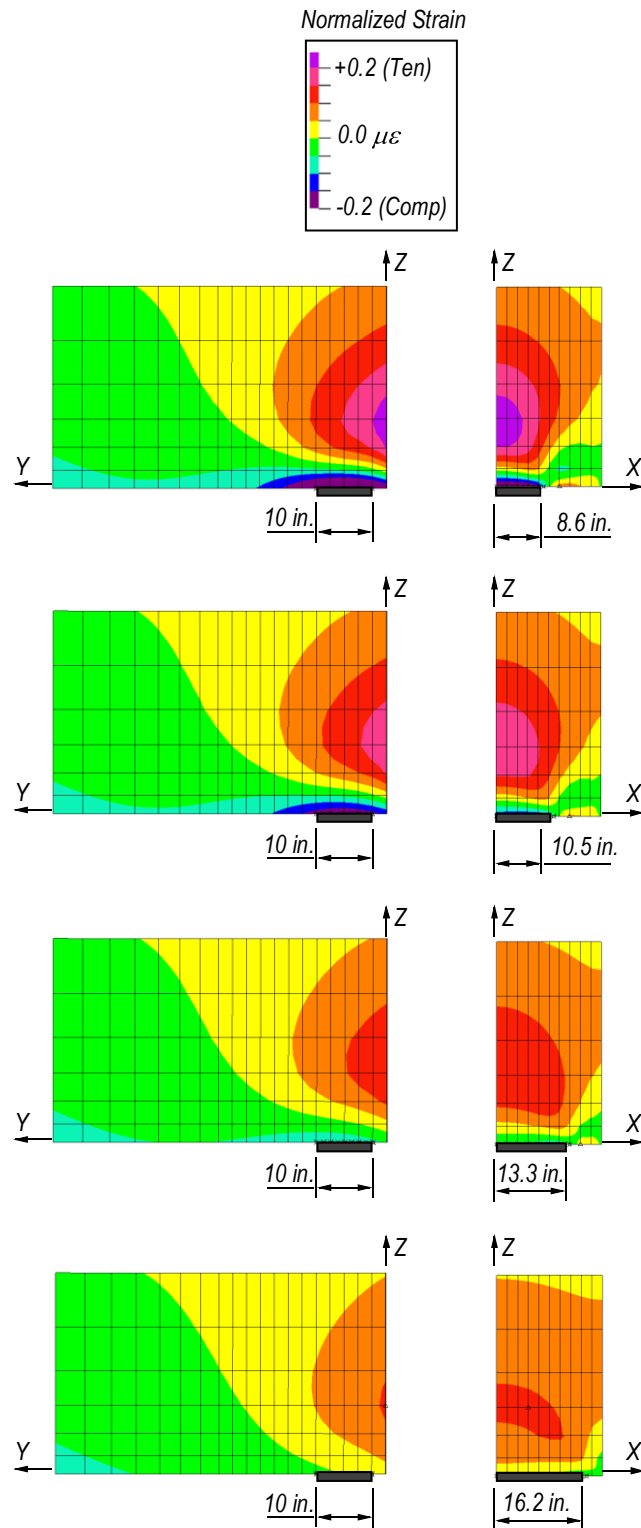


Figure 8-25. Normalized transverse (x-x) strain vs. bearing pad width, Rectangular Section

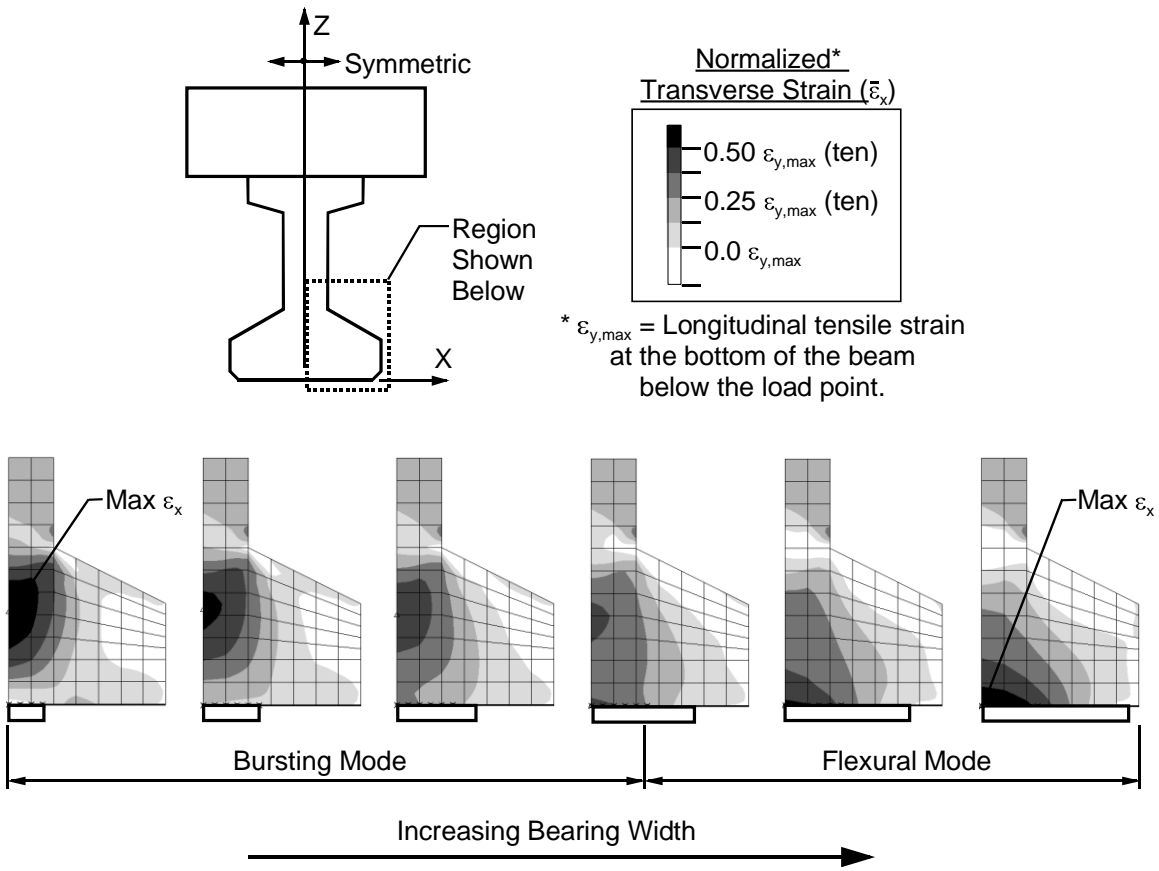


Figure 8-26. Normalized transverse (x-x) strain vs. bearing pad width, small beam

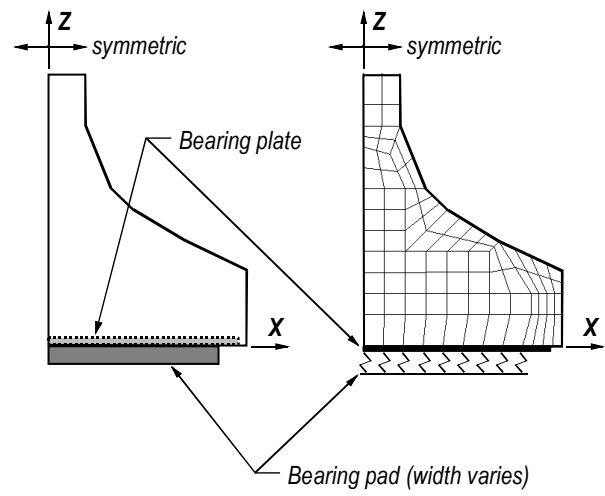
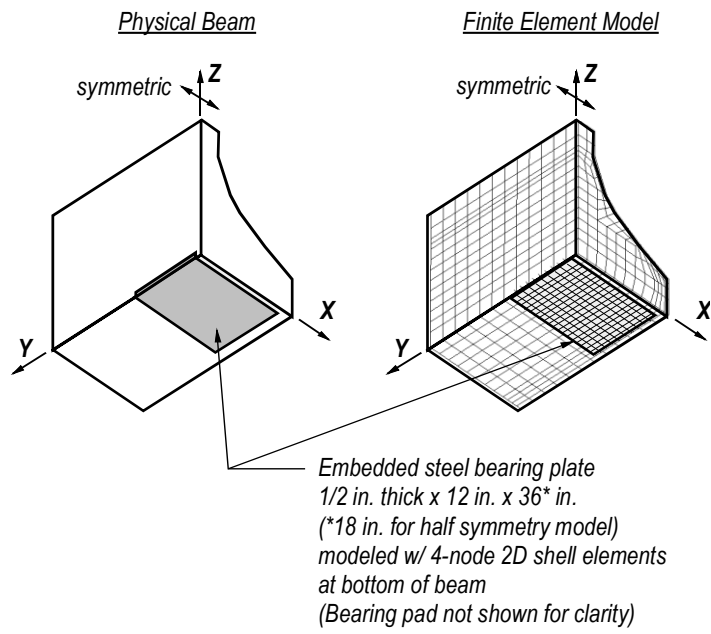


Figure 8-27. Steel bearing plate beam and model

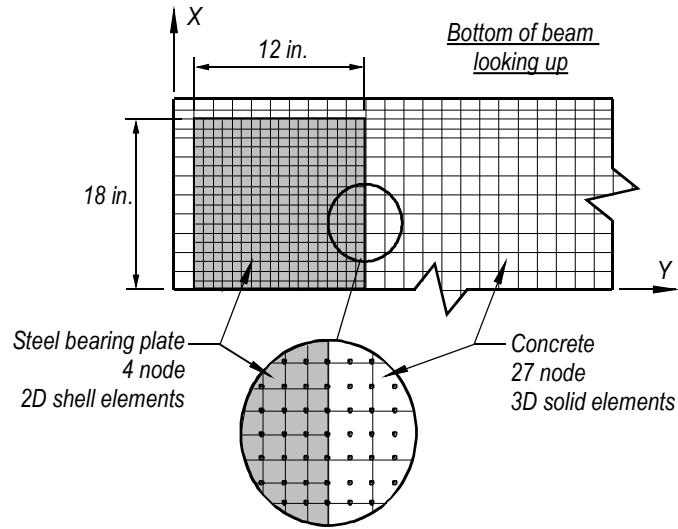


Figure 8-28. Bearing Plate Discretization

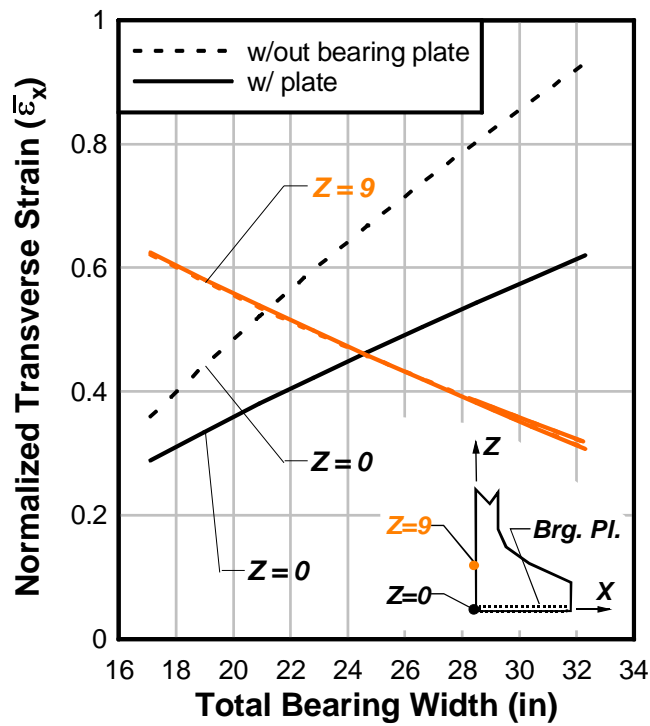


Figure 8-29. Effect of bearing plate and bearing pad width on transverse (x-x) strain

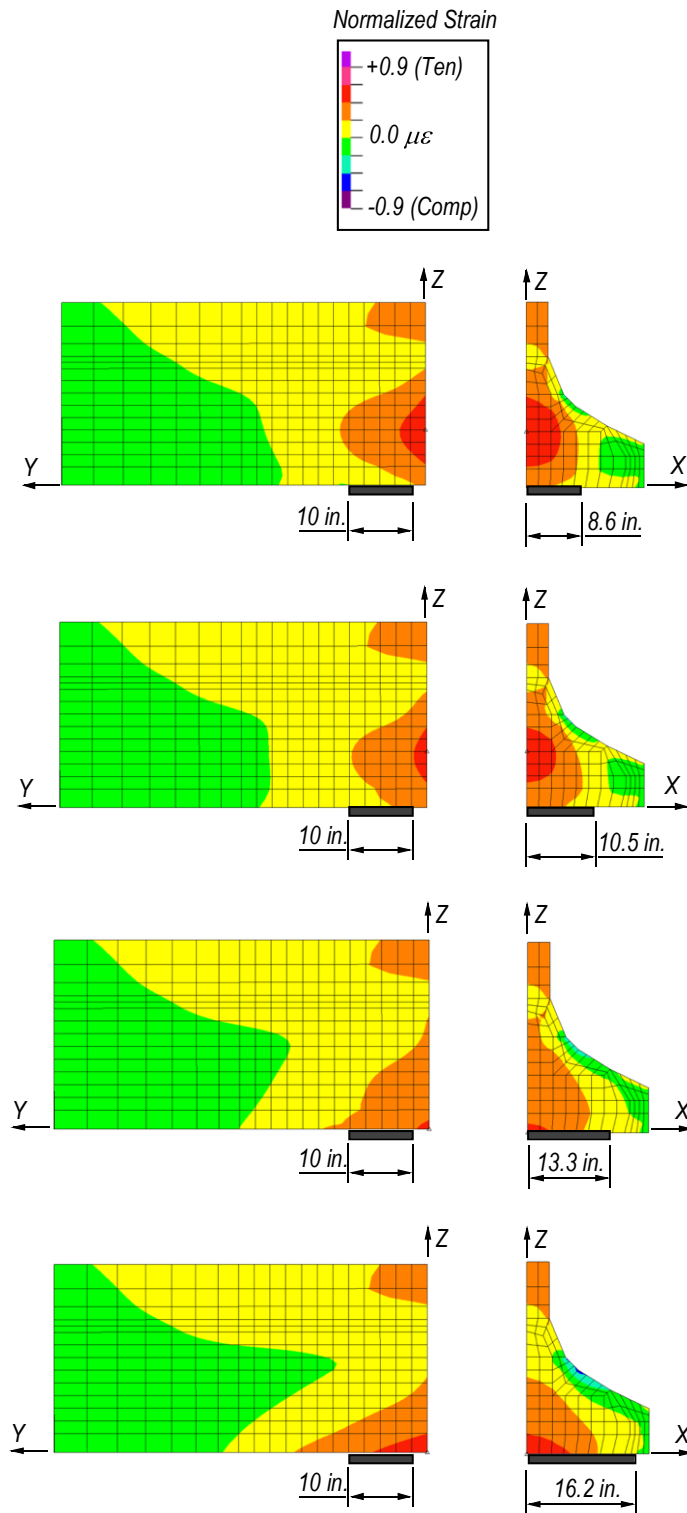


Figure 8-30. Normalized transverse (x-x) strain vs. bearing pad width, FIB Section with steel bearing plate

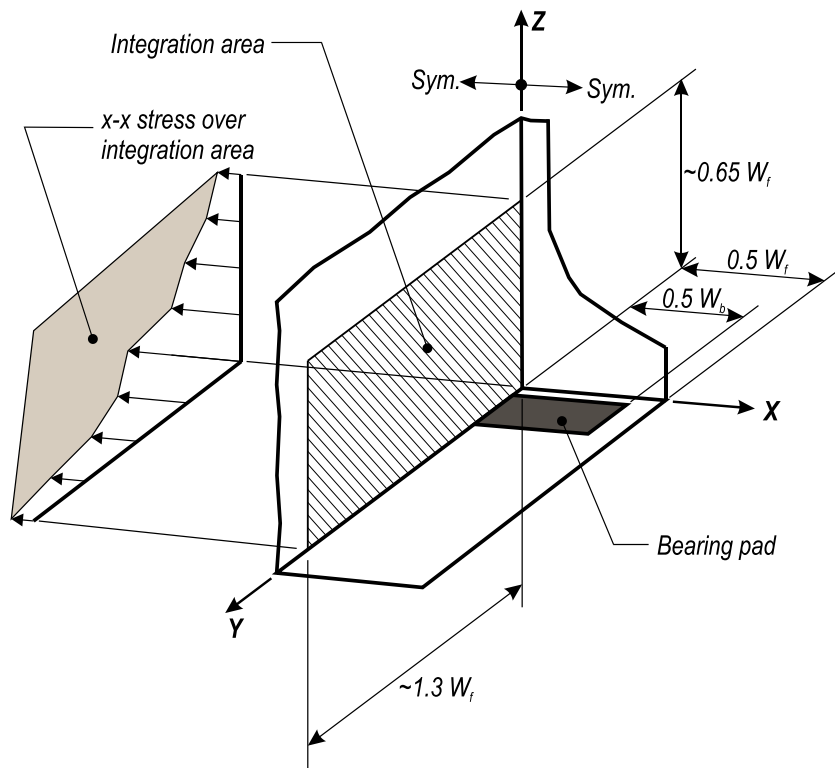


Figure 8-31. Integration area for transverse force

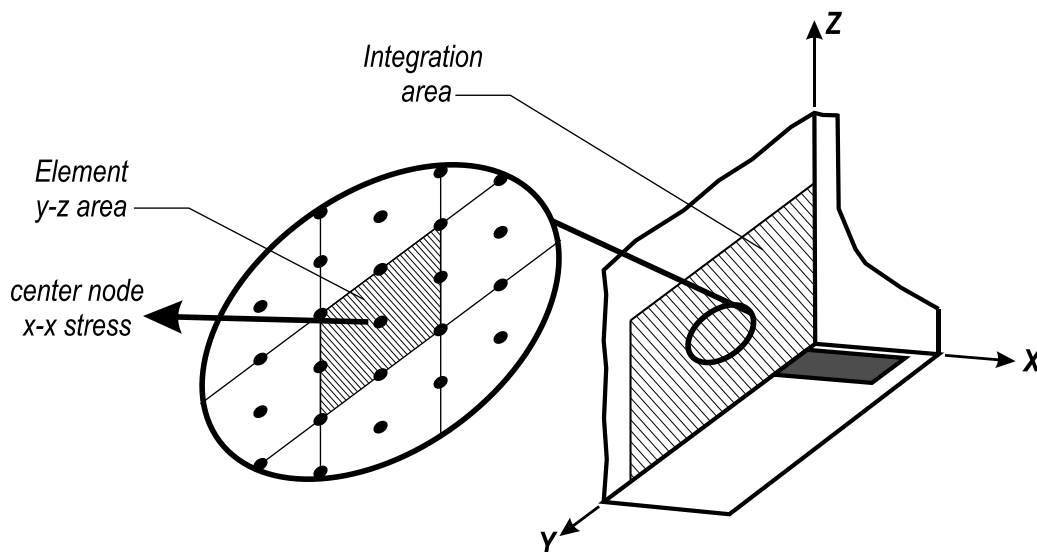


Figure 8-32. Element x-x stress and y-z area

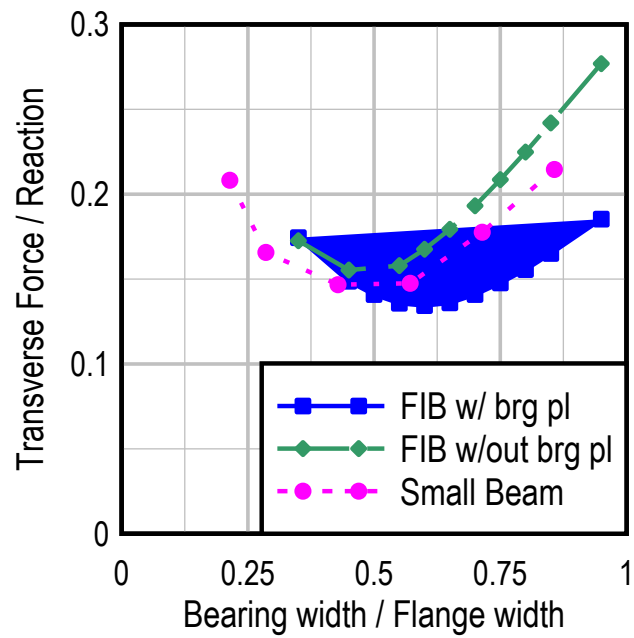


Figure 8-33. Transverse (x-x) force vs. bearing geometry

Table 8-1. Small beam FE model geometry

Dimension/Property	Value
A	29 in
B	11 in
C	90 in
D	28 in
CGz	17 in
Lp	10 in
Wp	5 in
Lb	7 in
Wb	6.5 in
Le	2 in
Near support Ka	8 kip/in
Near support Kv	0.05 kip/in
Far support Ka	1150 kip/in
Far support Kv	10 kip/in
3D solid element size	Approximately rectangular 1 in x 1 in x 1 in
2D shell element size	Approximately square 1 in x 1 in
1D beam element size	9 in

Table 8-2. Bearing stiffness sensitivity study details

Model ID	Axial stiffness (kip/in)	Shear stiffness (kip/in)	Max tensile transverse strain (e_x) for $V = 15$ kip (microstrain)	Change in max tensile transverse strain
Original	1150	10	26.64	--
x1/2 Axial stiffness	575	10	27.03	+1.5%
x2 Axial stiffness	2300	10	25.91	-2.7%
x1/2 Shear stiffness	1150	5	26.67	+0.1%
x2 Shear stiffness	1150	20	26.61	-0.1%

Table 8-3. Model details: parametric study of bearing pad width

a	120 in
b	32 in
c	1032 in
d	80 in
CGz	47.7 in
Lp	16 in
Wp	6 in
Lb	10 in
Wb	Varies

Table 8-4. Bearing pad properties

	Wb	Half Symmetry		Total	
		Ka	Kv	Ka	Kv
FIB-8, R-8	8.55 in.	2710 kip/in.	5.4 kip/in.	5420 kip/in.	10.8 kip/in.
FIB-9, R-9	9.50 in.	2995 kip/in.	6.0 kip/in.	5990 kip/in.	12.0 kip/in.
FIB-10, R-10	10.45 in.	3280 kip/in.	6.6 kip/in.	6560 kip/in.	13.2 kip/in.
FIB-11, R-11	11.40 in.	3565 kip/in.	7.2 kip/in.	7130 kip/in.	14.4 kip/in.
FIB-12, R-12	12.35 in.	3850 kip/in.	7.7 kip/in.	7700 kip/in.	15.4 kip/in.
FIB-13, R-13	13.30 in.	4135 kip/in.	8.3 kip/in.	8270 kip/in.	16.6 kip/in.
FIB-14, R-14	14.25 in.	4420 kip/in.	8.9 kip/in.	8840 kip/in.	17.8 kip/in.
FIB-15, R-15	15.20 in.	4710 kip/in.	9.4 kip/in.	9420 kip/in.	18.8 kip/in.
FIB-16, R-16	16.15 in.	4995 kip/in.	10.0 kip/in.	9990 kip/in.	20.0 kip/in.

Axial stiffness of individual springs at near support = 31.7 kip/in.

Shear stiffness of individual springs at near support = 0.0635 kip/in.

CHAPTER 9 ANALYTICAL EVALUATION OF GIRDERS DURING PRESTRESS TRANSFER

This chapter presents FE modeling that was conducted to 1) provide a better understanding of the elastic behavior of the end region during and immediately after prestress transfer, 2) quantify lateral forces in the bottom flange within the end region, and 3) evaluate the effects of variables such as transfer length and embedded steel bearing plates on end region behavior. The FE program ADINA (R&D 2009) was used to conduct the modeling. All models were linear elastic and were intended to model pre-cracked behavior. Strain gage and displacement data from construction of girders H and V were used to validate the FE model. The Hoyer effect was not considered in this chapter, but will be addressed in Chapter 11.

Model Configuration

The coordinate system defined in Chapter 4 was also used for FE models in this chapter (Figure 9-1a). The FE model configuration was designed to be computationally efficient, yet able to capture the overall behavior of girders as well as local behavior of the end region. The model's ability to capture the distribution of transverse (x-x) tensile strain in the bottom flange was of particular interest.

Conditions during and immediately after prestress transfer were considered using the model. During and after prestress transfer, the test girders were supported at each end by the stressing bed (Figure 9-1b). Transfer of prestress created negative bending moments in the test girders which were partially counteracted by self-weight. After sufficient prestress force had been transferred the self-weight was overcome and the girders camber upward. At this stage girders were supported vertically (Z-direction) at each end by the stressing bed. Girders also deformed (shortened) longitudinally due to

prestress forces. Friction forces were generated between test girders and the stressing bed and acted to resist shortening. In this chapter, friction forces were assumed to be small and were thus neglected in development of the FE model. The restraining force from uncut strands was also assumed to be negligible. These assumptions appear valid based on comparison with experimental data, as presented in the next section.

Details of the FE model are shown in Figure 9-2. The near end of the girder was modeled with 27-node 3D solid elements on a primarily rectangular mesh. Geometry of the solid elements matched the FIB-54 test girders. The extent of the solid elements was selected to fully capture the effects of the prestress and bearing forces on the end region. The remainder of the beam was modeled with 1D beam elements, with the transition from beam to solid elements made using rigid 2D shell elements and 1D rigid links. Rigid shell and link elements coupled the displacements of the 3D solid elements with the displacements and rotations of the 1D beam elements. Transitioning to beam elements reduced the computational demand while still modeling the global girder behavior and boundary conditions. Beam elements were placed at the centroid of the cross-section and were assigned cross-sectional properties equivalent to the FIB-54 test girders. A rigid link was provided to connect the beam elements to the physical location of the bearing at the bottom of the girder at the far end. The embedded steel bearing plate at the near end was modeled using shell elements.

Boundary and loading conditions of the FE model were consistent with the conditions of the physical test girders during and after prestress release. Vertical displacement was restrained along the bottom edge of the model at the near support and at the bottom of the rigid link at the far end. Prestressing forces were applied to

both ends of the model. Application of prestressing at the near end is discussed in detail later in this section. At the far end, prestressing was applied as a single point load at a height equal to the Z-centroid of the prestressing force.

The cross-section, boundary conditions and loads were symmetrical about the Y-Z plane, allowing for only half of the beam to be considered in the FE model. As such, transverse (x-x) translations were restrained at all nodes on the plane of symmetry.

Self-weight was modeled using the “mass-proportional” load feature in ADINA. This feature was employed by assigning mass density to the materials in the model, and assigning the direction and magnitude of gravity, and then allowing ADINA to calculate the body forces associated with self-weight.

The FE model was developed such that nodes in the bottom flange mesh aligned with the prestressing strand layout. Because element nodes coincided with the strand locations, the prestressing force could be applied as point loads to nodes within the transfer length (Figure 9-2). Prestressing in the FE model was based on test girders H and V which contained (39) fully bonded 0.6 in. diameter prestressing strands (Figure 9-3). Prestressing forces occurring at the centerline of the cross-section (plane of symmetry) were reduced by 50% to account for the model symmetry. Forces from the partially debonded strands were not included in the model. This simplification appears reasonable based on the validation presented in the next section. It is further justified by considering that the partially debonded strands in the test girders did not transfer loads within the area of primary interest. Individual steel strands were not explicitly included in the model.

A transfer length of 17.5 in. was used. This length was approximately half of the transfer length calculated using AASHTO LRFD provisions. A shorter length was used for multiple reasons. First, strand transfer lengths are shortest during and immediately after transfer (Barnes et al, 1998) which was the time that strain data were taken for validation. Second, the AASHTO LRFD transfer lengths are conservatively long relative to experimental data (Barnes et al., 1998). The transfer length in the FE model was denoted as T_L to distinguish it from the physical and code calculated transfer lengths.

Based on experimental data, the elastic prestress loss after all strands were released was approximately 10%. Elastic loss was indirectly considered in the FE model by reducing the magnitude of the applied prestress forces. Elastic loss was assumed to be proportional to the number of released strands. For example, a 10% elastic loss was applied to models with all strands released, and a 5% elastic loss was applied to models with half of the strands released.

The concrete modulus of elasticity for each model was set at 4700ksi, and the Poisson's ratio was set at 0.2. The modulus of elasticity value was chosen to match tested material properties from test girders used for validation.

The model configuration was validated by comparison with experimental data, and was then used in more general investigations of the stress and strain state in the end region. Details of the verification and validation are contained in the next section.

Model Validation and Verification

A verification study was conducted to determine that the mesh used in the proposed FE model had sufficient density to capture the end region behavior. Figure 9-4 shows the proposed mesh density and a refined mesh density, which was used for comparison. The refined mesh was twice as dense as the proposed mesh.

Principal tensile stress results from the proposed and refined models are compared in Figure 9-5. Differences between refined and proposed meshes occurred primarily in elements adjacent to the applied prestress forces. Locations away from the prestress forces had similar stress magnitudes and distributions for both meshes. Based on this comparison the proposed mesh was deemed acceptable for evaluating behavior away from the prestress forces, and the refined mesh was required for evaluations near the prestress forces.

During prestress transfer in the physical girders (H and V) used for validation, strands farthest away from the girder centerline were cut first with subsequent strand cuts made progressively closer to the centerline (Figure 3-24). Based on this release pattern, two stages were considered in the model validation. During stage 1 only the outer strands were released. During stage 2 all strands were released.

Comparisons with the experimental data indicate that the FE model did an adequate job of capturing both the global and local linear elastic behavior of the physical test beams. The exaggerated displaced shape calculated by the FE model is shown in Figure 9-6 for stage 2 (all strands cut). Camber at mid-span calculated by the FE model was 0.90 in., which was within 2 % of the experimentally measured camber of 7/8 in.

Cracking was not observed visually during or immediately after prestress transfer in girders H and V. Data from strain gages, however, indicate that cracking may have occurred in the physical girders as the prestressing strands were being cut. As shown in Figure 9-7 the magnitude of tensile strain reported by the gages exceeded the expected concrete rupture strain of 132 microstrain. The expected rupture strain was

derived from empirical relationships for elastic modulus and rupture strain in ACI 318 (2011). Based on the location and magnitude of the tensile strains calculated by the FE model, it is not surprising that strain gages reported strains greater than the expected cracking strain. This result suggests that the FE model captured the behavior of the physical girders at both stages of prestress transfer.

With the exception of the locations presented in Figure 9-7, the linear-elastic FE model calculated strain values at most locations were below the experimental rupture strain. Experimental data from most strain gages also demonstrated linear-elastic behavior. Data from these gages were used to validate the linear-elastic strains calculated by the FE model.

Transverse (x-x) strain was of particular interest because transverse concrete behavior is coupled with confinement reinforcement behavior. Strain data from gages embedded in the physical girders are presented in Figure 9-8 along with strain data from the FE model. As demonstrated in the figure, the FE model was in good agreement with the experimental data throughout the end region and at both stages. Gages located at $Y = 2$ in. were near the cracking that occurred prior to stage 1, hence the variability in those data points.

Longitudinal (y-y) strains at the edge of the bottom flange are compared in Figure 9-9. Strains predicted by the FE model were within the scatter of the strain data at stages 1 and 2. The good agreement between the FE model and the longitudinal experimental data suggest that the transfer length used in the model (17.5 in.) was consistent with the transfer length in the physical girders.

Figure 9-10 compares the vertical (z-z) strain from the FE model and the test girders. Trends and magnitudes were consistent between FE model and experimental data. The largest vertical strains occurred at the end of the girder ($y = 0$ in.) Vertical strains were larger during stage 2 than stage 1.

Strain and displacement data from the FE model were in good agreement with experimental data. The occurrence and location of cracking in the experimental girders were consistent with the locations of maximum tensile strains calculated by the FE model. It was concluded that the model accurately captured the global and local behavior of the physical girders at multiple stages of prestress transfer and that the model was adequate for more general parametric studies.

Transverse Force Quantification

Transverse tension forces in the bottom flange at the near support were of interest because they are resisted by confinement reinforcement in the event that the concrete cracks. This section describes the procedure used to quantify the transverse (x-x) force from the validated FE model.

Transverse force was calculated by integrating transverse stress over the area shown in Figure 9-11. This is the same area that was used previously for investigating the effects of bearing pad width (Figure 8-32). Boundaries of the integration area were selected to capture those portions of the girder end subjected to steep stress gradients due to prestressing. Boundaries were also selected to include portions of the bottom flange where confinement reinforcement is placed to carry transverse tension. Boundaries of the integration area were defined as a function of bottom flange width (W_f) so that similar integrations could be performed on girders with varied cross-sections.

Discrete x-x stress values from center nodes in the integration area were multiplied by the associated y-z areas to obtain transverse forces (Figure 9-12). The total transverse tensile force was calculated as the sum of all element tensile forces. Lateral force in the steel bearing plate was calculated in a similar manner. Compressive forces (when they occurred) were ignored in calculations of transverse force. I.e., transverse tensile force equals the gross tension and was not reduced by compressive forces. This approach was taken because transverse compressive forces are supported by concrete and do not typically lead to cracking of concrete or tension loading of confinement reinforcement.

Parametric Studies

Strand Release Parametric Study

Transverse (x-x) stresses and forces changed throughout prestress transfer as strands were sequentially cut. A parametric study was conducted to investigate the relationship between transverse force and the quantity of cut strands. This study used FE models of girders with FIB-54 and AASHTO Type IV cross-sections. The AASHTO girder model had the same configuration as the FIB model (Figure 9-2), with the exception of having cross-section dimensions of an AASHTO Type IV girder. Prestressing forces were applied as point loads over a transfer length of 17.5 in. Steel bearing plates were not included.

Elastic prestress losses were considered in the models. Losses were assumed to vary linearly from 0% when no strands were released to 10% when all strands were released. This magnitude of elastic loss was consistent with experimental data from girders H and V.

Strands in the experimental FIB girders were released from outside-in and bottom-to-top (Figure 3-24). To model this process, prestressing forces were added sequentially to FE models beginning at the location of outermost strands. Figure 9-13 show the locations of prestressing forces at different phases of prestress transfer in the FIB-54 model. Transverse (x-x) stress distributions are also shown. When only outer strands were released, the tensile stresses were concentrated within 10 in. of the girder end. Tensile stresses reduced in magnitude, but occurred over a greater portion of the integration area after inner strands were released. Stresses shown in the figure were due to prestressing forces and self-weight.

The bottom flange of the AASHTO Type IV section houses fewer strands than the FIB bottom flange. To normalize this difference, the quantity of strands in both AASHTO and FIB models was designed to be approximately 50% of the maximum possible strand quantity for the given section. Strand locations in the FIB model also matched the experimental girders H and V.

The transverse tensile force at the cross section centerline was calculated at each stage of prestress release following the previously described integration procedure. Calculated forces are plotted as a function of the percentage of cut strands in Figure 9-14. The calculated forces presented in the figure were normalized by the final prestress force for each girder.

For both girders the largest transverse tensile force occurred when approximately 40% of the strands were released. This percentage corresponds to the stage when only the strands in the outer portion of the flange had been cut. Transverse force decreased as the inner strands were cut. This observation is consistent with

experimental strain data that reported the largest transverse tensile strains when the outer strands were released and a commensurate reduction in those tensile strains as the inner strands were released.

The FIB-54 model had higher ratios of transverse force to final prestress force than the AASHTO Type IV model. This is attributed to the FIB section's relatively wide and slender bottom flange. Because of the greater width, strands in the FIB flange had a greater moment arm about the cross section centerline than did strands in the AASHTO flange.

Figure 9-14 also demonstrates the problem of partially debonding inner strands and fully bonding outer strands. In this circumstance, inner strands do not transfer prestress force at the end of the girder and consequently do not reduce the transverse tensile force at the centerline. This situation occurred in the experimental program in specimens FN and FB. Flange splitting cracks formed at the end of these girders at the centerline of the cross section. A similar situation and similar cracks were observed in experimental AASHTO Type IV girders by Llanos et al. (2009).

Bearing Plate Contribution

The validated FE model was used to evaluate transverse force carried by embedded steel bearing plates due to prestressing forces. This evaluation considered the same stages of prestress transfer as were used in model validation. For stage 1 only the outer strands were released. For stage 2 all of the strands were released. The presence or absence of the steel bearing plate was also included as a variable, resulting in four unique variable combinations.

Figure 9-15 and Figure 9-16 present the transverse (x-x) stress distributions along the plane of symmetry for each of the four variations considered. Transverse force was

calculated using the previously described integration procedure. Table 9-1 lists the maximum stresses and total forces of each model variation. Calculated force in the bottom flange was approximately 67 kip at stage 1. When the steel bearing plate was present, it attracted approximately 7 kip, or 10% of the transverse force. The steel bearing plate also changed the transverse stress distribution in the concrete adjacent to the plate, but did not change the total transverse force.

Calculated transverse force during stage 2 was approximately 27 kip. When the embedded steel plate was present it attracted 3 kip, or approximately 10% of the force. This percentage is similar to stage 1. Presence of the steel plate changed the stress distribution in the concrete near the plate but it did not significantly affect the total transverse force at the end of the girder.

Transfer Length Parametric Study

This section presents results of a parametric study investigating the effect of transfer length on the magnitude of the transverse tensile force. FE models were created with transfer lengths that varied from 12.5 in. to 47.5 in. This range included lengths shorter than were observed in the experimental program as well as lengths longer than calculated using the AASHTO LRFD code.

The FIB model without a steel bearing plate was used in this study. Models considered the stage shown in Figure 9-13 when 50% of the strands were cut. This stage was selected because it corresponded to the largest transverse tensile forces.

The previously described integration procedure was used to calculate transverse tensile forces at the cross-section centerline. Transverse force at the centerline had an approximately linear relationship with the transfer length (Figure 9-17). The largest force corresponded to the shortest transfer length. Transverse tensile force decreased as the

transfer length is increased. Thus, physical girders with relatively short transfer lengths have greater transverse forces and stresses than girders with longer transfer lengths.

According to the data in Figure 9-17, a 50% reduction in transfer length affected a 50% increase in transverse tensile force. For example, reducing the transfer length 50% from 40 in. to 20 in. resulted in an approximately 50% increase of transverse force from 48 kip to 70 kip.

Transverse tensile stresses due to prestressing forces are shown in Figure 9-20 and Figure 9-18 for sections through the centerline (CL) and bottom flange (MID). Tensile stresses formed near the member ends regardless of transfer length. The y-dimension of the tensile stress area was linearly related to the transfer length used in the FE models (Figure 9-20). Phase 1 experimental girders had a transfer length near 18in. For this transfer length, the FE model calculated that transverse tensile stress at the MID section of the bottom flange had a y-dimension of approximately 11in.

Transverse stress at the MID section is plotted as a function of y-coordinate in Figure 9-21 for transfer lengths of 17.5 in. and 42.5in. Shapes of the stress distributions in the figure are representative of other bottom flange sections when only the outer strands had been cut. Transverse tensile stresses were largest near the member end, and were distribution in an approximately triangular shape.

End Stresses due to Prestress Forces

Analytical results have shown that the largest stresses from the prestressing force occur at the girder end surface (Figure 9-13). In the experimental program, flange splitting cracks were often observed at the end surface (Figure 9-22). This section presents a study of stresses at the end surface due to prestressing forces. Results from

this study will later be used in development of a model for serviceability design of bottom flanges.

The FIB model without a steel bearing plate was used to study end stresses. Self-weight was eliminated to isolate the effects of the prestressing force on the section. A transfer length of 17.5 in. was used in the models. This length was chosen because previous results demonstrated that short transfer lengths produced the largest transverse effects. The refined mesh (Figure 9-5) was used in this study because stresses near the prestress forces (strands) were used in results interpretation. Strand pattern and strand cutting sequence demonstrated in Figure 9-13 was used in this study. This strand layout and cut pattern matched girders H, V, and D from the experimental program.

Four lines at the end surface of the model were selected for evaluation (Figure 9-23.). Lines were selected based on the location of cracks observed in the test girders (Figure 9-22) and to give a representative analysis of the entire bottom flange end. A height of 15in. was used for the centerline (CL) and the web line (WEB) based on the height of flange splitting cracks in test girders. Height of the mid-flange (MID) and flange edge (EDGE) lines were limited by the flange height at those locations.

Transverse (x-x) stresses were considered along each line. This was done because tension stresses at the end of the bottom flange primarily acted in the x-direction. This was evident from the vertical orientation of cracks in the experimental girders (Figure 9-22). It was also observed in comparisons of transverse (x-x) and principal tension stresses at the end of the FE model (Figure 9-24). Transverse and

principal tension stresses were effectively the same at areas away from the prestressing forces.

Stresses along each line were calculated at each stage of prestress transfer using an outside-to-in strand cutting pattern. Stress concentrations occurred in the FE model at nodes where prestress forces were applied (Figure 9-24). In lieu of the concentrated stress values, stresses at these nodes were taken as the average stress from the adjacent nodes. This resulted in stress distributions such as that shown in Figure 9-25. Figure 9-25 shows the stress distribution at the mid-flange line for the stage when 50% of the strands had been cut. During this stage the two strands located on the mid-flange line were cut and resulted in compressive stresses near the strand locations.

The average stress along each line varied with the different stages of strand cutting as shown in Figure 9-26. The box markers on Figure 9-26 indicate the stage when strands on an individual line were cut. Average stress on a given line fell abruptly when strands along that line were cut. For example, average stress at the centerline went from 170 psi tension prior to cutting the centerline strands to 680 psi compression after the centerline strands were cut.

Average stresses are summarized in Table 9-2 for each evaluation line. Tensile stress on a given line was greatest when only the strands outboard (closer to outside of flange) of the line had been cut. Maximum tensile stresses ranged from 1.12 ksi to 0.39 ksi. The largest compressive stresses occurred after all strands had been cut. Maximum compressive stresses ranged from -0.68 ksi to 0.41 ksi. The average compressive stress after all strands had been cut was -0.57 ksi.

Transverse tensile stresses occurred at the end of each evaluation line and for a distance of approximately 10in. from the girder end. The typical integration procedure was used to calculate the transverse tension force at sections along the MID and EDGE lines. These locations were of particular interest because of their proximity to flange splitting cracks observed in the experimental girders. The maximum transverse force occurred when strands outboard of each section had been cut. Cutting of strands along the section reduced the transverse tension force by 45% at the MID section and 28% at the EDGE line.

Transverse Action due to Self-Weight

The test girders cambered upward during prestress transfer after the girder self-weight was overcome by the prestressing moment. In this condition the girders were supported vertically at the bottom edge at each end (Figure 9-1). The FIB FE model was used to evaluate the transverse stresses and forces that occurred due to the self-weight during this condition. Prestress loads in the model were removed leaving only the mass-proportional load which modeled the girder self-weight. Boundary conditions remained the same as previous models in this chapter. Because prestress loads were removed and self-weight remained, the displaced shape of the model was sagging rather than cambering.

Figure 9-27 shows the transverse (x-x) stresses at the centerline and end due to self-weight. Transverse tensile stresses were largest at the bottom of the girder near the end. Magnitude of transverse stresses due to self-weight were small relative to transverse stress due to prestressing as calculated in the previous section. This is in part because the self-weight model was based on test girders H and V which were only approximately 35% as long as typical production girders with the same cross-section.

Thus the self-weight stresses reported in Figure 9-27 were also only 35% of stresses in typical production girders.

The typical integration procedure was used to calculate a transverse force of 6.7kip at the centerline. Self-weight reaction in the half-symmetry FE model was 12.0 kip. This reaction corresponded to a full reaction of 24 kip in the physical test girders. Thus the transverse force was equal to 28% of the physical reaction. This result is similar to the relationship derived between reaction force and transverse force shown in Figure 8-33.

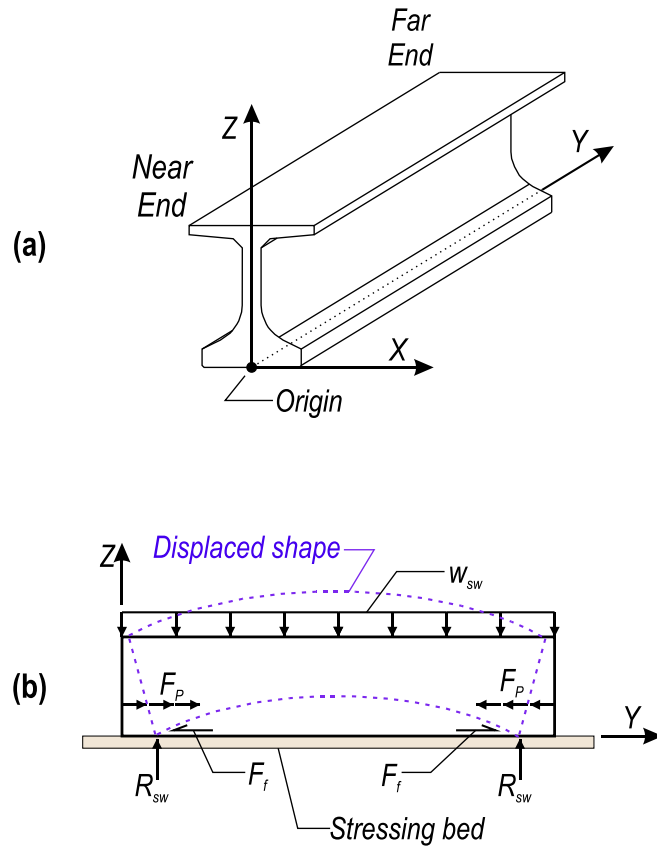
Transverse stresses at the girder end were calculated at the same four lines (Figure 9-23.) that were previously used to evaluate the effects of prestressing forces. Figure 9-28 shows stress that occurred at each line. Stresses below $Z=2\text{in.}$ are not shown because numerical errors occurred in the FE model near the boundary condition.

Maximum and average stresses at each line are summarized in Table 9-4. Average stresses in the table conservatively ignored compressive stresses below $Z=2\text{in.}$ The maximum tension stress was greatest at the centerline and was 3.4 times larger than at the line through the flange edge. The centerline section also had the largest average tension stress. At lines through the outer flange (MID and EDGE) the average stress was negligible or compressive. Average stresses at lines through the inner portion of the flange (CL and WEB) were tensile. Average tensile stresses at the CL and WEB lines were related to the reaction force by a factor of 1000. For example, the reaction force in the physical girders was 26 kip and the average tensile force on the inner lines was approximately 26 psi.

Parametric Study Summary and Conclusions

Linear-elastic finite element modeling was used to evaluate stresses and forces in the bottom flange of Florida I-girders during prestress transfer. Each stage of prestress transfer (strand cutting) was considered in the models. Stresses and forces due to girder self-weight were also evaluated. Stresses due to the Hoyer effect were not considered in this chapter. Thus the conclusions below are based only on the effects of the prestress force and girder self-weight. Conclusions assume strand cutting from outside-to-inside (Figure 3-24). The following conclusions are made based on results of the evaluations:

- For the given release sequence, the largest transverse (x-x) tensile stresses during prestress transfer occur at the centerline of a section at the girder end. Centerline tension stresses are greatest when only the strands in the outer portion of the flange have been cut. Cutting of inner strands reduces this transverse tension.
- Embedded steel bearing plates carry transverse tension during and after prestress transfer. In the linear-elastic range plates in FIB girders carry 10% of the tension force due to prestressing. The portion carried by the plates does not vary during different stages of strand cutting.
- Transverse stress and forces are inversely proportional to strand transfer length. Thus the greatest transverse effects occur in girders with the shortest transfer lengths. A 50% reduction in transfer length affects an approximately 50% increase in transverse tension.
- During prestress transfer the maximum transverse tensile stress on an arbitrary vertical line through the bottom flange occurs when only the strands outboard (closer to edge) of the line have been cut. Cutting of strands along or inboard (closer to centerline) of a line relieve tensile stresses on that line.
- Transverse stresses at the end of the bottom flange are compressive after all strands have been cut. An average compressive stress of 570 psi was calculated by the finite element models for conditions in experimental girders H and V.
- Self-weight reaction produces transverse tension forces in the bottom flange above the bearing. For Florida I-beams, the transverse tension force due to self-weight equals 28% of the reaction.



F_p = Prestress force
 F_f = Friction force
 R_{sw} = Self-weight reaction
 w_{sw} = Load due to self-weight

Figure 9-1. Coordinate system and free-body diagram of girder after prestress transfer

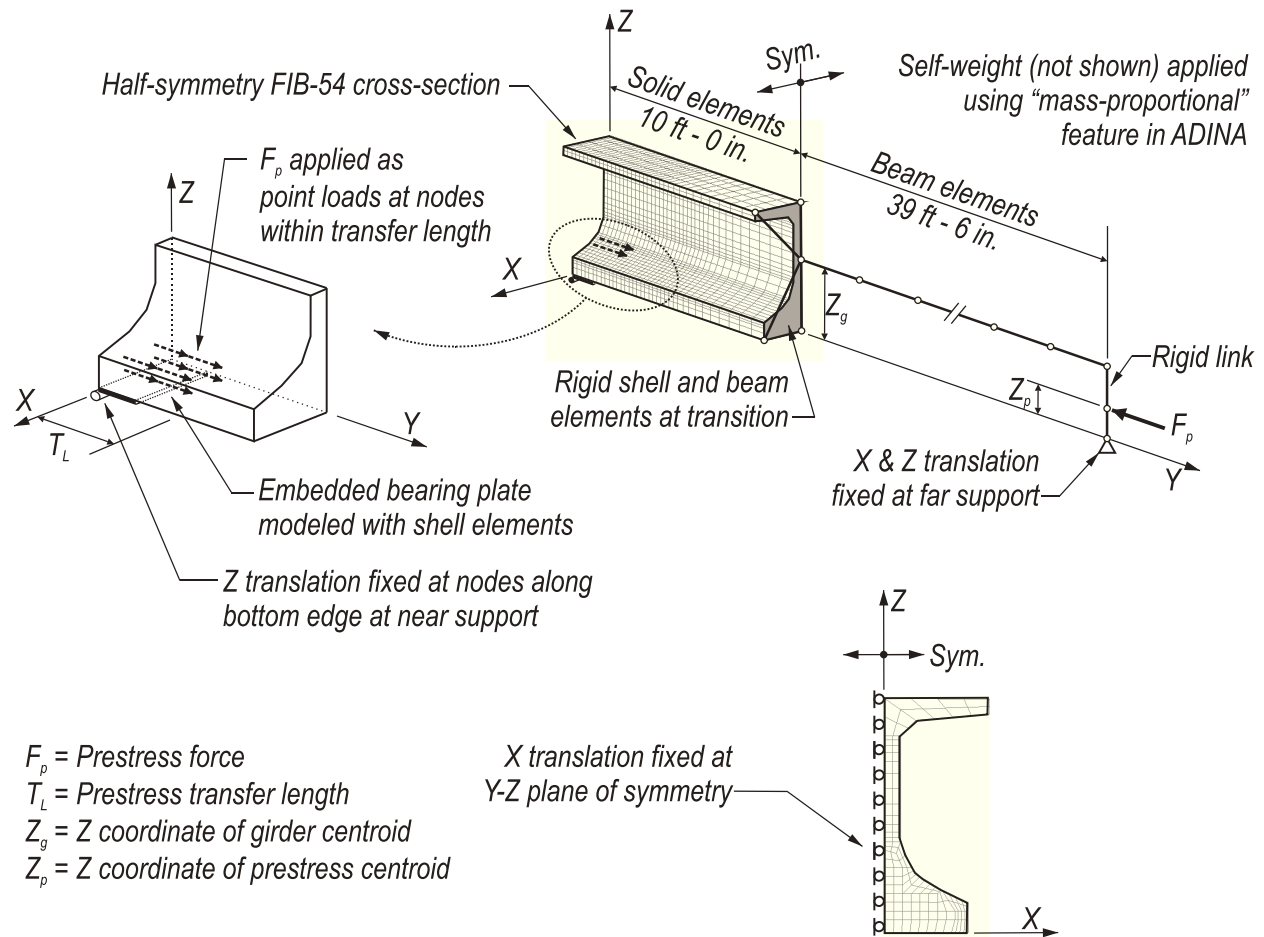


Figure 9-2. FE model details

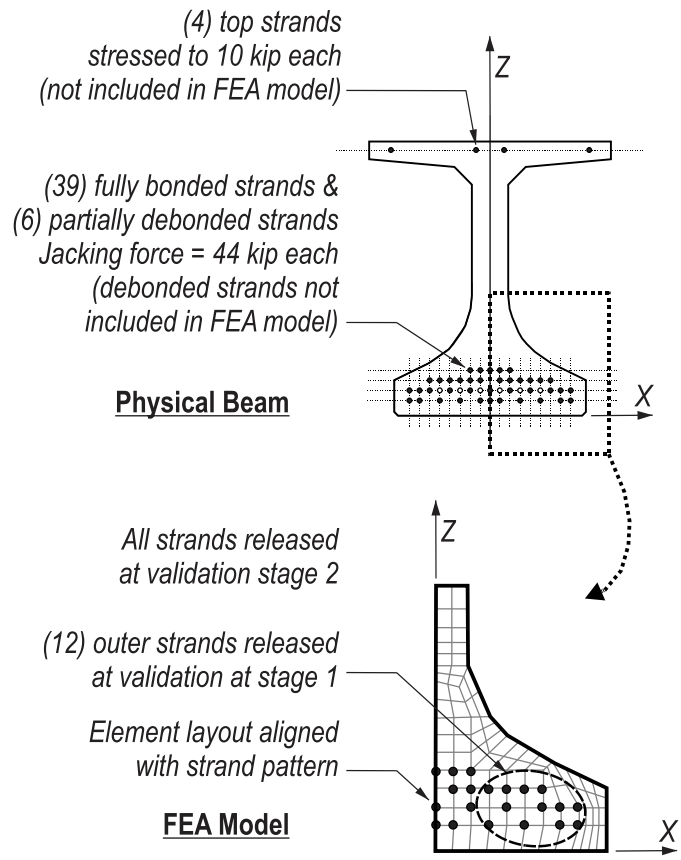


Figure 9-3. Strand layout and element mesh

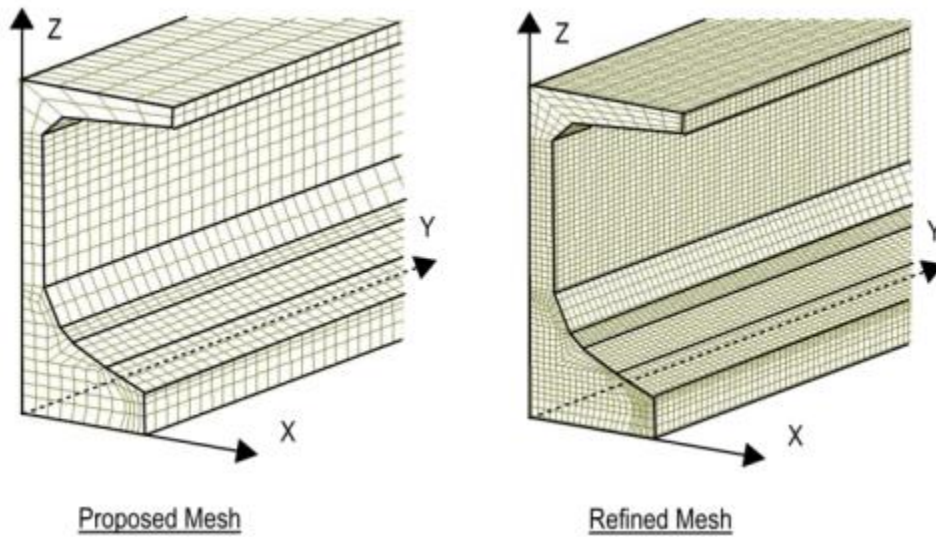


Figure 9-4. Verification study mesh densities

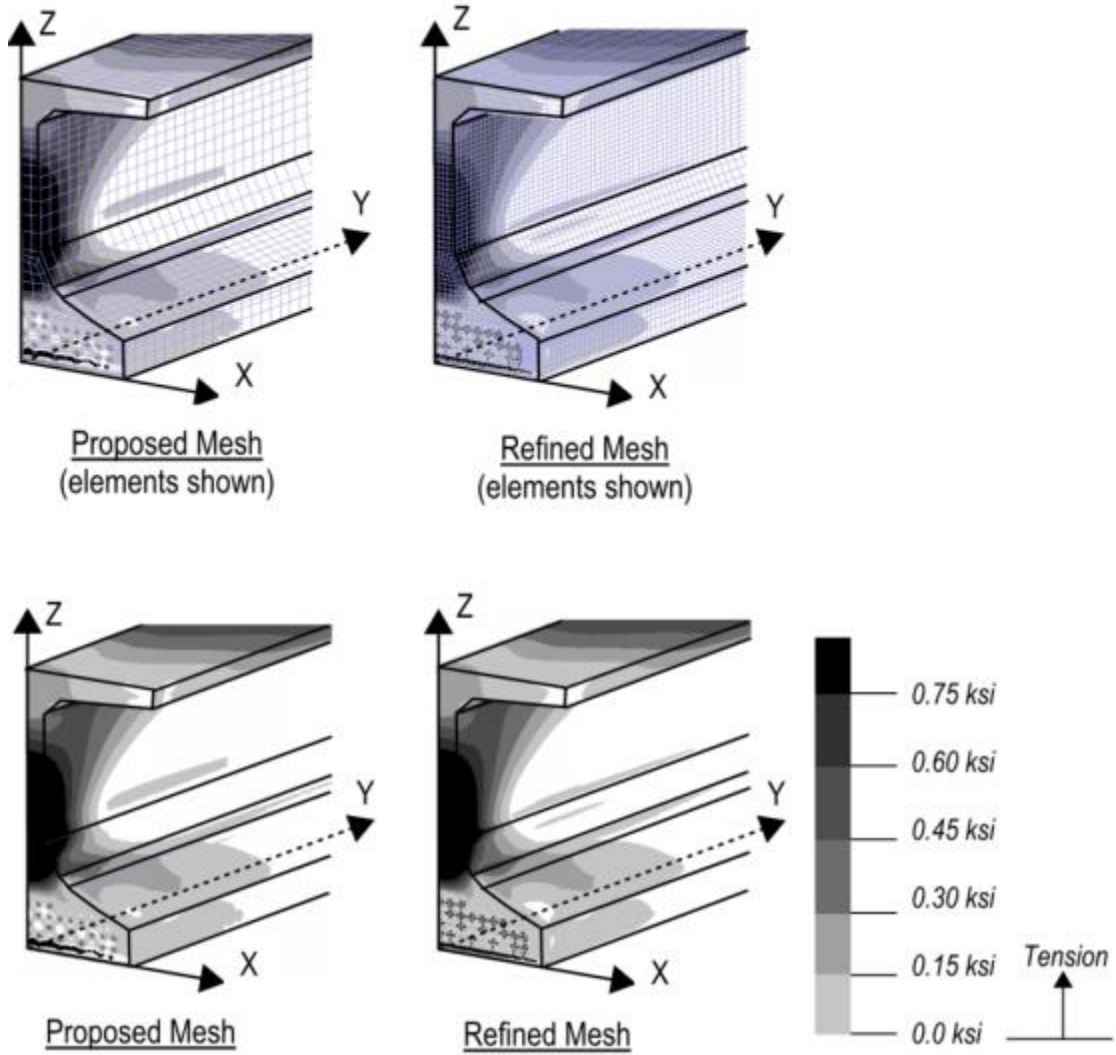


Figure 9-5. Verification study principal tensile stresses

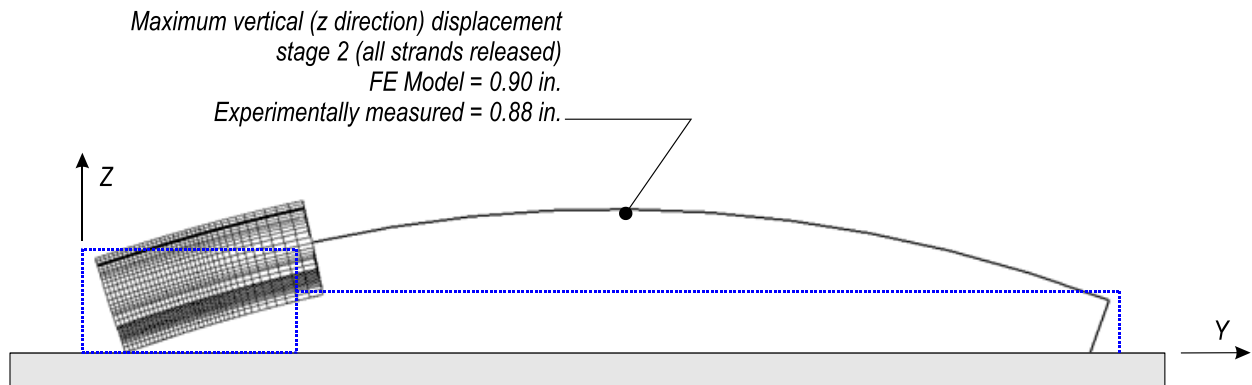


Figure 9-6. Displaced shape

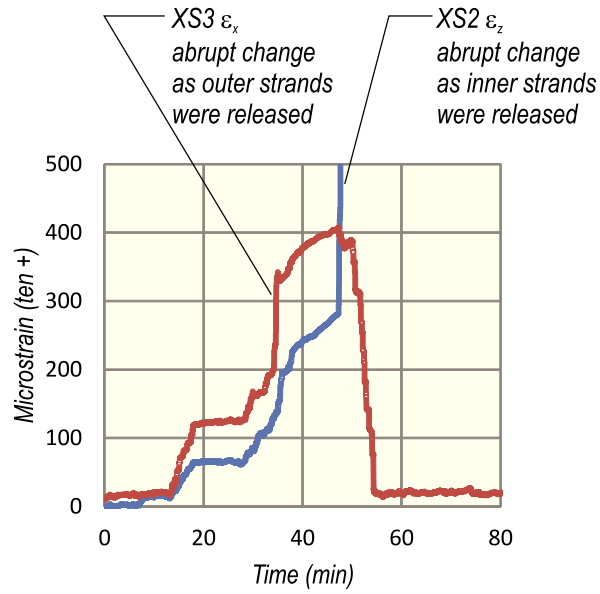
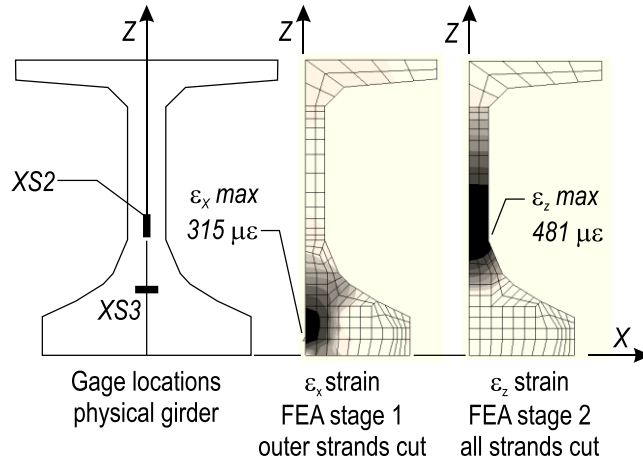


Figure 9-7. Comparison of experimental and FE model strains at cracks

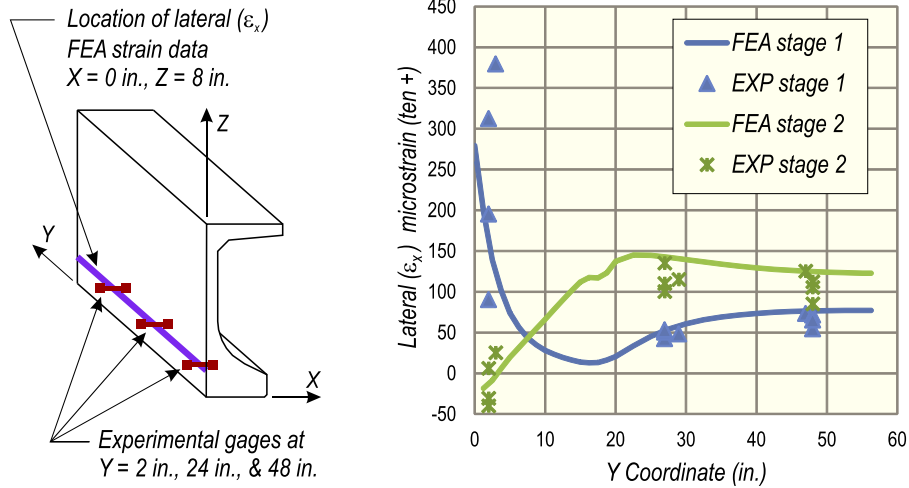


Figure 9-8. Comparison of experimental and FE model transverse (x-x) strain

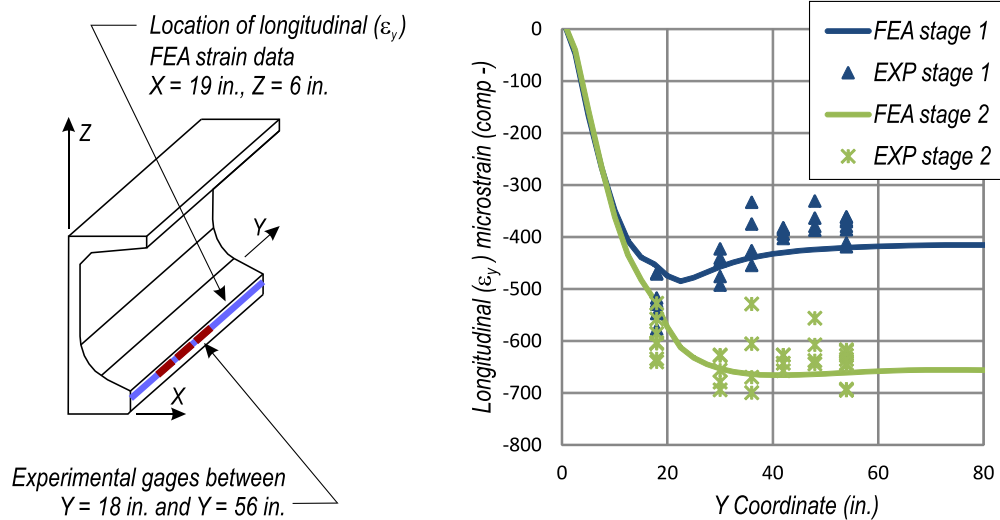


Figure 9-9. Comparison experimental and FE model longitudinal (y-y) strain

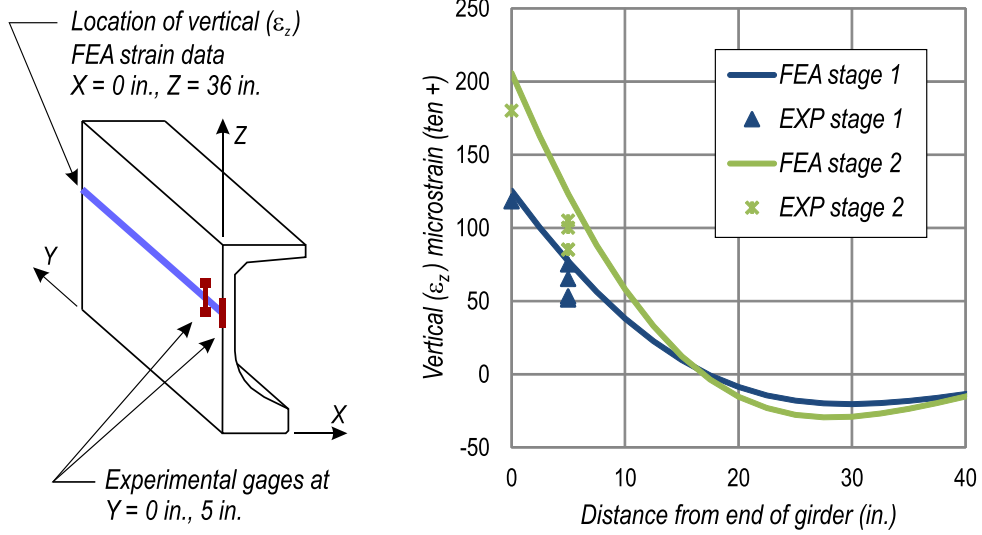


Figure 9-10. Comparison experimental and FE model vertical (z-z) strain

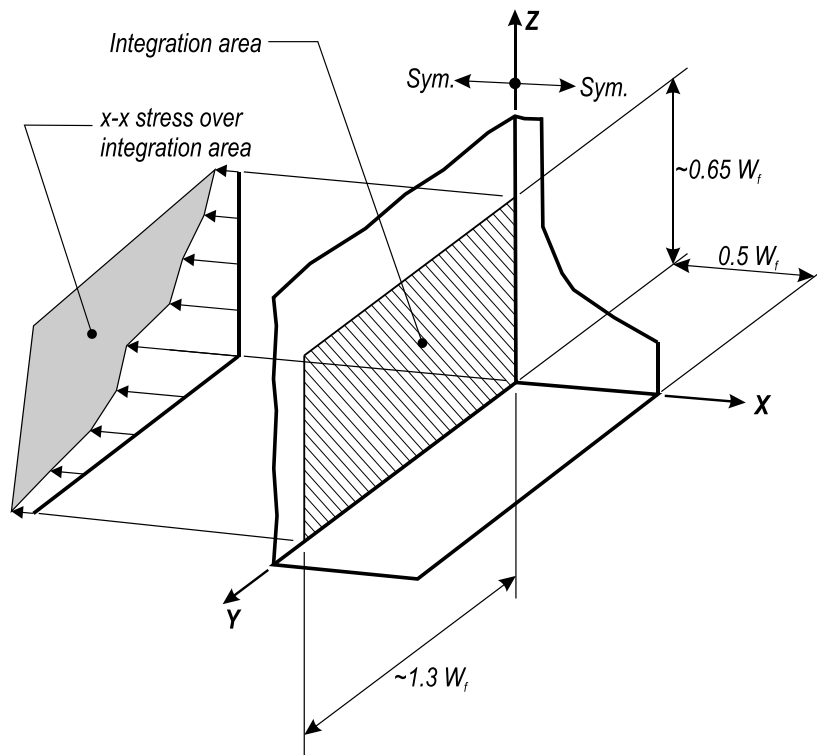


Figure 9-11. Integration area for lateral force

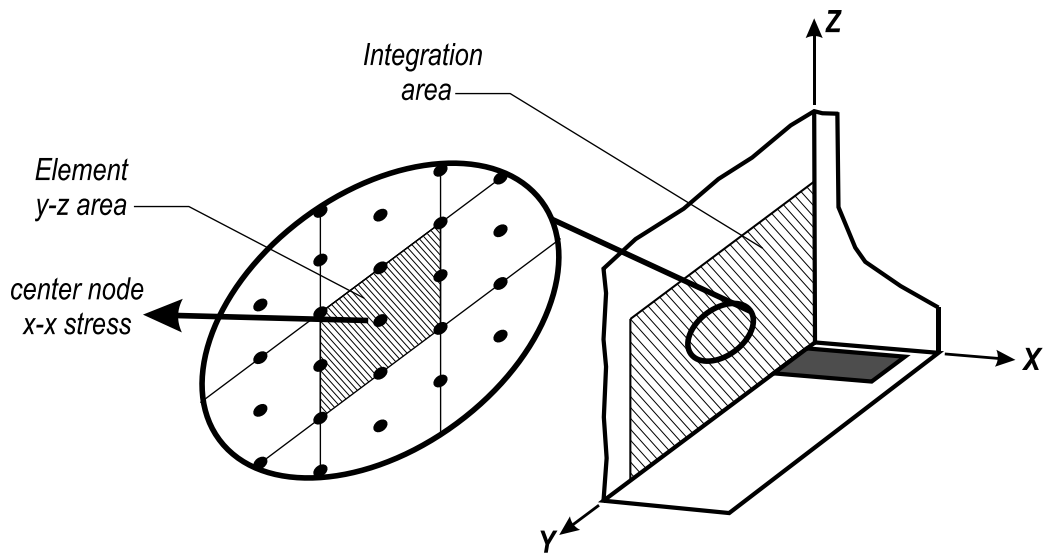


Figure 9-12. Element x-x stress and y-z area

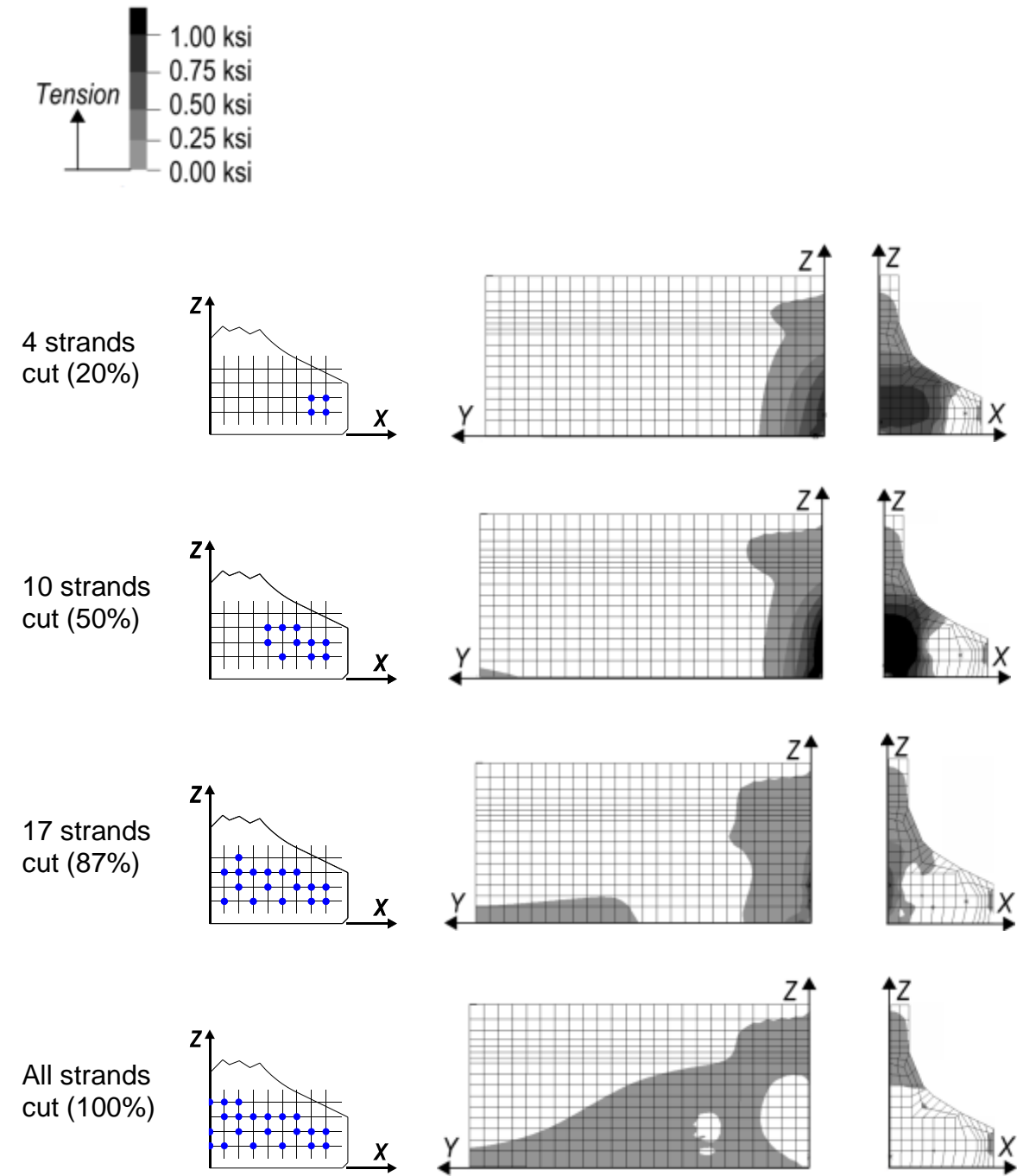


Figure 9-13. Transverse (x-x) stress at stages of prestress transfer

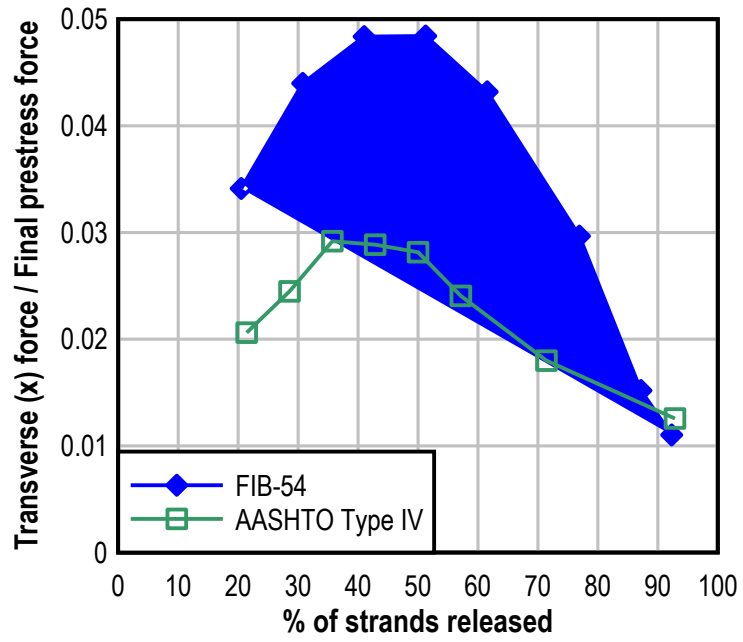
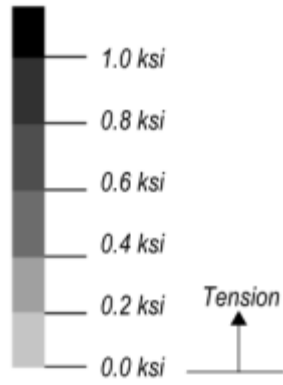
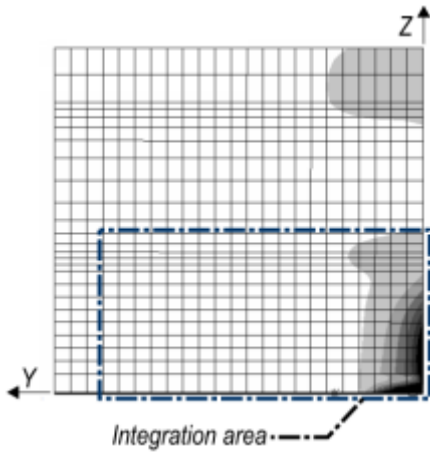


Figure 9-14. Transverse force vs. % strands released



With bearing plate



No bearing plate

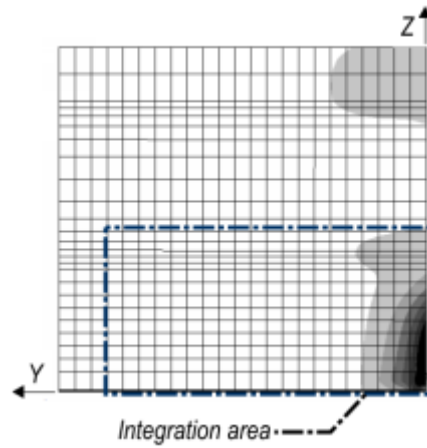
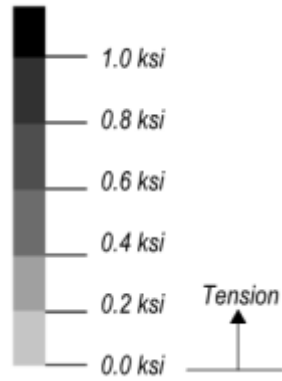
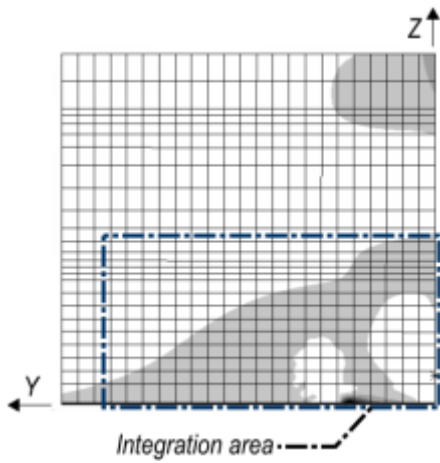


Figure 9-15. Transverse (x-x) stress distribution at stage 1 (outer strands cut) with bearing plate and without bearing plate



With bearing plate



No bearing plate

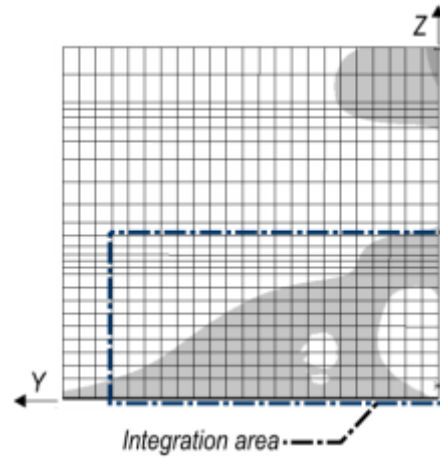


Figure 9-16. Transverse (x-x) stress distribution at stage 2 (all strands cut) with bearing plate and without bearing plate

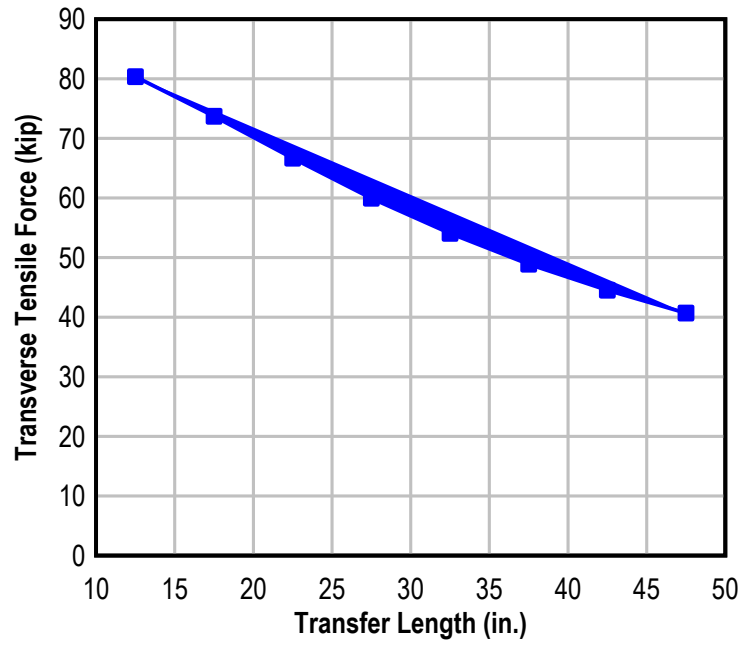


Figure 9-17. Transverse force vs. length of prestress transfer

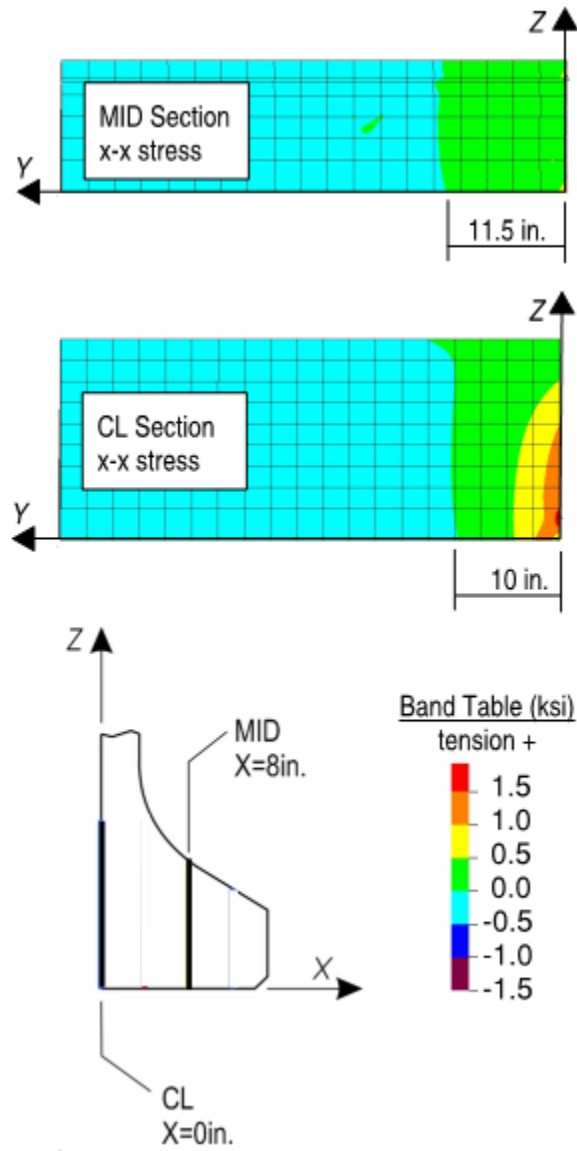


Figure 9-18. Transverse stress distribution 17.5in. transfer length

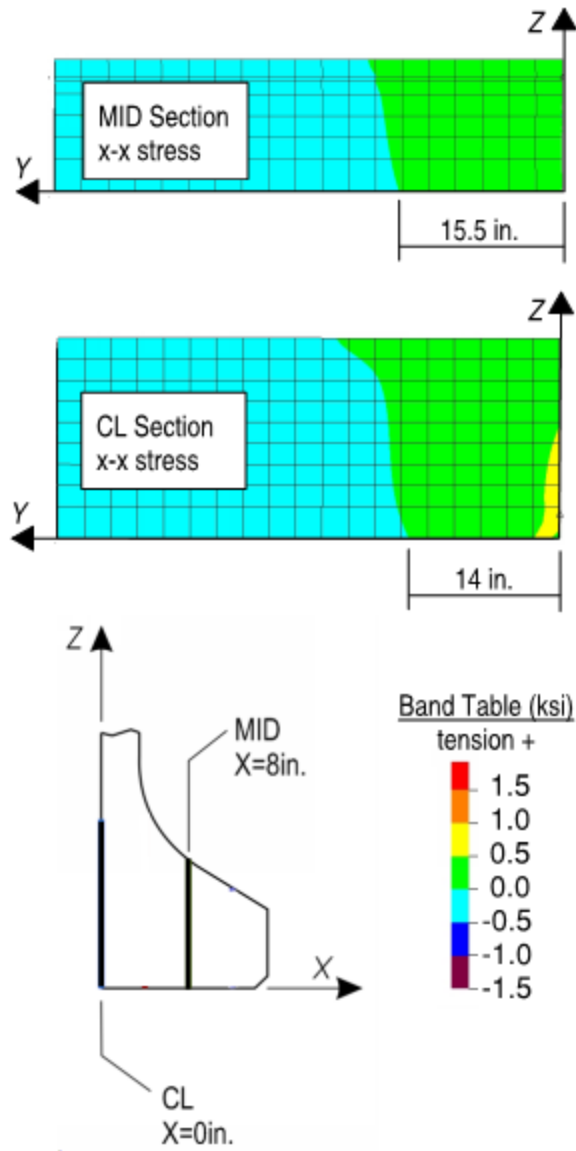


Figure 9-19. Transverse stress distribution 42.5in. transfer length

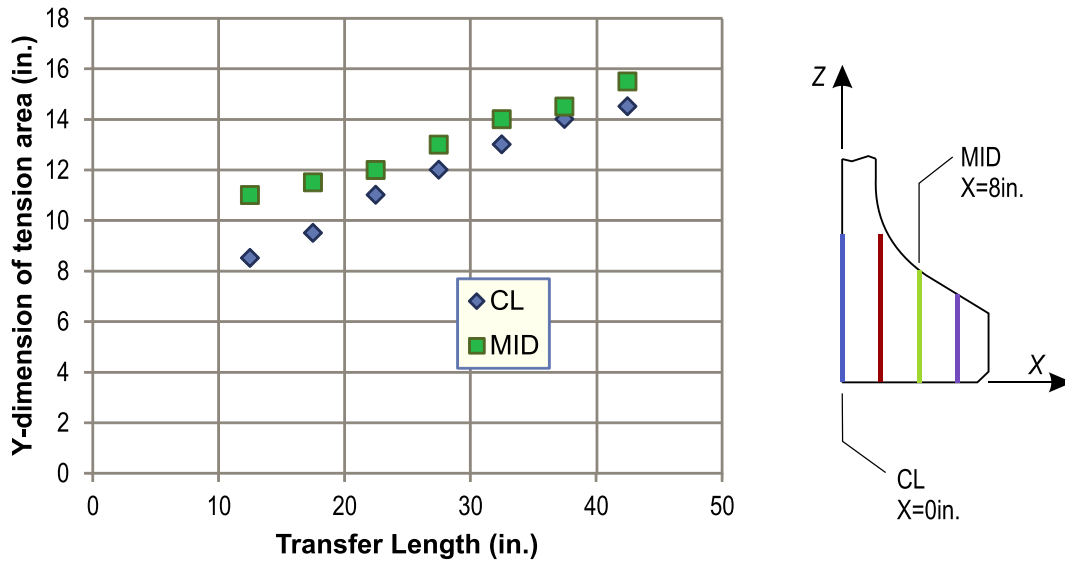


Figure 9-20. Length of tension area vs. transfer length

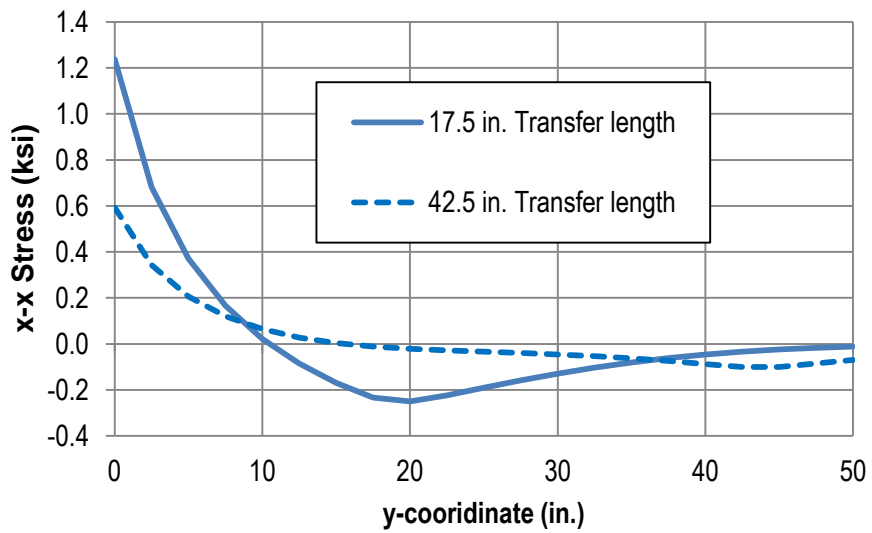


Figure 9-21. Transverse (x-x) stress at MID section through bottom flange

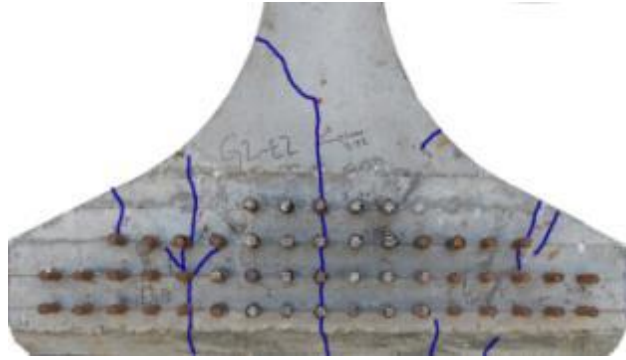


Figure 9-22. Flange splitting cracks at girder end

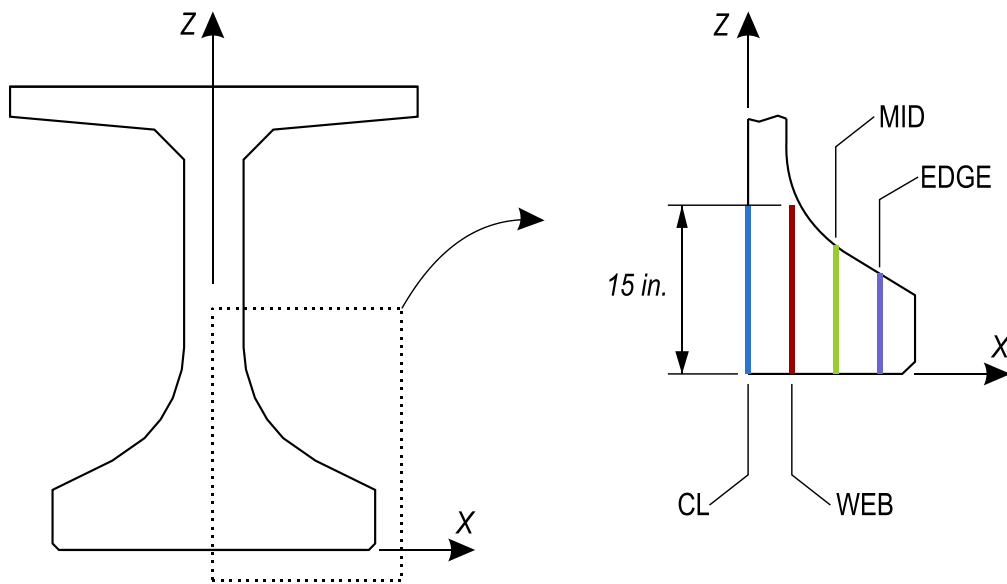


Figure 9-23. Lines for stress calculations

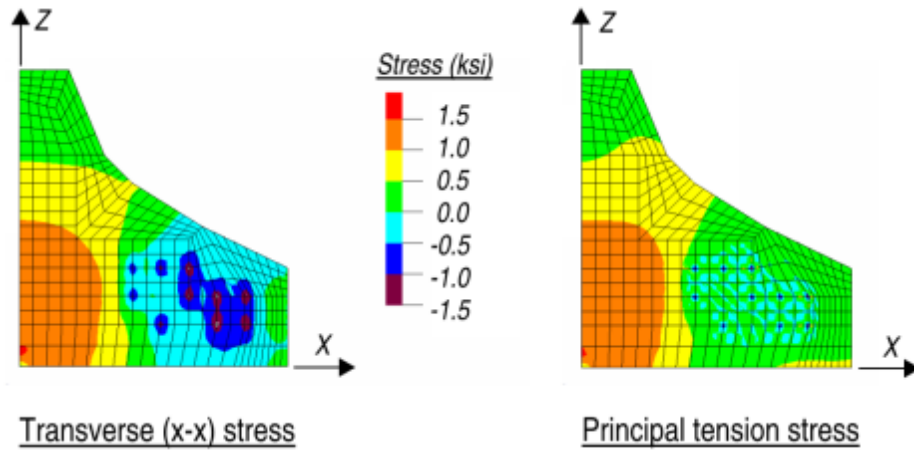


Figure 9-24. FE model stresses at girder end (50% strands cut)

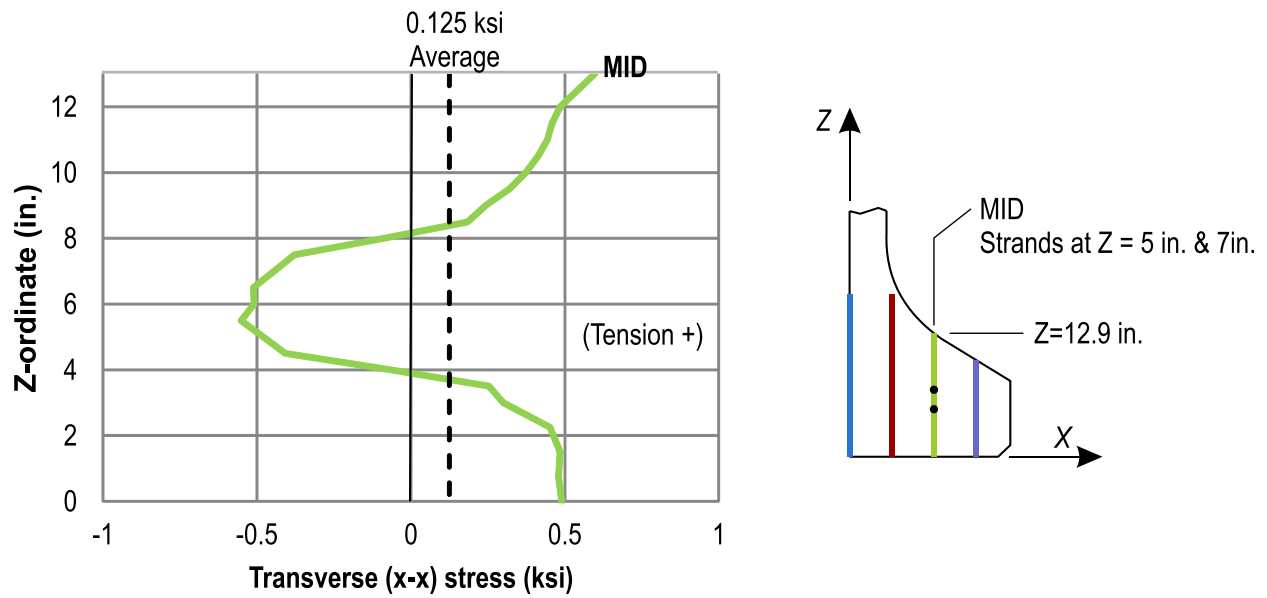


Figure 9-25. Transverse (x-x) stress at mid-flange line (50% strands cut)

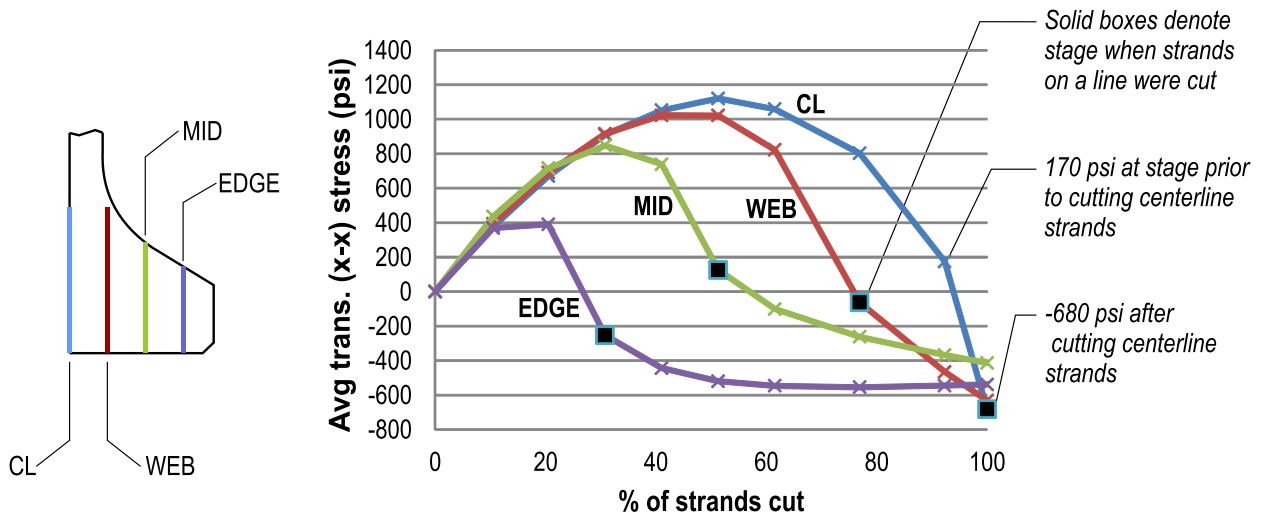


Figure 9-26. Average transverse (x-x) stress at end of girder due to strand cutting

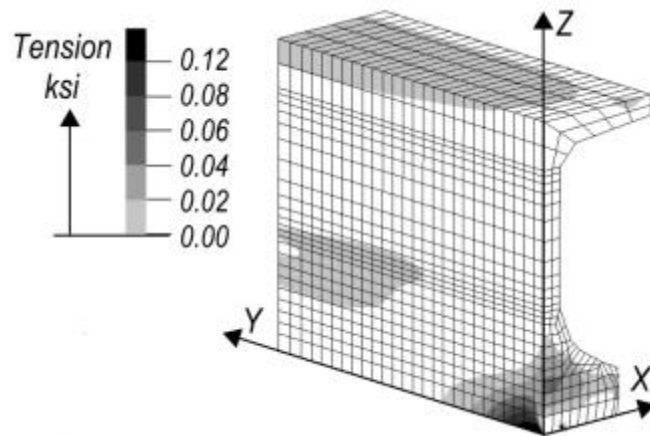


Figure 9-27. Transverse (x-x) stress due to self-weight

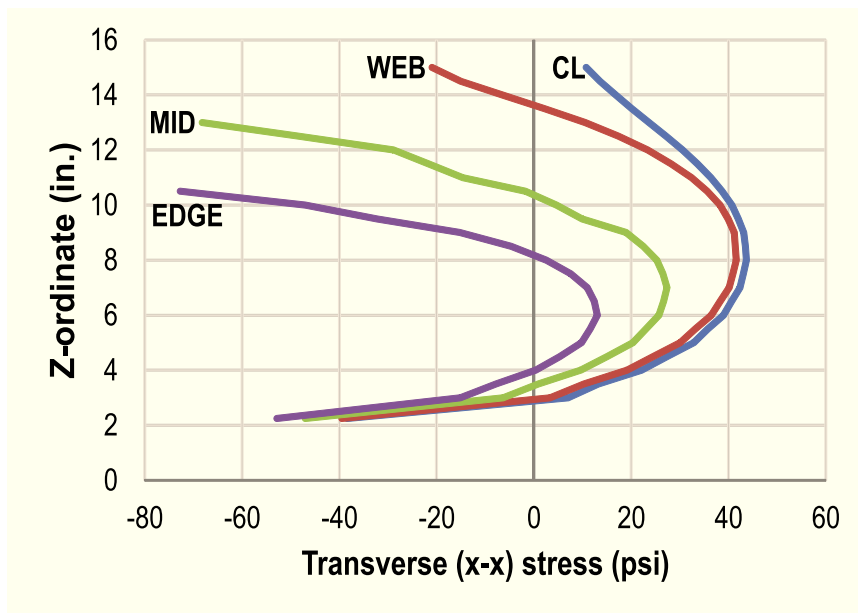
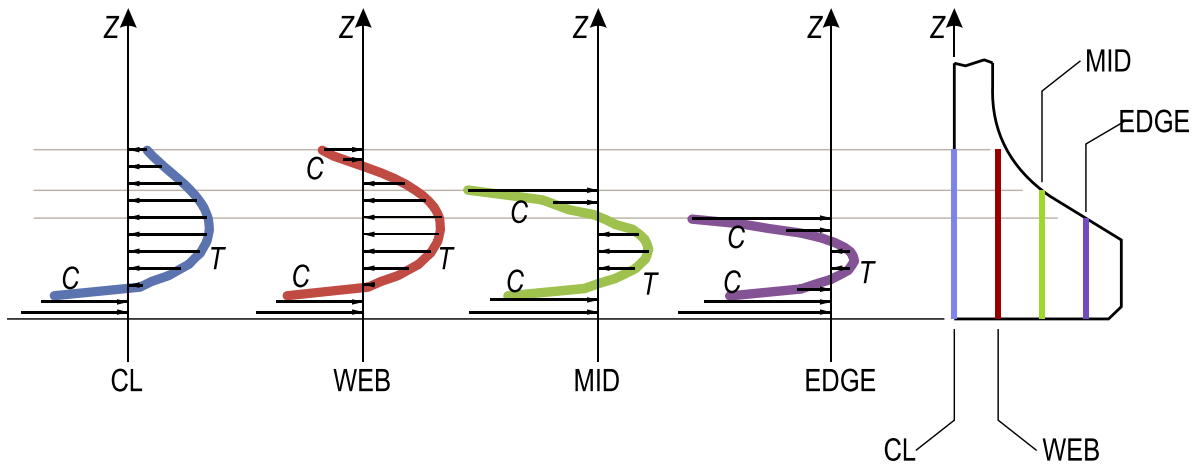


Figure 9-28. Transverse (x-x) stress due to self-weight

Table 9-1. Bearing plate study summary of transverse (x-x) stresses and forces

	With bearing plate		No bearing plate	
	Max x-x stress at integration point (ksi)	Transverse tension force (kip)	Max x-x stress at integration point (ksi)	Transverse tension force (kip)
Outer strands cut (stage 1)	0.94	60.2 concrete 6.6 plate 66.8 total	1.16	66.9
All strands cut (stage 2)	0.15	24.9 concrete 3.0 plate 27.9 total	0.15	26.6

Table 9-2. Summary of transverse (x-x) stress at girder end due to strand cutting

Line	Maximum stress at any stage (ksi)	Stress at stage when strands on line were cut (ksi)	Stress after all strands were cut (ksi)
CL	1.12	-0.68	-0.68
WEB	1.02	-0.06	-0.63
MID	0.85	1.25	-0.41
EDGE	0.39	-0.25	-0.54
Average	0.85	-0.22	-0.57

Table 9-3. Summary of transverse (x-x) stress at girder end due to strand cutting

Section	Maximum force at any stage (kip)	Force at stage when strands on line were cut (kip)
MID	36.1	20.3
EDGE	15.8	11.3

Table 9-4. Transverse (x-x) stress due to self-weight

	CL	WEB	MID	END
Maximum tension (psi)	44	42	27	13
Average stress (psi)	28	21	0.9	-10 (comp.)

CHAPTER 10 ULTIMATE STRENGTH DESIGN MODEL

The 2007 AASHTO LRFD Bridge Design Specifications contain prescriptive requirements for the quantity and placement of confinement reinforcement located in the bottom flange of pretensioned concrete I-girders. This chapter proposes a rational model that can be used to design confinement reinforcement as an alternative to the prescriptive requirements of AASHTO LRFD. The model considers a wide range of conditions and variations, yet is intended to be practical enough for use by bridge design engineers. Variables in the design model include: flange and bearing geometry, strand size and placement, effective prestress force, concrete and steel material properties, and the effects of steel bearing plates. Derivation of the model is presented, and the model is compared to experimental results from the published literature.

The proposed design model can be used to calculate the quantity of confinement reinforcement required to prevent lateral-splitting failure at ultimate load. The model is formulated to capture the multitude of variables that exist in pretensioned girders, but be practical enough for use by bridge designers. The model does not consider the function of confinement reinforcement in controlling cracks during prestress transfer. This topic, however, is covered in the Chapter 11.

Experimental and analytical work from the previous chapters has shown that confinement reinforcement carries transverse tension forces due to prestressing and applied loads. By carrying these forces the confinement reinforcement functions to prevent lateral-splitting failure and provides a normal force whereby strand tension forces can be transferred to the concrete once strut-and-tie behavior has initiated. The ultimate strength design model considers both of

these functions. Forces generated due to these functions are referred to as the transverse tie force (F_{TT}), and the strand anchorage force (F_{SA}).

Strand anchorage and transverse tie functions of confinement reinforcement are analogous to the local zone and general zone reinforcement in post-tensioned (PT) structures. Figure 10-1 shows the manner in which the anchorage zone in a post-tensioned (PT) structure is partitioned into local and general zones. The local zone is a highly stressed region that resides immediately under the anchorage device and requires significant confinement reinforcement to prevent bursting stresses from causing localized failure. It is within the local zone that PT forces are transferred to the concrete. The general zone in a PT structure is the area where PT forces are transmitted throughout the member.

Conceptually the end region of a pretensioned beam can be divided into a local and general zone (Figure 10-1). General zone size is comparable to that of a PT anchorage and can be designed by the same approach as is used for PT anchorage zones. Pretensioned local zones, however, are longer because force transfer occurs gradually throughout the transfer length rather than through an anchorage device. Large, very localized lateral bursting stresses that are present immediately under the anchorage in a PT local zone are thus avoided in pretensioned end regions.

In pretensioned local zones the concrete immediately surrounding a prestressing strand is subjected to radial stresses from the Hoyer effect, which is illustrated in Figure 10-2. The Hoyer effect occurs due to Poisson expansion of the strands in the lateral direction when the strands are cut at prestress transfer. The beneficial effect of this expansion is to generate sufficiently large frictional forces at the concrete-strand interface to transfer the prestressing force into the

concrete. As illustrated in Figure 10-1 this has been shown to occur in a relatively uniform manner over the transfer length.

Confinement reinforcement is typically placed such that the some bars support loads from both local and general zones. Accordingly, confinement force due to the transverse tie is also utilized as the force required for strand anchorage. The proposed design procedure calculates the load demand on confinement reinforcement as the larger of the local and general zone loads. Or in other words, the model calculates confinement reinforcement required for the greater of the strand anchorage or transverse tie force.

Model Derivation

Transverse Tie Force

Calculation of the transverse tie force is based on the strut-and-tie models shown in Figure 10-3. This figure describes transfer of the ultimate reaction (R_u) from the web, through the bottom flange and into the bearing pad. The struts and ties are symmetric about the z (vertical) axis.

Compressive force BC_z equals the ultimate reaction and is carried to the support through three separate load paths. Force in each path is assumed to be proportional to the quantity of strands associated with that path; strands in the flange are assumed to connect to D nodes and strands below the web are assumed to connect to node F . Thus the vertical (z -direction) component of load traveling path $C-D-E$ can be calculated by Equation 10-1:

$$CD_z = DE_z = E_z = R_u \frac{n_f}{n_{strand}} \quad (10-1)$$

Where:

- CD_z = z -component of force in member CD
- DE_z = z -component of force in member DE
- E_z = Reaction at node E
- R_u = Factored reaction force
- n_f = number of strands in the flange

Using the strut and tie model shown in Figure 10-4a the slope of strut CD can be determined as follows:

$$Slope_{CD} = \frac{3t_f}{b_f - b_w} \quad (10-2)$$

Where:

- t_f = Minimum thickness of bottom flange
- b_f = Bottom flange width
- b_w = Web width z-component of force in member CD

Cross-sections from AASHTO, FDOT, Nebraska Department of Roads, and Washington State Department of Transportation were used to determine Equation 10-2. If exceptionally slender bottom flanges such as that shown in Figure 10-4b are used, then Equation 10-2 does not apply and the angle must be calculated directly.

Member DE slope can be calculated by Equation 10-3. When the bearing width is close to the flange width (Figure 10-3a), the slope calculated by Equation 10-3 is positive indicating that x-component of force in member DE acts in the positive x-direction. When the bearing width is smaller than the flange width (Figure 10-3b), the slope of member DE is negative, indicating that the x-component acts in the negative direction.

$$Slope_{DE} = \frac{1}{3.1 \frac{W_b}{b_f} - 3} \quad (10-3)$$

Where:

- W_b = Width of bearing

The horizontal (x-direction) force components in members CD and DE are calculated by Equations 10-4 and 10-5, respectively. These equations are derived from the vertical (z-direction) force component from Equation 10-1 and the slopes from Equations 10-2 and 10-3.

$$CD_X = R_u \frac{n_f}{n_{strands}} \frac{b_f - b_w}{3t_f} \quad (10-4)$$

$$DE_x = R_u \frac{n_f}{n_{strands}} \left(3.1 \frac{W_b}{b_f} - 3 \right) \quad (10-5)$$

The transverse tie force is equal to the force in member DF , and can be calculated from equilibrium in the x-direction at node D :

$$F_{TTu} = CD_x - DE_x \quad (10-6)$$

Substituting for CD_x and DE_x and simplifying, Equation 10-6 can be rewritten as:

$$F_{TTu} = R_u \frac{n_f}{n_{strands}} \left(\frac{b_f - b_f}{3t_f} - 3.1 \frac{W_b}{W_f} + 3 \right) \quad (10-7)$$

Strand Anchorage Force

Strand anchorage force refers to the normal force required to generate strand forces through friction. This force must be resisted by the concrete tensile strength, the confinement reinforcement, or both to ensure that the frictional force transfer between strands and concrete is maintained. If the concrete tensile strength and confinement are not sufficient bond is lost and the strand slips.

In addition to friction, force transfer between strands and concrete also occurs due to adhesion, mechanical interlock. Adhesion and mechanical interlock, however, are relatively small and are conservatively neglected. Also, it is thought unlikely that adhesion and mechanical interlock are significant at ultimate load after concrete around the strands has cracked.

At ultimate load it is assumed that internal forces in the end region can be described by strut-and-tie modeling as was done in calculating the transverse tie force. Strut-and-tie models conservatively neglect concrete tensile strength. This assumption will also be made in calculation of the strand anchorage force. Concrete around the strands will be assumed to have cracked and unavailable to provide the normal force required to generate friction at the

strand-concrete interface. In calculating the strand anchorage force, it is assumed that all of the normal force is supplied by confinement reinforcement.

Aknoukh (2010) presented a similar friction-based approach for designing confinement reinforcement. The Aknoukh model considered strand anchorage through on a horizontal section using a friction coefficient of 1.4. The proposed method is distinct from Aknoukh because it considers anchorage forces on vertical sections through the bottom flange, and because it uses a more conservative (and realistic) friction coefficient of 0.4. The proposed model is also distinct in that transverse tie forces are considered.

Equilibrium in the direction of the strand length requires that the total frictional force at the strand-concrete interface be equal and opposite of the effective prestress in the strand. The normal force required to generate the frictional force is equal to the frictional force divided by the friction coefficient at the strand-concrete interface. Based on this rationale, the normal force required to develop the effective prestress in an individual strand can be calculated by Equation 10-8:

$$F_N = \frac{A_{ps}f_{pe}}{\mu} \quad (10-8)$$

Where:

- F_N = Normal force on an individual strand required to develop prestress
- A_{ps} = Cross-sectional area of prestressing strands
- f_{pe} = Effective prestress
- μ = Coefficient of friction between concrete and strand, taken as 0.4

Although seven-wire strand does not have a circular cross section, it is believed that this simplification does not significantly affect the results of the strand anchorage force model. The same assumption was made by Oh et al (2006) in the development of a strand transfer length model. Using this assumption the Oh model correlated well with experimental data. The round strand assumption is also considered reasonable for the current model derivation.

Figure 10-5 illustrates the idealized normal stress acting on a single strand within the transfer length. The normal stress (f_N) can be calculated by assuming that the normal force (F_N) required to prevent strand slip is distributed evenly around the circumference and along the transfer length.

The geometric properties of the strand can then be used to form equation 10-9:

$$f_N = \frac{F_N}{d_p L_T \pi} \quad (10-9)$$

Where:

f_N = Normal stress at strand-concrete interface
 d_p = Diameter of prestressing strand

Substituting Equation 10-8 into Equation 10-9 into gives:

$$f_N = \frac{A_{ps} f_{pe}}{d_p L_T \pi \mu} \quad (10-10)$$

The transverse (x-direction) component of the normal force on an individual strand can be calculated using a pressure vessel analogy by multiplying the stress in Equation 10-10 by the projected area of the strand over the transfer length:

$$F_{Nx} = f_N d_p L_T \quad (10-11)$$

Where:

F_{Nx} = Transverse normal force on an individual strand

Substituting Equation 10-10 into Equation 10-11 and simplifying gives:

$$F_{Nx} = \frac{A_{ps} f_{pe}}{\pi \mu} \quad (10-12)$$

The total x-direction force along an arbitrary section can be determined from the product of the transverse component and the number of strands along the section. This force is defined as the strand anchorage force and is given as:

$$F_{SA} = F_{nX}n_c = \frac{A_{ps}f_{pe}n_c}{\pi\mu} \quad (10-13)$$

Where:

F_{SA} = Strand anchorage force
 n_c = Number of strands along critical section

Equation 10-13 can be used to calculate the strand anchorage force on any arbitrary section. The maximum strand anchorage force occurs through the section that intersects the maximum number of strands.

Quantity and Placement

Preceding sections have presented equations for calculating the transverse forces resisted by confinement reinforcement at ultimate load. The design force in the confinement reinforcement is equal to the greater of the transverse tie or strand anchorage forces:

$$F_{CRu} = \text{maximum} (F_{SA}, F_{TTu}) \quad (10-14)$$

Where:

F_{CRu} = Factored design force in confinement reinforcement

The reason for using the greater for the transverse tie or strand anchorage forces can be understood by considering the forces acting on a node in the bottom flange strut-and-tie model. For example, forcing acting on node D in Figure 10-3 come from struts in the concrete and ties in the reinforcement. In deriving the transverse tie force it was shown that the forces at node D are based on equilibrium and geometric properties. The same forces acting on node D are also the forces that generate the strand forces (acting in the y-direction at node D) through friction. Additional strand anchorage force is not required. Thus confinement reinforcement capacity need only be the greater of the strand anchorage force or the transverse tie force.

The quantity of confinement required at ultimate load is equal to the confinement reinforcement design load divided by the specified yield stress of the reinforcement:

$$A_{CR} = \frac{F_{CRu}}{f_{yCR}} \quad (10-15)$$

Where:

A_{CR} = Required area of confinement reinforcement

f_{yCR} = Yield stress of confinement reinforcement

The proposed model is intended for use in load and resistance factor design (LRFD). Accordingly an appropriate strength reduction (ϕ) factor is needed. For strut-and-tie modeling, such as that used to derive the transverse tie force, the ACI (2008) code uses a strength reduction factor 0.75. This value is also recommended for use in the proposed ultimate strength design model.

Data from the experimental program demonstrate that steel bearing plates contribute confinement to the bottom flange at ultimate load. To account for this, the proposed design model allows the bearing plate to replace up to 50% of the confinement required by Equation 10-15. The plate is not allowed to totally replace confinement reinforcement because the confining influence of the plate on its own was not enough to prevent lateral-splitting failure in experiments. Bearing plates should not be considered as confinement reinforcement unless the bearing width and the spacing between plate anchorage points are *both* greater than 75% of the flange width. These requirements ensure that the bearing plate is in tension (Figure 10-3b), and is sufficiently anchored to provided confinement.

The confining effect of end diaphragms has also been shown to prevent splitting failures in experimental tests (Ross et al. 2011b). End diaphragms, however, are not present during prestress transfer and therefore do not constitute a replacement for confinement reinforcement.

Results from the experimental program demonstrate that confinement reinforcement is most effective when placed near the end of the girder. As such, confinement reinforcement

required by Equation 10-15 should be placed as close to the end of the girder as reasonable, but should also be placed over a distance of at least the transfer length.

Model Comparison with Experimental Results

In this section the proposed design model is evaluated against experimental data from 41 unique tests of pretensioned concrete girders reported in the literature (Llanos et al. 2009, Ross et al. 2011a, Morcous et al. 2010, Tadros et al 2010, Deatherage et al 1994). Figure 10-6 compares confinement reinforcement installed in each test girder with the required confinement reinforcement calculated using the proposed model (Equation 10-15). The factored reaction force used to calculate the transverse tie force (F_{TT}) was taken as the nominal shear strength. Provided confinement reinforcement, plotted on the vertical axis, was taken as the area of confinement reinforcement placed within the transfer length. If present, the embedded steel bearing plate area was allowed to contribute up to 50% of the confinement requirement. Prestress losses were assumed to be 20 percent.

Points that fall below the solid line have less confinement than calculated by the model, and are predicted to fail due to splitting or lateral-bursting. The proposed model correctly identified all but two of the specimens that failed in lateral-splitting, bearing, or similar modes. Splitting and similar failures are denoted by the 'X' markers. The model incorrectly predicted failure in eight cases, as denoted by the diamond shaped markers that fall below the solid line. In most cases where the failure mode was not accurately predicted, the provided confinement reinforcement was within 1.5 in² of the calculated requirement, indicating a desirable degree of conservatism in the model.

The point marked "FL Bulb Tee" on Figure 10-6 shows the greatest level of disagreement with the proposed model. This data point represents a Florida Bulb Tee section (Tadros et al. 2010), which had only 35% of the calculated confinement reinforcement, but still did not fail due

to lateral-splitting. Shear reinforcement in this specimen terminated in a hook at the bottom of the beam. Hook tails were placed under the strands, were oriented transverse to the axis of the beam, and extended to the edge of the bottom flange. Additional splitting resistance demonstrated by the specimen is attributed in-part to the confinement provided by these hook tails. Confining effects from hooks are neglected in the proposed model due to inadequate hook development. The Florida Bulb Tee was supported on a steel plate during testing. Splitting resistance of the specimen is also attributed to frictional force between the girder and plate. Friction force at the bearing is thought to have had a greater impact on the bottom flange confinement than the hook tails from the vertical reinforcement.

The point label “WSDOT” on Figure 10-6 represents four tests of Washington wide flange girders (Tadros et al. 2010); each girder had identical calculated and provided confinement reinforcement. Numerous strands were located in the outer portion of the slender bottom flanges. During prestress transfer, it was observed that splitting cracks formed in the bottom flanges. Although not explicitly identified in the research, photographs of the failed beams suggest that lateral-splitting action occurred during testing.

The ultimate strength design model was also compared to the experimental data pool using the maximum shear force. For each data point, the maximum shear force reported in the literature was substituted into the model in lieu of the factored reaction force. As with the comparison at nominal shear capacity, the model also compares well with the maximum experimental shear forces (Figure 10-7). Points on the figure labeled “FL Bulb Tee” and “PC Bulb Tee” did not exhibit splitting failure in spite of having less confinement than calculated by the model. As with the FL Bulb Tee section discussed in Figure 10-6, the indicated specimens in Figure 10-7 were also supported on steel plates during testing. These plates were not

embedded plates and were not considered in the model calculations; however they are thought to have provided additional splitting resistance to the FL and PC Bulb Tee specimens. This result indicates that the model may be conservative for girders that are supported on rigid surfaces such as steel plates or concrete bent caps.

Figure 10-8 shows the data set if the external steel bearing plates used in the tests were considered to provide confinement similar to embedded steel bearing plates. The external steel bearing plates were only considered if they were wide enough to provide confinement (Figure 10-3b). External steel bearing plates were not considered in specimens that also had embedded plates. Accuracy of the model in categorizing failure model improved when the external bearing plates were considered. All but one of the incorrectly categorized results was within 0.5 in^2 of the solid black line that denotes the border between failure modes.

Summary and Conclusions

A rational design model was developed for designing confinement reinforcement at ultimate strength. The model considers strand anchorage and transverse tie requirements, which are analogous to local and general zone requirements in post-tensioned concrete members. The ultimate strength model was compared to 41 unique tests of pretensioned concrete girders reported in the literature. The model was found to have good agreement with the published test results. The model is recommended for the design of confinement reinforcement and bearing plates at ultimate load.

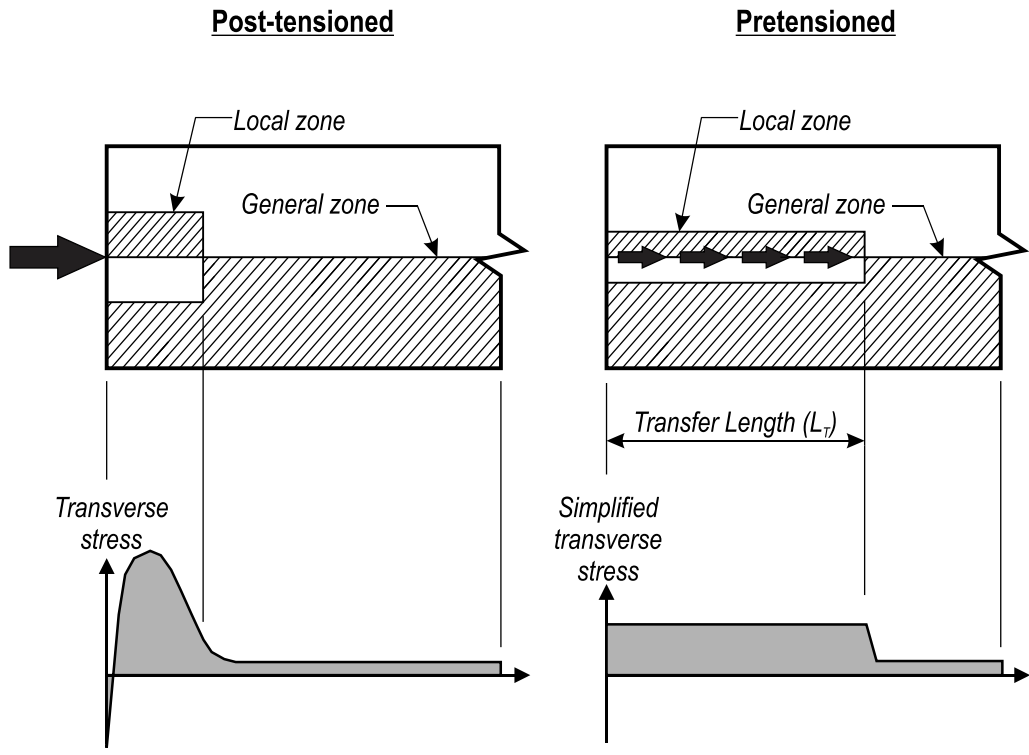


Figure 10-1. Local and general zones

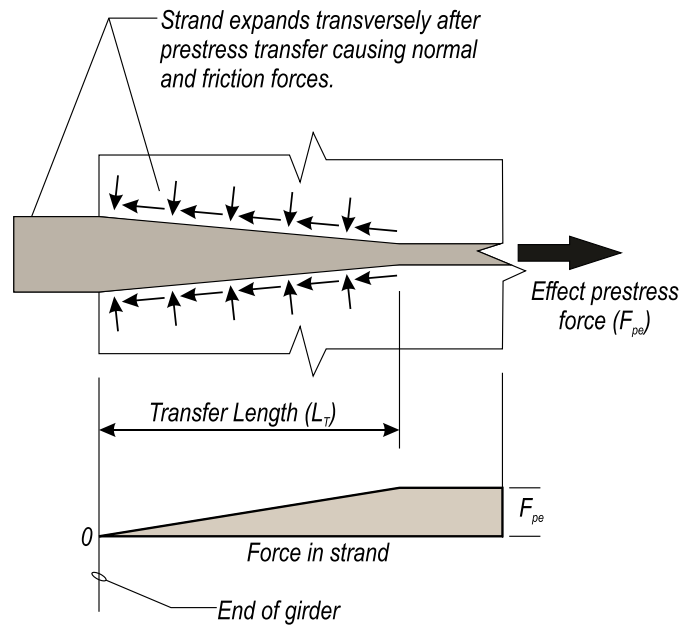
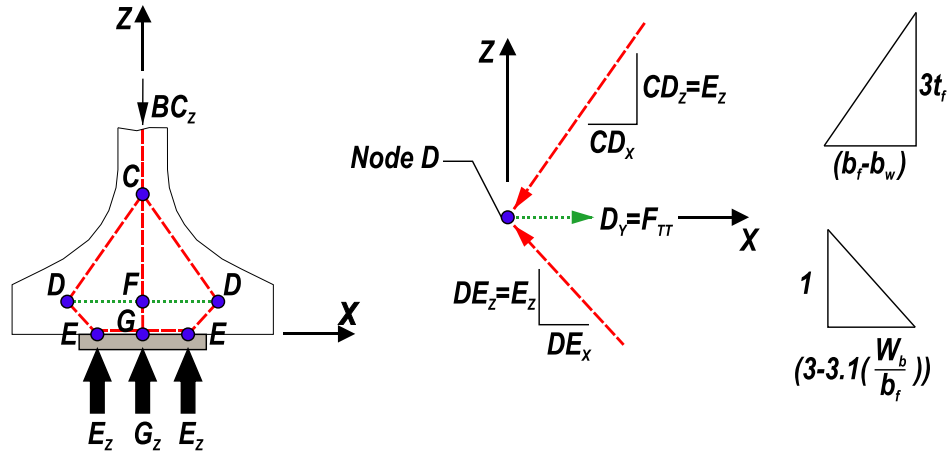
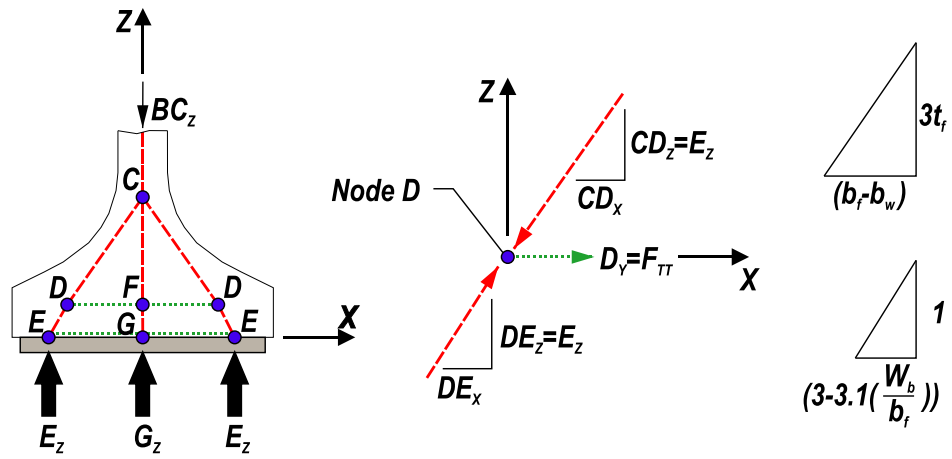
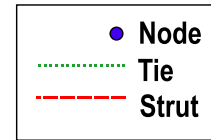


Figure 10-2. Illustration of transverse and frictional forces caused by the Hoyer effect



(a) Narrow Bearing



(b) Wide Bearing

Figure 10-3. Transverse tie force strut-and-tie models

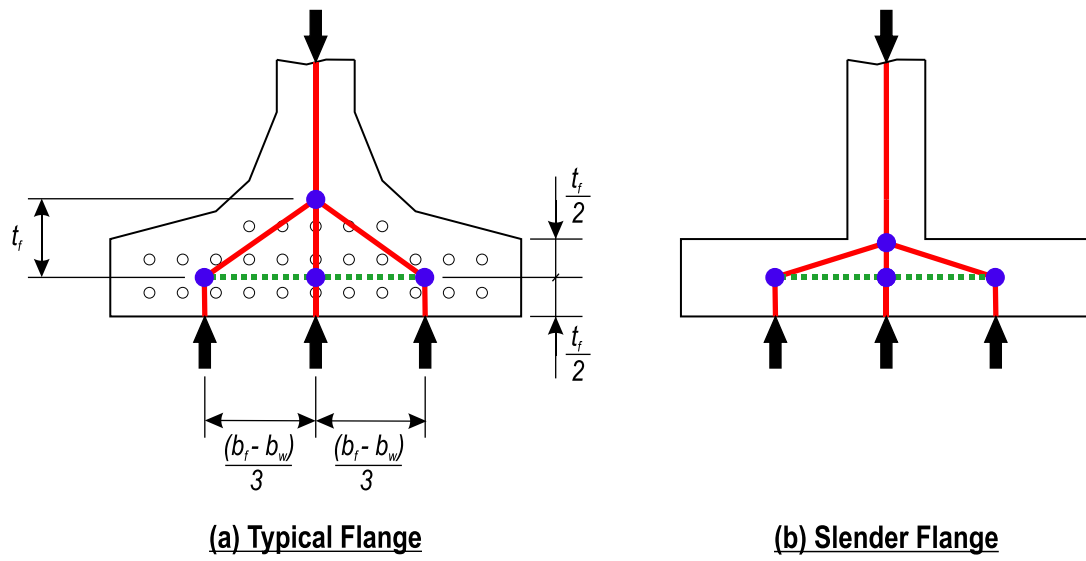


Figure 10-4. Node layout

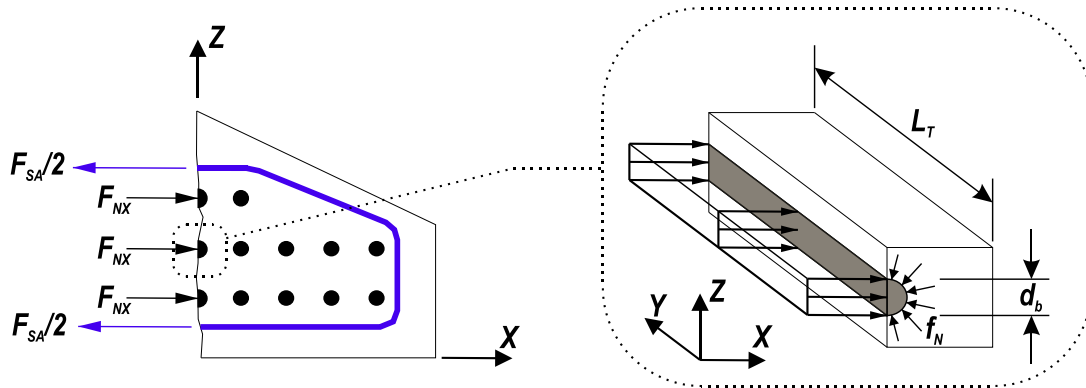


Figure 10-5. Strand anchorage force

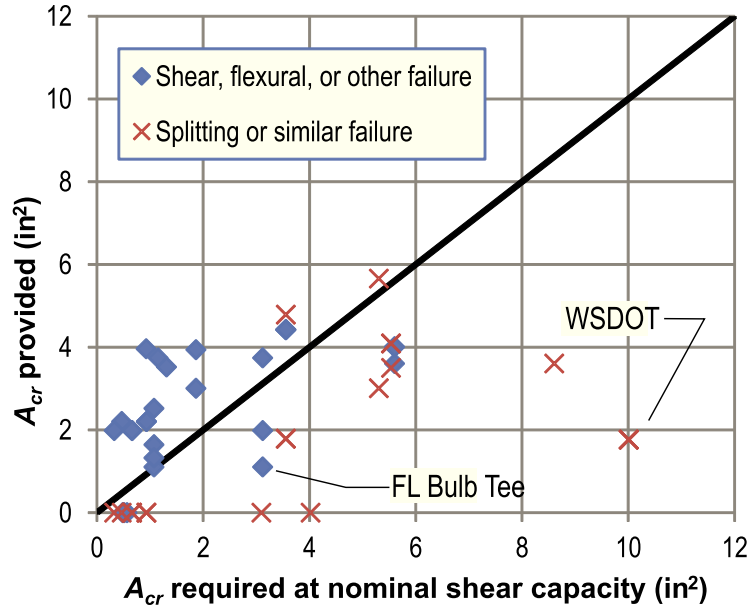


Figure 10-6. Design model compared to nominal strength of experimental girders

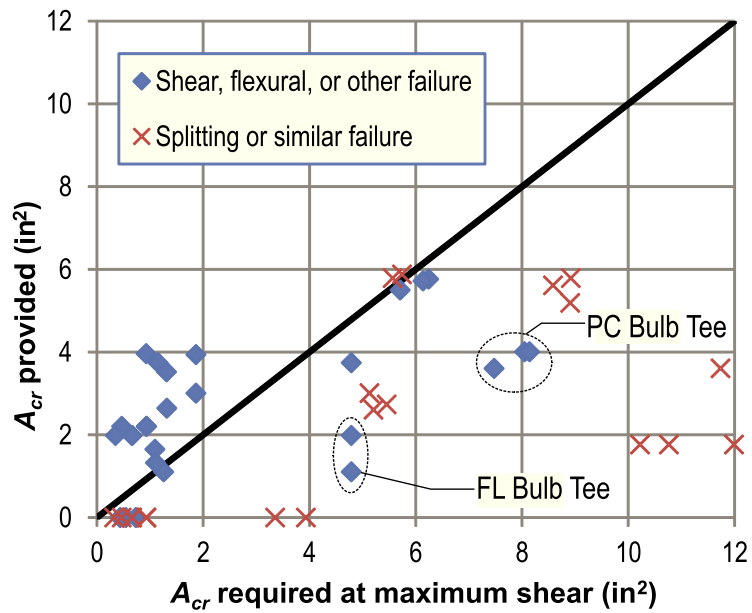


Figure 10-7. Design model compared to experimental girders at maximum shear

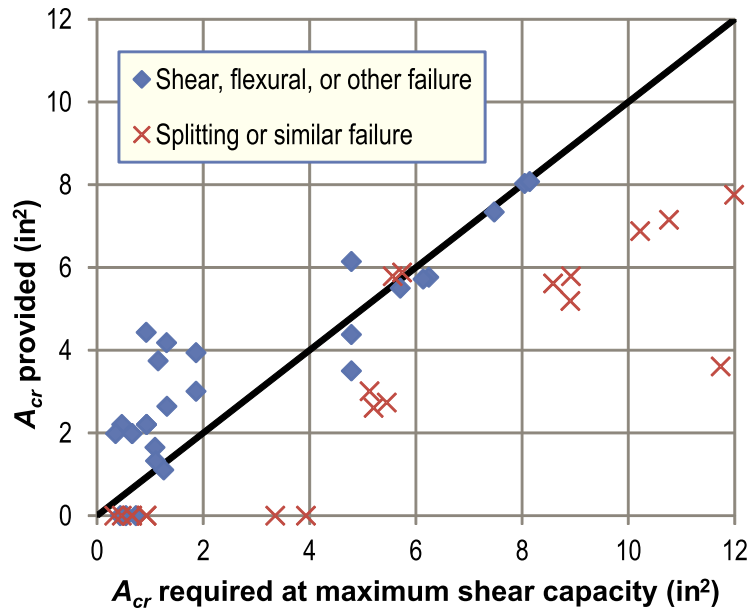


Figure 10-8. Design model compared to experimental girders at maximum shear (external bearing plates considered)

CHAPTER 11 SERVICABILITY MODEL

Experimental and analytical research presented in previous chapters demonstrates that transverse tensile stress in the bottom flange of pretensioned I-girders can lead to flange splitting cracks during fabrication. It is believed that the following behaviors contribute to tensile stress and flange cracking:

- Hoyer effect
- Eccentric prestress forces
- Self-weight reaction

Flange splitting cracks can reduce the durability of concrete I-girders by allowing contaminants to enter the bottom flange and initiate corrosion of prestressing steel or chemical attack on the interior concrete. A serviceability design model is presented in this chapter for quantifying bottom flange splitting stress. Stress from the model can be compared to concrete tensile capacity to determine the likelihood of bottom flange splitting cracks.

The serviceability model is derived from a variety of sources including the work of other researchers, finite element modeling, and basic mechanics. The proposed model contains empirical features specific to FIB girders. Although this formulation is not broadly applicable, the model could conceivably be re-tooled for use with other cross-sections.

Experimental and analytical research indicates that the largest transverse tensile stresses in the bottom flange occur at the member end. The majority of flange-splitting cracks in the experimental girders were located at or close to the specimen ends. Accordingly, the serviceability model provides equations for calculating the worst-case transverse tensile stress occurring at member ends. Calculated stresses at the member end can be compared to concrete tensile strength criteria to evaluate the likelihood of flange splitting cracks. Possible strength criteria are discussed later in this chapter.

In the final section of this chapter, experimental cracks data are compared to stresses calculated from the proposed model. The model and data are found to have a high degree of correlation.

Causes of Bottom Flange Splitting at Prestress Transfer

Flange splitting cracks in the bottom flange are caused by transverse splitting stresses that occur due to a combination of the Hoyer effect, eccentric prestress forces, and the self-weight reaction. The following sections describe the mechanics associated with each of these effects.

Hoyer Effect

The diameter of a prestressing strand decreases during pretensioning due to the Poisson effect (Figure 11-1a and b). When tension is released during prestress transfer the strands expand towards their original diameter. Expansion is partially restrained by the surrounding concrete resulting in normal stresses and proportional frictional forces at the strand-concrete interface. This behavior was named for Ewald Hoyer, the German Engineer who first wrote of radial expansion of prestressing strands (Hoyer 1939).

Expansion of prestressing strands is greatest at the edge of the concrete where strand tension is zero after prestress transfer (Figure 11-1d). At locations beyond the transfer length the strand expansion is negligible because strand tension is nearly the same before and after release. Change in radial expansion is approximately linear between the concrete edge and the end of the transfer length (Oh et al. 2006). Consequently, radial and annular stresses in the concrete also vary linearly along the transfer length.

Variable expansion of the strands leads to a wedge-like shape after prestress transfer. This shape creates mechanical bond between strand and concrete. Additional bond improvement comes from the radial stresses at the interface, which allow the generation of

frictional forces. Wedge action and frictional forces are thus beneficial consequences of the Hoyer effect because they enable the transfer of prestress forces. The Hoyer effect can also have detrimental consequences on the behavior and capacity of pretensioned girders. Concrete surrounding strands cracks when stresses due in-part to the Hoyer effect exceed concrete tensile capacity.

Eccentric Prestress Forces

Tension forms in the bottom flange as prestressing forces from the outer strands are transferred to the concrete (Figure 11-2). This tension forms in response to the eccentricity between prestressing forces from outer strands and the equal and opposite resultant force in the member. Tension is partially relieved as inner strands are released. This process has been demonstrated experimentally and analytically in previous chapters and is dependent on the strand bond pattern and strand cutting pattern. Tension stress due to eccentric prestress forces is referred to as “peeling” stress because they act to peel the outer portion of the bottom flange away from the web. Strands in the experimental program and in analytical models were cut from the outside-in (Figure 3-5). This detensioning pattern is assumed in the equations derived in this chapter.

Self-Weight Reaction

Girders camber upward during prestress transfer after the prestressing moment exceeds the self-weight moment (Figure 11-3). After cambering, girders are supported by reactions at each end. Tensile stresses form in the bottom flange above the reaction points due to the flange bending illustrated in Figure 11-4.

Previous analyses show that self-weight reactions produce tensile and compressive transverse stresses in the FIB bottom flange (Figure 9-28). Analysis also demonstrate that self-weight reaction stresses are small relative to peeling stresses, and that average stress on

sections through the outer flange is near zero or slightly compressive (Table 9-4). Because of this, self-weight reaction stresses on sections through the outer portion of the FIB bottom flange are conservatively neglected in the proposed serviceability model. This assumption may not be reasonable for other cross-sections and for long-span FIB girders.

Transverse Splitting Stress Model Derivation

Experimental results indicate that vertical splitting cracks can occur at multiple locations in the bottom flange (Figure 11-5). The proposed model focuses on splitting cracks through the outer portion of the flange. Bottom flange splitting cracks below the web are not considered because they are associated with extreme strand bond patterns that are not permitted in FDOT production girders. Splitting cracks below the web were observed in the experimental program, but only in specimens with bonding patterns that placed fully bonded strands in the outer flange and shielded strands below the web.

An outside-in cut pattern is commonly used in FDOT production girders. As such, the serviceability model assumes an outside-in cut pattern. This pattern was used in construction of the experimental girders, as well as the FE models used to develop the serviceability model. The model does not apply to girders with other cut patterns.

Two critical conditions are considered in the design model:

- **Maximum Peeling.** Previous experimental and analytical research show that the maximum peeling stress along a given section occurs when only the outboard (closer to the outside edge) strands are cut (Figure 11-6). This condition is referred to as the “maximum peeling” condition.
- **Combined.** This condition occurs when strands along a given section are cut and Hoyer stresses are superimposed with peeling stress. It is referred to as the “combined” condition.

The model does not consider stress conditions when inboard (closer to the centerline) strands have been cut. Previous analytical work shows that cutting of inboard strands reduces peeling stresses on a given section.

Hoyer Stress

Hoyer stress is calculated using a model developed by Oh et al. (2006). The Oh model is based on equilibrium, material constitutive properties, and strain compatibility. It assumes radial expansion of a steel cylinder surrounded by concrete (Figure 11-7). Equation 11-1 is for calculating radial stress at the steel-concrete interface. Figure 11-8 shows the radial stress distribution calculated from Equation 11-1 for a strand in the experimental girders. As described by the Hoyer effect, radial stress is greatest at the member end and reduces to near zero at the end of the transfer length.

$$p = \frac{r_o \ 1-\nu_p f_{pz} \ E_p \ -r_j \ 1-\nu_c f_{cz} \ E_c}{1-\nu_p \ r_o \ E_p + [\nu_c - (r_j^2 + c^2) \ (r_j^2 - c^2)] r_j \ E_c} \quad (11-1)$$

Where:

- p = Radial stress at strand-concrete interface
- r_o = Strand radius before pretensioning
- ν_p = Strand Poisson ratio
- f_{pz} = Axial stress in strand
- E_p = Strand Elastic Modulus
- r_j = Strand radius immediately after pretensioning
- ν_c = Concrete Poisson ratio
- f_{cz} = Concrete stress in direction parallel to strand
- E_c = Concrete Elastic Modulus
- c = Concrete cover distance

The equation above assumes linear-elastic behavior. Recognizing the possibility of concrete cracks forming near the strand, the Oh model also includes features to calculate the average stress in cracked concrete. Applying these features results in stresses that are smaller than those calculated by assuming linear-elastic behavior. Cracking features in the Oh model

are neglected in the current model development. This approach allows superposition of Hoyer stresses with stresses derived from linear-elastic finite element modeling.

Stress calculated by Equation 11-1 is not sensitive to concrete cover (c) distance for cover values greater than approximately 10 times the strand diameter (Figure 11-9). By assuming that the cover distance is large relative to the strand diameter, the term $(r_j^2 + c^2) / (r_j^2 - c^2)$ in the denominator of Equation 11-1 approaches negative one, and Equation 11-1 can be simplified to:

$$p = \frac{r_0 (1 - \nu_p) f_{pz} E_p - r_j (1 - \nu_c) f_{cz} E_c}{1 - \nu_p r_0 E_p + \nu_c + 1 r_j E_c} \quad (11-2)$$

Assuming large concrete cover distance is conservative and results in slightly higher calculated stresses. For typical strand diameters and minimum cover dimensions, this assumption increases the calculated stress by less than 2%.

The serviceability model considers stresses at the girder end. At this location, strand expansion and the associated Hoyer stresses are at their maximum. Axial stress in the strand ($f_{pz} = 0$) and concrete ($f_{cz} = 0$) are equal to zero at the member end, which reduces Equation 11-2 to:

$$p_{edge} = \frac{r_0 - r_j}{1 - \nu_p r_0 E_p + \nu_c + 1 r_j E_c} \quad (11-3)$$

Where:

p_{edge} = Radial stress at strand-concrete interface at end of member

Concrete circumferential stresses are a function of the interfacial stress, strand size, concrete cover, and distance from the strand. Oh et al. provide the following equation for calculating circumferential stresses:

$$\sigma_{\theta}(r) = \frac{-p (1 - c^2 + 1 - r^2)}{(1 - c^2 + 1 - R^2)} \quad (11-4)$$

Where:

- σ_{θ} = Radial stress at strand-concrete interface at end of member
- r = Ordinate in the radial direction
- R = Radius of prestressing strand

Figure 11-10 shows the concrete stress distribution calculated by Equations 11-3 and 11-4 for a single strand in the experimental girders. Values used to calculate the stress distribution are listed in Table 11-1. The maximum concrete stress is 7.35ksi and occurs adjacent to the strand. Stress decreases rapidly with increasing distance from the strand. At locations 2in. from the strand-concrete interface the stress is less than 0.125ksi.

Large Hoyer stress adjacent to strand can cause local damage and cracking in the concrete. If tension through the flange is sufficient, then the localized cracking may propagate and form a crack through the entire flange. For this reason it is important to check the average stress due to the Hoyer effect through the flange thickness.

Rather than calculating average stress from the stress distribution described by Equation 11-4, average stress in the model is calculated indirectly using the interfacial stress. This is done to simplify the design model for design purposes and to avoid integration of concrete stress such as shown in Figure 11-10. Average stress calculated indirectly from the interfacial stress is the same as average stress calculated by integrating Equation 11-4.

Applying equilibrium to an idealized strand, the interface stress must equal the internal stress in the strand (Figure 11-11a). Equilibrium can also be applied along a section cut through the strand and concrete (Figure 11-11b) to show that the resultant force acting on the strand is equal and opposite the concrete force. This equilibrium condition is described by Equation 11-5.

$$\Sigma F_x = 0 = -p d_b d_y + f_{hs} h_f - d_b d_y \quad (11-5)$$

Where:

- d_b = Strand diameter
- d_y = Differential length in y direction
- f_{hs} = Average Hoyer stress on the section from a single strand
- h_f = Thickness of flange at section under consideration

Rearranging Equation 11-5, average stress due to the Hoyer Effect can be described as:

$$f_{hs} = \frac{p d_b}{h_f - d_b} \quad (11-6)$$

The average Hoyer stress on a given line is a function of the quantity of strands on that line. For sections with multiple strands the average stress can be calculated by multiplying the stress from Equation 11-6 by the number of strands. Both shielded and bonded strands along a section displace the area of concrete that carries Hoyer stresses. The denominator in Equation 11-7 is adjusted to account for displaced concrete due to all strands:

$$f_h = \frac{n_s p d_b}{h_f - n_{st} d_b} \quad (11-7)$$

Where:

- f_h = Average stress on the section due to Hoyer Effect
- n_s = Quantity of fully bonded strands on section under consideration
- n_{st} = Quantity of all strands on section under consideration

The serviceability model considers stress at the end of the member. At this location the interfacial stress between the strand and the concrete can be calculated using Equation 11-3. Substituting Equation 11-3 into Equation 11-7 results in Equation 11-8 for calculating the average Hoyer stress on a line through the bottom flange at the member end:

$$f_h = \frac{n_s d_b}{h_f - n_{st} d_b} \frac{r_0 - r_j}{1 - \nu_p r_0 E_p + \nu_c + 1 r_j E_c} \quad (11-8)$$

Peeling Stress

Peeling stress calculations are based on the free body diagram shown in Figure 11-12. This diagram is a simplified illustration of forces acting on the outer portion on a bottom flange during prestress transfer. Prestressing forces from the eccentric outer strands (F_{pos}) create a moment about the Z-axis. Moment equilibrium is maintained by x-direction tensile stresses in the concrete acting on the Y-Z cut plane. This equilibrium condition is described in equation 11-9:

$$\Sigma M_Z = 0 = F_{pos}x_p - F_{tos}l_y \quad (11-9)$$

Where:

- F_{pos} = Prestressing force from strands outboard of cut plane
- x_p = Distance from cut plane to centroid of prestressing force
- F_{tos} = Transverse tension force acting on cut plane due to eccentric prestressing
- l_y = Internal moment arm in y-direction

Rearranging Equation 11-9 results in the following equation for the transverse tension force due to the eccentric strands:

$$F_{tos} = \frac{F_{pos}x_p}{l_y} \quad (11-10)$$

Transverse tensile force in Equation 11-10 is the resultant of peeling stress in the concrete at the member end, which is assumed to have a triangular tensile stress distribution. Peeling stress is assumed to be largest at the member end and zero at a distance l_{tos} from the end (Figure 11-12). Previous FE modeling shows that a triangular stress distribution and a value of 10in. for l_{tos} are reasonable assumptions for the FIB cross-section with outer strands cut (Figure 9-21). The following equation of equilibrium ensures that the resultant force from the assumed peeling stress distribution is equal the transverse tensile force:

$$F_{tos} = \frac{F_{pos}x_p}{l_y} = \frac{1}{2}f_{tos}l_{tos}h_f \quad (11-11)$$

Where:

- f_{tos} = Peeling stress

l_{tos} = Length of the assumed tensile stress distribution
 h_f = Thickness of the flange at the section under consideration

Equation 11-11 can be rearranged to solve for the peeling stress at the member end:

$$f_{tos} = \frac{2F_{pos}x_p}{l_y l_{tos} h_f} \quad (11-12)$$

Strands along a given section displace the concrete area that carries peeling stress. The denominator in Equation 11-12 must be adjusted to account for the area displaced by shielded and bonded strands. Doing so results in:

$$f_{tos} = \frac{2F_{pos}x_p}{l_y l_{tos} h_f - n_{st} d_b} \quad (11-13)$$

The term l_y in Equation 11-13 is the length of the internal moment arm in the y-direction. The value of l_y varies according to the quantity of cut strands, shape of the cross-section, and location within a given cross-section. Equation 11-14 and 11-15 are empirical equations for calculating l_y in FIB girders. These equations were found to give values of l_y -and consequently of F_{tos} - that are in agreement with previous FE results.

$$l_{y1} = 36 \frac{\bar{h}_f}{x} \quad (11-14)$$

$$l_{y2} = 53 \frac{h_f}{x} \quad (11-15)$$

Where:

- l_{y1} = Internal moment arm in the y-direction for maximum peeling condition
- l_{y2} = Internal moment arm in the y-direction for combined condition
- h_f = Thickness (z-dimension) of the flange at the section under consideration
- x = x-ordinate of the section under consideration

Transverse forces calculated using Equation 11-14 and Equation 11-15 are compared with FE results in Table 11-2 and Table 11-3. Results are compared for the MID and EDGE sections (Figure 9-23.), for the 'design' strand bond pattern (Figure 3-4). Values from the model

equations are within 1% of FE results for all but the combined condition at the MID section, for which the model is 7% conservative. Consistency between the model and FE results indicates that Equations 11-14 and 11-15 are acceptable approximations for calculating I_y in FIB girders.

Substituting I_{y1} and I_{y2} in into Equation 11-13 results in Equations 11-16 and 11-17. These equations are calibrated for sections through the outer portion of the bottom flange in FIB girders. They should not be used in conjunction with other girder shapes, or at sections in the FIB bottom flange that are below the web.

$$f_{tos1} = \frac{2F_{pos}x_p}{l_{y1}l_{tos} h_f - n_{st}d_b} \quad (11-16)$$

$$f_{tos2} = \frac{2F_{pos}x_p}{l_{y2}l_{tos} h_f - n_{st}d_b} \quad (11-17)$$

Self-Weight Reaction Stress

Analytical modeling has shown that self-weight reaction stress at the end surface of FIB girders can be neglected at locations in the outer portion of the bottom flange. As such, the self-weight reaction stress (f_{sw}) in the serviceability model is assumed to be zero. This assumption may not be reasonable for all cross-sections.

Superposition of Stresses

Horizontal spitting stress is defined as the superposition of Hoyer, peeling, and self-weight reaction stresses:

$$f_{hsp} = f_h + f_{tos} + f_{sw} \quad (11-18)$$

Where:

- f_{hsp} = Horizontal splitting stress
- f_h = Average Hoyer effect stress
- f_{tos} = Peeling stress
- f_{sw} = Self-weight reaction stress

As previously discussed, stress due to self-weight reaction is negligible at the end face of the FIB bottom flange. Self-weight reaction is included in Equation 11-18 only as a reminder

that self-weight effects may be critical in some long-span girders and in girders with other cross-sections. For FIB girders, Equation 11-18 can be reduced to:

$$f_{hsp} = f_h + f_{tos} \quad (11-19)$$

Two critical conditions have been discussed for horizontal splitting stresses. The maximum peeling condition occurs when only the strands outboard of a section are cut. Strands at the section in question are not yet cut in the maximum peeling condition and Hoyer stress on the section is assumed to be zero. The combined condition occurs when strands on a section have been cut and peeling stress is superimposed with Hoyer stress. The maximum horizontal splitting stress on a given section is the greater of the stress from the maximum peeling or combined conditions:

$$f_{hsp1} = f_{tos1} \quad (11-20)$$

$$f_{hsp2} = f_h + f_{tos2} \quad (11-21)$$

Where:

f_{hsp1} = Horizontal splitting stress for maximum peeling condition

f_{hsp2} = Horizontal splitting stress for combined condition

In FIB girders transverse splitting stresses is checked for the five outermost columns of strands (Figure 11-13). Stresses are checked at strand locations because Hoyer stresses are greatest near prestressing strands, and because splitting cracks in the experimental program were observed to intersect strands. Stress is checked at each of the five locations for both of the critical stress conditions. Maximum stress from these locations and conditions is compared to concrete tensile strength criterion, which is discussed later.

Stress Calculations for Experimental Girders

In this section the serviceability model is used to compute stresses at the end of specimen WN (Figure 11-14). The end of specimen WN had two fully bonded strands placed at the outside of the flange. All other strands in the outer flange were shielded.

Hoyer stresses were calculated using Equation 11-8 and are summarized in Table 11-4. The value of interfacial pressure (p) listed in Table 11-4 was calculated using Equation 11-3 and the values from Table 11-1. The calculated Hoyer stress is zero for all but section A. This is because the model assumes that Hoyer stresses from shielded strands are negligible.

Peeling stresses were calculated using Equations 11-16 and 11-17 and are summarized in Table 11-5. Peeling stresses at section B require additional discussion. The maximum peeling condition is intended to have the maximum peeling stress, however, it has a lower peeling stress than the combined condition at section B. This is because empirical equations for the internal moment arm resulted in a shorter arm, and consequently at larger peeling stress, for the combined condition. This limitation of the model only affects section B and is of little concern. As shown later in the chapter, splitting stress at section B does not govern in any of the stress calculations for the experimental specimens. Also, this limitation makes the model conservative at section B because it superimposes the larger peeling stress with the Hoyer stress.

Horizontal splitting stresses were calculated using Equations 11-20 and 11-21 and the stresses from Table 11-4 and Table 11-5. Results are presented graphically in Figure 11-15. The maximum calculated splitting stress at the end of WN occurs at section A during the combined condition. Because no peeling stress occurred at section A, the entire calculated splitting stress is due to the Hoyer effect. Splitting stresses at the other sections in WN are smaller than at section A because Hoyer stress from the shielded strands is assumed to be negligible. Calculated splitting stresses at sections B through E are solely due to peeling stresses caused by the bonded strands at section A.

The same procedures used above for WN were also used calculate transverse splitting stresses for each specimen in the experimental program. Additionally, stresses were calculated for four additional specimens from FIB-63 girders that were constructed at the same time as specimens W, F, and D. Strand shielding patterns for the FIB-63 specimens are shown in Figure 11-16 and Figure 11-17. Complete details of these specimens will be available in a forthcoming FDOT report (Ross et al. in preparation).

The serviceability model was derived for calculating stresses at the end of pretensioned I-girders. To test the applicability of the model to other locations, it was also used to estimate stress in specimens WN, WB, and SL (FIB-63) where shielding terminated.

The maximum transverse splitting stress for each specimen and location are listed in Table 11-6, along with the governing section, governing stress condition, and flange splitting crack data. When stresses were calculated at two locations on the same specimen, crack data were assigned to the location where the cracks were observed in the physical girder. For example, no splitting cracks were observed at the end of specimen WN and the table lists zero for the crack length and area. Splitting cracks were observed 10 ft away from the end of WN, and the table lists the length and area of those cracks in the row labeled "WN (10 ft.)".

From Table 11-6 it can be observed that the combined stress condition governs for each specimen and location. For the combined condition Hoyer stress accounted for 85% of the splitting stress, on average. The remaining 15% (on average) was from peeling stress. This result indicates the significance that the Hoyer effect has on flange splitting cracks.

Section C has the governing (maximum) stress in 12 of 17 specimens and locations. Experimental observations support this result. Flange splitting cracks were more likely to be observed at section C than at any other location in the experimental program. The governing

stress from the model never occurs at sections B or E. This result supports the previous statement that model limitations at section B do not impact overall results.

Model Comparison with Experimental Crack Data

Stresses calculated using the serviceability model correlate well with crack data from the experimental girders (Table 11-6 and Figure 11-18). This can be seen from the linear curve in Figure 11-18 that is fit to the stress and crack data from the specimen ends. The line has an R^2 value of 0.85, indicating a high degree of correlation between calculated stresses and experimental crack lengths. When stress and crack data away from the ends (WN, WB, and SL) are included, correlation drops to 0.73. This suggests that the model is more accurate for calculating stress at member ends than at sections away from the end. Additional data are required, however, to quantify the degree to which the model can reasonably be applied to locations away from the member end.

A high degree of correlation is also observed when the calculated stresses are compared to the area of the flange splitting cracks in the experimental girders (Figure 11-19). Considering the random nature of cracking in concrete this level of correlation suggests that the model does an excellent job of capturing the physical phenomenon which cause bottom flange splitting cracks.

It is common in prestressed concrete design to compare concrete tensile stress to the square root of the compressive strength. Dashed vertical lines in Figure 11-18 and Figure 11-19 indicate 1.20ksi which is equal to $0.47 \sqrt{f'_{ci}}$ (for f'_{ci} in ksi). This value is approximately equal to the x-intercept of the linear curves fit to the data. The x-intercept corresponds to the stress below which flange cracking are unlikely according to the sample data. All but one of the specimens and locations in the sample have stresses higher than this value. The lone location

below this value, SL (5ft.), did not have flange splitting cracks in the experimental girder. A more conservative stress limit, and one that is already used in other circumstances by AASHTO LRFD, is $0.24 \overline{f'_{ci}}$. This is approximately half of the limit indicated by the experimental data. Additional data are required to calibrate the reliability associated with different splitting stress criteria. Nevertheless, available data suggest that the proposed model is an adequate tool for calculating transverse splitting stress in the bottom flange of FIB girders.

Summary and Conclusions

A model was derived for calculating transverse splitting stresses in the bottom flange of FIB girders. The model considers contributions to splitting stress from the Hoyer effect and from the horizontal eccentricity of strands in the outer flange. Stresses due to these effects are referred to as Hoyer stresses and peeling stresses, respectively. Self-weight also contributes to transverse splitting stress, however effects of self-weight are considered negligible in the outer flange of FIB girders. The work of Oh et al (2006) was utilized to derive an equation for Hoyer stress. An equation for peeling stress was derived using FE modeling and basic mechanics. The equation for peeling stress contains empirical relationships that are specific to FIB girders.

The model was compared to crack data from the experimental girders and was found to have a high degree of correlation with said data. An R^2 value of 0.80 was obtained for linear trend line that was fit to the calculated and experimental data. Analysis indicates that flange splitting cracks are likely when the calculated splitting stress exceeds $0.45 \overline{f'_{ci}}$ (for f'_{ci} in ksi). A lower threshold stress is recommended for controlling flange splitting cracks. One possible threshold is $0.24 \overline{f'_{ci}}$, which is currently used by AASHTO LRFD to limit concrete tensile stresses in situations similar to the FIB bottom flange.

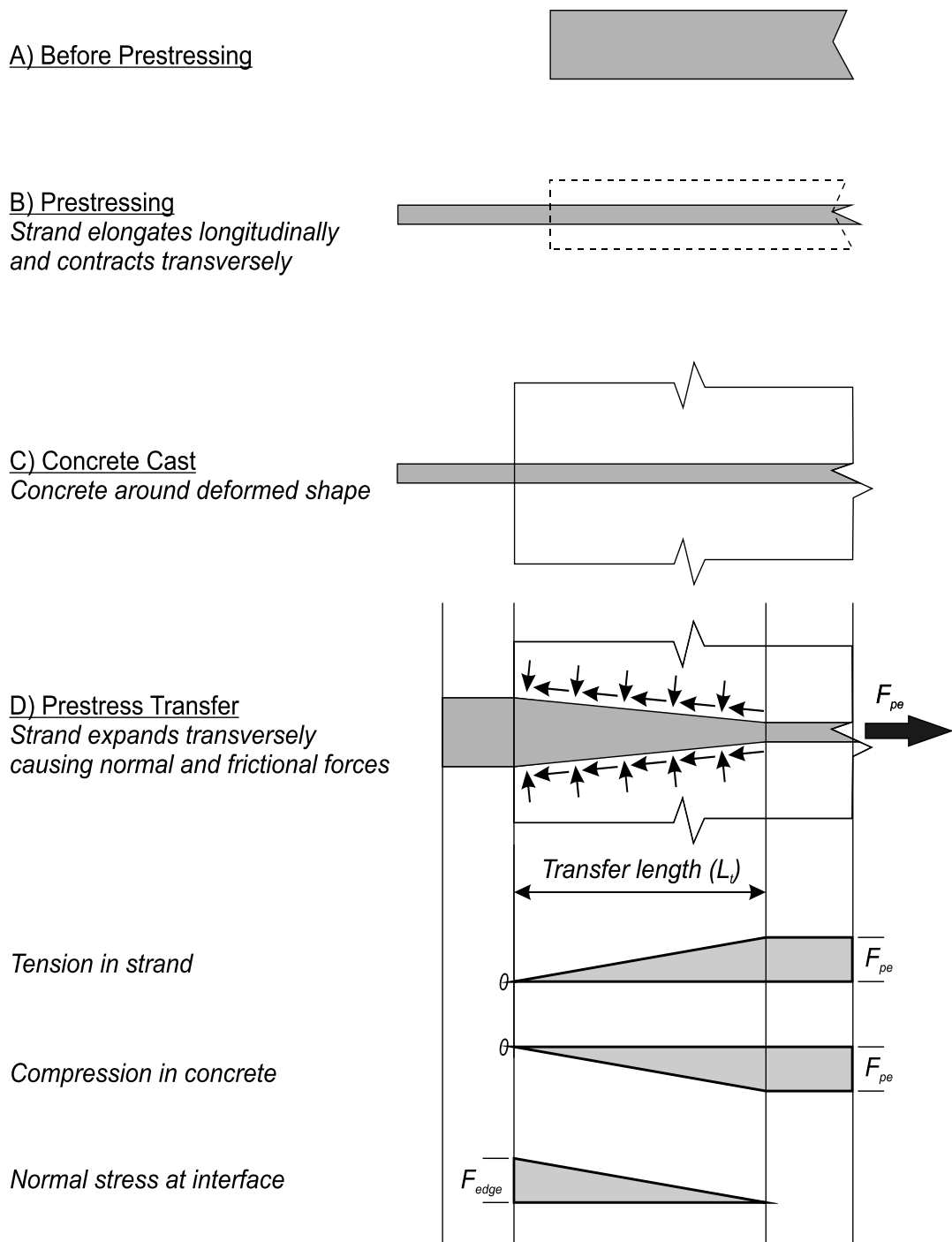


Figure 11-1. Hoyer Effect. A) Strand before stressing, B) Strand after prestressing, C) Concrete cast around strand, D) Stresses and forces after transfer.

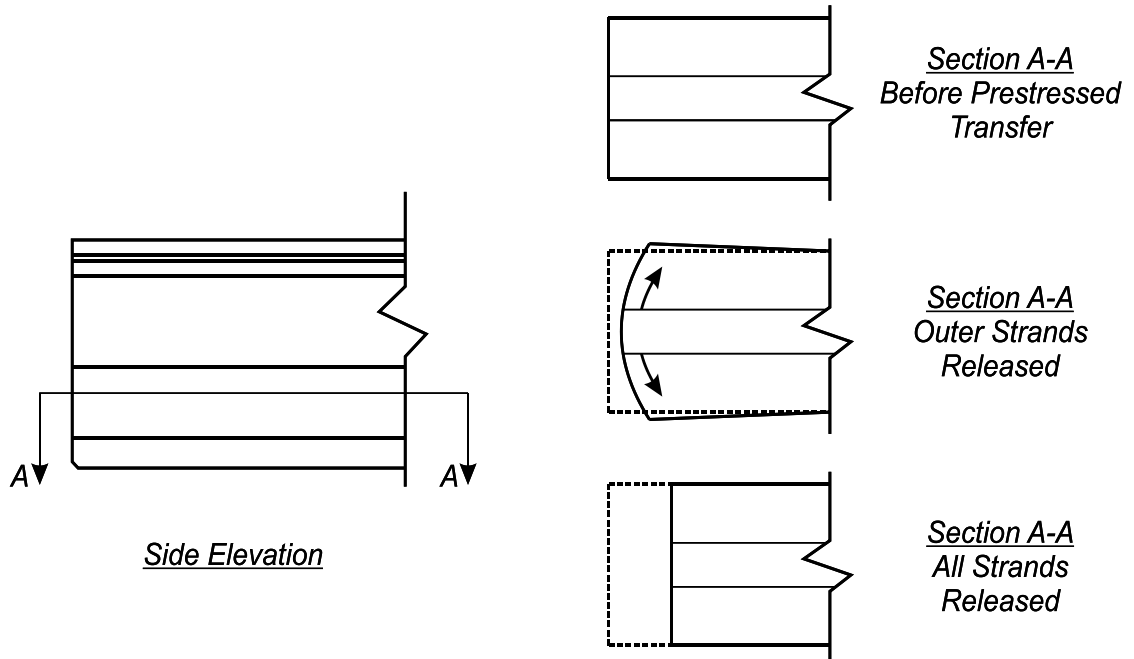


Figure 11-2. Flange tension due to outer strands

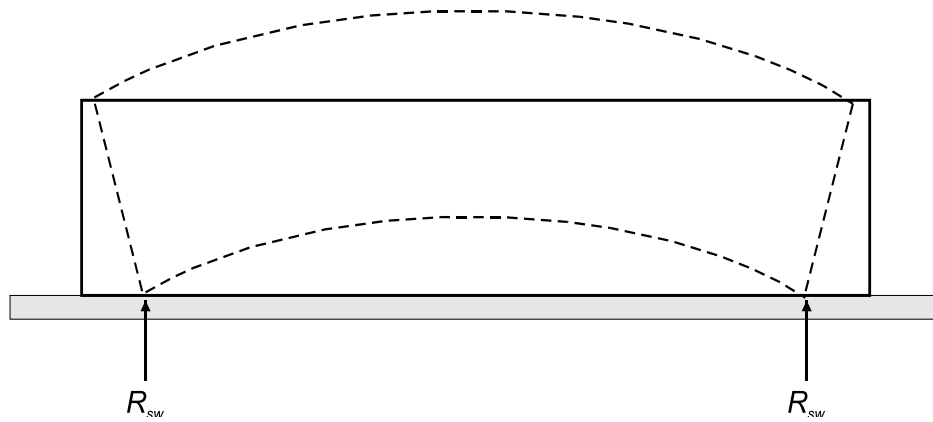


Figure 11-3. Camber due to prestress force

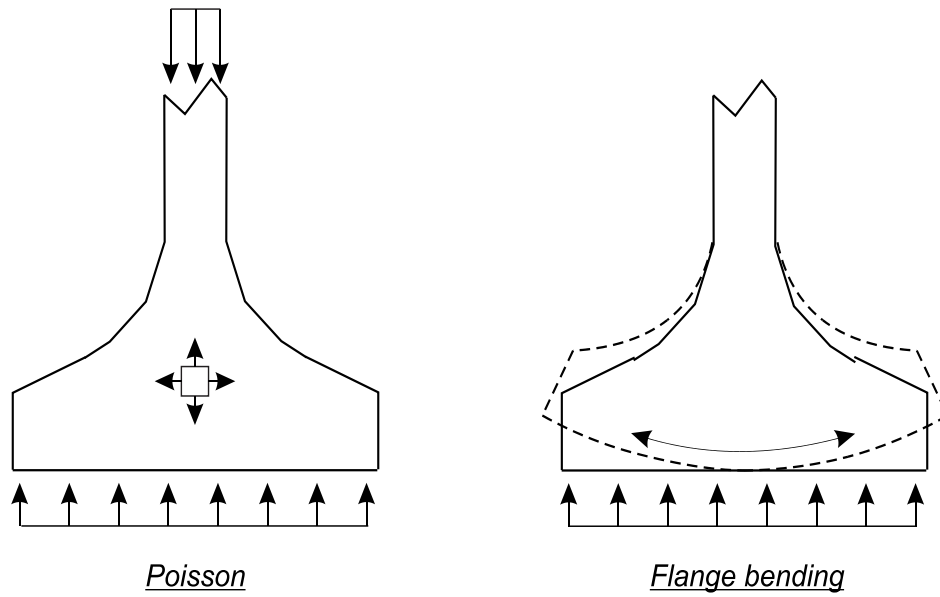


Figure 11-4. Self-weight reaction effects



Figure 11-5. Flange splitting in experimental girder. (Photo courtesy of B.E. Ross)

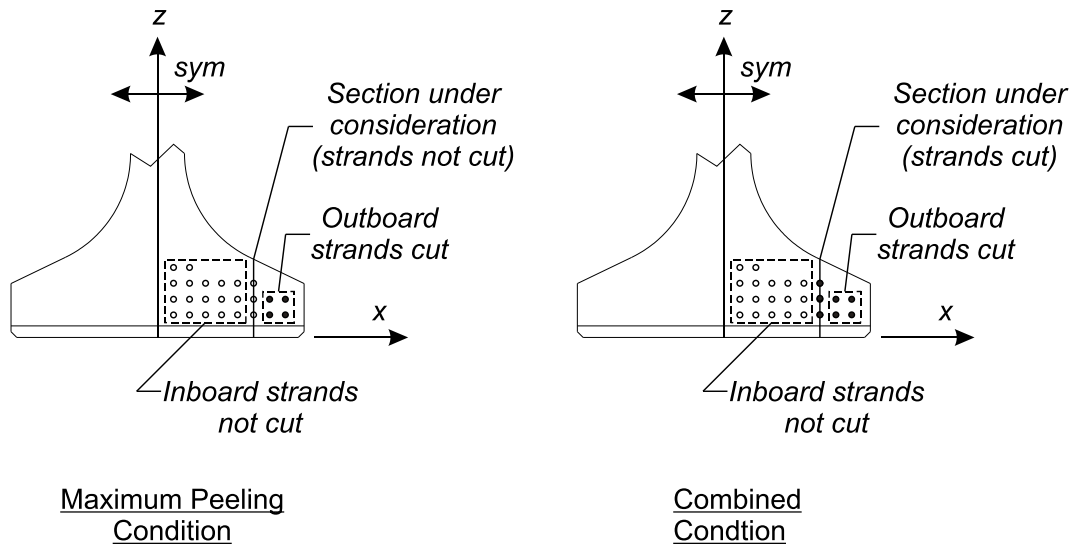


Figure 11-6. Strand cutting conditions

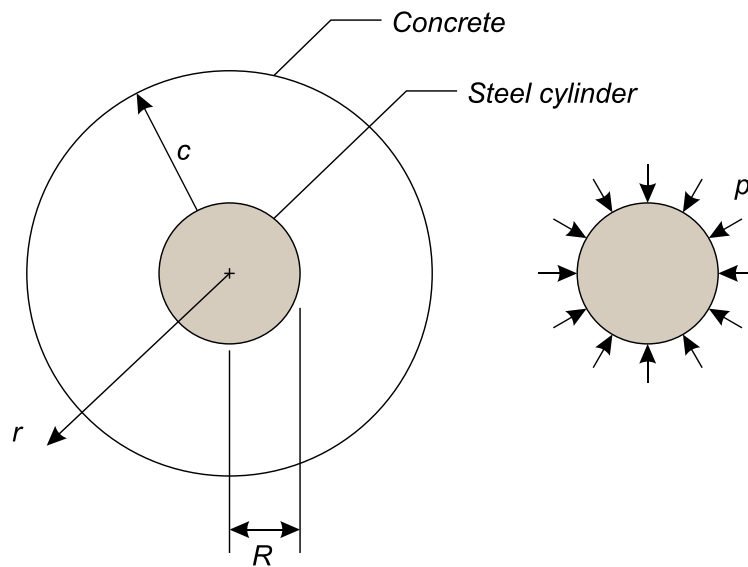


Figure 11-7. Strand physical analog (Based on Oh et al. 2006)

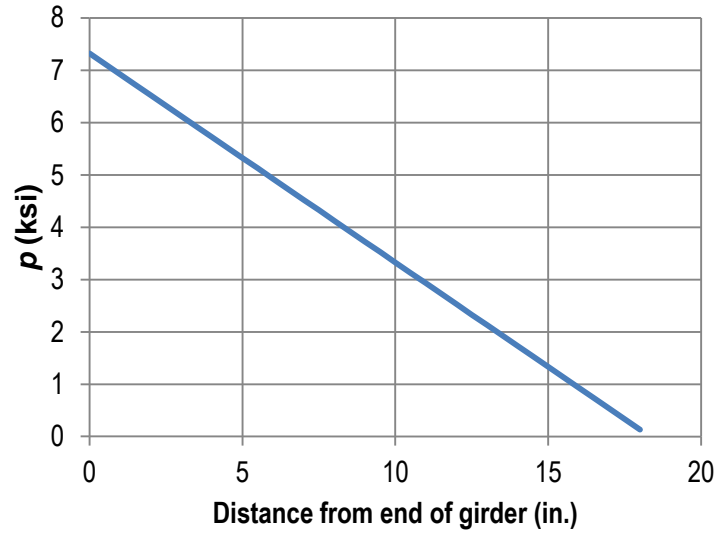


Figure 11-8. Calculated radial stress (p) distribution (Based on Oh et al. 2006)

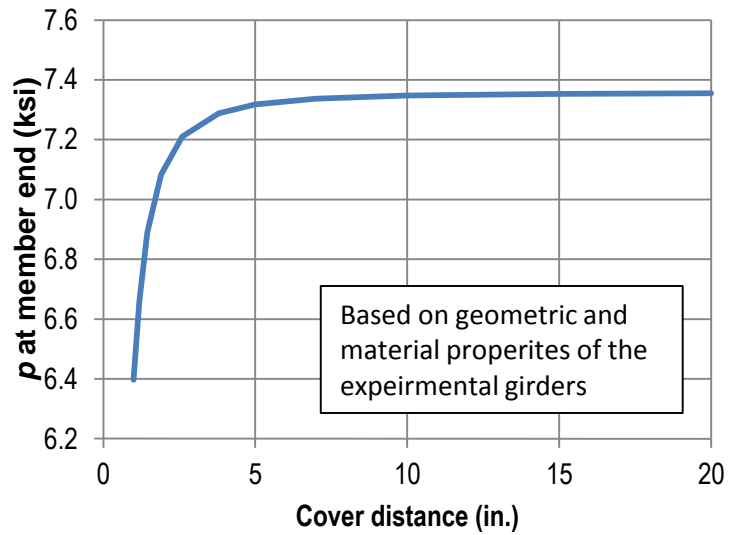


Figure 11-9. Effect of cover distance on calculated radial stress (p)

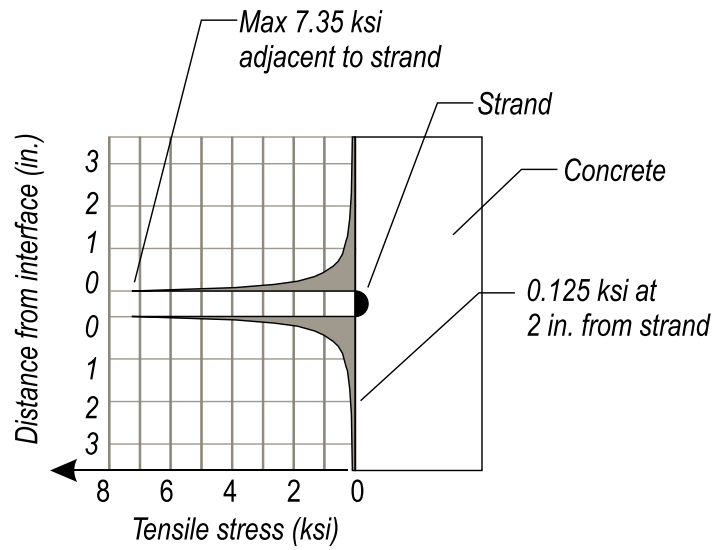


Figure 11-10. Concrete stress distribution due to Hoyer Effect

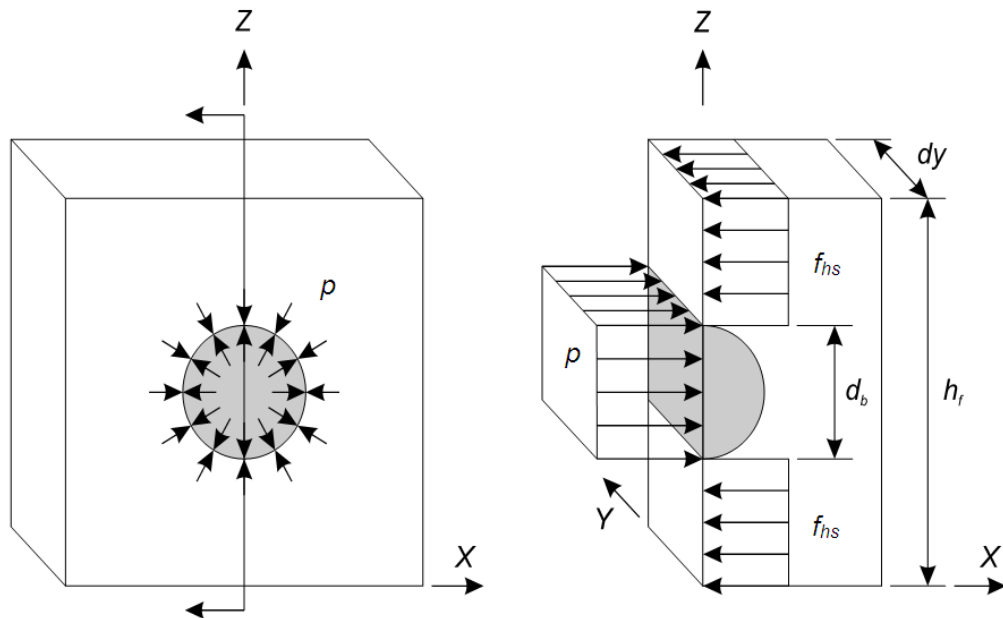


Figure 11-11. Stresses at plane cut through strand and concrete

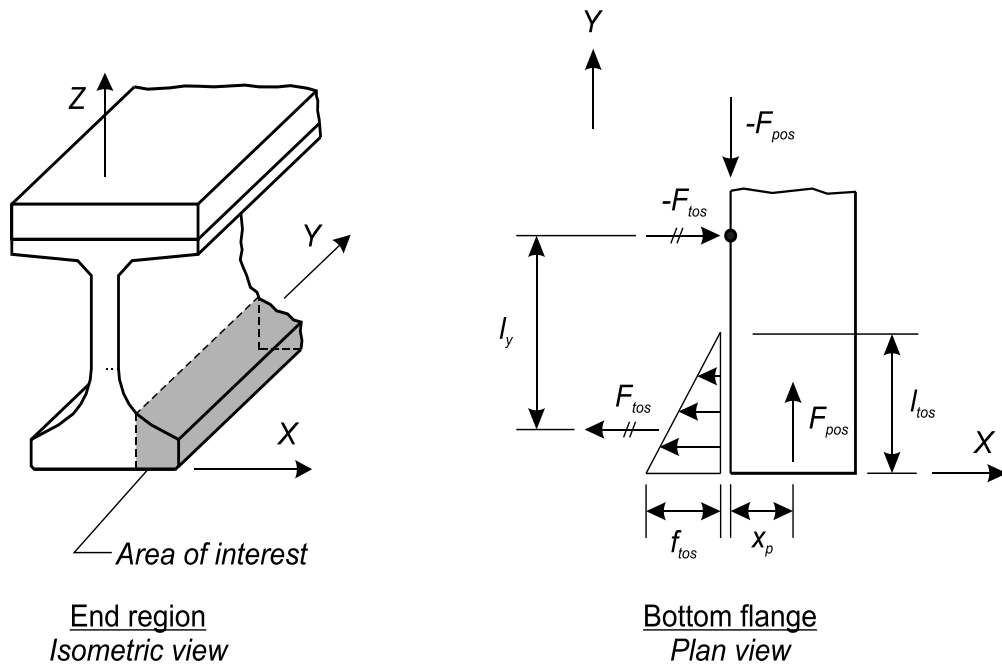


Figure 11-12. Bottom flange free body diagram

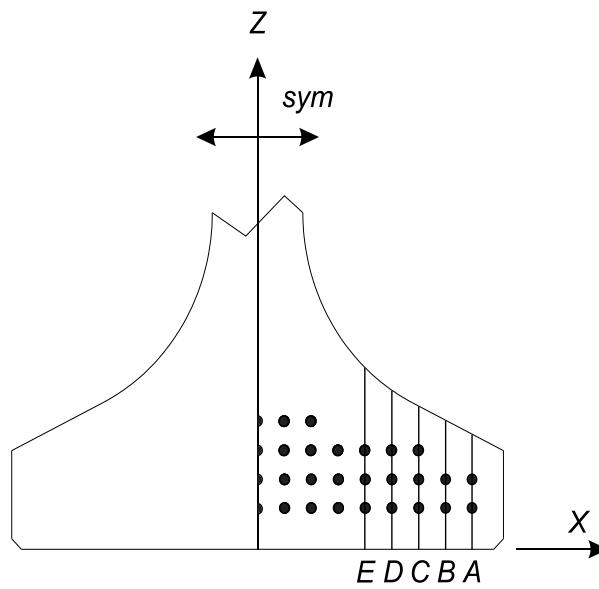


Figure 11-13. Analysis sections for FIB bottom flange

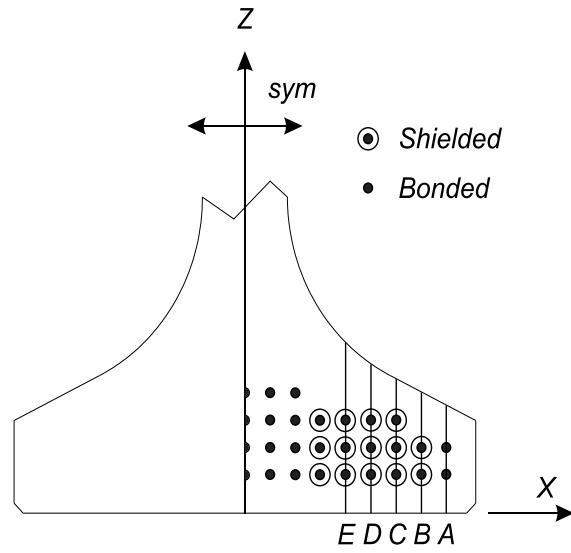


Figure 11-14. Strand bond and shielding pattern specimen WN

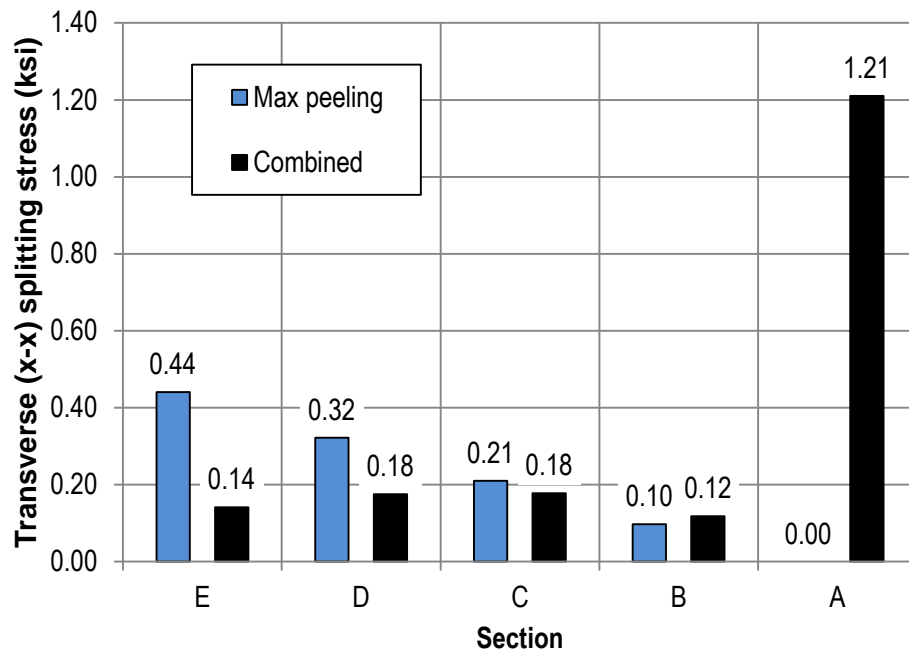
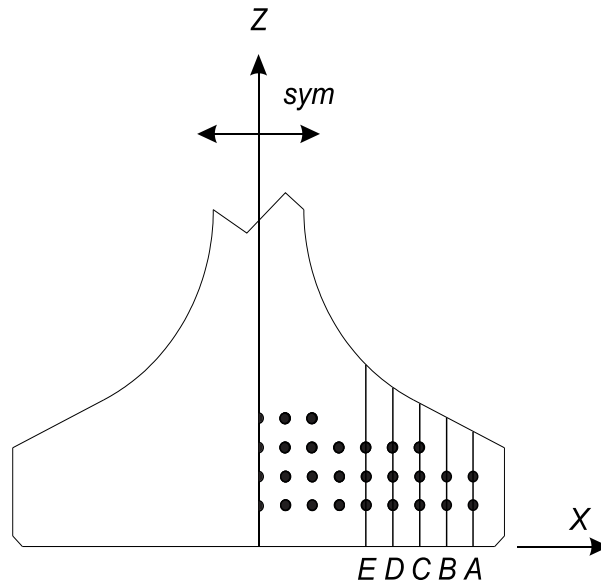


Figure 11-15. Transverse (x-x) splitting stress at end of specimen WN



All strands fully bonded

Figure 11-16. Strand pattern CN, PT, and LB

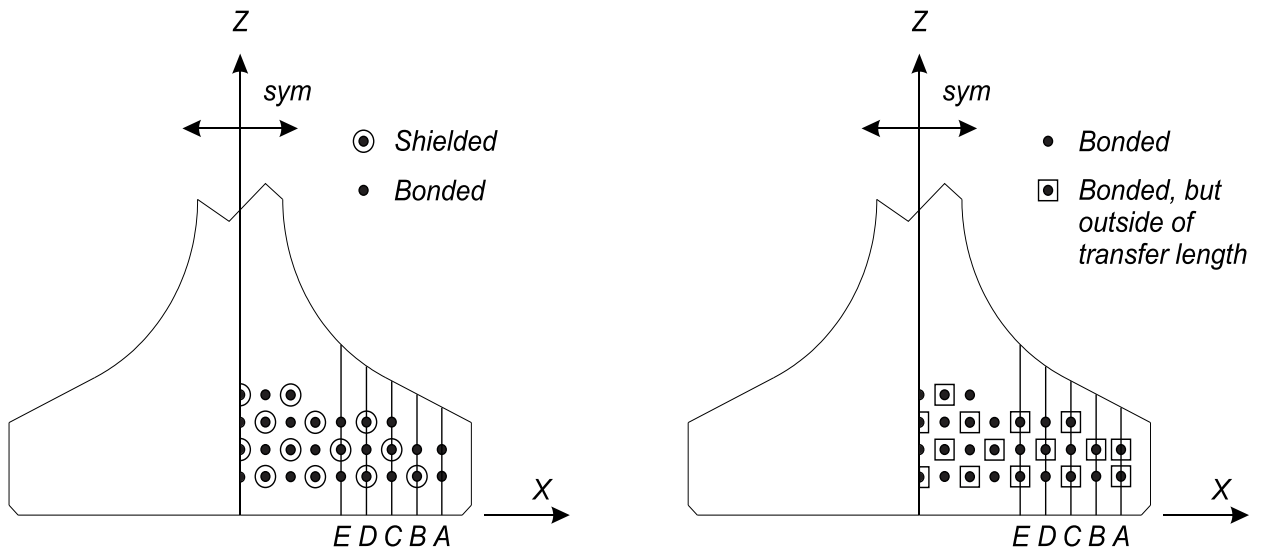


Figure 11-17. Strand pattern SL end (left), SL 5ft from end (right)

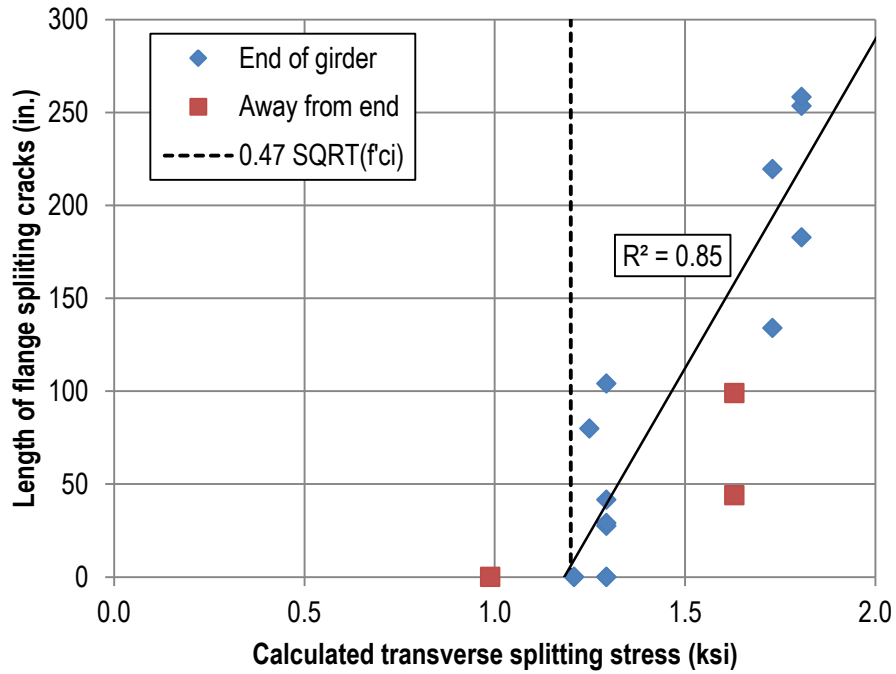


Figure 11-18. Calculated transverse splitting stress vs. experimental crack length

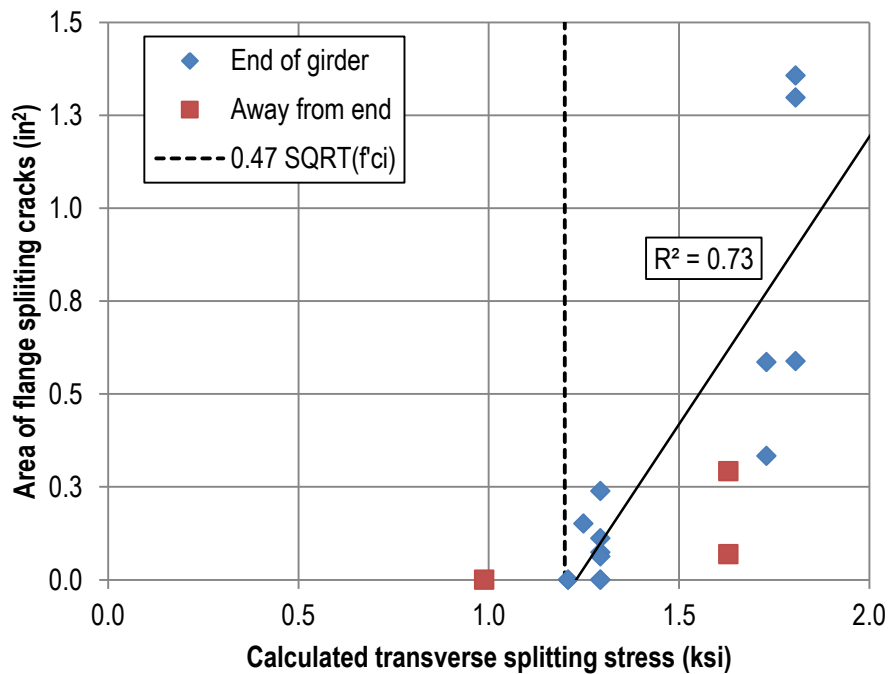


Figure 11-19. Calculated transverse splitting stress vs. experimental crack area

Table 11-1. Strand and concrete properties of experimental girders

Concrete Elastic Modulus	4700 ksi
Concrete Poisson Ratio	0.2
Strand Elastic Modulus	29,000 ksi
Strand Poisson Ratio	0.3
Strand radius prior to jacking	0.3 in.
Strand radius after jacking	0.2994 in.

Table 11-2. Model vs. FE for maximum peeling stress condition

Section	h_f (in.)	x (in.)	l_{y1} (in.)	F_{tos} Model (kip)	F_{tos} FE (kip)	Model / FE
EDGE	10.5	12	46.4	11.4	11.3	1.01
MID	12.9	8	85.5	20.6	20.3	1.01

Table 11-3. Model vs. FE for combined stress condition

Section	h_f (in.)	x (in.)	l_{y2} (in.)	F_{tos} Model (kip)	F_{tos} FE (kip)	Model / FE
EDGE	10.5	12	33.7	15.7	15.9	0.99
MID	12.9	8	45.7	38.5	36.1	1.07

Table 11-4. Hoyer stresses end of specimen WN

Section	n_s	p (ksi)	d_b (in.)	n_{st}	h_f (in.)	f_h (ksi)
A	2	7.36	0.6	2	8.5	1.21
B	0	7.36	0.6	2	8.5	0
C (EDGE)	0	7.36	0.6	3	8.5	0
D	0	7.36	0.6	3	8.5	0
E (MID)	0	7.36	0.6	3	8.5	0

Table 11-5. Peeling stresses at end of specimen WN

Section	F_{pos} (kip)	x_p (in.)	x (in.)	h_f (in.)	n_{st}	d_b (in.)	l_{y1} (in.)	l_{y2} (in.)	f_{tos1} (ksi)	f_{tos2} (ksi)
A	NA	NA	16	8.5	2	0.6	NA	NA	0	0
B	88	2	14	9.5	2	0.6	43.7	36.0	0.097	0.118
C (EDGE)	88	4	12	10.4	3	0.6	38.7	45.9	0.212	0.178
D	88	6	10	11.6	3	0.6	33.4	61.5	0.322	0.175
E (MID)	88	8	8	13.2	3	0.6	28.0	87.5	0.441	0.141

Table 11-6. Transverse splitting stresses and splitting crack data

Specimen	Max transverse splitting stress (ksi)	Section	Critical Condition	Length of flange splitting cracks (in.)	Area of flange splitting cracks (in ²)
HC	1.29	C	Combined	0	0
HU	1.29	C	Combined	40	0.112
VC	1.29	C	Combined	0	0
VU	1.29	C	Combined	41	0.087
WN (10 ft.)	1.63	C	Combined	32	0.05
WB (10 ft.)	1.63	C	Combined	99	0.292
WN (end)	1.21	A	Combined	0	0
WB (end)	1.21	A	Combined	0	0
FN	1.73	D	Combined	190	0.469
FB	1.73	D	Combined	115	0.295
DC	1.29	C	Combined	104	0.239
DM	1.29	C	Combined	41.5	0.112
PT	1.81	C	Combined	142	0.316
LB	1.81	C	Combined	183	0.429
CN	1.81	C	Combined	175	0.368
SL	1.25	C	Combined	73	0.144
SL (5 ft.)	0.99	D	Combined	0	0

CHAPTER 12 CONCLUDING REMARKS

Confinement reinforcement is placed in the bottom flange of pretensioned I-girders to enclose the prestressing strands at member ends. The 2007 AASHTO LRFD Bridge Design Specifications contain prescriptive requirements for the quantity and placement of confinement reinforcement. These requirements are based on limited experimental data and apparently do not have a theoretical underpinning. Available research has demonstrated the beneficial aspects of confinement reinforcement but has not established the function that confinement reinforcement serves. Experimental and analytical work presented in this document address these limitations in the current understanding of confinement reinforcement. Outcomes of the work include:

- An understanding of the functions of confinement reinforcement during prestress transfer and at ultimate load
- An understanding of the interaction between confinement reinforcement and other design variables
- A serviceability design model for the bottom flange at prestress transfer
- An ultimate strength design model for confinement reinforcement

This chapter begins with summaries of the experimental and analytical research programs presented in this document. Conclusions of the programs are then summarized and are discussed in terms of the four outcomes presented above. The final section of this chapter offers design and detailing recommendations for the end region of FIB girders.

Experimental Program Summary

Ten uniquely detailed FIB-54 test specimens were built and tested. Variables in the test program included:

- Presence/absence of confinement reinforcement

- Quantity and configuration of confinement reinforcement
- Presence/absence of end region horizontal reinforcement
- Quantity of end region vertical reinforcement
- Presence/absence of embedded steel bearing plates
- Strand quantity
- Strand placement

Strain data were collected from the concrete and reinforcement during and immediately after prestress transfer. Formation and propagation of cracks in the specimens were monitored during prestress transfer and in the weeks and months following prestress transfer. Effects of the test variables on behavior and cracking were compared using strain and crack data.

Specimens were taken to the FDOT Structures Research Center in Tallahassee, FL, where cast-in-place slabs were poured on the specimens. After the slabs were sufficiently cured, specimens were load tested in three-point bending. Load was applied at a shear span-to-depth ratio of 2.0 to determine ultimate shear capacity. Strain, load, strand-slip, and displacement data were collected during load testing. Data were used to compare the effects of test variables on ultimate capacity and behavior.

Analytical Program Summary

Finite element (FE) modeling was used to analyze girders during prestress transfer and under service loading. FE models were linear-elastic and were intended to capture pre-cracking behavior of the girders. Experimental data were used to validate the FE models. Models compared well with experimental data and were found to effectively capture overall girder behavior as well as the local behavior in the end region. Validated models were then used to conduct parametric studies of prestress transfer and loading. Parametric studies of prestress transfer assumed an outside-in strand cutting pattern. Variables in the parametric studies included:

- Transfer length

- Quantity of cut strands
- Embedded bearing plate
- Self-weight
- Bearing pad width
- Bearing pad stiffness
- Bottom flange geometry

Conclusions

Function of Confinement Reinforcement

Transverse tensile stresses form in the bottom flange of pretensioned I-girders during prestress transfer and during loading. Cracks form in the bottom flange when tensile stress exceeds the concrete tensile strength. Confinement reinforcement is placed in the bottom flange to control concrete cracking and to carry transverse tensile loads after the concrete cracks.

Crack control is a serviceability function of confinement reinforcement and is of primary concern during prestress transfer. During transfer cracks are most likely at the girder ends where transverse splitting stresses are the highest. To best control cracks, confinement reinforcement should be placed as near the member end as practical, and should also be placed throughout the strand transfer length.

At ultimate strength confinement reinforcement carries transverse tension forces. Transverse tension forces can lead to lateral-splitting failure if sufficient bottom flange confinement is not provided. In addition to mitigating lateral-splitting failure, confinement reinforcement also assists in force transfer between strands and concrete, thereby reducing - but not eliminating- the propensity of a girder to fail in bond-shear mode. To best perform these functions confinement reinforcement should be placed throughout the strand transfer length.

Interaction of Variables with Confinement Reinforcement

Embedded steel bearing plates and variations in strand bond pattern have significant effect on the load carried by confinement reinforcement. Embedded steel bearing plates provide additional confinement to the bottom flange of I-girders and decrease load demand on confinement reinforcement. In the test program, the presence of a steel bearing plate reduced forces in confinement reinforcement during prestress transfer by up to 50% relative to forces in specimens without bearing plates. Presence of a steel bearing plate also aided in crack control of flange splitting cracks.

Confinement reinforcement carries transverse tensile forces which occur to eccentric prestress forces from strands in the outer portion of the flange. Thus strand bond patterns with bonded strands in the outer flange create larger load demand on confinement reinforcement than patterns with bonded strands below the web. In the test program, specimens with fully bonded strands in the outer flange had up to 2.3 times more force in the confinement reinforcement during prestress transfer than did specimens with fully bonded strands placed below the web. Flange splitting cracks were also more severe in specimens with strands in the outer flange.

Bottom Flange Serviceability Design Model

A serviceability design model was derived to calculate stresses in the bottom flange of FIB girders during prestress transfer. The model considers stresses due to the Hoyer Effect, eccentric prestressing forces, and girder self-weight. An outside-to-in strand cutting pattern is assumed by the model and the model contains features that were derived empirically for FIB girders. Stresses calculated by the model were found to have excellent correlation ($R^2=0.8$) with flange splitting crack data collected from the experimental girders.

Confinement Reinforcement Ultimate Strength Design Model

An ultimate strength design model was derived to calculate the amount of confinement reinforcement required to anchor prestressing strands at ultimate load and to prevent lateral-splitting failure. Strand anchorage and lateral-splitting criteria are analogous to local-zone and general-zone requirements in post-tensioned concrete structures. The ultimate strength model considers girder geometric properties, prestressing strand layout, and geometric properties of the bearing. The effect of embedded steel bearing plates is included in the model. The model is general enough for application in wide variety of circumstances, as evidenced by favorable comparison with experimental data. Data from the current study and from the experimental results in the literature were used for comparison. In almost all cases the model accurately categorized experimental specimens which failed in lateral-splitting mode.

Recommendations

Confinement reinforcement currently specified by the FDOT (FDOT 2009b) performed well in the research program with respect to serviceability and ultimate strength criteria.

Confinement reinforcement helped to control bottom flange splitting cracks and mitigate lateral-splitting failures. Continued use of the current FDOT confinement detail is recommended. The current detail places confinement over a distance approximately $1.2d$ from the member end and has tighter spacing of reinforcement over the bearing location. Both of these practices are validated by experimental and analytical work presented in this document. In special cases where additional crack control or lateral-splitting capacity is required, #4 bars can be used for confinement reinforcement in lieu of the currently specified #3 bars.

As with confinement reinforcement, embedded steel bearing plates also performed well in the research program with respect to serviceability and strength criteria. Bottom flange splitting cracks were smaller and ultimate strengths were larger in test specimens with bearing plates.

As such, the continued use of steel bearing plates is recommended. Use of longer studs on bearing plates is recommended for future research. It is believed that longer studs engage a greater portion of concrete, thereby providing additional confinement to the bottom flange. Wider (in the direction of the span length) bearing plates are also recommended as a test variable. Wider bearing plates may prevent cracking near the member end, and thereby improve bond-shear capacity.

Of all the variables in the research program, strand quantity and strand shielding pattern had the greatest effect on test specimen behavior and capacity. The following recommendations are made regarding the design of strand layouts and strand shielding patterns:

- Fully bonded strands should be placed as close to the cross-section centerline and with as much top cover as practical. This practice will reduce the likelihood of bottom flange splitting cracks and lateral-splitting failure.
- Placement of fully bonded strands at the outermost location in the third row should be avoided. This location has a high propensity for splitting cracks.
- Current AASHTO LRFD limits on termination of strand shielding at a given section are recommended for controlling flange splitting cracks within the transfer length of partially shielded strands. Confinement reinforcement is believed unnecessary at these locations if shielding termination complies with the AASHTO limits.
- The percentage of shielded strands can reasonably exceed the 25% limit specified by AASHTO LRFD if sufficient reinforcement and strands are provided to meet minimum longitudinal steel requirements at the girder end. As currently specified by AASHTO LRFD, any lack of full development must be considered when evaluating the minimum longitudinal steel.
- Partially shielded strands (when used) should be placed towards the outside of the bottom flange. Clustering of shielded strands below the web is strongly discouraged.
- Prestress force in the outermost strands in the bottom two rows should be reduced from the currently specified level. A prestress force of 10 kip is recommended in order to support reinforcement during fabrication. This practice will reduce the likelihood of bottom flange splitting cracks and lateral-splitting failure.

Final Comments

Pretensioned concrete I-girders have been successfully used in Florida's highway bridges since the 1950s. The recently introduced Florida I-Beam (FIB) presents new opportunities and challenges to Florida's bridge engineers. Because of a relatively wide bottom flange, FIB girders can support more prestressing and can span longer distances than the formerly used AASHTO girders. The wide bottom flange can also be problematic if splitting cracks and lateral-splitting failure are not considered by designers. Confinement reinforcement, embedded bearing plates, and strand bond patterns can be used to control the likelihood of bottom flange splitting cracks and lateral-splitting failure. The serviceability and ultimate strength models presented in this document are tools for designing effective confinement reinforcement, bearing plates, and strand bond patterns. Well-designed FIB girders add to the durability, strength, and efficiency of Florida's highway bridges.

LIST OF REFERENCES

- "AASHTO LRFD Bridge Design Specifications 4th Edition." (2007). American Association of State Highway and Transportation Officials (AASHTO). Washington, DC.
- Aknoukh, A. (2010) "The Effect of Confinement on Transfer and Development Length of 0.7 Inch Prestressing Strands." Concrete Bridge Conference. Phoenix, AZ.
- Barnes, R., Burns, N., and Kreger, M. (1998). "Development Length of 0.6-Inch Prestressing Strand in Standard I-Shaped Pretensioned Concrete Beams." Rep. No. 1388-1, Texas Department of Transportation, Austin, TX.
- Breen, J., Burdet, C., Sanders, D., Wollmann, G. (1991) "Anchorage Zone Reinforcement for Post-Tensioned Concrete Girders". National Highway Cooperative Research Program. Transportation Research Board. Washington, DC.
- "Building Code Requirements for Structural Concrete and Commentary." (2011) *ACI 318-11*, American Concrete Institute (ACI), Farmington Hills, MI.
- Cook, R., Reponen, M. (2008) "Prevention of Splitting Failure at the Ends of Prestressed Beams during Fabrication." Rep. No. BD545-30. Florida Department of Transportation, Tallahassee, FL.
- Csagoly, P. (1991). "A Shear Moment Model for Prestressed Concrete Beams." Rep. No. 9900-1550, Florida Department of Transportation, Tallahassee, FL.
- Deatherage, J., Burdette, E., and Chew, C. (1994). "Development Length and Lateral Spacing Requirements of Prestressing Strand of Prestressed Concrete Bridge Girders." *PCI J*, 39(1), 70-83.
- Englekirk, R. E., and Beres, A. (1994). "Need to develop shear ductility in prestressed members." *Concr.Int*, 16(10), 49-56.
- Fallaha, S. (2009). Telephone and E-mail correspondence with Brandon Ross.
- FDOT. (2008). "Interim Design Standard Index No. 20054." Florida Department of Transportation, Tallahassee, FL.
- FDOT. (2009a). "Temporary Design Bulletin C09-01." Florida Department of Transportation, Tallahassee, FL.
- FDOT. (2009b). "Temporary Design Bulletin C09-03." Florida Department of Transportation, Tallahassee, FL.
- FDOT. (2009c). "Structures Design Guidelines." Florida Department of Transportation, Tallahassee, FL.

- FDOT (2009d). "Interim Design Standard Index No. 20510." Florida Department of Transportation, Tallahassee, FL.
- FDOT. (2010). "Interim Design Standard Index No. 20054A." Florida Department of Transportation, Tallahassee, FL.
- FHWA.(2010) "Federal Highway Administration National Bridge Inventory."
<http://www.fhwa.dot.gov/bridge/nbi/mat09.cfm> (accessed December 1, 2010).
- Hoyer, E. (1939). "Der Stahlasitenbenton [Piano-String-Concrete]", Otto Elsner, Berlin. [In German].
- Kaufman, M. K., and Ramirez, J. A. (1988). "Re-Evaluation of the Ultimate Strength Behavior of High-Strength Concrete Prestressed I-Beams." *ACI Struct.J*, 85(3), 295-303.
- Kuchma, D., Kim, K. S., Nagle, T. J., Sun, S., and Hawkins, N. M. (2008). "Shear tests on high-strength prestressed bulb-tee girders: Strengths and key observations." *ACI Struct.J*, 105(3), 358-367.
- Llanos, G., Ross, B., and Hamilton, H. (2009). "Shear Performance of Existing Prestressed Concrete Bridge Girders." Rep. No. BD 545-56, Florida Department of Transportation, Tallahassee, FL.
- Magus, R. (2010). Brandon Ross notes from pre-construction meeting. Dura-Stress, Leesburg, FL.
- Maruyama, K., and Rizkalla, S. H. (1988). "Shear Design Consideration for Pretensioned Prestressed Beams." *ACI Struct.J*, 85(5), 492-498.
- Morcous, G., Hanna, K., Tadros, M. (2010). "Bottom Flange Reinforcement in NU I-Girders." Nebraska Department of Roads. Lincoln, NE. 2010.
- North American Strand Producers Association (NASP) (2009). "Standard Test for Strand Bond."
- Nolan, S. (2009). Telephone and E-mail correspondence with Brandon Ross.
- Oh, B., Lim, D., Park, S. (1997). "Stress Distribution and Cracking Behavior at Anchorage Zones in Prestressed Concrete Members." *ACI Struct J*, 94(50), 549-557.
- Patzlaff, Q., Morcous, G., Hanna, K., and Tadros, M. (2010). "Bottom Flange Reinforcement of Precast-Prestressed Bridge I-Girders." 2010 Concrete Bridge Conference.
- R&D Inc. (2009). "ADINA." Finite element analysis software version 8.6. Watertown, MA.

- Roberts, C. (1990). "Behavior and Design of Local Anchorage Zone of Post-Tensioned Concrete Members." M.S. Thesis. University of Texas. Austin, TX.
- Ross, B., Hamilton, H., Consolazio, G. (2011a). "Experimental and Analytical Evaluations of Confinement Reinforcement in Pretensioned Concrete Beams." *Trans Research Record*. 2251, 59-67.
- Ross, B., Ansley, M., Hamilton, H. (2011b). "Load Testing of 30-year-old AASHTO Type III Highway Bridge Girders." *PCI J*, 56(4), 152-163.
- Ross, B. Hamilton, H., Consolazio G. "End Region Detailing of Pretensioned Concrete Bridge Girders." Florida Department of Transportation. Tallahassee, FL. (In preparation)
- Russell, B. W., and Burns, N. H. (1996). "Measured transfer lengths of 0.5 and 0.6 in. strands in pretensioned concrete." *PCI J.*, 41(5), 44-65.
- Shahawy, M., Robinson, B., and deV Batchelor, B. (1993). "An Investigation of Shear Strength of Prestressed Concrete AASHTO Type II Girders." Florida Department of Transportation, Tallahassee, FL.
- Tadros, M., Badie, S., Tuan, C. (2010) "Evaluation and Repair Procedures for Precast/Prestressed Concrete Girders with Longitudinal Cracking in the Web." National Cooperative Highway Research Program, Report 654. Transportation Research Board. Washington, DC. 2010.
- Yura, J., Kumar, A., Yakut A., Topkaya, C., Becker, E. and Collingwood, J. (2001) "Elastomeric Bearing Pads: Recommend Test Methods." National Cooperative Highway Research Program report 449. Transportation Research Board. Washington, DC. 2001.

BIOGRAPHICAL SKETCH

Brandon E. Ross hails from the great state of Wyoming. He attended the University of Wyoming, earning a Bachelor of Science in architectural engineering (2001) and a Master of Science in civil engineering (2002). Upon completion of his degrees at the University of Wyoming he worked as a structural engineer for PCS Structural Solutions of Seattle, WA, and Engineering Systems Solutions (ES²) of Idaho Falls, ID. He obtained a Professional Engineer (Idaho #12054) license in 2005. A marquee project from his early career was the structural design of *Our Lady of the Snows* Catholic Church in Sun Valley, ID. The decision to pursue a PhD. and academic career was based on Brandon's love of research and of mentoring young engineers. The decision to pursue a PhD. at the University of Florida was based on Brandon's love of the beach. Brandon is married to Michelle (Stone), an accomplished choral conductor. The couple has three children. Brandon has accepted a position at Clemson University as an Assistant Professor and will begin fall semester 2012.